Cellular Signaling Events Serving at the Interface of Cognition, Stress, and Circadian Clock Entrainment

Dissertation

Presented in Partial Fulfillment of the Requirements for the Degree Doctor of Philosophy in the Graduate School of The Ohio State University

By

Sydney Aten

Graduate Program in Neuroscience
The Ohio State University

2021

Dissertation Committee

Dr. Min Zhou, Advisor

Dr. John Oberdick

Dr. Dana McTigue

Dr. Jonathan Godbout

Dr. Jason Wester

Abstract

Cellular signaling events are integral processes that govern the activity of cells throughout the body and help coordinate key physiological and behavioral processes within organisms. Indeed, the capacity for cells to relay external signals and convert those signals into information that leads to the actuation of signal transduction pathways /induction of genes that mediate a variety of behavioral responses, is crucial to the maintenance of homeostasis within an organism. Such signaling events serve at the interface of complex processes such as circadian clock timing, in addition to cognition and stress—topics that are covered in this dissertation.

The suprachiasmatic nucleus (SCN) of the hypothalamus serves as the master circadian timekeeper within the brain. This pacemaker allows for the maintenance of circadian rhythms—endogenous 24-hour oscillations found in nearly every system within the body which enables organisms to adapt to external light timing cues. Notably, in the SCN (and in ancillary brain regions that also express core circadian clock genes), several signaling pathways are involved in the modulation of the transcriptional translational feedback loop (TTFL)—an auto-regulatory model wherein circadian clock genes are negatively regulated by their protein products. One of these pathways is the extracellular signal-regulated kinase (ERK)/mitogen activated protein kinase (MAPK) cellular signaling cascade—a pathway that is central to the light entrainment process, which also

serves as a link to higher functions such as cognition and mood. In this dissertation, I utilize a host of knockout and transgenic mouse models to expand upon and discuss how the ERK/MAPK pathway and downstream transcription factors such as CREB (cAMP response element-binding protein) and CREB-regulated small, non-coding microRNAs affect circadian clock timing, cognition, and mood. I first present evidence that SynGAP-- a GTPase-activating protein that serves as a negative regulator of Ras/ERK signaling—is expressed in the SCN and regulates circadian-gated locomotor activity and light entrainment capacity. I also show that individuals with *Syngap1* gene mutations have alterations in sleep—a circadian-gated process **(Chapter 2).** I then demonstrate how circadian clock timing can influence learning and memory. Along these lines, I show that the CREB-regulated microRNA-132 oscillates within the hippocampus (a region known to underlie cognition) and how the dysregulation of the microRNA-132/212 locus alters circadian-gated cognitive capacity **(Chapter 3).** Furthermore, I show that the miR-132/212 locus is induced by stress and that its dysregulation also influences anxiety-related behaviors **(Chapter 4).** Given that dysregulation of circadian timing is widely recognized as a core feature of individuals with Major Depressive Disorder, I then expand upon the current understanding of the cellular-level relationship between clock dysregulation and depressive-like behaviors by profiling circadian clock timekeeping capacity after an Unpredictable Chronic Mild Stress (UCMS) paradigm **(Chapter 5).**

Using the same UCMS (mouse model of depression), I also show how a type of non-neuronal cell within the brain—astrocytes—are affected by this chronic stress protocol. Along these lines, I provide evidence that anatomical and functional

impairments are observed in the astrocyte syncytial network—which is established within the brain via gap junction coupling **(Chapter 6).** Finally, I use serial blockface scanning electron microscopy (SBF-SEM) to examine the ultrastructure of astrocyte-neurite contacts within the murine hippocampus **(Chapter 7).** Taken together, these results provide further support for the role(s) of the ERK/MAPK pathway and CREB-dependent microRNA-132 in circadian clock entrainment, cognition, and stress. They also provide novel insights regarding how chronic stress can lead to perturbations in astrocyte morphology and astrocytic gap junction coupling, and the ultrastructural studies raise interesting questions about astrocyte-neurite interactions within the brain.

Acknowledgments

I would first like to extend my deepest thanks to my advisor, Dr. Min Zhou. Thank you so much for taking me in and for being supportive and encouraging as you helped me develop as a scientist and finish graduate school. My gratitude also extends to Dr. Karl Obrietan: thank you for allowing me to train in your lab. I am grateful for all the fantastic science that I was able to perform over the years.

I would also like to thank my amazing dissertation committee. I truly cannot thank you all enough for supporting me during challenging times in graduate school. To Dr. Dana McTigue: thank you for being my role model and mentor. Your support over the last year has meant so much to me. To Drs John Oberdick and Jonathan Godbout: thank you for helping me with numerous stress and circadian projects over the years – your scientific advice and mentorship was invaluable (and thank you for mentoring me during both my undergraduate AND graduate studies, Dr. Oberdick!) To Dr. Jason Wester: thank you for providing your expertise for many of my projects, for your willingness to listen to some of my ideas, for your mentorship over the last 18 months, and for your overall excitement about science. My ‘thanks’ also extends to Dr. Laurence Coutellier who served on my candidacy committee.

Additionally, I want to thank my senior graduate student/research scientist mentors for their scientific knowledge, wisdom, and technical/experimental support: Dr.

Diego Alzate-Correa, Dr. Kaitlin Snider, Dr. Katelin Hansen, Dr. Conrad Kiyoshi, Dr. Yixing Du, and Dr. Kelin Wheaton—you are all remarkably talented scientists, and I was so lucky to have the opportunity to work alongside each of you. I would also like to thank former labmates, rotation students, and NGP classmates/friends for all of the wonderful times we shared together: To Dr. Chloe Page, Dr. Kyle Sullivan, Paul Horning, Josh Rieskamp, Ashley Garcia, June Yoon, Anisha Kalidindi, Meretta Hanson, Olivia Taylor, Courtney Dye, Susan Xu, Dany Boyle, and Yen Anh Nguyen: thanks for making me laugh so hard that I cried on countless occasions. I also want to give my deepest thanks to Toni Stubbs for being my rock during my last year of grad school. To Isabella Palazzo and Alex Campbell: thank you for being awesome classmates and for allowing me to borrow behavioral testing equipment for many of my projects (in addition to various reagents that I came to you, scrambling for, when I ran out...). To Matthew Thomas, Kelsey Collins, Lindsey Trank, Hannah Galinger, Michaela Witt, Jasmine Liu, and Devin Mediratta: I was so lucky to have the opportunity to mentor you during your undergraduate research endeavors—you are all so dedicated, intelligent, and fun to be around. I can't wait to see the fantastic things that you'll do in the future.

The Neuroscience Department/Neuroscience Graduate Program administrators also have my deepest gratitude. To Melissa Stenger, Kelsey Wheeler, Phoebe Long, and Keri Knowles: Thank you so much for your support during my graduate studies. I am grateful for all of your help over the years. I would also like to give a shout-out to Drs Judy Hickman-Davis and Toi Collins, and to Steve Ogden, Emily Filippone, Beth

Makley, and the many other veterinarians and laboratory animal technicians for helping to take care of all of my animals during my time here at OSU.

I also want to thank all of my co-workers/employers at Sitting Made Simple, Panera Bread, OSU coffee shops, and Wilce Student Health Center for financially supporting me throughout my undergraduate career so that I could pursue graduate studies.

Most importantly, I'd like to thank my family for teaching me compassion, hard work, and resilience. I couldn't have done it without your unwavering support and guidance. I am incredibly thankful for all the sacrifices that you made so that I could have the privilege to attend graduate school and further my education.

Vita

Lakota East High School ……..2013

B.S. Molecular/Cellular Neuroscience; Ohio State University ……2016

M.S. Neuroscience; Ohio State University ……...2019

Graduate Research Fellow; Ohio State University…….……...2018-2020

Graduate Research Associate; Ohio State University…….……..2021

Publications

Kiyoshi CM[#], **Aten S[#],** Arzola EP, Taylor AT, Du Y, Guiher AM, Philip M, Gerviacio Camacho E, Mediratta D, Collins K, Benson E, Kidd G, Terman D, Zhou M. (2021). Ultrastructural view of astrocyte-astrocyte and astrocyte-synapse contacts within the hippocampus. *BioRxiv* https://doi.org/10.1101/2020.10.28.358200/Under review.

Alzate-Correa DF, **Aten S**, Campbell M, Hoyt KR, Obrietan K. (2021). Light-induced changes in the suprachiasmatic nucleus transcriptome regulated by the ERK/MAPK pathway. *Under review—PLOS One.*

Safa A[#], Lau AR[#], **Aten S[#]**, Bales KL, Miller VA, Fitzgerald J, Chen M, Hill K, Dzwigalski K, Obrietan K, Phelps MA, Schilling K, Sadee W, and Oberdick J. (2020). Pharmacological prevention of neonatal withdrawal in a guinea pig model of neonatal opioid withdrawal syndrome. *Front. Pharmacol,* 11:613328.

Aten S, Kalidindi A, Yoon H, Rumbaugh G, Hoyt KR, Obrietan K. (2021). SynGAP is expressed in the murine suprachiasmatic nucleus and regulates circadian-gated locomotor activity and light entrainment capacity. *Eur J Neurosci*, 53: 732-749.

Wang Q, Wang W, **Aten S**, Kiyoshi CM, Du Y*, Zhou M*. (2020). Epileptiform Neuronal Discharges Impair Astrocyte Syncytial Isopotentiality in Acute Hippocampal Slices. *Brain Sci*, 10: 208.

Aten S, Page CE, Kalidindi A, Wheaton KL, Niraula A, Godbout JP, Hoyt KR, Obrietan K. (2018). Data highlighting the expression of two miR-132/212 target genes-Sirt1 and Pten-after chronic stress. *Data Brief.* 21: 2323-2329.

Aten S, Page CE, Kalidindi A, Wheaton K, Niraula A, Godbout JP, Hoyt KR, Obrietan K. (2019). miR-132/212 is induced by stress and its dysregulation triggers anxiety-related behavior. *Neuropharmacology.* 144: 256-270.

Wheaton KL, Hansen KF, **Aten** S, Sullivan KA, Yoon H, Hoyt KR*, Obrietan K*. The Phosphorylation of CREB at Serine 133 Is a Key Event for Circadian Clock Timing and Entrainment in the Suprachiasmatic Nucleus. (2018). *J Biol Rhythms*, 33: 497-514.

Aten S, Hansen KF, Snider KH, Wheaton K, Kalidindi A, Garcia A, Alzate-Correa D, Hoyt KR, Obrietan K. (2018). miR-132 couples the circadian clock to daily rhythms of neuronal plasticity and cognition. *Learn Mem*, 25: 214-229. Cover article.

Wheaton K, **Aten S**, Quieroz LS, Sullivan K, Hoyt KR*, Obrietan K*. (2018). Circadian expression and functional characterization of PEA-15 within the mouse suprachiasmatic nucleus. *Eur J Neurosci*, 47: 845-857.

Choi YS, Horning P, **Aten S**, Karelina K, Alzate-Correa D, Arthur JSC, Hoyt KR, Obrietan K. (2017). Mitogen- and Stress-Activated Protein Kinase 1 Regulates Status Epilepticus-Evoked Cell Death in the Hippocampus. *ASN Neuro*, 9: 175909141772660.

Aten S, Hansen KF, Hoyt KR, Obrietan K. (2016). The miR-132/212 locus: a complex regulator of neuronal plasticity, gene expression and cognition. *RNA & Disease*, 3: e1375.

Choi YS, Lee B, Hansen KF, **Aten S**, Horning P, Wheaton KL, Impey S, Hoyt KR, Obrietan K. (2016). Status epilepticus stimulates NDEL1 expression via the CREB/CRE pathway in the adult mouse brain. *Neuroscience*, 331: 1-12.

Snider KH, Dziema H, **Aten S**, Loeser J, Norona FE, Hoyt K, Obrietan K. (2016). Modulation of learning and memory by the targeted deletion of the circadian clock gene Bmal1 in forebrain circuits. *Behav Brain Res*, 308: 222-235.

Hansen KF, Sakamoto K, **Aten S**, Snider KH, Loeser J, Hesse AM, Page CE, Pelz C, Arthur JS, Impey S, Obrietan K. (2016). Targeted deletion of miR-132/-212 impairs memory and alters the hippocampal transcriptome. *Learn Mem*, 23: 61-71. Cover article.

Fields of Study

Major Field: Neuroscience

Table of Contents

List of Tables

List of Figures

List of Abbreviations

SCN	Suprachiasmatic nucleus
TTFL	Transcriptional translational feedback loop
ERK	Extracellular signal regulated kinase
MAPK	Mitogen activated protein kinase
CRE	cAMP response element
CREB	cAMP response element binding protein
miR	microRNA
UCMS	Unpredictable chronic mild stress
SBF-SEM	Serial blockface scanning electron microscopy
CNS	Central nervous system
PKA	Protein kinase A
PKC	Protein kinase C
IEG	Immediate early gene
GEF	Guanine exchange factor
GAP	GTPase activating protein
GC	Glucocorticoid
AMPAR	α-amino-3-hydroxy-5-methyl-4-isoxazolepropionic acid receptor
GABA	Gamma-aminobutyric acid
DOPAC	3,4-Dihydroxyphenylacetic acid
TH	Tyrosine hydroxylase
NAcc	Nucleus accumbens

VTA	Ventral tegmental area
NMDA	N-methyl-D-aspartate
HPA	Hypothalamic pituitary adrenal
shRNA	short hairpin RNA
RISC	RNA-induced silencing complex
UTR	Untranslated region
CA1	Cornu ammonis-1
Tet	Tetracycline
LTP	Long term potentiation
WT	Wild-type
PCR	Polymerase chain reaction
DAB	3,3'- diaminobenzidine
PBS	Phosphate buffered saline
PBST	Phosphate buffered saline (with Triton)
NGS	Normal goat serum
IgG	Immunoglobulin G
IgY	Immunoglobulin Y
aCSF	Artificial cerebral spinal fluid
HBSS	Hanks' balanced salt solution
BSA	Bovine serum albumin
CT	Circadian time
SDS-PAGE	Sodium dodecyl sulfate polyacrylamide gel electrophoresis

ECL	Enhanced chemiluminescence
ZT	Zeitgeber time
DD	Constant darkness (dark/dark)
LD	Light/dark
LL	Constant lighting
ASD	Autism spectrum disorder
TF	Transcription factor
CaMKII	Ca^{2+}/calmodulin-dependent protein kinase II
PRC	Phase response curve
GTP	Guanosine triphosphate
GDP	Guanosine diphosphate
RHT	Retinohypothalamic tract
EPSC	Excitatory postsynaptic current
FISH	Fluorescent in situ hybridization
PFA	Paraformaldehyde
LNA	Locked nucleic acid
CT (PCR)	Cycle threshold
CA3	Cornu ammonis-3
GCL	Granule cell layer
SEM	Standard error of mean
KO	Knockout
cKO	Conditional knockout

NOL	Novel object location
RT-qPCR	Quantitative reverse transcription polymerase chain reaction
CFC	Contextual fear conditioning
DI	Discrimination index
snRNA	Small nuclear RNA
NAD	Nicotinamide adenine dinucleotide
IHC	Immunohistochemistry
mRNA	Messenger RNA
CFP	Cyan fluorescent protein
tTA	Tetracycline transactivator
PVN	Paraventricular nucleus
BNST	Bed nucleus of the stria terminalis
E/I	Excitation/inhibition
PI3K	Phosphoinositide 3-kinase
AKT	Protein kinase B
mEPSC	Mini excitatory postsynaptic current
UCMS	Unpredictable chronic mild stress
GFP	Green fluorescent protein
ROI	Region of interest
MDD	Major depressive disorder
BAC	Bacterial artificial chromosome
CUBIC	Clear, unobstructed brain/body imaging cocktails

NDS	Normal donkey serum
PFC	Prefrontal cortex
Vm	Membrane potential
OFT	Open field test
TST	Tail suspension test
SST	Sucrose splash test
U0126	1,4-diamino-2,3-dicyano-1,4-bis (2-aminophenylthio) butadiene
PAP	Perisynaptic astrocyte process
ANOVA	Analysis of variance
PACAP	Pitutiary adenylate-cyclase activated polypeptide
MRD5	Mental retardation, autosomal dominant 5
mTOR	Mechanistic (previously ‘mammalian’) target of rapamycin
NORD	National Organization of Rare Disorders

CHAPTER 1

General Introduction

Cellular signaling pathways, small non-coding RNAs, and various cell types (both neuronal and non-neuronal) are involved in the regulation of various aspects of mammalian physiology and behavior including learning and memory capacity, stress regulation, and entrainment of the body's circadian clock. The work presented in this dissertation is focused on detailing how a negative regulator of the ERK/MAPK pathway influences circadian clock timekeeping capacity and how the microRNA miR-132 influences time-of-day (i.e. circadian) dependent cognition within the forebrain. I also branch out and provide novel insights into how miR-132 expression can regulate anxiety and stress response, and how circadian clock gene expression is altered by chronic stress. Furthermore, I extend upon these findings by examining how astrocytes—non-neuronal cells within the CNS—are altered by chronic stress and how gap junction coupling is weakened by a chronic stress paradigm. Indeed, having a better understanding of the mechanisms that underlie these physiological and behavioral processes (i.e. cognition, stress, and clock entrainment capacity) may aid in the design of chronotherapeutic treatments and in the identification of non-neuronal targets that could be harnessed to help treat many neuropsychiatric disorders.

Circadian Clock Timing within the SCN—an Overview

Nearly every aspect of mammalian physiology and behavior is shaped by a ~24 hour (i.e. circadian) rhythm. Importantly, this biological timekeeping process—formed by a transcription/translation feedback loop—is intrinsic and self-sustaining, functioning to adjust the body to geophysical time, even in the absence of a zeitgeber, or external timing cue (as reviewed in the following papers: Buhr and Takahashi, 2013; Ko and Takahashi, 2006)). At the core of this feedback loop is a basic helix-loop-helix transcription factor heterodimer formed by CLOCK and BMAL1. This activator complex functions to drive the expression of *period (per1 and per2)* and *cryptochrome (cry1 and cry2)* gene families. After dimerizing, PER and CRY—serving as a repressor complex—then translocate to the nucleus to inhibit the CLOCK:BMAL1 dimer, thus negatively regulating their own transcription (Sangoram et al., 1998a; Shearman et al., 2000). Degradation of the PER: CRY complex occurs via a phosphorylation and ubiquitin-dependent degradation pathway, relieving the repressive effect of the CLOCK:BMAL1 complex and allowing for a second round of *Per1* and *Cry* gene expression to occur in order to generate a ~24 hour rhythm. Though this cell autonomous, auto-regulatory feedback loop is controlled by four main clock genes, the pace and amplitude of the circadian oscillator is controlled by many additional regulatory mechanisms (for review, see the following: Nicolas Cermakian and Sassone-Corsi, 2000; Partch et al., 2014; Zheng and Sehgal, 2012a)).

Here, it should also be noted that while this core transcription translation feedback loop (TTFL) is (for the most part) self-sustaining, several key kinases such as protein kinase A (PKA), protein kinase C (PKC) and the ERK/MAPK cellular signaling cassette

also influence its maintenance and function (Bonsall and Lall, 2013; Impey et al., 1998; Jakubcakova et al., 2007; K. Obrietan et al., 1998a; Tischkau et al., 2000) (a topic that will be discussed in greater detail below). Furthermore, an additional feedback loop, which is believed to improve the amplitude and robustness of the canonical TTFL (described above) is mediated by the nuclear receptors Rev-erbα and RORα. These two nuclear receptors compete for the binding to the BMAL1 promoter to activate tis transcription, which is critical to for the proper maintenance of core circadian clock machinery (Akashi and Takumi, 2005; Guillaumond et al., 2005; Preitner et al., 2002; Sato et al., 2004).

Role of the ERK/MAPK Pathway in SCN Circadian Clock Timing and Entrainment

The p44/42 mitogen activated protein kinase (ERK/MAPK) pathway has been shown to play a critical role in circadian clock timing and entrainment capacity of the master SCN oscillator (Goldsmith and Bell-Pedersen, 2013a). For example, Obrietan et al first showed that activated ERK (phospho-ERK) exhibits a baseline time-of-day rhythm, with highest activity during the subjective day (K. Obrietan et al., 1998a). Furthermore, Akashi et al demonstated that MAPK inhibition leads to an a reduction of clock gene rhythms and an abrogation of neuronal firing within the SCN (Akashi et al., 2008).

With respect to entrainment of the SCN clock, photic stimulation during the circadian night (but not during the circadian day) has been shown to trigger a rapid increase in activated ERK expression within the SCN (Butcher et al., 2002a; K. Obrietan et al., 1998a), and inhibition of ERK/MAPK signaling has been shown to alter light-evoked circadian clock resetting capacity (Coogan and Piggins, 2003a).

Notably, the activation of ERK also triggers an increase in intracellular calcium levels, which in turn, activates cAMP to activate the CRE-binding protein (CREB). This activation of CREB (by a light pulse) through its phosphorylation at serine-133 subsequently leads to the activation of many immediate early genes (IEGs) (Ginty et al., 1993). Here, it should also be mentioned that in order for IEGs such as c-Fos and Per1 to exhibit light inducible expression, an intact ERK/MAPK pathway is necessary (Dziema et al., 2003). Hence, activation of the ERK/MAPK pathway is critical for proper activation of the CREB signaling cassette within the SCN, which in turn drives the expression of the core circadian clock gene *Per1.* As a core circadian clock gene, changes in *Per1* expression ultimately lead to resetting of the circadian clock.

Given the profound effects that the MAPK pathway has on circadian entrainment, it is not surprising that many groups have studied ERK scaffolds and regulators in order to tease apart the intracellular signaling events that couple light to the activation of ERK. Indeed, one such scaffold—which was shown to sequester ERK in the cytoplasm (and hence prohibit the translocation of ERK into the nucleus to activate gene expression) is Phosphoprotein Enriched in Astrocytes 15 (PEA-15) (Formstecher et al., 2001; Renganathan et al., 2005). Interestingly, Wheaton et al recently reported the expression of PEA-15 within the murine SCN and demonstrated that PEA-15 regulates ERK/MAPK-dependent activation of *Per1*(K. Wheaton et al., 2018a). Other studies that have examined GEFs/GAPs found upstream of the ERK/MAPK cellular signaling cassette (such as Dexras1 (Cheng et al., 2004, 2006a)), highlight the importance of this pathway in the maintenance of circadian entrainment capacity.

Ancillary and Peripheral Circadian Clock Timing—an Overview

For years it was believed that circadian timekeeping capacity was restricted to the SCN—a pair of nuclei located within the anterior hypothalamus. However, recent work has revealed that circadian clock gene expression and circadian oscillatory capacity exists in several regions throughout the brain—including areas of the hippocampus, cortex, and amygdala (Abe et al., 2004; Al-Safadi et al., 2014; Chun et al., 2015; Kristin L Eckel-Mahan et al., 2008; Harbour et al., 2013; Jilg et al., 2010; Lamont et al., 2005)—regions that underlie both cognition, mood, and stress response (Drevets et al., 2008; Lucassen et al., 2014; Petersen and Sporns, 2015). Further, circadian gating of cellular excitability and output from several other brain regions (including the prefrontal cortex, hippocampus, amygdala, habenula, raphe nuclei, and locus coeruleus) has also been reported (Albrecht and Stork, 2017; Aston-Jones et al., 2001; Baño-Otálora and Piggins, 2017; González and Aston-Jones, 2006; Smarr et al., 2014a).

It is now widely accepted that circadian timing occurs not only in the brain, but also within tissues of peripheral organs. Indeed, nearly every organ system of the body contains cells that oscillate (for review, see (Dibner et al., 2010; Mohawk and Takahashi, 2011)). In mammals, the circadian timing system is hierarchically organized, with the SCN serving as the master pacemaker for the multi-oscillatory network of numerous peripheral or local clocks. To this end, timekeeping capacity, phasing, and synchronization of this peripheral (and ancillary) clock network is tightly coupled to the SCN. Indeed, without synchronizing cues from the master clock, the phase coherence of peripheral clocks is lost, subsequently leading to damped rhythmic output (Nagoshi et al.,

2004; Welsh et al., 2004). In this regard, the SCN allows for coordination amongst local oscillator populations, and this synchronization is largely driven by homeostatic cues from humoral signaling networks. Along these lines, cortisol (or corticosterone in rodents)—released in a circadian manner by the adrenal gland—has been shown to modulate hippocampal rhythms (Conway-Campbell et al., 2010; Woodruff et al., 2016). Further, cognitive and affective behaviors are thought to be under the control of plasma glucocorticoid (GC)/adrenal rhythms (Gilhooley et al., 2011; Lamont et al., 2005; Malek et al., 2007; Woodruff et al., 2016), suggesting that this GC rhythm links circadian rhythms of biochemistry, physiology, and even behavior by connecting the master clock with local clocks (for excellent reviews, we direct readers to (Oster et al., 2017; Son et al., 2018)). Given these studies that highlight the importance of extra-SCN clocks in the maintenance of circadian rhythms of brain plasticity-associated processes, it is not surprising that there exist circadian rhythms in both cognitive efficiency and in neuromodulator release—processes that are governed by many signaling effectors.

Circadian Clock Regulation of Cognition and Affect—Signaling Effectors Underlying Brain Plasticity and Behavior

Circadian rhythms in cognitive efficiency

Circadian rhythms in cognitive efficacy are evident in both animal models and in humans. With respect to rodent model systems, using the passive avoidance task, Davies et al were the first to demonstrate that rats acquired the memory and recalled the task better during the day relative to the night (Davies et al., 1973). Notably, Stephan et al confirmed these results and showed that rats with SCN lesions did not display differences

in day versus nighttime retention performance in the passive avoidance task (Stephan and Kovacevic, 1978a).

Paralleling these data, using a variety of fear conditioning paradigms in mice, several other groups have demonstrated more efficient acquisition (Chaudhury and Colwell, 2002a) and fear memory recall (Chaudhury and Colwell, 2002a; Kristin L Eckel-Mahan et al., 2008; Wang et al., 2009) during the daytime domain. In rats, increased fear memory (to a conditioned tone) is also observed when animals are trained and tested during the day (Kumar and Jha, 2012). Interestingly, a recent study conducted by Woodruff et al found that rats subjected to an auditory-cued fear conditioning task exhibited enhanced extinction memory (loss of conditioned training) at night, relative to those rats trained/tested during the day (Woodruff et al., 2015). These results suggest a diurnal modulation of extinction learning and support findings of Chaudhury and Colwell who also noted superior conditioned fear extinction in rodents trained and tested during the active (i.e. nighttime) phase (Chaudhury and Colwell, 2002a). The fact that the daily rhythm in recall performance appears to be antiphase of the rhythm in extinction learning raises interesting questions about the different brain structures and molecular mechanisms that underlie fear memory recall versus extinction memory. Interestingly, an abundance of literature (from several species) has suggested that neural substrates—containing different types of memory information—are assembled into distinct systems throughout the brain (Gaffan, 1994; Poldrack and Packard, 2003; White et al., 2013). Hence, it would be logical to posit that different types of cognitive information (stored in various brain regions), may be differentially affected by the circadian timing system. Indeed, future

studies will be necessary in order to distinguish the role of the circadian clock in these two learning processes.

Turning to tests of spatial learning and memory, numerous groups have reported that in mice, rats, and hamsters, novel object location and novel object recognition memory is enhanced at night (Ruby et al., 2008; Shimizu et al., 2016a; Snider et al., 2016a; Takahashi et al., 2013a). Furthermore, Gritton et al found that while time-of-day did not affect acquisition or performance in the Morris water maze, when rats were tested again two weeks after their last training day, they exhibited better memory only if the original training occurred at night (Gritton et al., 2012). Finally, in the radial arm maze, Haber and Bareiss noted superior working memory at night (Hauber and Bareiss, 2001), while Rawashdeh et al noted fewer errors in this task during the day, suggestive of better working memory during the light phase (Rawashdeh et al., 2014a). Species, protocol, and testing timepoint differences may have contributed to the disparate findings in the radial arm maze tests (Snider et al., 2018a). Taken together, these data provide support for this circadian-gating-of-cognition phenomenon in rodent models.

Here, it is important to note that circadian rhythms in memory efficiency are also observed in humans. Indeed, Nathaniel Kleitman was the first to note a diurnal change in the speed and accuracy of complex cognitive tasks—with optimal cognition in the afternoon hours and poor cognitive capacity late at night and early in the morning (Kleitman, 1963, 1933). Notably, this daily rhythm in cognition is likely governed by the relationship between sleep inertia, homseostatic sleep pressure, and circadian timing (for review, see (Wright et al., 2012a)). Along these lines, Cohen et al and Grady et al found

that neurobehavioral performance in cognitive and attention tasks is worse near the circadian nadir in brain arousal (typically corresponding to morning hours) (Cohen et al., 2010; Grady et al., 2010). This is especially true after being awake for a prolonged period of time. In order to assess cognition across the circadian cycle (independent of the time since waking), forced desynchrony paradigms are typically utilized (Wright et al., 2002; Wyatt et al., 1999). This protocol, wherein subjects are exposed to an artificial light cycle to which they are unable to entrain, allows researchers to discern the role of circadian versus homeostatic (sleep) modulation of cognition. Utilizing these paradigms, several studies have shown that arousal, attention control, visual working memory, cognitive speed, memory retention, reward motivation, and mood appear to be influenced (in part) by time-of-day (Boivin et al., 1997; Murray et al., 2009; Pomplun et al., 2012; Silva et al., 2010). Furthermore, in healthy young adult males, extinction of conditioned fear is learned more efficiently (and better generalized) in morning hours relative to night hours, which corresponds to higher levels of cortisol (Pace-Schott et al., 2013). Interestingly, cortisol, which is regulated by the circadian clock and has a peak during morning hours, has been shown to regulate emotionally memory (for review, see (Aubry et al., 2016; de Quervain et al., 2009; Meir Drexler and Wolf, 2017; Montoya et al., 2012)). Hence, it is likely that the circadian rhythm in cognitive efficiency is also modulated (in part) by rhythms in stress-related neuromodulators, a topic that will be discussed in a later section.

Effects of circadian disruption on cognition

As noted previously, the efficiency of cognitive acquisition, maintenance, and recall changes across the circadian day (for a detailed review, see (Snider et al., 2018a)), and work from several labs has shown that hippocampal-dependent cognition is reliant upon an intact master clock. Indeed, lesioning of the SCN leads to impairments in novel object recognition (Shimizu et al., 2016a), contextual fear conditioning and spatial memory recall (Phan et al., 2011a). Further, Wardlaw et al found that global deletion of *BMAL1* led to impaired contextual fear and spatial memory and decreased LTP (Wardlaw et al., 2014). These data are in line with results obtained from Kondratova et al who found that *BMAL1* null mice exhibit a hyperactive phenotype and impaired short and long term memory formation (Kondratova et al., 2010). Notably, this group also found that mice with *CLOCK* gene mutations display normal immediate memory formation, but impairments in long-term memory (Kondratova et al., 2010). Along these same lines, animals with germline deletion of both Cry1 and Cry2 exhibit deficits in time-place learning (Van der Zee et al., 2008). Further, *Per2* null mice display deficits in trace fear memory (Wang et al., 2009), and *Per1* null mice display impairments in the radial arm maze (spatial learning) (Jilg et al., 2010).

The work referenced above clearly depicts a role for the SCN in proper cognitive functionality. However, it is worth emphasizing that many of the studies utilized electrolytic lesioning to ablate the SCN. Such a technique may also damage tissue surrounding the central pacemaker. Further, several of these studies were conducted in animals with germline/global deletion of core clock genes. As such, this germline deletion approach likely leads to developmental/compensatory confounds and ‘off

target'/unrelated effects. In this latter case, it is important to note that many clock genes appear to be pleiotropic, wherein they serve functional roles that are unrelated to circadian timing (for review, see (Rosenwasser, 2010)). For instance, CLOCK and BMAL1 are trans-activators, and it is therefore likely that they have functions independent of circadian clock regulation. Hence, additional experiments that employ inducible gene deletion approaches in adult animals are of merit. Along these lines, in an effort to avoid potential confounding effects of SCN lesioning or developmental compensation/pleiotropic effects in germline null animals, Ruby et al conducted an elegant set of non-invasive experiments in which they utilized a one-time photic treatment that rendered Siberian hamsters arrhythmic. Remarkably, they found that these rodents displayed deficits in memory performance (Ruby et al., 2008), providing further support that SCN output plays a role in modulating learning and memory capacity.

Turning to the role of forebrain circadian clock regulation of cognition, here, we again reference a paper recently published by our lab. Using a *BMAL1* floxed mouse line (wherein BMAL1 is deleted from excitatory neurons of the frontal cortex, hippocampus, amygdala, etc), Snider et al characterized the functional relevance of BMAL1 within forebrain circuits (Snider et al., 2016a). Importantly, this floxed-cre deletor strategy excluded the SCN, and therefore, this genetic deletion approach eliminated BMAL1 specifically within ancillary circuits, thus allowing for the investigation of non-SCN cell autonomous cognitive functionality. No apparent differences in health or brain morphology were observed in these animals (unlike animals with germline *BMAL1* deletion, which exhibit accelerated aging, decreased body weight, and overall poor

health) (Andrews et al., 2010; Laposky et al., 2005; Sun et al., 2006). However, these mice showed deficits in time-of-day dependent novel object location memory and impairments in Barnes maze performance (Snider et al., 2016a), suggesting that hippocampal clock timing is necessary for daily oscillations in cognition. Consistent with this, Shimizu et al also used a BMAL1 conditional deletion approach to suppress *BMAL1* levels within the forebrain, and they too found a significant decline in nighttime memory performance in the novel object recognition paradigm (Shimizu et al., 2016a).

To finish this section, it is worth mentioning that a definitive cellular (or even systems-based) understanding of the mechanistic connection between clock timing and cognitive/affect-related behaviors is yet to be elucidated. However, it is likely that several physiological processes interact at multiple levels in order to produce coherent cellular synchrony/oscillatory capacity within limbic brain regions.

Circadian rhythms in neuromodulator/neurotransmitter release

In many mammals, 24 hour rhythms in both hormone secretion and neuromodulator/neurotransmitter release have been shown to influence synaptic plasticity and neuronal excitability (for review, see (Frank, 2016; Parekh and McClung, 2016)). Given that alterations in cellular plasticity and excitability are hallmarks of stress and mood-related disorders, it is likely that rhythmicity of these molecules is important in the proper functioning of affective behaviors.

Glucocorticoid rhythms

Perhaps the most robust ‘neuromodulator’ (i.e. hormonal) rhythm is that of glucocorticoids. Indeed, work over the past 60 years has shown that there exists a strong

circadian rhythm in plasma glucocorticoid levels in both humans and in rodents (Halberg, 1959; Migeon et al., 1956), which is believed to mediate several physiological and psychological processes related to immunity/inflammation, cognition, affect, and metabolism (Oster et al., 2017). As such, GCs serve as important internal time-regulators—influencing the circadian landscape of not only organs/tissues within the periphery, but also of several regions within the brain (for review, see (Chung et al., 2011)). Notably, concentrations of plasma corticosterone (the most prominent glucocorticoid in nocturnal rodents) are highest at the start of the dark period and reach their lowest point in the morning hours (Dalm et al., 2005), whereas in humans, cortisol levels increase during night hours and peak early in the morning (Debono et al., 2009; Krieger et al., 1971; Weitzman et al., 1971). This rhythmic release of GCs from the adrenal gland is regulated by the paraventricular nucleus, a structure neighboring the SCN within the hypothalamus. Hence, GCs are intimately involved in stress response (and stress-inducing fear memory) (Albrecht et al., 2013; Brown, 2009) via activation of the hypothalamic-pituitary-adrenal (HPA) axis (Smith and Vale, 2006; Tsigos and Chrousos, 2002). While the exact role of GC rhythms in the modulation of stress and mood/affect-related behaviors remains unknown, several bodies of work have suggested a cyclic AMP (cAMP)/protein kinase A (PKA)-mediated mechanism of GC receptor modulation (Eickelberg et al., 1999; Miller et al., 2002; Rangarajan et al., 1992). The fact that antidepressants are believed to increase neurogenesis in a cAMP/PKA-dependent manner (Anacker et al., 2011) and that over-expression of cAMP-response element binding protein (CREB) results in anti-depressant effects (Chen et al., 2001), leads one to

postulate that modulation of GC rhythms may play a role in the therapeutic action and behavioral effects of anti-depressants (for review, see (Anacker et al., 2011)). Interestingly, clamping/flattening the rhythm in corticosterone levels in rats inhibits fluoxetine-dependent neurogenesis in the dentate gyrus (Huang and Herbert, 2006) and attenuates the ability of antidepressants to elevate forebrain levels of serotonin (Gartside et al., 2003).

Further, the circadian nature of glucocorticoid release is thought to be a powerful modulator of synaptic strength. Indeed, corticosterone has been shown to influence cellular excitability, AMPAR trafficking, and synaptic transmission (for excellent reviews, see (Frank, 2016, 2012)). Along these lines, circadian rhythms in cortical and hippocampal spine density also appear to be modulated by the cycling of glucocorticoid secretion (Ikeda et al., 2015; Liston et al., 2013). To this end, disruption of the endogenous secretion of corticosterone (via adrenalectomy or administration of exogenous corticosterone) eliminates the circadian rhythm in dendritic spine density (Cirelli and Tononi, 2015; Liston et al., 2013). Given that alterations in spine complexity are believed to contribute to behavioral manifestations of several neuropsychiatric conditions (Jiang et al., 2018), one may posit that GC rhythms serve as key conduit by which brain and peripheral clocks regulate synaptic plasticity that underlies stress response, mood, and memory.

Neurotransmitter rhythms

In addition to GCs, mood is also thought to be regulated by multiple neurotransmitter systems. For example, limbic regions of the brain that contribute to

affect behaviors communicate with one another via dopaminergic and serotonergic (i.e. monoaminergic) neural networks/circuits (for review, see (Kim et al., 2017; Nestler and Carlezon, 2006)). Glutamate and GABA—two of the most abundant neurotransmitters within the CNS (Nicholls, 1993; Petroff, 2002)—have also been implicated in the pathophysiology of several neuropsychiatric disorders (for review, see (Femenía et al., 2012; Lener et al., 2017)). Notably, all of these transmitters have been shown to be gated by the circadian clock.

With respect to monoaminergic signaling, dopamine—a catecholamine known for its regulation of movement and reward—exhibits circadian oscillations within the retina (Popova, 2014), olfactory bulb (Corthell et al., 2013), striatum (Webb et al., 2009), and midbrain (Chung et al., 2014; Webb et al., 2009) (for review, see (Korshunov et al., 2017)). Additionally, dopamine precursors and metabolites also exhibit circadian expression. For example, using microdialysis techniques, Castandea et al found a circadian rhythm in DOPAC and homovanillic acid within the striatum (Castañeda et al., 2004). Likewise, tyrosine hydroxylase (TH)—the rate limiting enzyme in catecholamine biosynthesis—also exhibits circadian fluctuations within striatal and motor regions of the brain (Chung et al., 2014; Webb et al., 2009; Weber et al., 2004). Along these lines, an interesting study conducted by Webb et al examined the relationship between the diurnal expression of TH levels and rhythms in sex or amphetamine reward. Using the conditioned place preference paradigm—the authors found that the peak in TH expression within the NAcc coincided with the peak timing in sex reward, while the peak in TH expression within the VTA positively correlated with the peak timing in

amphetamine reward (Webb et al., 2009). Results from this study suggest that the circadian rhythm in reward (both natural and drug-induced) may be modulated by the circadian cycling of mesolimbic dopaminergic activity, driven (to some degree), by local circadian clock oscillators. Moreover, rhythms in serotonin have also been reported. Along these lines, whole brain levels of serotonin were first noted by Albrecht et al (Albrecht et al., 1956), and this finding has since been corroborated in several other species (Asano, 1971; Dudley et al., 1998; Mateos et al., 2009; Rueter and Jacobs, 1996) (for review see (Martin, 1991)). Hippocampal and amygdalar serotonin rhythms have also been observed, with higher expression occurring during the dark period (Moriya et al., 2015). Furthermore, the major metabolite of serotonin, (5-HIAA) also shows circadian variations within the nucleus accumbens and striatum (Paulson and Robinson, 1996, 1994).

In addition to monoaminergic neurotransmitters, glutamate and GABA rhythms have also been reported in the mammalian brain. Using in vivo microdialysis, Marquez de Prado et al found significant oscillations in both of these transmitters within the striatum of awake rats, with higher levels during the dark period and lower levels during the day (Marquez de Prado et al., 2000). In a follow-up study, Castaneda et al also reported that glutamate and GABA levels exhibit circadian oscillations in both the striatum and nucleus accumbens. Notably, these rhythms were independent of any zeitgeber (external timing cue), including light (Castañeda et al., 2004). The fact that there exist circadian fluctuations of GABA and glutamate within the nucleus accumbens (and the ventral striatum as a whole) is interesting given that decreased activity within

these particular brain regions is a common feature in people with depression (Arrondo et al., 2015; Drevets et al., 1992).

From a mechanistic standpoint, it is important to note that both monoaminergic (i.e. dopamine and serotonin) ***and*** GABA/glutamatergic rhythms likely mediate the pathophysiological symptoms related to mood/affect disorders. In this respect, here we digress and make note of two key (competing) ideas related to the molecular underpinnings of depression. To this end, the monoamine hypothesis of depression, which has dominated the psychiatric field over the last fifty years, posits that depressive symptoms (and associated cellular pathology) arise from the reduced availability of monoamines within the brain (Hirschfeld, 2000; Schildkraut, 1965). Consequently, antidepressants increase monamines within the brain to abrogate depressive-like symptoms (Owens, 2004). In more recent years; however, the glutamate hypothesis of depression has garnered much attention. Indeed, the findings of Trullas and Skolnick, which showed that NMDA antagonists mimic the effects of antidepressant treatments, insinuate that the NMDA subtype of glutamate receptors (and glutamatergic signaling in general) play important roles in the pathophysiology of mood disorders (Trullas and Skolnick, 1990). Hence, it is likely that both hypotheses are implicated in the etiology (and resolution) of depressive-like behaviors. Indeed, monoamines like dopamine and serotonin modulate limbic circuitry that underlies motivation, emotion and mood, while excitatory and inhibitory neurotransmission (regulated by glutamate and GABA) mediate many of these catecholaminergic-driven processes (for an excellent review, see (Sanacora et al., 2012))—perhaps through synaptic plasticity dependent mechanisms. Given that

each of these noted neurotransmitter systems are gated (to some degree) by the circadian clock, one may postulate that a feedback circuit exists.

Relationship between Circadian Disruption and Depressive-Like Behavior

Studies in both humans and in animal models have demonstrated a link between neuropsychiatric/affective disorders, cognition and circadian timekeeping capacity (for review, see (Jagannath et al., 2013; Wulff et al., 2010)). With respect to depression, in particular, recent work has shown that chronic stress alters the circadian clock. However, evidence also suggests that circadian clock dysregulation may precipitate the psychopathology of affect-related disorders, and thus, a bidirectional relationship between depression and circadian clock dysfunction likely exists. As such, in this section, we summarize support for both of these ideas.

Association between circadian disruption and depression-like behavior—human subjects

A large body of work has shown that depression is associated with the disruption of numerous clock-gated physiological and behavioral processes, including the circadian release of neuromodulatory hormones and rhythms in sleep and cognition (Boyce and Barriball, 2010; Ehlers et al., 1988; Germain and Kupfer, 2008a; Salgado-Delgado et al., 2011; Srinivasan et al., 2010). For example, Keller et al found that cortisol levels are increased during the evening hours in individuals diagnosed with psychotic major depression, relative to control subjects (Keller et al., 2006). Furthermore, in depressed patients, variations in the endogenous secretion of melatonin have also been reported, with studies noting either a delayed (Crasson et al., 2004; Nair et al., 1984) or an advanced (Rubin et al., 1992) circadian phase. Of note, age and gender likely play a

prominent role in the phasing heterogeneity/discrepancy of these phase shift findings, as Robillard et al noted that melatonin phase delays are common in young adults with mood disorders (Robillard et al., 2013). Further, sex differences in the phase angle of entrainment and amplitude of melatonin rhythms have also been observed (Cain et al., 2010; Gunn et al., 2016). Nonetheless, these findings highlight a likely connection between disturbances in cyclic (circadian-gated) hormone release and depression-like behavior.

Sleep disturbances are perhaps the best example of a link between circadian disruption and depression in humans. Indeed, epidemiological studies estimate that nearly 90 percent of depressed patients experience some type of sleep disturbance (i.e. insomnia, hypersomnia, frequent awakenings) (for excellent reviews, see (Nutt et al., 2008; Tsuno et al., 2005)). Given these striking sleep-comorbidity statistics, several circadian hypotheses of depression have been proposed (for an excellent review, see (Germain and Kupfer, 2008a)). These hypotheses are reinforced by observations that, in depressed patients, sleep-wake rhythms have haven been shown to be blunted (with respect to amplitude)(Souêtre et al., 1989), markedly phase-shifted (advanced—with early awakening, or delayed—with difficulty falling asleep)(Emens et al., 2009), or misaligned (relative to melatonin or other physiological rhythms)(for reviews, see (Boivin, 2000; McClung, 2007; Quera Salva and Hartley, 2012)). Further support for these models is strengthened by sleep deprivation, bright light, and pharmacological treatments—therapeutic antidepressant strategies that have been shown to shift or resynchronize the circadian clock, and in some cases, alleviate many sleep problems associated with

depression (McClung, 2007). Whether these interventions alter the function of master clock (SCN) or ancillary clocks within the forebrain, is an interesting topic for further investigation.

Genetic studies in humans have also implicated the role of the circadian clock in the manifestation of affect-related disorders. To this end, Utge et al analyzed single-nucleotide polymorphisms in 18 circadian clock genes in both control and depressed individuals and found a statistically significant association between sleep disturbances and variants in the circadian genes *Timeless* and *Per1* (Utge et al., 2010). Along these lines, Benededtti et al found that a T to C nucleotide substitution in the 3' flanking region of the human CLOCK gene may be associated with the recurrence of illness episodes in patients with bipolar disorder (Benedetti et al., 2003). Finally, in a study conducted by Kripke and colleagues, 23 associations between circadian-related gene polymorphisms and mood symptoms were found to be statistically significant (Kripke et al., 2009), with the NR1D1 gene (REV-ERB-alpha; OMIM 602408) showing the strongest association. Interestingly, with respect to REV-ERB-alpha, to date, several studies have demonstrated that alterations in its expression influence mood and depressive/manic states (Chung et al., 2014; Severino et al., 2009), suggesting that this circadian gene may be a key player in affective disorders. Taken together, these studies, and others like it, suggest that genetic (and potentially epigenetic) variations/polymorphisms in clock genes may predispose individuals to develop neuropsychiatric disorders (for excellent reviews, see (Kronfeld-Schor and Einat, 2012; Liu and Chung, 2015)).

Effects of circadian clock disruption on mood and depressive-like behaviors—rodent models

With respect to the association between circadian rhythms and depression, it remains incompletely understood whether circadian clock dysfunction in the master clock (SCN), or in ancillary circuits (or both) leads to depressive-like behaviors. Along these lines, in rodent models, there is conflicting work on the role of SCN disruption in the development of depression-like behavior. Indeed, a study by Landgraf et al knocked down the expression of a core circadian clock gene—*BMAL1*—specifically within the SCN and found that these mice displayed an increase in depressive-like behaviors (i.e. helplessness, behavioral despair, and anxiety) (Landgraf et al., 2016a). The *BMAL1* SCN-KD mice also exhibited abnormal rhythms in circulating GC and an attenuated increase in corticosterone response after stress (Landgraf et al., 2016a). These observations are in congruence with studies showing that bilateral lesions of the SCN disrupt both behavioral and endocrine rhythms, such as the daily oscillations in HPA activity (Abe et al., 1979; Moore and Eichler, 1972; Stephan and Zucker, 1972; Szafarczyk et al., 1979). In contrast; however, Tataroglu et al reported that bilateral lesioning of the SCN (which leads to behavioral arrhythmia) has a protective effect in the induction of behavioral despair—an animal model of depression (Tataroğlu et al., 2004). Given these discrepant findings, whether certain network features of the SCN render it resilient to stress perturbations and subsequent depressive phenotypes, remains an important area of future inquiry. Nevertheless, if SCN dysfunction is not the single source of the observed circadian deficits associated with depression-like behaviors, it is likely that the disruption

of clock timing within mood circuits (or in the periphery) is also a key event in the development of depression.

In addition to examining the role of the master clock, several labs have also investigated the contribution of ancillary brain clocks in the etiology of affect-related behaviors. Using RNA interference and viral gene transfer, Mukherjee et al knocked down CLOCK (an important circadian gene) expression specifically within the VTA and found that these mice exhibited an increase in depressive-like behavior and an overall mixed-manic state (Mukherjee et al., 2010). Notably, this group also reported that dopaminergic neurons expressing the CLOCK shRNA displayed increased activity relative to controls, suggestive of an important role for VTA expressing CLOCK neurons in the regulation of dopaminergic signaling and manic behavioral states (Mukherjee et al., 2010). Furthermore, in another study, Chung et al showed that ventral midbrain-specific pharmacological inhibition of the circadian clock gene/nuclear receptor—REV ERB alpha—produces mania-like behavioral tendencies (Chung et al., 2014). Interestingly, REV ERB alpha has been shown to decrease TH expression via competitive interactions with NURR1, thus leading to the rhythmic nature of the dopaminergic system (Chung et al., 2011). Given that dopamine regulates mood and affect, these data suggest that REV ERB alpha expression in extra-SCN brain regions could serve as a potential chronotherapeutic target for the treatment of mood disorders.

Furthermore, depression and anxiety-like behaviors have been observed in rodents exposed to constant light conditions (which disrupts clock timing) (Borniger et al., 2014; Tapia-Osorio et al., 2013), as well as in animals with *Per1* and *Per2* knockdown within

the nucleus accumbens (Spencer et al., 2013). On a related note, Son et al examined the effects of peripheral BMAL1 disruption of humoral rhythms and psychiatric illnesses. They found that adrenal-specific knockdown of BMAL1 dampens the daily rhythm in adrenal glucocorticoid production and attenuates circulating glucocorticoid content (Son et al., 2008). Notably, the symptomology of these mice appears to phenocopy that of patients diagnosed with chronic fatigue syndrome (Chung et al., 2011; Son et al., 2008). These observations highlight the importance of both central *and* peripheral circadian neuromodulator rhythms in the control of processes—such as HPA activity—that modulate affect-related behaviors. Together, these BMAL1 conditional deletion studies suggest that ancillary and peripheral clock timing is important in regulating processes that underlie mood.

Effects of chronic stress/depressive-like behaviors on the circadian clock—rodent models

In the last decade, several rodent studies have reported that chronic stress/depression leads to alterations in clock timing within mood (i.e. limbic) circuits. To this end, RNA-based profiling in animals subjected to chronic mild stress revealed abrogated clock gene rhythms within the forebrain (hippocampus, nucleus accumbens, amygdala) (Christiansen et al., 2016; Savalli et al., 2015). Further, Colleen McClung's research group recently utilized a chronic stress paradigm in combination with a *period2*-luciferase clock reporter mouse model to show that depression-like behaviors correlate with a decrease in the amplitude of circadian rhythms within the nucleus accumbens (Logan et al., 2015). Paralleling this, Landgraph et al also used a period-luciferase reporter mouse to show that the learned-helplessness procedure led to a loss of circadian

rhythmicity in the nucleus accumbens and periaqueductal grey (Landgraf et al., 2016a): two brain regions that play a significant role in mood, affect, and stress response (Behbehani, 1995; Fanselow, 1991; Shirayama and Chaki, 2006). Collectively, these data support the idea that the functional properties of mood circuits are under the influence of the circadian clock, and that chronic stress and depression are associated with a dysregulation of molecular events that underlie such oscillatory capacity.

Here, it is worth mentioning that the studies mentioned above used whole brain-region based approaches, and as such, the aggregate readout of many cells with varying phenotypes was combined to obtain an index of the amplitude and phasing of the clock timing system. Given that these cellular averaging approaches do not provide definitive insight into the precise nature of clock dysregulation, future work should focus on a cellular-specific reporter of clock timing to discern the mechanism of clock disruption after stress. Nevertheless, the work referenced in this section supports the idea that stress and depressive-like states perturb circadian clock functionality in extra-SCN brain regions.

microRNA Overview

Since their discovery nearly two decades ago, microRNAs—small, single-stranded RNA molecules—have been established as potent modulators of gene expression (Lagos-Quintana et al., 2002; Lee et al., 1993; Wightman et al., 1993). These small RNA molecules have been shown to be essential to development and have been reported to mediate many key biological processes (Fu et al., 2013). Furthermore, altered expression of miRNAs has been reported in many disease conditions (Ardekani and

Naeini, 2010; Paul et al., 2018). Given the fact that miRNAs can also be expelled into the extracellular fluid, they are now considered to be novel biomarkers of potential disease states (Hayes et al., 2014; Wang et al., 2016).

With respect to their processing, miRNAs are transcribed by RNA polymerase II into primary miRNAs (also called pri-mRINAs), which are further processed into precursor miRNAs (pre-miRNAs) after being cleaved by the enzyme known as Drosha. Finally, this pre-miRNA is cleaved (to ~22 nucleotides) into a mature miRNA by the enzyme known as Dicer (Denli et al., 2004; Han et al., 2004; O'Brien et al., 2018; Okada et al., 2009; Zhang et al., 2004). A single strand from this mature miRNA can then be loaded into the RNA-induced silencing complex (RISC), and miRNA can thus bind to mRNA targets via complementary base pair recognition.

A majority of studies have demonstrated that miRNAs bind to (and interact with) the 3' untranslated region (UTR) of target mRNAs in order to cause repression of translation (Huntzinger and Izaurralde, 2011). Notably, the interaction between miRNAs and their mRNA targets is largely dependent on the 'seed region' of each miRNA (typically a few nucleotides in length) (Kehl et al., 2017). Given that over 2500 miRNAs have been annotated within the human genome alone (Griffiths-Jones et al., 2006), it is not surprising that miRNA dysfunction contributes to a multitude of diseases/disorders within the CNS.

Role of the miR-132/212 Locus within the CNS

The miR-132/212 gene locus is a miRNA cluster that is regulated by the CREB/CRE transcriptional pathway—a pathway that couples synaptic activity to the

expression of genes that underlie plasticity within the brain. Along these lines, Vo *et al* were the first to identify CRE sites within this tandem-miRNA cluster (Vo et al., 2005). With respect to its processing, the miR-132/212 gene locus is transcribed from the non-coding transcript, AK006051 (found on chromosome 11 in mice). It is likely that both miR-132 and miR-212 were formed as a result of gene duplication given that the two miRNAs share an identical 'seed sequence'(Remenyi et al., 2010), and that both miRNAs share many mRNA targets.

Neuronal stimulation/synaptic activation have been shown to lead to an increase in transcription from the miR-132/212 locus. Specifically, learning tasks, photic induction, and acute/chronic stress exposure all increase the expression from this cluster (Cheng et al., 2007a; Hansen et al., 2013; Mellios et al., 2011; Nudelman et al., 2010), suggesting that both miR-132 and miR-212 are potent regulators of cognition, circadian clock entrainment, and stress—topics discussed in greater detail below. Furthermore, several groups identified a role for miR-132/212 in the regulation of synaptic plasticity and neuronal morphology. For example, knockdown of miR-132 expression was shown to decrease dendritic arborization within the hippocampus (Magill et al., 2010; Wayman et al., 2008). Furthermore, transgenic overexpression of miR-132 was also found to increase CA1 dendritic spine density (Hansen et al., 2010). These results, coupled with the fact that miR-132 was shown to alter synaptic transmission (Impey et al., 2010; Lambert et al., 2010; Magill et al., 2010; Pathania et al., 2012), raised the prospect that the miR-132/212 locus (via the targeting of many synaptic plasticity-associated mRNAs) modulates many behavioral states.

miR-132/212 regulation of cognition

The fact that miR-132/212 is 1) modulated by neuronal activity and 2) that it regulates dendritic spine density and morphology, led to the hypothesis that it may regulate learning and memory capacity—perhaps through the targeting of plasticity-associated mRNAs. Along these lines, using a TET-off transgenic mouse lines, Hansen et al was the first to show that miR-132 overexpression leads to deficits in memory capacity (Hansen et al., 2010). Scott et al also showed that overexpression of miR-132 within the perirhinal cortex led to deficits in the Novel Object Recognition (NOR) paradigm (Scott et al., 2012). Hansen et al also employed a miR-132/212 excitatory-forebrain specific conditional knockout mouse line and showed that these animals displayed significant deficits in the NOR task, the Barnes maze paradigm, and in fear conditioning memory (Hansen et al., 2016). Similar deficits were also observed in miR-132/212 germline knockout mice (Hernandez-Rapp et al., 2015), suggesting that *both* knockdown *and* supraphysiological expression of miR-132 lead to similar cognitive deficits.

Interestingly, Hansen et al further investigated the role of miR-132 and cognition, once again employing the transgenic miR-132 mouse line, and found that slight increases in miR-132 expression (~2 fold above baseline—less than the ~5 fold increase observed with no doxycycline administration) actually led to enhancement of cognition (Hansen et al., 2013). Notably this slight increase paralleled the levels of miR-132 expression observed after a learning paradigm (Hansen et al., 2013). These results suggest that a tight range of miR-132 (and perhaps miR-212 expression) is necessary for proper cognitive function. Along these lines—both knockdown of miR-132 and extensive

overexpression of transgenic miR-132 negatively impact memory function, while moderate increases in miR-132 expression positively impact memory.

Here it should be noted that while a number of miR-132/212 mRNA targets—including *Mmp-9, p250GAP, Mecp2, Mash1, and Stx1a* have been shown to mediate some of these morphological and behavioral changes observed in animals with dysregulation of the miR-132/212 locus (Hansen et al., 2016, 2010; Impey et al., 2010; Jasińska et al., 2016; Vo et al., 2005), it is likely that miR-132/212 targets many other mRNAs that mediate/contribute to these effects.

miR-132 regulation of circadian clock entrainment

A seminal finding by Cheng et al first revealed a role for miRNAs in the regulation of circadian clock timing and entrainment (Cheng et al., 2007a). In this study (and in a follow-up study), miR-132 was shown to be expressed in a circadian manner within the SCN, to be induced by light, and to alter the behavioral phase-shifting capacity after a light pulse (Alvarez-Saavedra et al., 2011; Cheng et al., 2007a). As mentioned in a previous section, given that the ERK/MAPK pathway plays a key role in entrainment capacity (and that it activates downstream CREB/CRE dependent transcription) and that miR-132 is a CREB-regulated miRNA, Cheng et al infused the MEK1/2 inhibitor (U0126) into the lateral ventricle (note that MEK lies just upstream of ERK). They found that pretreatment of U0126 prevented the light-induced increase in miR-132 levels within the SCN—suggesting that the light induced induction of miR-132 requires proper ERK/MAPK signaling (Cheng et al., 2007a).

Further support for the role of miR-132 in circadian clock timing came from a recent study which showed that deletion of the miR-132/212 locus alters entrainment capacity (to non 24 hour day-night cycles known as T-cycles), in addition to the expression of the circadian clock gene *Per2* after either short or long days (Mendoza-Viveros et al., 2017). Interestingly, this group also found an increase in the amplitude of circadian clock protein oscillations in the SCN of miR-132./212 knockout animals in constant dark/free-running conditions. They also found that SCN neurons in miR-132/212 knockout animals exhibited a reduced dendritic spine density in addition to alterations in methyl CpG-binding protein (MeCP2)—a bona-fide miR-132 target—oscillations (Mendoza-Viveros et al., 2017). Taken together, this study confirmed the role of the miR-132/212 locus in the regulation of circadian clock timing and it revealed that, by modulating the dendritic structure of neurons within the SCN (likely in an MeCP2-dependent manner), miR-132/212 also influences the ability of the master clock to translate seasonal photoperiods.

miR-132/212 in neuropsychiatric conditions

With respect to the contribution of the miR-132/212 locus to neuropsychiatric conditions in humans, dysregulation of miR-132/212 expression has been reported in many patients diagnosed with schizophrenia and bipolar disorder (Kim et al., 2010; Perkins et al., 2007). Furthermore, a study conducted by Li et al found that serum miR-132 levels are increased in patients with depression. Finally, Miller et al showed that miR-132 was significantly decreased in prefrontal cortex tissue from schizophrenic subjects and that several genes (such as *DNMT3A, GATA2*, and *DPYSL3*) –which are

modulated by miR-132—exhibited alterations in expression during development (or alterations in expression in tissue derived from adult schizophrenic patients) (Miller et al., 2012)

Turning to animal models of neuropsychiatric conditions, Smalheiser et al demonstrated that miR-132 expression is increased in animals that exhibit non-learned helplessness (Smalheiser et al., 2011). Furthermore, Shaltiel et al showed that footshock stress leads to increases in miR-132 expression (Shaltiel et al., 2013), while Uchida et al demonstrated that miR-132 expression is increased in pups that have experienced maternal separation (Uchida et al., 2010).

These studies—in both human subjects and in animal models—coupled with the fact that miR-132 has been shown to potently regulate neuronal morphology and cellular physiology within the forebrain, raise the prospect that this locus also influences other behaviors such as anxiety and stress response.

Role of Astrocytic Gap Junction Coupling

Astrocytes—one of the most prevalent glial (i.e. non-neuronal) subtypes within the brain, have recently been characterized as critical players in CNS functionality. While astrocytes are not electrically excitable (unlike their neuronal counterparts), they have been found to closely interact with neurons, and they express receptors for many neurotransmitters, such as glutamate (Cornell-Bell et al., 1990), GABA (Kang et al., 1998a), and acetycholine (Perea and Araque, 2005). Given their structural complexity, close interaction to neurons, and the presence of receptors for many transmitters, these

cells are integral components of normal CNS physiology—in both healthy and disease states.

Astrocyte gap junction coupling in health and disease

Astrocytes—unique, star-shaped glial cells—are connected via gap junctions to form an extensive network within the CNS. Notably, gap junctions enable astrocytes to communicate with one another (and with other cell types) within the brain. While recent studies have provided insights into the role of gap junction coupling between cells, the gap junction coupling phenomenon was actually discovered over 50 years ago (Furshpan and Potter, 1959; Kuffler and Potter, 1964). More recently, it was discovered that these intercellular gap junctions allow for astrocytes to be electrically coupled such that they are in a state of 'syncytial isopotentiality' (a topic discussed in greater detail below) wherein astrocytes can aid in the maintenance of homeostasis and act as a functional unit, or network (Kiyoshi and Zhou, 2019; Ma et al., 2016).

With respect to the composition of gap junctions, these cellular conduits are comprised of members of the connexin protein family (composed of nearly 20 members within the mouse genome and 21 members in the human genome, respectively) (Söhl and Willecke, 2004). These connexin subunits (which ultimately make up gap junctions) help to facilitate metabolic, biochemical, and electrical coupling between cells (Meşe et al., 2007). The importance of these connexin proteins is reinforced by the fact that alterations in the expression of many connexin subunits are observed in a host of neurological/neuropsychiatric conditions (in both human patients and in animal models) such as chronic stress/depression (Miguel-Hidalgo et al., 2018; Nagy et al., 2016),

anxiety (Quesseveur et al., 2015), and Alzheimer's disease (Kajiwara et al., 2018; Yi et al., 2016).

Syncytial isopotentiality within astrocyte networks

A recent discovery by Ma et al established a key functional role for astrocytic gap junction coupling, helping to mechanistically demonstrate how an astrocyte syncytium can function as single unit, or system (Ma et al., 2016). To begin to tease apart the significance of isopotentiality, it should first be noted that one of the most prominent roles of an astrocyte network is to allow for K+ spatial buffering—a model wherein K+ ions are spatially buffered from areas of high intracellular K+ (especially after neurotransmission) to areas of lower K+ (Chen and Nicholson, 2000; Kofuji and Newman, 2004; Orkand et al., 1966).

In a seminal study performed by Ma et al, it was discovered that gap junction coupling lowers the electrical resistance amongst coupled astrocytes in such a way that (if the coupling strength is quite strong) then it is possible for the electrical difference between two neighboring cells to be insignificant. Thus, the neighboring astrocytic cells—which again, are coupled to one another via their gap junctions—are able to equalize their membrane potentials (to similar levels) to permit the astrocyte syncytium to act as one cohesive unit.

'Syncytial isopotentiality'was first demonstrated using an innovative electrophysiological approach (patch clamp) (Ma et al., 2016). The underpinnings of this phenomenon were based on the idea that an individual (i.e. dissociated) astrocyte obeys the Nernstian prediction for the K+ gradient in a cell membrane. Hence, if one were to fill

a cell with Na+ containing solution (with no K+), then the membrane potential would depolarize. Therefore, this astrocyte (now deficient in K+) serves as a reporter of astrocyte network coupling strength such that the membrane potential from neighboring astrocytes compensates for the membrane potential for the reporter astrocyte. In this way, the coupling strength of an astrocyte network can be determined by filling a single astrocyte with Na+ and evaluating the Vm steady state after pipette breakthrough (Kiyoshi and Zhou, 2019; Ma et al., 2016).

While insights into the mechanistic underpinnings of the astrocyte syncytium have been observed as a result of this syncytial isopotentiality discovery, it should be noted that its relevance in many CNS disease/disorder states still remains a largely unexplored topic. To this end, the impact of neuropsychiatric disorders (such as depression and stress-related behaviors) on gap junction coupling/isopotentiality is still in its infancy.

Astrocyte-Neuron Communication in Health and Disease

While astrocytes may have once been considered as mere 'support cells' to their neuronal counterparts, increasing evidence suggests that they are integral players in synaptic transmission and important biological processes such as learning and memory/cognition (Dallérac et al., 2013; Santello et al., 2019; Vesce et al., 1999). Along these lines, given their ability to contact many neurites, astrocytes are thought to play significant roles in the modulation of synaptic function (Papouin et al., 2017). For example, many groups have shown that astrocytes can respond to synaptic events that regulate neuronal transmission (Adamsky et al., 2018; Henneberger et al., 2010; Jourdain et al., 2007; Panatier et al., 2011; Perea and Araque, 2007). Furthermore, astrocytic

activation has been shown to generate *de novo* neuronal potentiation and cognitive enhancement (Adamsky et al., 2018).

Astrocytes are not only able to regulate neuronal plasticity, but they (themselves) are actually quite 'plastic' and can undergo alterations in response to neuronal activity (in spite of the fact that they are not excitable cells) (Piet et al., 2004). Along these lines, neurons have actually been reported to control gap junctions within astrocytes—thus altering astrocyte-astrocyte communication (Giaume et al., 2010). Hence, the aforementioned studies highlight the bidirectional communication between astrocytes and neurons.

While these studies (and many others) clearly delineate a role for astrocytes in the regulation of plasticity and other higher order processes, there is still much to learn about the interactions between astrocytes and neurons in disease/disorder states. Several groups have begun to tease apart the relationship between neurons and astrocytes and various brain pathological/neurological states (from Alzheimer's to autism, to name just a few) (Molofsky et al., 2012; Siracusa et al., 2019); however, a deeper understanding of the *ultrastructural* interactions between both astrocytes and neurites (under baseline, i.e. non-pathological conditions) would aid in determining how synapse-astrocyte contacts are altered in disease/disorder states.

The following chapters in this dissertation provide insights into the signaling pathways, miRNA regulators, and astrocytic properties that influence circadian clock entrainment, cognition, and stress.

CHAPTER 2

SynGAP is expressed in the murine suprachiasmatic nucleus and regulates circadian-gated locomotor activity and light-entrainment capacity, and individuals with *Syngap1* gene mutations display sleep disruptions

Introduction

The suprachiasmatic nucleus (SCN) of the hypothalamus functions as the master circadian (24 hr) pacemaker (Hastings et al., 2018; Welsh et al., 2010). Synaptic and paracrine output from the SCN serves as a phasing cue to ancillary oscillator populations throughout the body, thus ensuring that precise, clock-gated, cellular- and systems-level biochemistry and physiology is achieved (Kriegsfeld and Silver, 2006; Silver and Kriegsfeld, 2014).

The phasing of the SCN oscillator is tightly regulated by photic input signals from the retina, and this entraining effect allows clock-gated physiology and behavior to be properly segregated across the 24 hr light/dark cycle (Fernandez et al., 2016; Golombek and Rosenstein, 2010; Hattar et al., 2006; Ibata et al., 1989; Tanaka et al., 1997, 1993).

At a molecular level, the circadian timing system arises from a well-characterized set of interlocking and autoregulatory processes formed from a transcriptional-translational feedback loop. This feedback loop is centered on the rhythmic (24 hr) expression of *period* and *cryptochrome* classes of genes, where the transcriptional drive

for this rhythm is mediated by a heterodimeric basic helix-loop-helix transcription factor formed by CLOCK and BMAL1, and autoregulatory transcriptional inhibition is achieved via the association of PERIOD/CRYPTOCHROME heterodimers with the CLOCK/BMAL1 transcriptional complex (N. Cermakian and Sassone-Corsi, 2000; Meng et al., 2008; Sangoram et al., 1998b; Zheng and Sehgal, 2012b).

The periodicity and phasing of this core molecular clock feedback loop is modulated by numerous kinase signaling pathways. For example, via its phosphorylation-mediated degradation of PERIOD, Casein Kinase 1δ/ε plays a key role in regulating clock periodicity (Gallego and Virshup, 2007, 2007; Lee et al., 2009; Meng et al., 2008). Further, via its ability to couple light to the induction of *period* gene expression, the p44/42 mitogen activated protein kinase (ERK/MAPK) pathway is a key conduit by which photic input sets the phasing of the SCN oscillator (Butcher et al., 2002b; Coogan and Piggins, 2003b; Goldsmith and Bell-Pedersen, 2013b; Karl Obrietan et al., 1998). Focusing on ERK/MAPK signaling, complementary studies examining ERK modulators (e.g. scaffolds and phosphatases), as well as studies examining signaling via the small GTPase Ras (an upstream regulator of ERK/MAPK activity), have provided important insights into the molecular events that regulate the ERK/MAPK cascade in the SCN (Cheng et al., 2006b; Doi et al., 2007; Serchov and Heumann, 2017; K. Wheaton et al., 2018b). However, there is still much to learn about the second messenger pathways that affect the RAS/ERK/MAPK signaling cassette. To this end, we examined the expression and function of the GTPase SynGAP (Synaptic Ras GTPase-activating protein) in the SCN.

SynGAP is one of the most abundant postsynaptic density proteins, where it functions as a negative regulator of Ras and Rap1 signaling and serves as a component of the NMDA receptor signaling complex (Chen et al., 1998; J. H. Kim et al., 1998; Rumbaugh et al., 2006; Walkup et al., 2018). Importantly, NMDA receptor activity has been shown to trigger CaMKII-mediated phosphorylation of SynGAP, which leads to an increase in its Ras GAP activity; this, in turn, increases the rate of inactivation of RAS at the synapse (Oh et al., 2004; Walkup et al., 2015). RAS activity has profound effects on synaptic physiology, including increased AMPA receptor insertion into the active zone, spine remodeling and enhanced LTP (Arendt et al., 2004; Manabe et al., 2000; Qin et al., 2005; Zhu et al., 2002). Notably, many of these effects are mediated by the induction of ERK/MAPK signaling. Consistent with these ideas, *Syngap*$^{+/-}$ mice exhibit elevated levels of ERK/MAPK signaling, potentiated excitatory transmission, and the early consolidation period of LTP (Komiyama et al., 2002; Rumbaugh et al., 2006). These findings, coupled with the well-established role of ERK/MAPK signaling in the SCN, raise the possibility that SynGAP could serve as an important signaling intermediate that regulates ERK/MAPK activity, and in turn, the sensitivity of the SCN clock to light.

Here we show that SynGAP expression is gated by the SCN clock and that its phosphorylation state is regulated by photic input. Further, we utilized *Syngap1* WT and Heterozygous mice to examine the expression and functional contribution of SynGAP to ERK/MAPK activation within the SCN. We show that *Syngap1* heterozygosity alters circadian-gated locomotor activity and entrainment capacity and potentiates the

activation of the ERK/MAPK pathway after nighttime light exposure. Finally, using survey-based techniques, we report that individuals with mutations in the *Syngap1* gene show disruptions in sleep—a process that is known to be regulated by the circadian clock. Hence, these findings suggest that SynGAP may function upstream of the ERK/MAPK cellular signaling cassette to modulate light-mediated entrainment of the master circadian clock.

Materials and Methods

Mice

All procedures were approved by the Institutional Animal Care and Use Committee at The Ohio State University. In total, ~ 220 mice (male and female—age and sex-matched between groups) were used. In order to minimize the number of animals, whenever possible, animals were utilized for more than one experiment (e.g., they were used for behavioral wheel running assays and then were sacrificed for tissue collection). Experiments were carried out in C57/Bl6 WT animals (Fig. 2.1-2.5) derived from our in-house breeding colony, or from animals derived from the *Syngap1*$^{lx\text{-}st}$ mouse line (referred to here as *Syngap1*$^{+/-}$, Jax Stock No. 029304: (Clement et al., 2012) (Fig. 2.6-2.10). *Syngap1*$^{+/-}$ mice (males or females) were crossed to *Syngap1*$^{+/+}$ mice (males or females) in order to generate *Syngap1*$^{+/-}$ and *Syngap1*$^{+/+}$ experimental animals. *Syngap1*$^{+/-}$ mice were generously provided by Dr. Gavin Rumbaugh (Scripps Research Institute) and were genotyped using the methods described previously (Clement et al., 2012; Creson et al., 2019a; Ozkan et al., 2014). PCR-based genotyping results are also depicted in Fig. 2.6A. *BMAL1*$^{-/-}$ mice were generated from breeder animals that were

acquired from Jackson Laboratories (Jax Stock No. 009100); genotyping was performed as previously described (Bunger et al., 2000a). Animals were kept on a standard 12h/12h light-dark (LD) cycle—unless otherwise noted—and were fed *ad libitum*.

Tissue processing for immunolabeling and Western blotting

Animals were sacrificed via cervical dislocation under white light (Fig. 2.1, 2.2, 2.3 and Fig.2.6), or under dim red light for CT (circadian time)/light pulse experiments (Fig. 2.4, 2.5, and 2.10). Brains were then removed and placed in ice-cold artificial cerebral spinal fluid and cut into 600 µm-thick (SCN-containing) coronal slices using a Leica vibratome (Leica VT1200). These SCN-containing sections were placed on a rocker for 6 hours in 4% paraformaldehyde in phosphate buffered saline (PBS) at 4°C and were then cryoprotected overnight at 4°C in 30% sucrose in PBS. For immunolabeling assays, SCN-containing sections were thin cut into 40 µm-thick sections, using a microtome.

For Western blotting experiments (Fig. 2.4), a similar process was used as described above. However, once the 600 µm-thick SCN-containing section was collected with the vibratome, the section was transferred to a glass slide (pre-cooled to -80° C). The SCN and cortex were then micro-dissected using a razor blade and placed in an Eppendorf tube and stored at -80° C. Tissue from three animals was pooled for each sample.

Immunohistochemical labeling, imaging, and analysis

For 3,3'-diaminobenzidine (DAB)-based immunolabeling, ~ 40 µm-thick, free-floating tissue sections containing the SCN were washed in PBS containing 1% Triton X-

100 (PBST) 3 times for 5 minutes. Tissue was then incubated in 0.3% hydrogen peroxide in PBST for 20 minutes at room temperature. Following this, tissue was blocked with 10% normal goat serum (NGS) diluted in 1X PBST for one hour at room temperature and incubated overnight at 4°C with one of the following primary antibodies: rabbit polyclonal anti-SynGAP1 (1:300 dilution; Cat. #: 19739-1-AP; Proteintech), rabbit anti-phospho-Threonine-202/Tyrosine-204 ERK (pERK; 1:3,000 dilution; Cat #: 9101; Cell Signaling Technology) or rabbit anti-serine 1138 phosphorylated SynGAP (SynGAP pSer1138) 1:350 dilution)). The SynGAP pSer1138 antibody was generously provided by Dr. Richard Huganir's laboratory and has been previously described (Araki et al., 2015). On the second day, tissue was washed in PBST and then incubated for two hours at room temperature in biotin-conjugated goat anti-rabbit IgG secondary antibody (1:1,000 dilution; Vector Laboratories; Cat. # BA-1000). Next, tissue was processed using an ABC labeling kit (Vector Laboratories Cat# PK-6100). The DAB signal was visualized using nickel intensified DAB processing (Vector Laboratories; Cat # SK-4100). Sections were then mounted onto gelatin-coated glass slides, washed in distilled water, and coverslipped using Permount Mounting Medium (Fisher Chemical).

Bright field images of the SCN (15X or 20X optical magnification) were acquired using a 16-bit digital camera (Micromax YHS 1300; Princeton Instruments) on a Leica DMIR microscope with Metamorph Software (MetaMorph Microscopy Automation and Image Analysis Software). For quantification of pERK, SynGAP, or SynGAP pSer1138 intensity, an ROI was digitally traced around the total SCN, the SCN core, or the SCN shell (a demarcation of core and shell regions of the SCN is presented in Fig. 2.1B2) from

1-2 sections per animal. Intensity levels for each section were then background subtracted from the lateral hypothalamus and analyzed using ImageJ software. For statistical analysis, the intensity was averaged from each animal and displayed as the mean ± SEM for each condition/genotype.

Immunofluorescent labeling, imaging, and analysis of SCN tissue

For immunofluorescent labeling, tissue sections containing the SCN (two sections/mouse) were permeabilized in 1% Triton X-100 in PBST and blocked for one hour in 10% NGS in 1X PBST. These sections were then washed (5 minutes/wash) in PBST between each subsequent labeling step. Tissue was then incubated in 5% NGS in PBST (overnight at 4 C) in the following primary antibodies: rabbit anti-SynGAP1 (1:150 dilution; Cat. #: 19739-1-AP; Proteintech), mouse anti-NeuN (1:3000 dilution; Cat. # MAB377; Millipore), mouse anti-GAD67 (1:400 dilution), or guinea pig anti-AVP (1:200 Cat. # 4562; Peninsula Laboratories International). On the following day, tissue was incubated in one or more of the following secondary antibodies in 5% NGS PBST: Alexa Fluor 488 goat anti-rabbit IgY, Alexa Fluor 594 goat anti-mouse IgY, or Alexa Fluor 594 goat anti-guinea pig IgY, (all at a 1:1000 dilution; Invitrogen). Finally, tissue was washed and incubated for in DraQ5 (Cat. # 62251; ThermoFisher) diluted in PBST in order to visualize nuclei. All tissue was then mounted onto glass slides and coverslipped using Fluoromount-G (Cat # 0100-01; SouthernBiotech).

Of note, for the analysis of SynGAP/VIP (vasoactive intestinal peptide) colocalization, tissue sections were sequentially labeled with the anti-SynGAP1 primary antibody (1:150 dilution; Cat # 19739-1-AP; Proteintech), and then labeled with Alexa-

Fluor 594 goat-anti rabbit. Tissue was then washed thoroughly and labeled with Alexa Fluor 488-conjugated VIP (1:200; Cat. # BS-0077R-A488; Bioss). This sequential labeling process was necessary to ensure that no cross-reactivity occurred, given that both primary antibodies (SynGAP1 and VIP) were made in rabbit.

For immunofluorescent image acquisition, 10X, 20X, 30X, or 63X images were collected using a Leica SP8 confocal microscope. Notably, image/acquisition parameters (speed, line average, pinhole, contrast, etc.) remained unchanged for each experimental condition/group.

Primary dissociated SCN cell culture

Brains were dissected from P0-P1 C57/Bl6 pups, immersed in sterile, oxygenated aCSF (120 mM NaCl, 3.5 mM KCl, 10 mM HEPES, 1.2 mM Na2H2PO4, 0.5 mM CaCl2, 3 mM MgSO4, 32.3 mM NHCO3, 10 mM Dextrose as previously described(K. L. Wheaton et al., 2018)) for ~1 min, and were then cut into ~180 µm thick coronal sections using a vibratome (Leica VT1200). A coronal brain section containing the SCN was then carefully transferred to a 60 mm dish containing dissection media: aCSF containing 1% Penicillin-Streptomycin (Gibco cat. #15140-122), 0.06% Nystatin suspension (Cat. # N1638; Sigma-Aldrich), and 0.1 µM MK801 (Cat. # 0924; Tocris). A dissecting scope was used to visualize the SCN and dissect it out from each coronal section, and a pipette was used to transfer each SCN from the 60 mm dish into a 1.5 mL Eppendorf microcentrifuge tube containing 150 µL of HBSS (Cat. # 14170112; ThermoFisher). Note that this process was repeated, as SCN from 5-7 separate pups were pooled into this HBSS containing tube (the tube was kept ice cold during the dissections). Tissue was

then triturated with a pipette ~20 times, allowed to settle, and 60 µL of the cell suspension (in HBSS) was transferred into a 1.5 mL Eppendorf tube filled with 40 µL of Neurobasal media (Cat. # 1088022; Gibco), complete with 0.5 mM Glutamax (Cat. # 35050061; Gibco), 1% penicillin/streptomycin (Gibco cat. #15140-122), and 2% B-27 supplement (Cat. # 17504044; Gibco). The entire 100 µL suspension was then plated inside a small pyrex cloning cylinder (6 x 8 mm; Cat. # 3166-10; Thomas Scientific) onto a 100 µg/mL poly-L-lysine coated Deutsch Deckglasern coverslip (Cat. # GG-12-oz) in a 35 mm dish. The cells were then placed in a 35 C CO_2 incubator. After 1 hour, the cloning cylinder was removed, and media was exchanged. ~2 mL of media was added in order to fill/cover the 35 mm dish. SCN neurons were kept in the incubator until ~ 11 DIV when they were fixed with 4% PFA for 15 min at 37 C, washed in PBS (3 times/5 min per wash) and stored at 4 C.

Immunofluorescent labeling, imaging, and analysis of SCN dissociated cells

For immunofluorescent labeling of SCN dissociated cultures, cells were permeabilized in 0.4% Triton-X 100/PBS for 20 min at room temperature. They were then blocked for one hour at room temperature in 10% BSA/PBS. Subsequently, cells were incubated for 3 hr at room temperature in 5% BSA/PBS with the rabbit anti-SynGAP1 primary antibody (1:300 dilution; Cat # 19739-1-AP; Proteintech) and either: mouse anti-GAD67 primary antibody (1:600 dilution), mouse anti-NeuN primary antibody (1:1500 dilution; Cat. # MAB377; Millipore), or guinea pig anti-AVP antibody (1:150 dilution; Cat. # 4562; Peninsula Laboratories International). After washing, cells were then incubated for 1 hr at 37 C in PBS in the following secondary antibodies

(1:1000 dilution of each): Alexa-Fluor 594 goat anti-rabbit and Alexa-Fluor 488 goat anti-mouse. Finally, cells were washed (3 times/5 min washes) in PBS and were incubated for 5 min (at room temperature) in 1:5000 DraQ5 before being coverslipped with Fluoromount G.

Similar to the immunofluorescent staining in SCN tissue sections, sequential labeling was performed in SCN dissociated cells in order to examine co-localization of SynGAP1 and VIP (both antibodies raised in rabbits). To this end, cells were first labeled with the rabbit anti-SynGAP1 primary antibody (1:300 dilution; Cat # 19739-1-AP; Proteintech), followed by labeling with Alexa-Fluor 594 goat-anti rabbit. Cells were then thoroughly washed and labeled with Alexa Fluor 488-conjugated VIP antibody (1:200 dilution; Cat. # BS-0077R-A488; Bioss) in order to prevent cross-reactivity between antibodies.

For immunofluorescent image acquisition of dissociated cells, 63X images were collected using a Leica SP8 confocal microscope. Notably, image/acquisition parameters (speed, line average, pinhole, contrast, etc.) remained unchanged for each experimental condition/group.

Western blotting and blot quantification

For analysis of SynGAP expression during the circadian day and night timepoints (Fig. 2.4B-2.4C), three separate cohorts of C57/Bl6 WT animals were sacrificed at CT6 and CT14. 600 µm-thick coronal brain sections containing the SCN or cortex were collected from each animal (3 animals were pooled together to create a single sample). SCN tissue was lysed in 100 µL of radioimmunoprecipitation assay buffer and cortical

tissue was lysed in 200 µL of buffer. Protein (10 µg/lane) was run on a 12% SDS-PAGE gel, and then transferred onto polyvinylidene difluoride membranes (Immobilon-P; EMD Millipore). After transferring, the membrane was blocked for 1 hour at room temperature in 10% milk (in PBST) and incubated overnight at 4^{o} C with the anti-rabbit SynGAP antibody in 5% NGS in PBST (1:1,000; dilution; Cat # 19739-1-AP; Proteintech). The next day, membranes were incubated in 10% milk (prepared from Bio-Rad Blotting-Grade Blocker non-fat dry milk #1706404) in PBST with goat anti-rabbit IgG horseradish peroxidase-conjugated antibody (1:1,000 dilution; PerkinElmer). A bioluminescent signal was generated using the Western Lightning Plus-ECL, Enhanced Chemiluminescence Substrate (PerkinElmer) and the signal was acquired using BioBlue Lite Western Blot film (Alkali Scientific). PBST washes (3 times, 5 minutes each) were carried out between each of the noted steps. Additionally, as a loading control, membranes were also probed for mouse total ERK1/2 (1:2,000 dilution in 5% NGS/PBST; Cat. # 4696S; Cell Signaling Technology).

Western blot densitometric band analysis was carried out using ImageJ software. To this end, the band intensity of SynGAP was digitally traced, inverted, background subtracted, and finally divided by the ERK1/2 band signal from the same lane. Note that the intensity from both the ERK1 and ERK2 signal was averaged for each lane/sample. An average (from each of three pools) for the SCN and cortex was then obtained.

Visual tracking/vision tests

The visual tracking test has been previously described by our lab (Snider et al., 2016b). In short, mice were placed in a rotating optokinetic response drum. The walls of

this drum were covered in white and black vertical stripes. Animals were given ~ 3 min to habituate to the drum. Following this habituation period, each animal underwent four trials (each trial lasting ~ 2 sec), during which period the drum was randomly turned to the left or to the right by the observer. Each turn of the head was scored as 'correct' (i.e. the mouse turned following the direction of the spinning drum) or 'incorrect' (i.e. the mouse turned in the opposite direction as the spinning drum). The percentage of correct head turns was then tallied for each mouse. This experiment was run during the subjective daytime (~ZT6-10) under 500 lux white light illumination.

After the optokinetic response test was conducted, all animals were also screened for proper visual acuity by assessing whether they reach for the surface with their forelimbs before making contact with the counter.

Circadian clock timing and entrainment-wheel running assays and assessment

As described in our recent publication (K. L. Wheaton et al., 2018), mice were individually housed in polycarbonate cages containing running wheels (16.5 cm diameter). Wheel revolutions were recorded in 5 min binned periods using VitalView data collection software (Actimetrics). For all assays, mice were initially entrained to a 12-hr light/12-hr dark cycle (white light: 250-300 lux at cage level) for at least 10 days. For experiments that examined locomotor activity under LD conditions, data were collected from a subsequent 2 week period; activity data over a 10-day period were processed using ClockLab Analysis software.

For experiments that examined the free running period (tau), mice were transitioned to constant darkness (DD) and were permitted to run for 17-21 days. The free

running period was then determined using ClockLab software. To this end, a regression line was drawn through the onset of daily activity for an ~ 2 week period during the DD experiment. Further, using ClockLab software, average total activity per day in DD was determined from an ~ 2 week period. Similarly, to assess the circadian period under constant lighting (LL) conditions, mice were first entrained to a standard 12-hr lights on/12-hr lights off LD cycle, and then transferred into constant illumination (10 lux) condition for 3-4 weeks. Analysis of period and total activity in LL was conducted using regression analysis with the assistance of ClockLab software (as described above for DD conditions). A comparison of total activity in LL relative to LD (see Fig. 2.8B4) was conducted over the last two weeks of LD (before mice were transferred to LL) and the last two weeks of LL.

Light-evoked phase-shifting-behavioral and cellular profiling

To assess the entraining effects of light on wheel running activity, mice were initially entrained using the noted LD paradigm, and then dark-adapted (i.e., maintained under constant darkness: DD) for at least 2 weeks before being exposed to white light (15 min; 40 lux) at circadian time (CT) 15. Mice were then returned to (DD) for at least 2 additional weeks before being pulsed again at either CT6 or CT22. The phase-shifting effects of CT6, 15, and 22 light pulses were determined utilizing the linear regression method described by Daan and Pittendrigh, 1976 (Daan and Pittendrigh, 1976). ClockLab Analysis software was used to generate the pre- and post-light pulse regression lines.
As a cellular-level readout of phase-shifting responses to light, mice were dark adapted for two days before being exposed to white light (15 min; 40 lux) at either CT6, 15, or

22. Control ('No Light') animals were not exposed to light. Mice were then sacrificed and SCN tissue was isolated, sectioned, and immunolabeled for pERK, using the methods described above.

Statistical analysis

All statistical analyses were performed using GraphPad Prism 7.0 (GraphPad Prism) software and data are presented as mean ± SEM and statistical significance ascribed to p-values < 0.05. Comparisons between two sets of group means were performed using Student's t-test, while comparisons among three (or more) group means were conducted using one-way or two-way ANOVA followed by post-hoc testing. Grubb's test was conducted on data obtained from each group to determine whether outliers were statistically significant ($p < 0.05$). Along these lines, Grubb's test was used to exclude the following: one WT mouse sacrificed at CT18 for SynGAP pSer1138 analysis (Fig. 2.5C), one *Syngap1* WT wheel running mouse used in LD activity experiments (Fig. 2.7A), one *Syngap1* WT wheel running mouse used in DD activity experiments (Fig. 2.8A), one *Syngap1* WT wheel running mouse used in LL experiments (Fig. 2.8B and 2.9A), one *Syngap1* $^{+/-}$ wheel running mouse used in CT15 phase shift experiments (Fig. 2.10E), and one *Syngap1* WT mouse used in CT22 phase shift experiments (Fig. 2.10F).

Collection/analysis of participant data from a SYNGAP1 study registry

Collection of participant data from the *Syngap1* Patient Registry followed a similar protocol as described in recent publications (Creson et al., 2019a; Michaelson et al., 2018). In brief, this patient registry is funded via the National Organization of Rate

Disorders (NORD). Note that because the data that was used for this study was de-identified prior to our analysis, IRB oversight was not necessary. Nevertheless, access to SYNGAP1 (MRD5) data was approfed by the SYNGAP1 (MRD5) Natural History and Registry Advisory Board Charter Committee. This patient registry is a longitudinal natural history study wherein parents or guardians give informed consent before depositing medical data into the registry. MRD5 participants are followed throughout their lives, and demographic, qualityof life, medical history data, genetic reports, disease/disorder data, diagnostic data, and much other information if accrued for researchers' use. Questionnaires/survey-based forms (including those pertaining to sleep/circadian rhythms) can be created by researchers and are then reviewed and approved by the registry Board of Trustees.

To gather participant data regarding sleep issues (and/or diagnosed sleep disorders), sleep and circadian/chronotype questionnaires were constructed. The registry database was then probed, and all particpants who reported having sleep issues (or who reported no issues) were recorded and analyzed. Note that in addition to the sleep data, participant demographic information, medication lists, and genetic reports were also recorded (when/if available).

Results

SynGAP expression in the SCN

Initially, C57/Bl6 mice were sacrificed during the middle of the light period (~ZT 6) and coronal brain sections containing the SCN were labeled via DAB-based immunohistochemistry for SynGAP. Representative low-magnification whole-brain

images in Fig. 2.1A reveals SynGAP expression throughout the brain, including the cortex, hippocampus, and SCN.

Higher magnification photomicrographs revealed expression of SynGAP throughout the rostro-caudal extent of the SCN. Indeed, SynGAP is broadly expressed within the SCN, and at an anatomical level, this expression pattern is consistent with expression in both the core (Fig. 2.1B2 inset; demarcated in blue) and shell (Fig. 2.1B2 inset; demarcated in red) subdivisions.

To test the specificity of the SynGAP antibody used in figure 1, Western blotting was conducted on SCN and cortical lysates. With this approach, a single major band with a mass of ~148 kDa was detected (Fig. 2.4B), which is consistent with the expected molecular weight of SynGAP (Chen et al., 1998).

SynGAP has been reported to be expressed solely within neurons of the brain (Chen et al., 1998; Jee Hae Kim et al., 1998; Zhang et al., 1999), where it is found mainly in excitatory neuronal sub-populations (Zhang et al., 1999). Indeed, double immunofluorescent labeling of SynGAP and the neuronal marker NeuN showed that SynGAP is expressed within neurons of the SCN (Fig. 2.2A-2.2B). This finding was interesting, given that the SCN is comprised mainly of GABAergic/inhibitory cell types (Antle and Silver, 2005). Further, double immunostaining with GAD67, revealed that SynGAP is expressed within GABAergic-positive cells (Fig. 2.2C-2.2D).

Though SynGAP is expressed throughout the SCN, we found that it is quite highly expressed within the dorsomedial and lateral regions (typically denoted as the SCN ‘shell’ region), when compared to the ventro-medial SCN (the SCN ‘core’) (Fig.

2.3A). Notably, this SCN 'shell' region contains many arginine vasopressin (AVP)-positive neurons, and as expected, co-immunolabeling experiments in both SCN tissue sections and in primary dissociated SCN cells, revealed strong expression of SynGAP within AVPergic neurons (Fig. 2.3B-2.3C). In addition to its expression in AVPergic neurons, SynGAP was also expressed in VIP-positive 'core' neurons (Fig. 2.3D-2.3E).

Circadian expression profile of SynGAP in the SCN

We next examined whether SynGAP expression changes as a function of circadian time. To this end, C57/Bl6 WT mice were dark-adapted for 2 days, and then SCN (and cortical) lysates were collected (in three different pooled cohorts) at CT6 (circadian day) and CT15 (circadian night) (Fig. 2.4A-2.4B) and examined via Western analysis for SynGAP. Quantitative densitometric analysis revealed that SynGAP expression was higher during the circadian night compared to the circadian day within the SCN (Fig. 2.4C; $t_{(4)} = 10.79$; $p = 0.0004$; Student's t-test). In contrast, a time-of-day difference in SynGAP expression was not detected in the cortex (Fig.2.4C; $t_{(4)} = 1.319$; $p = 0.2575$; Student's t-test).

To further explore the temporal profile of clock-gated SynGAP expression, C57/Bl6 WT mice were sacrificed at 4 hour intervals over a 24 hour period and SCN tissue was immunolabeled for SynGAP (Fig. 2.4D). Densitometric analysis revealed a time-of-day difference in SynGAP expression, with peak expression occurring during the mid-subjective night (CT18) and nadir/lowest expression occurring during the mid-subjective day (CT6) (Fig. 2.4E; $F_{(5, 22)} = 4.343$; $p = 0.0067$; One-way ANOVA). Along these lines, SynGAP expression was significantly different at CT2 and CT18, CT6 and

CT18, and CT18 and CT22 (Fig 2.4E; adjusted p values = 0.0327; 0.0173; and 0.0334; Tukey post-hoc tests). Further, to determine whether the SynGAP SCN rhythm was regulated by the circadian clock, SynGAP expression was examined in tissue from *BMAL1*$^{-/-}$ animals. *BMAL1* deletion results in a loss of circadian clock timekeeping capacity since it is a core constituent of the molecular clock (Bunger et al., 2000a). We did not detect a time-of-day difference in SynGAP expression in *BMAL1* $^{-/-}$ mice (Fig. 2.4F; $t_{(11)} = 0.4914$; $p = 0.6328$; Student's t-test). Together, these data support the idea that SynGAP expression in the SCN is under the control of the circadian timing system.

SCN clock-regulated SynGAP phosphorylation at serine 1138

Phosphorylation has been shown to function as a rapid and dynamic regulator of SynGAP-mediated signaling. Notably, SynGAP phosphorylation at serine 1138 (pSynGAP) plays a key role in coupling synaptic activity to the rapid redistribution of SynGAP from dendritic spines, which in turn facilitates Ras and Rap signaling (Araki et al., 2015). To examine whether SynGAP phosphorylation at serine 1138 is regulated by clock timing, SCN tissue from animals sacrificed at 4 hour intervals over the circadian cycle was labeled with an antibody directed against the serine 1138 phosphorylated form of SynGAP. Representative IHC labeling and quantitative profiling (Fig. 2.5A-2.5C) revealed that SynGAP phosphorylation varied across the circadian cycle. Interestingly, distinct temporal patterns of pSynGAP were detected within the SCN core and shell regions. For example, within the SCN core, peak pSynGAP was detected during the mid-subjective night (CT18), and the lowest expression level was detected during the late subjective night (CT22) (Fig 2.5C; $F_{(5, 29)} = 2.593$; $p = 0.0468$; One-way ANOVA).

Specifically, a significant difference was observed in SCN core pSynGAP expression at CT18 and CT22 and a trending difference was noted at CT14 and CT22 (Fig 2.5C; adjusted p values = 0.0292 and p = 0.0822 respectively; Tukey post-hoc tests). In contrast, within the shell, peak levels of pSynGAP were observed during the middle of the subjective day (CT6) (Fig 2.5C; $F_{(5, 28)} = 2.849$; p = 0.0335; One-way ANOVA).Specifically, a significant difference was observed in SCN shell pSynGAP expression at CT6 and CT22 and a trending difference was observed at CT10 and CT22 (Fig 2.5C; adjusted p values = 0.0280 and 0.0744 respectively; Tukey post-hoc tests). Together, these data indicate that SynGAP phosphorylation is regulated by the circadian clock. Further, the differential time-gated patterns of phosphorylation within the core and shell suggests distinct upstream signaling processes drive pSynGAP within each region.

Photic regulation of SynGAP phosphorylation at serine 1138

Given that NMDA receptor-mediated signaling is a key event in light-evoked clock entrainment, we examined whether photic stimulation regulated SynGAP phosphorylation at serine 1138. To this end, WT C57/Bl6 mice were dark adapted for two days and, exposed to light for 15 min (~100 lux) at CT15, and then sacrificed. Immunohistochemical labeling (Fig. 2.5D) revealed that photic stimulation led to an increase in pSynGAP (Fig. 2.5E; $t_{(8)} = 2.873$; p = 0.0207; Student's t-test). Of note, elevated levels of pSynGAP were concentrated within the core region (Fig. 2.5D; high magnification panels). These data indicate that light has the capacity to trigger rapid changes in the functional state of SynGAP in the SCN.

Syngap1 heterozygous mice

Next, we moved to an examination of a SynGAP heterozygous mouse model (*Syngap1*$^{lx\text{-}st}$) wherein a LoxP-STOP-LoxP cassette was inserted downstream of Exon 5 on the *Syngap1* gene—a design that leads to truncation of the full-length protein, and thus inactivates SynGAP (Clement et al., 2012). Importantly, this construct parallels *Syngap1* haploinsufficiency in human subjects, which also results from truncation of the full-length SynGAP protein (Hamdan et al., 2009a, 2011). Prior work with this mouse model has shown that *Syngap1* $^{+/-}$ mice exhibit the anticipated (~50%) reduction in SynGAP protein levels (Clement et al., 2012), in addition to profound behavioral abnormalities that have been observed with other *Syngap1* $^{+/-}$ mouse models (Clement et al., 2012; Guo et al., 2009). Of note, *Syngap1* $^{-/-}$ (null) animals were not used in our study since they die within a week after birth (Kim et al., 2003; Komiyama et al., 2002). Similar to previously published studies with this mouse line (Clement et al., 2012; Creson et al., 2019a), the *Syngap1* $^{+/-}$ animals used in our study were viable and fertile, exhibited no obvious gross anatomical abnormalities, and displayed a reduction in SynGAP protein levels (Fig. 2.6B).

Further, given that transmission of photic input from the retina to the SCN is critical in light timekeeping and entrainment capacity, we assessed vision in a subset of *Syngap1* Het and WT mice using an optokinetic drum. Importantly, we found no significant genotypic differences in percent correct-direction head tracking in this assay (Fig. 2.6C; $t_{(19)} = 0.3017$; $p = 0.7661$; student's t-test). Further, a one-way t-test determined that both genotypes displayed visual acuity that was 'above chance' (i.e. 50%--noted by the dashed line)—suggesting a strong response for correct-direction head

tracking (Fig. 2.6C; $t_{(10)} = 19.36$; $p < 0.0001$ for WT and $t_{(9)} = 14$; $p < 0.0001$; one-sample t-tests). Additionally, animals were screened for proper vision by reaching for the surface of the bench (with their forelimbs) before their vibrissae made contact with the bench. No visual issues were detected in any of the mice, according to this assay. Hence, these studies suggest that visual acuity is intact in *Syngap1* Het mice.

Syngap1 heterozygous mice display alterations in locomotor activity

In the following studies, we used wheel running activity assays to test the role of *Syngap1* in SCN clock timing and photic entrainment. To begin, *Syngap1* $^{+/+}$ and *Syngap1* $^{+/-}$ mice were transferred to a 12/12 LD cycle, and activity during both the day and night time periods was examined. Representative wheel running actograms (Fig. 2.7A1) and daily activity profiling (Fig. 2.7B) reveal an elevated level of locomotor activity in *Syngap1* $^{+/-}$ mice. In specific, *Syngap1* $^{+/-}$ mice exhibited an overall increase in mean activity during the dark period (i.e. 'active' phase) relative to WT mice (Fig. 2.7A2; $t_{(26)} = 2.066$; $p = 0.0490$; Student's t-test). In contrast, no difference in the ratio of light/dark period activity between *Syngap1* $^{+/-}$ and *Syngap1* $^{+/+}$ mice was detected (Fig. 2.7A3), or when the daily activity data were averaged across the light period (Fig. 2.7A4).

To assess the effects of *Syngap1* heterozygosity on the period of the master clock, light-entrained mice were placed in constant darkness (DD) and permitted to free-run for a 2-3 week period (Fig. 2.8A1). No statistically significant differences in period (Fig. 2.8A2; $t_{(26)} = 0.3042$; $p = 0.7634$; Student's t-test), were observed between the genotypes, indicating that *Syngap1* haploinsufficiency does not affect the inherent oscillatory

capacity of the SCN clock under standard DD/free-running conditions. Analysis of daily locomotor activity also did not detect a phenotypic difference (Fig. 2.8A3; $t_{(25)} = 0.7252$; $p = 0.4751$), though, an increase in the number of daily bouts of transient activity during the 'rest period' (i.e. the 'inactive' phase) was observed in *Syngap1* $^{+/}$ mice, relative to $^{+/+}$ animals (Fig. 2.8A4; $t_{(24)} = 2.475$; $p = 0.0208$; Student's t-test).

We next examined the effects of *Syngap1* heterozygosity on the circadian period under constant lighting (LL) conditions (Fig. 2.8B1). In rodents, exposure to constant light has been shown to lengthen the circadian period and to suppress wheel-running behavior/activity (Aschoff, 1960; Daan and Pittendrigh, 1976). Interestingly, LL triggered an increase in tau length in *Syngap1* $^{+/-}$ mice compared to $^{+/+}$ animals (Fig. 2.8B2; $t_{(13)} = 2.33$; $p = 0.0366$; Student's t-test; also see Fig. 2.9). Further, total wheel running activity in LL was increased in *Syngap1* $^{+/-}$ animals (Fig. 2.8B3; $t_{(14)} = 2.284$; $p = 0.0385$; Student's t-test; also see Fig. 2.9); however, a comparative activity analysis revealed that the enhanced LL activity in *Syngap1* $^{+/-}$ animals was a function of the increase activity under observed LD conditions (Fig. 2.8B4).

SynGAP regulates light-evoked ERK/MAPK activation and light-evoked clock entrainment

The potent inhibitory effects that SynGAP has on the Ras/ERK/MAPK signaling pathway (Komiyama et al., 2002; Rumbaugh et al., 2006; Wang et al., 2013), coupled with the well-characterized role of the ERK/MAPK signaling cassette in SCN photic entrainment, led us to investigate whether light-evoked ERK/MAPK activation and clock resetting might be altered in *Syngap1* heterozygous mice. To begin, *Syngap1* $^{+/-}$ and $^{+/+}$

animals were dark-adapted for two days and then exposed to a light pulse (15 min; ~40 lux) during the middle of the subjective day (CT6), the early subjective night (CT15) or the late subjective night (CT22) and immediately sacrificed. Control animals were not exposed to light. Coronal SCN sections were immunolabeled for the dual threonine and tyrosine phosphorylated form of ERK1/2 (pERK) a marker of ERK/MAPK pathway activation (Fig. 2.10A-2.10C). At CT6, no interaction between light pulse and genotype was observed (Fig. 2.10A; $F_{(1, 20)} = 0.05899$; $p = 0.8106$; 2-way ANOVA). Turning to the CT15 timepoint, we found an interaction between light and genotype on pERK expression (Fig. 2.10B; $F_{(1, 19)} = 17.07$; $p = 0.0006$; 2-way ANOVA). We also observed an effect of genotype (Fig. 2.10B; $F_{(1, 19)} = 16.27$; $p = 0.0007$; 2-way ANOVA). Specifically, we found a significant difference in pERK expression between light-pulsed *Syngap1* WT and heterozygous mice (Fig. 2.10B; adjusted p value < 0.0001; Tukey post-hoc test). Finally, an interaction between photic stimulation and genotype on pERK expression was also observed during the late subjective night (CT22) (Fig. 2.10C; $F_{(1, 16)} = 13.19$; $p = 0.0022$; 2-way ANOVA). An effect of genotype was also noted during this late night timepoint (Fig. 2.10C; $F_{(1, 16)} = 12.76$; $p = 0.0025$; 2-way ANOVA). Specifically, we found a significant difference in pERK expression between light-pulsed Syngap1 WT and heterozygous mice (Fig. 2.10C; adjusted p value = 0.0006; Tukey post-hoc test). Together, these data suggest that *Syngap1* functions as a negative regulator of ERK/MAPK signaling. In specific, light-induced ERK/MAPK activation is potentiated in *Syngap1* $^{+/-}$ mice during the subjective night time domain, but *Syngap1* haploinsufficiency does not affect the temporal gating of ERK/MAPK activation

(i.e. light evoked pERK1/2 expression was not observed in *Syngap1* $^{+/-}$ mice during the subjective day).

Next, to test whether SynGAP contributes to light-evoked clock entrainment, mice were challenged using an Aschoff type 1 photic entrainment paradigm (Aschoff, 1960). To begin, *Syngap1* $^{+/-}$ mice and $^{+/+}$ littermates were dark-adapted for at least 2 weeks before being exposed to a light pulse (15 min; 40 lux) at CT6, CT15 or CT22 and the phase shifting effects were analyzed using regression analysis. At CT6 (Fig 2.10D) phase-shifting responses to the mid-day light pulse were not observed in *Syngap1* $^{+/+}$ or *Syngap1* $^{+/-}$ mice (Fig. 2.9D; $t_{(13)} = 0.01498$; $p = 0.9883$; Student's t-test). At CT15 (Fig. 2.10E) *Syngap1* $^{+/-}$ mice displayed an increased light-evoked phase-delay relative to *Syngap1* $^{+/+}$ mice (Fig. 2.10E; $t_{(14)} = 2.571$; $p = 0.0222$; Student's t-test). At CT22 (Fig 2.10F), *Syngap1* $^{+/-}$ mice exhibited a light-evoked phase advance, while the phasing of the circadian rhythm was not altered by light in $^{+/+}$ mice (Fig. 2.10F; $t_{(23)} = 2.526$; $p = 0.0189$; Student's t-test). Taken together, these data indicate that SynGAP functions as a negative regulator of the entraining effects of light in the SCN. As such, the deletion of a single *Syngap1* allele augments light-evoked MAPK activation and enhances the photic response of the SCN clock to light.

MRD5 participants report sleep disturbances and sleep-related disorders

Given that our animal studies demonstrated a key role for SynGAP in the regulation of circadian clock entrainment, we became interested in whether mutations in the *Syngap1* gene lead to deficits in sleep, as sleep is modulated by the circadian clock. Thus, we mined an MRD5 (mental retardation 5) registry—which included data from

~136 participants, and we subsequently recorded demographic information (Table 2.1) from the surveys. Here, we should note that while all of these individuals are believed to have a *Syngap1*-related mutation, only a subset of participants' parents/guardians uploaded genetic reports that confirmed a variant in the actual gene. Further, only subsets of information are available for many of the participants (i.e. only partial information was available).

Upon analyzing sleep surveys/questionnaires, we noted that a large percentage of partcipants/participants' guardians reported sleep issues (Table 2.2). Indeed, nearly 78% of all particpiants (regardless of age) reported some sort of sleep disruption. This number was striking, and we then sought to delve into the details relating to the specific types of sleep issues these participants were experiencing.

To this end—we perused the sleep/circadian-specific questionnaires (for which fewer participants responded). We then cross-referenced the circadian/sleep participants with the larger database that listed information related to participant medication use (Table 2.3). Interestingly, we noted that 20 (out of 35 total participants who answered the sleep/circadian surveys) reported using melatonin as a sleep aid. Furthermore, 7 of the 35 individuals who responded to the sleep/circadian questionnaires had also been formally diagnosed with a sleep disorder (Table 2.4). Interestingly, 5 out of these 7 participants also uploaded complete genetic reports, making it possible for us to report the exact *Syngap1* variant that resulted in the clinical phenotype (Table 2.4). Finally, we constructed a detailed analysis of sleep-related issues in MRD5 participants which depicted the number of particpants who had been prescribed chronotherapy/other

medication for sleep issues, in addition to those individuals who reported fragmented sleep, early waking, trouble remaining asleep, and/or trouble falling asleep (Fig. 2.12). Given that a diagnosis of Autism Spectrum Disorder (ASD) is observed in many indiviudals with *Syngap1* mutations (Berryer et al., 2013), we compared the percentage of MRD5 participants who experienced sleep issues with the prevelance of sleep issues in individuals with Autism Spectrum Disorder (ASD) and to typically-developing indiviudals. To do this, we surveyed the clinical literature to gain an estimate of the percentage of individuals with ASD and typically-developing individuals who display sleep disturbances (Cotton and Richdale, 2006; Gail Williams et al., 2004, p. 200; Krakowiak et al., 2008; Liu et al., 2006; Miano et al., 2007; Polimeni et al., 2005; Wiggs and Stores, 2004). Interestingly, the frequency of those indiviudals prescribed chronotherapy/sleep disorders, those experiencing early wakening, and those with trouble remaining asleep were higher in MRD5 participants than the general ASD population and also higher than in typically developing individuals (Fig. 2.12). Together, these data suggest that sleep disturbances are highly prevelant in MRD5 participants.

Discussion

Here, we provide data showing that SynGAP functions as a regulator of light-evoked SCN clock entrainment. The key findings of our study reveal that 1) SynGAP is enriched within the SCN, 2) the circadian clock regulates total and phosphorylated SynGAP levels, 3) SynGAP signaling decreases the responsiveness of the MAPK pathway to light and 4) SynGAP modulates the sensitivity of the master clock to light.

Immunohistochemical profiling revealed SynGAP expression throughout the SCN, with marked labeling in both the core and shell regions. As a downstream effector of NMDA receptor signaling, the widespread expression pattern of SynGAP suggests that these two major functional subdivisions of the SCN are under the influence of NMDA receptor-mediated signaling. Consistent with these ideas, both core and shell regions of the SCN express the ion channel forming subunit of the NMDA receptor (NR1) (Duffield et al., 2012; Stamp et al., 1997), and robust NMDA-evoked calcium transients and currents have been detected throughout the rostrocaudal extent of the SCN (Colwell, 2001). Further, SCN core neurons receive a direct monosynaptic glutamatergic input from the retina, and NMDA receptor activity has been implicated in photic entrainment (Abe et al., 1991; Colwell, 2001; Ebling, 1996; Moriya et al., 2000; Pennartz et al., 2001). SCN shell neurons receive glutamatergic inputs from the cortex, and basal forebrain (Leak et al., 1999; Moga and Moore, 1997), though the precise functional roles of these inputs is not known. Interestingly, recent work has also shown that glia-mediated glutamatergic signaling regulates the activity of pre-synaptic NMDA receptors within the shell region, and that this inter-SCN astrocytic-neuronal signaling circuit regulates SCN pacemaker activity (Brancaccio et al., 2017). Given the widespread expression of SynGAP in the SCN, these findings indicate that SynGAP could be contributing to a diversity of physiological processes.

Our initial finding—the high expression of SynGAP within the SCN—was an interesting early discovery. Along these lines, the SCN is comprised mainly of GABAergic neurons, (Abrahamson and Moore, 2001; Moore and Speh, 1993) while the

majority of SynGAP literature has focused on its functional role within glutamatergic, excitatory neurons where it is localized to synapses (Jeyabalan and Clement, 2016). It is important to note, however, that a recent study corroborated our findings that SynGAP is expressed in inhibitory neurons. To this end, Berryer *et al* found that GAD67 positive cells co-localized with SynGAP positive cells and that *Syngap1* haploinsufficiency in GABAergic cells impaired their connectivity and reduced inhibitory synaptic activity (Berryer et al., 2016). This study conducted by Berryer *et al*, coupled with our results here, raise interesting questions about the role of SynGAP in inhibitory neuronal populations.

With respect to its circadian expression pattern, we found that SynGAP displayed peak expression during the late subjective night and low expression during the mid-subjective day. These results, coupled with the fact that a time-of-day difference in expression was not detected in *BMAL1* null animals, indicates that SynGAP is under the control of the circadian clock. Consistent with this finding, microarray-based RNA profiling also detected a circadian rhythm in *Syngap1* in the SCN (see cycling transcript on CircaDB; probeset 10443108) (Pizarro et al., 2013a). Of note, genomic database analysis did not identify a canonical E-box (CACGTG) motif within the 5' regulatory region of *Syngap1* (1 kbp flanking the transcription start site) (Cunningham et al., 2019). Thus, *Syngap1* SCN transcriptional rhythms are likely under the control of an ancillary core-clock-gated transcriptional mechanism. Consistent with this, numerous clock-regulated transcription factors (TFs) bind to the regulatory region of the *Syngap1* promoter, including AP-1 and CRE binding TFs, as well as GC

box element binding TFs (Rouillard et al., 2016). Finally, recent work showing that SynGAP expression is dynamically regulated by the clock-gated RNA binding protein FUS (Jiang et al., 2018; Wang et al., 2018; Yokoi et al., 2017) raises the prospect that daily oscillations in mRNA stability could also contribute to the data reported here.

Turning to its regulation, neuronal activity-mediated changes in SynGAP phosphorylation have been shown to play a key role in its functional effects (Jeyabalan and Clement, 2016; Walkup et al., 2015). Along these lines, phosphorylation of SynGAP at serine 1138 (pSynGAP) by CaMKII leads to its rapid dispersion from dendritic spines, which in turn, results in increased Ras/MAPK signaling (Araki et al., 2015). Here we show that SynGAP phosphorylation at Ser1138 was both rhythmic and induced by light within the SCN. Interestingly, the high levels of daytime pSynGAP within the shell corresponds with the time period of elevated levels of neuronal firing (Inouye and Kawamura, 1982; for review, see Welsh et al., 2010), and increased cytoplasmic Ca2+(Brancaccio et al., 2013; Enoki et al., 2017; Noguchi et al., 2017). This, coupled with the well characterized role of CaMKII in the SCN timing (Kon et al., 2014), raises the prospect that rhythmic SynGAP phosphorylation may be a functional output of a clock-gated rhythm in CaMKII activity. It should also be noted that while the increased nighttime expression of pSynGAP (within the SCN core) appears to coincide with total expression of SynGAP (see Fig. 2.4D), the ratio of pSynGAP to total SynGAP could actually remain unchanged (or even decrease) during the subjective night. If such a case were true, it may suggest that at night, SynGAP could be especially responsive to photic input, thus leading to robust plasticity changes. Clearly, further studies are required in

order to tease apart the nature of the changes in the temporal profile of pSynGAP expression within the SCN shell and core subregions.

Similar to LTP paradigms, which show that SynGAP is rapidly phosphorylated at serine 1138 (Araki et al., 2015), we found that a brief photic stimulation paradigm triggered SynGAP phosphorylation in the SCN. Given the noted model, wherein SynGAP phosphorylation leads to enhanced Ras activity, we postulated that light-evoked ERK activation would be enhanced in *Syngap1* $^{+/-}$ mice. Consistent with this idea, we detected elevated levels of light-evoked MAPK signaling during both the early and late subjective night in Syngap1 $^{+/-}$ mice, compared to $^{+/+}$ animals. We should mention that we did not detect a significant baseline elevation in ERK/MAPK expression in *Syngap1* $^{+/-}$ mice, though several studies have reported such increases (Komiyama et al., 2002; Rumbaugh et al., 2006). The reason for this difference is not clear, although it is reasonable to consider that ERK signaling in the SCN is modulated by a distinct set of regulatory processes from other brain regions that have shown the upregulation of basal ERK activity in *Syngap1*$^{+/-}$ mice; a salient example of one such mechanism is the tight, time-of-day, regulation of MAPK activity by the SCN timing system (Karl Obrietan et al., 1998).

The increased sensitivity of the MAPK pathway that we observed in light-pulsed *Syngap1* $^{+/-}$ mice corresponded with an increased phase-shifting effect of light. Given prior work showing that the MAPK pathway plays a key role in light evoked clock entrainment (Butcher et al., 2002b; Coogan and Piggins, 2003b; Karl Obrietan et al., 1998), the data provided here support the idea that SynGAP functions as a modulator of

light-evoked clock entrainment, via its effects on MAPK signaling. Clearly, additional experiments that examine the role of SynGAP in shaping the light-evoked PRC (phase response cure) profile, as well as inducible gene expression programs are highly merited. Nevertheless, to place our current data into a larger context, we have included a potential model outlining how SynGAP may be functioning to facilitate light-evoked MAPK-dependent, circadian clock entrainment (Fig. 2.11). Finally, it is worth noting that while a late night (~CT20-23) light pulse typically leads to a phase advance, our lab (and others) have found that phase advances are weak (and sometimes absent) in C57/Bl6 mice that receive low intensity (~30–40 lux), short duration (≤15 min), light pulses (for a few examples, see (Antoun et al., 2012; Cheng et al., 2006b). As such, the limited phase advancing effects of light reported here are consistent with prior studies.

While several groups have shown that *Syngap1* $^{+/-}$ mice display hyper-locomotion in both novel and familiar cages/spaces (Berryer et al., 2016; Clement et al., 2012; Guo et al., 2009; Muhia et al., 2012, 2010; Nakajima et al., 2019; Ozkan et al., 2014), time-of-day activity-based activity profiling in *Syngap1* $^{+/-}$ mice is limited. Here, we observed a marked increase in wheel-running activity during the nighttime domain in *Syngap1* $^{+/-}$ mice housed in LD conditions, replicating a recent finding that used video tracking software to assess the motor activity of WT and heterozygous animals across the day (Sullivan et al., 2020). Interestingly, our studies show that this same hyperactive phenotype was also observed in LL conditions—wherein *Syngap1* $^{+/-}$ mice displayed increased overall activity relative to their WT littermates. Whether or not SynGAP

signaling within the SCN contributes to this increased level of locomotor activity has yet to be examined.

An analysis of the circadian timing properties of the SCN did not detect an effect on periodicity (tau) in *Syngap1* heterozygous mice under DD conditions. This lack of an effect on free running periodicity in DD indicates that a reduction in SynGAP expression/signaling is not sufficient to affect SCN clock timing properties. Clearly, a more complete picture of SynGAP functionality in the SCN would require the use of mice that are homozygous for null alleles of *Syngap1*; unfortunately, *Syngap1* null mice die early in postnatal development (Kim et al., 2003; Komiyama et al., 2002).

In contrast to the lack of an effect under DD conditions, under LL, a marked tau lengthening phenotype was detected in *Syngap1* $^{+/-}$ mice compared to $^{+/+}$ mice. Constant light-evoked changes in Tau lengthening is a well-characterized phenomenon (Aschoff, 1979, 1960; Daan and Pittendrigh, 1976; DeCoursey, 1959; Pittendrigh, 1960) that has been postulated to be a function of the shape of the phase response, with period lengthening resulting from greater phase delaying versus phase advancing effects of light. Notably, tau lengthening effects of LL increase as a function of light intensity (Aschoff, 1979, 1960; Daan and Pittendrigh, 1976; Hofstetter et al., 1995).

Placed within this mechanistic model, the most parsimonious explanation for the data reported here, is that the enhanced tau lengthening in *Syngap1* $^{+/-}$ mice results from an increased photic sensitivity of the SCN to early night light (although increased photic sensitivity was also observed during the late night). Additional experiments that more fully characterize the light sensitivity as a function of clock time would help clarify the

mechanism. Likewise, experiments that examine MAPK signaling and clock gene rhythms within the core and shell under LL conditions could provide mechanistic insights into this tau lengthening phenotype.

In humans, *de novo* genetic variants in the *Syngap1* gene that result in haploinsufficiency (named MRD5; OMIM#603384) are functionally characterized by a number of neurological deficits which manifest in early childhood, including reduced intellectual aptitude/cognitive capacity, delayed language development, and autistic-like tendencies (Berryer et al., 2013; Mignot et al., 2016; Parker et al., 2015). In addition to these neurodevelopmental abnormalities, 60-70% of individuals with *Syngap1* gene mutations also report sleep issues (Jimenez-Gomez et al., 2019; Prchalova et al., 2017; Vlaskamp et al., 2019). Our MRD5 participant registry data extends upon these findings, as we noted that nearly 78% of respondents displayed sleep issues, and many of these participants had actually been diagnosed with sleep disorders. Interestingly, both sleep and cognition are processes that are modulated by the circadian clock (Fisk et al., 2018; Potter et al., 2016; Snider et al., 2018b; Waterhouse, 2010; Wright et al., 2012b). Given that the *Syngap1* $^{+/-}$ mice used in our study serve as a construct-valid/translatable model of *Syngap1* gene haploinsufficiency in humans (Jeyabalan and Clement, 2016; Kilinc et al., 2018; Ogden et al., 2016), these mice could serve as a powerful tool to further our understanding of how disruption(s) in the circadian timing system might contribute to the clinical characteristics observed in MRD5 patients. Furthermore, though our data did not extensively profile other circadian-modulated processes within MRD5 participants, it would be interesting to examine rhythms in hormone release, in addition to gaining a

better understanding of typical activity patterns (i.e. chronotype details) from individuals with *Syngap1* mutations. Such information could provide critical details regarding the optimal time-of-day administration of medication, etc. (a topic known as chronomedicine).

Acknowledgements

Dr. Richard Huganir (and lab) donated the phospho-SynGAP antibodies. Dr. Andrew Fischer (and lab) allowed me to use their optokinetic drum for the visual acuity assay. Dr. Karl Obrietan was involved in the design, construction, and editing of the schematic. Monica Weldon (Bridge the Gap) assisted in the distribution, collection, de-identification, and organization of data obtained from MRD5 participants. We would also like to thank the MRD5 registry and NORD for allowing us to gather sleep information from MRD5 participants.

Figure 2.1 Expression of SynGAP in the SCN
(A) Coronal mouse brain section immunolabeled for SynGAP. Marked immunoreactivity is observed within the hippocampus (Hi), cortex (CTX), and SCN (boxed in black). Scale bar = 1 mm. (B1) High-magnification image of SynGAP expression in the central SCN. Note that SynGAP is observed throughout the SCN, with strong expression in the dorsal and lateral regions (white asterisks). 3V: third ventricle; OC: optic chiasm. Scale bar = 200 μm. (B2) The neuroanatomical demarcation of the SCN shell (red) and core (blue) is denoted. (B3) As an immunolabeling control, SCN tissue was processed without incubation with the primary antibody.

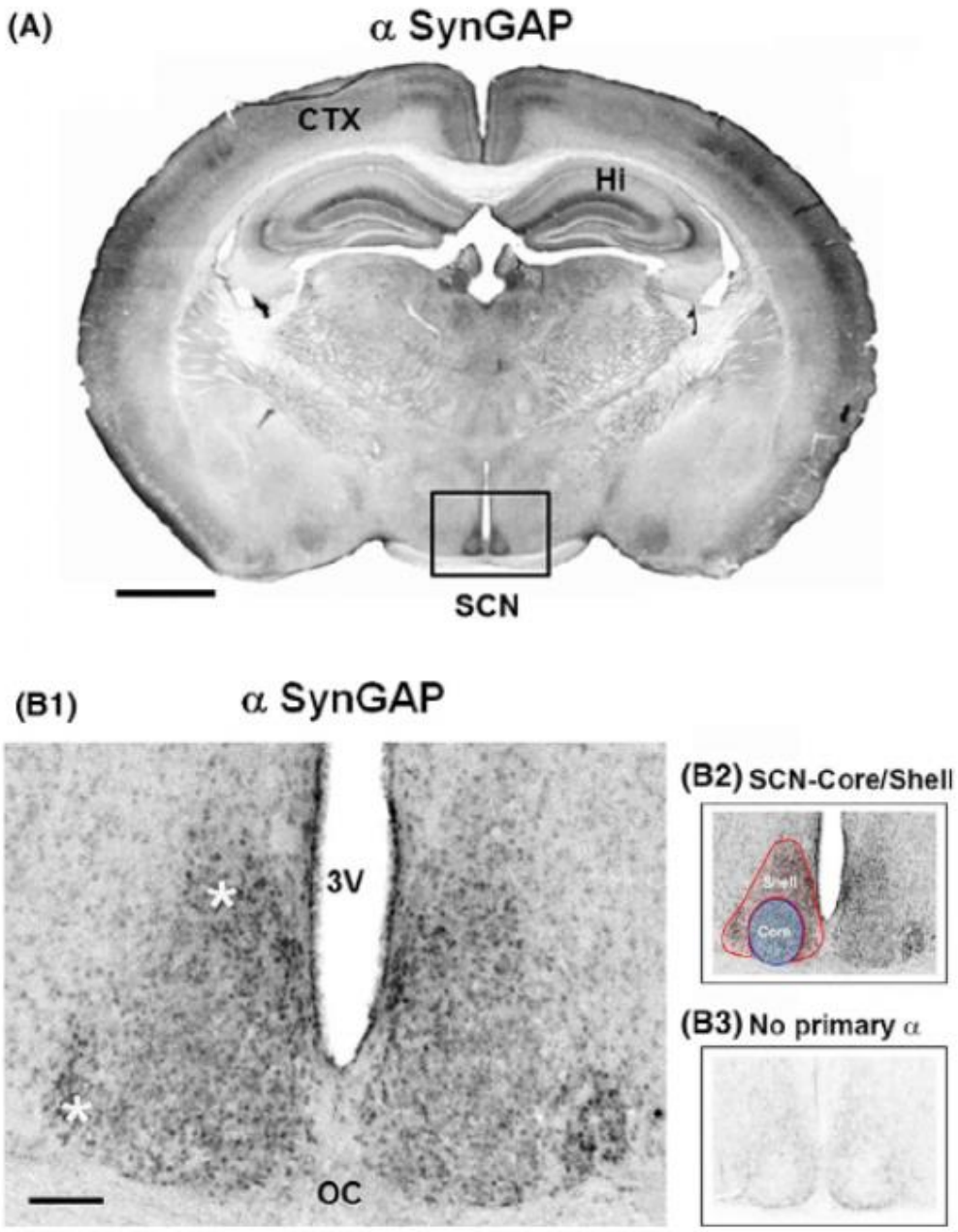

Figure 2.2 Cellular-level expression of SynGAP in the SCN
(A) Left panel: 20X image of the SCN labeled with SynGAP (green), the neuronal marker NeuN (red) and the DNA stain DraQ5 (blue). Scale bar = 100 µm. Right panels: magnified 63X images taken from the central SCN. The white asterisk in the low magnification image on the left approximates the regions that are magnified in the panels on the right. Note the expression of SynGAP within the cytoplasm and perinucleus. White arrows denote neurons, as determined by NeuN labeling. Scale bar = 10 µm. (B) 63X images of SCN dissociated cells labeled with SynGAP (green), NeuN (red), and DraQ5 (blue). White arrows denote SynGAP positive cells that are also positive for NeuN. Scale bar = 10 µm. (C) Left panel: 20X image of the SCN labeled with SynGAP (green), GABAergic neuron marker Gad67 (red), and DraQ5 (blue). Note the expression of Gad67 within the perinuclear region of the cells. Right panel: 63X magnified images taken from the central SCN. (D) 63X images of SCN dissociated cells labeled with SynGAP (green), Gad67 (red), and DraQ5 (blue). Note the colocalization of SynGAP and Gad67. White arrows denote colocalization between SynGAP and Gad67 positive cells. Scale bar = 10 µm.

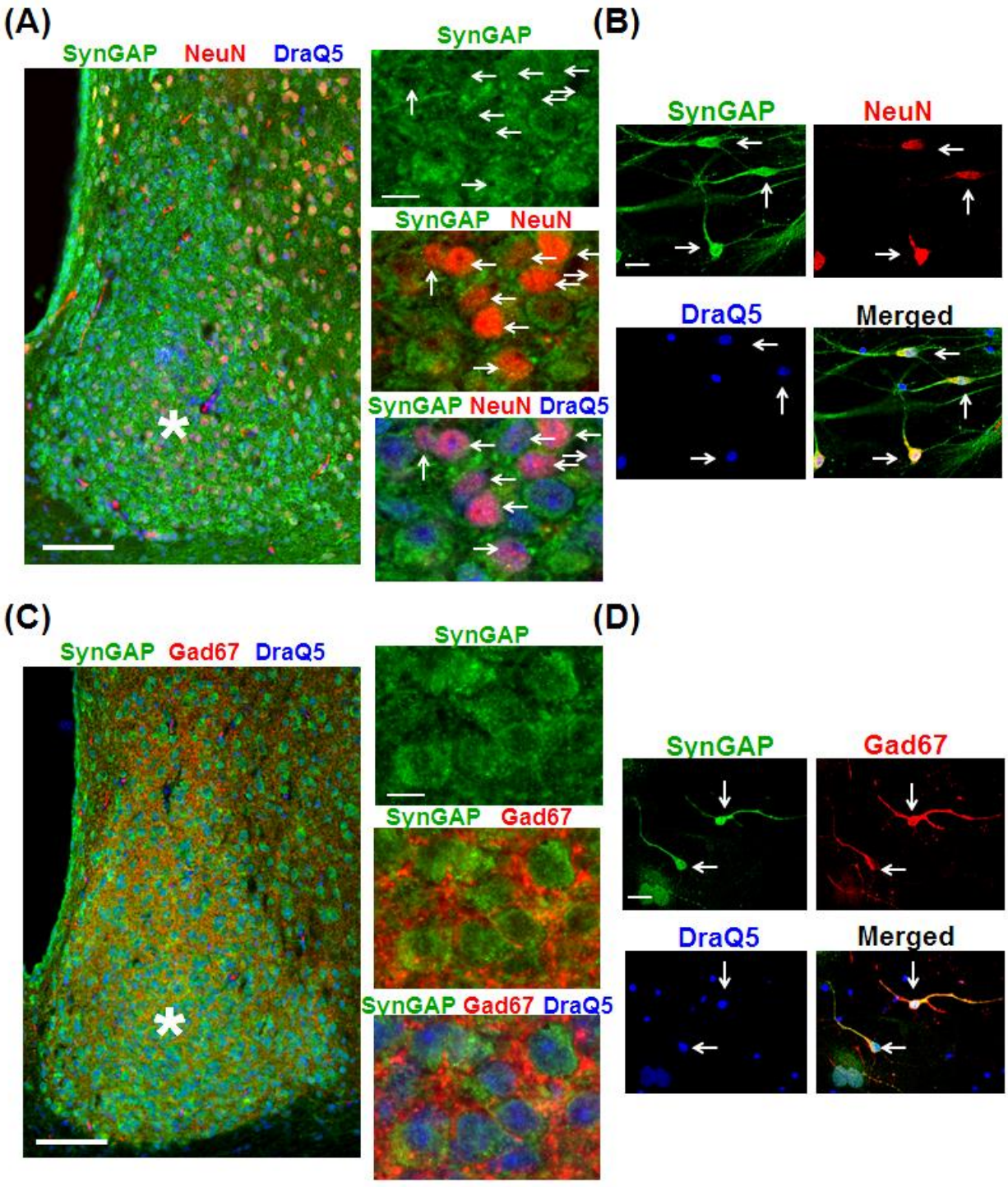
(A)
SynGAP NeuN DraQ5
SynGAP
SynGAP NeuN
SynGAP NeuN DraQ5
(B)
SynGAP
NeuN
DraQ5
Merged
(C)
SynGAP Gad67 DraQ5
SynGAP
SynGAP Gad67
SynGAP Gad67 DraQ5
(D)
SynGAP
Gad67
DraQ5
Merged

Figure 2.3 SynGAP colocalization with SCN neuropeptides
(A) DAB immunolabeling of SynGAP in a central SCN section. Note that SynGAP expression is observed throughout the SCN, with marked expression found in the dorsal and lateral regions. Scale bar = 100 µm. (B) Left panel: 20X representative immunofluorescent-labeled central SCN section. Staining depicts SynGAP (green), AVP (red), and DraQ5 (blue). Scale bar = 100 µm. The white astrices approximate the regions shown in the high-magnification images. Right panel: 63X images of SynGAP and AVP. Note the co-localization between SynGAP and AVP expressing neurons. Scale bar = 10 µm. (C) 63X images of SCN dissociated cells labeled with SynGAP (green), AVP (red), and DraQ5 (blue). White arrows denote neurons positive for both SynGAP and AVP. Scale bar = 10 µm. (D) Left panel: 20X representative immunofluorescent-labeled central SCN section. Staining depicts SynGAP (green), VIP (red), and DraQ5 (blue). Scale bar = 100 µm. Right panel: 63X images of SynGAP and VIP. Note the co-localization between SynGAP and VIP expressing neurons. Scale bar = 10 µm. (E) 63X images of SCN dissociated cells labeled with SynGAP (green), VIP (red), and DraQ5 (blue). White arrows denote neurons positive for both SynGAP and VIP. Scale bar = 10 µm.

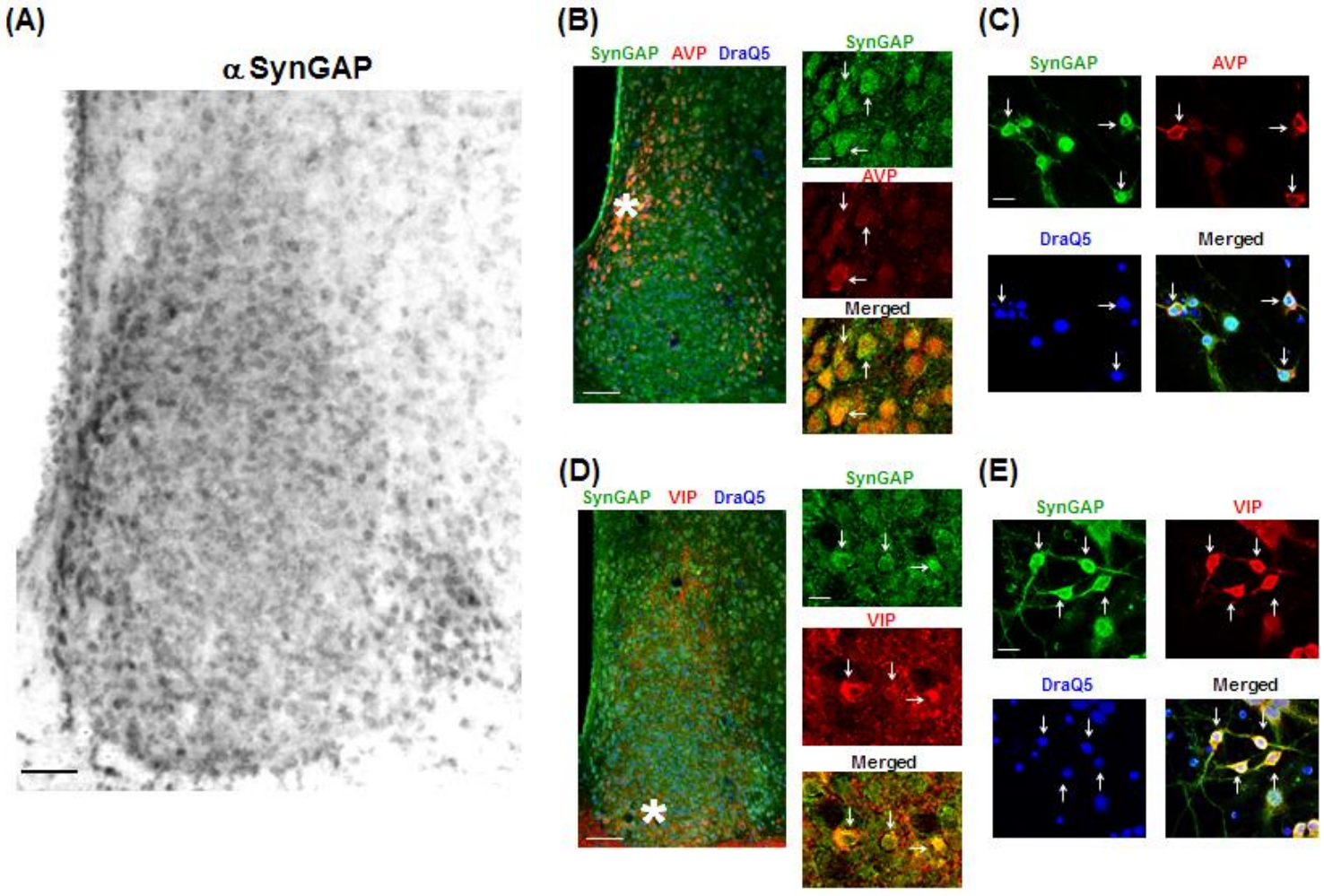

Figure 2.4 SynGAP expression across the circadian cycle
(A) Diagram illustrating the 24 hr circadian cycle under dark-adapted (no light) conditions. The white section of the horizontal bar refers to the circadian day (experimental time points are noted: CT2, CT6, and CT10), a period when lights would normally be 'on'. The gray horizontal bar represents the circadian night (experimental time points are noted: CT14, CT18, and CT22) when lights would normally be 'off'. (B) Representative Western blots from SCN and cortical lysates probed for SynGAP and ERK1/2 (the loading control). Samples were obtained from three separate tissue pools (biological triplicates) for the circadian day (CT 6) and the circadian night (CT 14) timepoints. (C) Quantitation of SynGAP expression. Data are presented as the normalized expression ratio of SynGAP/ERK1/2 (please see the Methods section for a description of the quantitation method). Statistical significance was assessed using the Student's t-test. ***: $p < .001$; n.s.: not significant. (D) Immunohistochemical profiling of SynGAP expression in the SCN over the circadian cycle. Animals were sacrificed at 4-hr intervals beginning at CT2. Scale bar = 100 μm. (E) SynGAP expression profiled as a function of circadian time. Data were normalized to the mean value at CT2, which is set equal to a value of 1. N = 4–5 animals per timepoint; Data were analyzed using one-way ANOVA followed by post hoc tests. **: $p < .01$; *: $p < .05$. (F) Left panels: Representative images of SynGAP immunolabeling in SCN sections obtained from BMAL1 -/- animals sacrificed at CT6 and CT15 timepoints. Scale bar = 100 μm. Right panel: Densitometric analysis of SynGAP expression in BMAL1 -/- animals sacrificed at CT6 and CT15. All values were normalized to the sample with the highest expressing value of SynGAP at CT15, which was set equal to a value of 1. SynGAP expression did not differ between these timepoints. Data were analyzed using the Student's t-test. n.s. = not significant. N = 6–7 mice analyzed per timepoint.

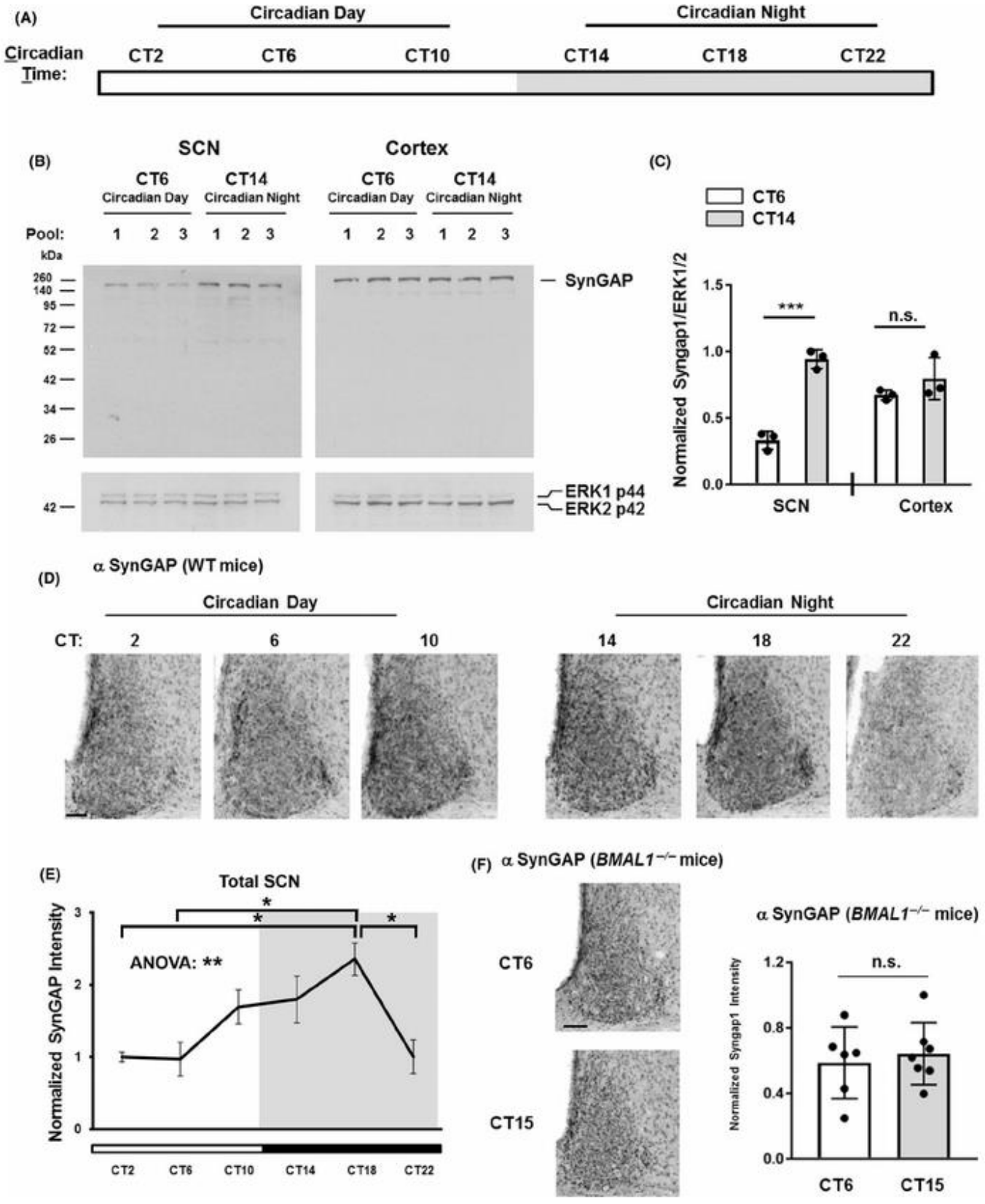
(A)
Circadian Day
Circadian Night
Circadian Time:
CT2
CT6
CT10
CT14
CT18
CT22
(B)
SCN
Cortex
CT6
CT14
Circadian Day
Circadian Night
Pool:
1 2 3 1 2 3
kDa
260
140
95
72
52
42
34
26
SynGAP
ERK1 p44
ERK2 p42
(C)
CT6
CT14
Normalized Syngap1/ERK1/2
1.5
1.0
0.5
0.0
***
n.s.
SCN
Cortex
(D)
α SynGAP (WT mice)
Circadian Day
Circadian Night
CT:
2
6
10
14
18
22
(E)
Total SCN
Normalized SynGAP Intensity
ANOVA: **
CT2
CT6
CT10
CT14
CT18
CT22
(F)
α SynGAP (BMAL1−/− mice)
CT6
CT15
α SynGAP (BMAL1−/− mice)
Normalized Syngap1 Intensity
n.s.
CT6
CT15

Figure 2.5 SynGAP phosphorylation at serine 1138 (pSynGAP) in the SCN across the circadian day and after a nighttime light pulse

(A) Immunolabeling-based profiling of pSynGAP over the circadian cycle: tissue was collected at four hour intervals beginning at CT2. Scale bar = 100 µm. (B) As a reference, the neuroanatomical demarcation of the SCN shell (red) and core (blue) is denoted. (C) pSynGAP expression as a function of circadian time is profiled in the SCN core (left panel) and shell (right panel). Data were normalized to the CT2 mean intensity values, which were set equal to 1. N = 5-6 animals per timepoint; data were analyzed using one-way ANOVA followed by post-hoc tests. *: $p < .05$; n.s. = not significant. (D) Representative immunolabeling for pSynGAP after a 15 minute (~100 lux) light pulse (or no pulse) at CT15. Note that the asterisks in the low magnification images (left panels) approximate the locations of the magnified regions in the right panels. Scale bar = 200 µm for low magnification images and 100 µm for high magnification images. (E) Graphical representation of relative pSynGAP intensity under the two conditions. Data were normalized to the light-pulsed animal with the highest pSynGAP expression, which was set equal to 1. N = 5 animals per timepoint; data were analyzed using the Student's t-test. *: $p < .05$.

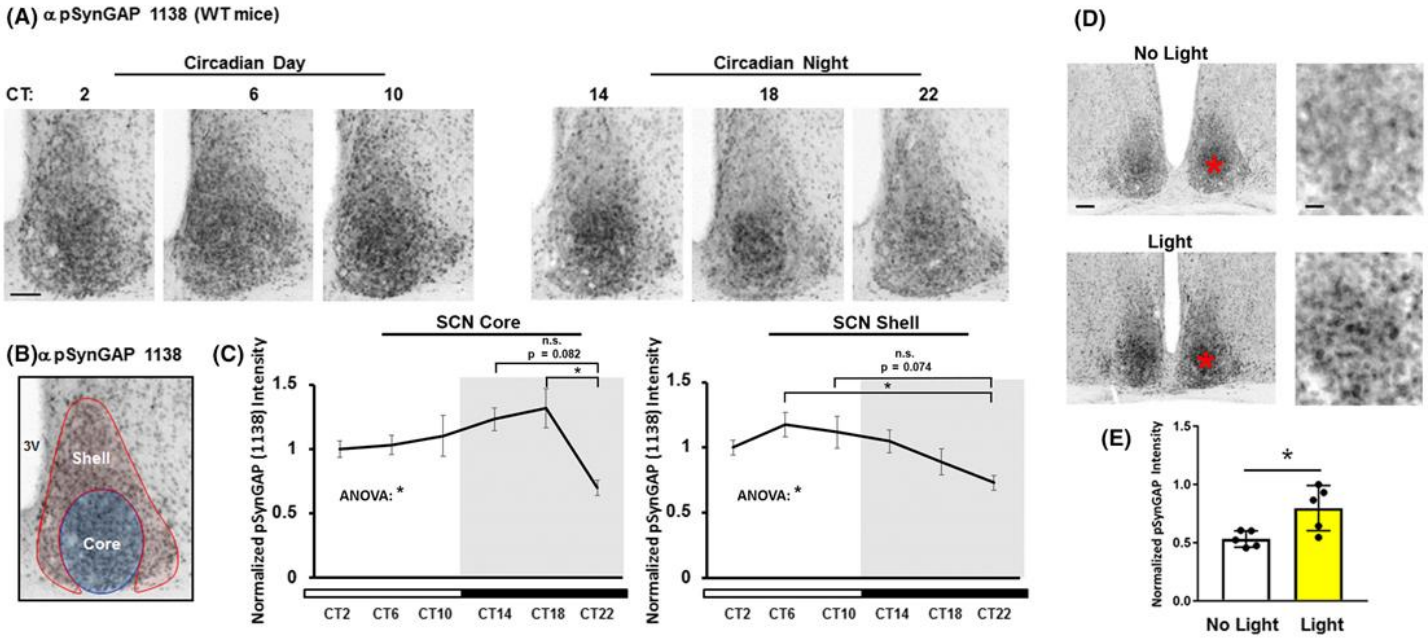

Figure 2.6 Characterization of *Syngap1* $^{+/-}$ mice
(A) Polymerase chain reaction (PCR)-based genotyping results for *Syngap1* WT (left panel) and mutant (right panel) alleles. PCR products were run on a 1.5% agarose gel and were visualized using ethidium bromide. Animal 1 represents a *Syngap1* $^{+/+}$ animal (containing only the *Syngap1* WT allele) whereas Animal 2 represents a *Syngap1* $^{+/-}$ animal (containing one *Syngap1* WT and one *Syngap1* mutant allele). Note that the gel images have been compressed. (B) Representative IHC-based labeling for SynGAP expression within the SCN of a *Syngap1* $^{+/+}$ and *Syngap1* $^{+/-}$ animal. Scale bar = 100 µm. (C) Graphical representation of the optokinetic response test—a measurement of visual acuity—in *Syngap1* $^{+/+}$ and $^{+/-}$ mice. All mice were tested for the number of correct head turns. Note that there was no significant difference in visual acuity between genotypes. Also note that the percentage of correct responses was significantly different than chance levels (i.e. 50%--is denoted by the black dashed line). N = 10-11 mice per genotype. n.s. = not significant.

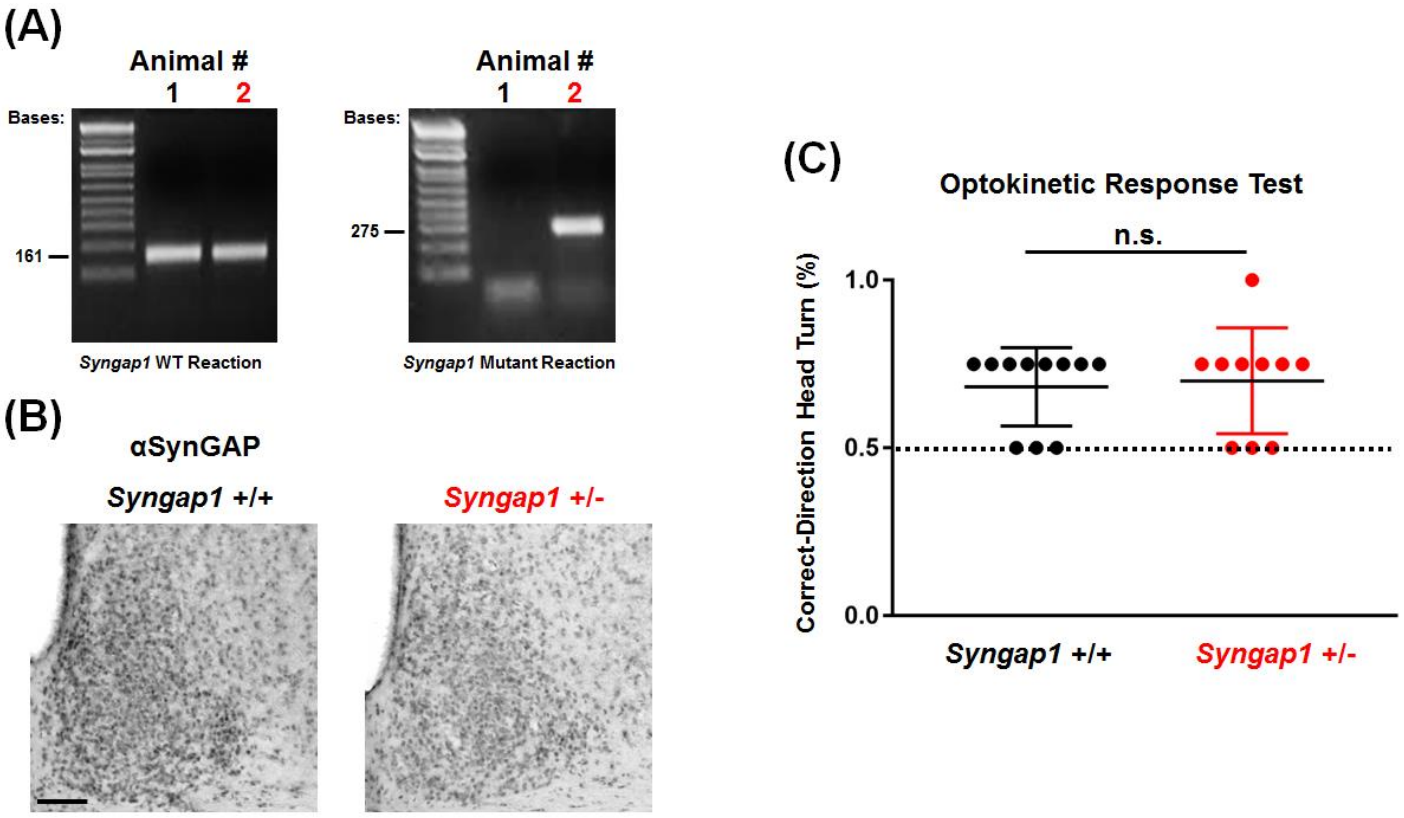

Figure 2.7 Light-gated locomotor activity in *Syngap1* $^{+/-}$ mice
(A: A1) Representative double-plotted actograms of wheel-running activity from a Syngap1+/+ and Syngap1+/−animal. Throughout the profiling, mice were maintained on a 12:12 hr light/dark (LD) cycle. (A2) Daily activity (wheel rotations) during the 'Dark Period' is presented as the mean ± SEM value for each genotype; mean dark period activity for each animal is also presented as a scatter plot. (A3) The mean ± SEM dark/light period activity ratio for each genotype is plotted, as is the mean daily ratio for each animal. (A4) Daily activity (wheel rotations) during the 'Light Period' are presented as the mean ± SEM value for each genotype; mean daily light period for each animal is also presented as a scatter plot. Data presented in A were averaged from 13 to 14 animals per genotype. *: p < .05; n.s. = not significant; assessed via Student's t-tests. (B) Mean daily activity profiles of Syngap1 +/+ and Syngap1 +/− mice over a 24 hr LD cycle. Plotted data were averaged from 14 to 15 mice per genotype.

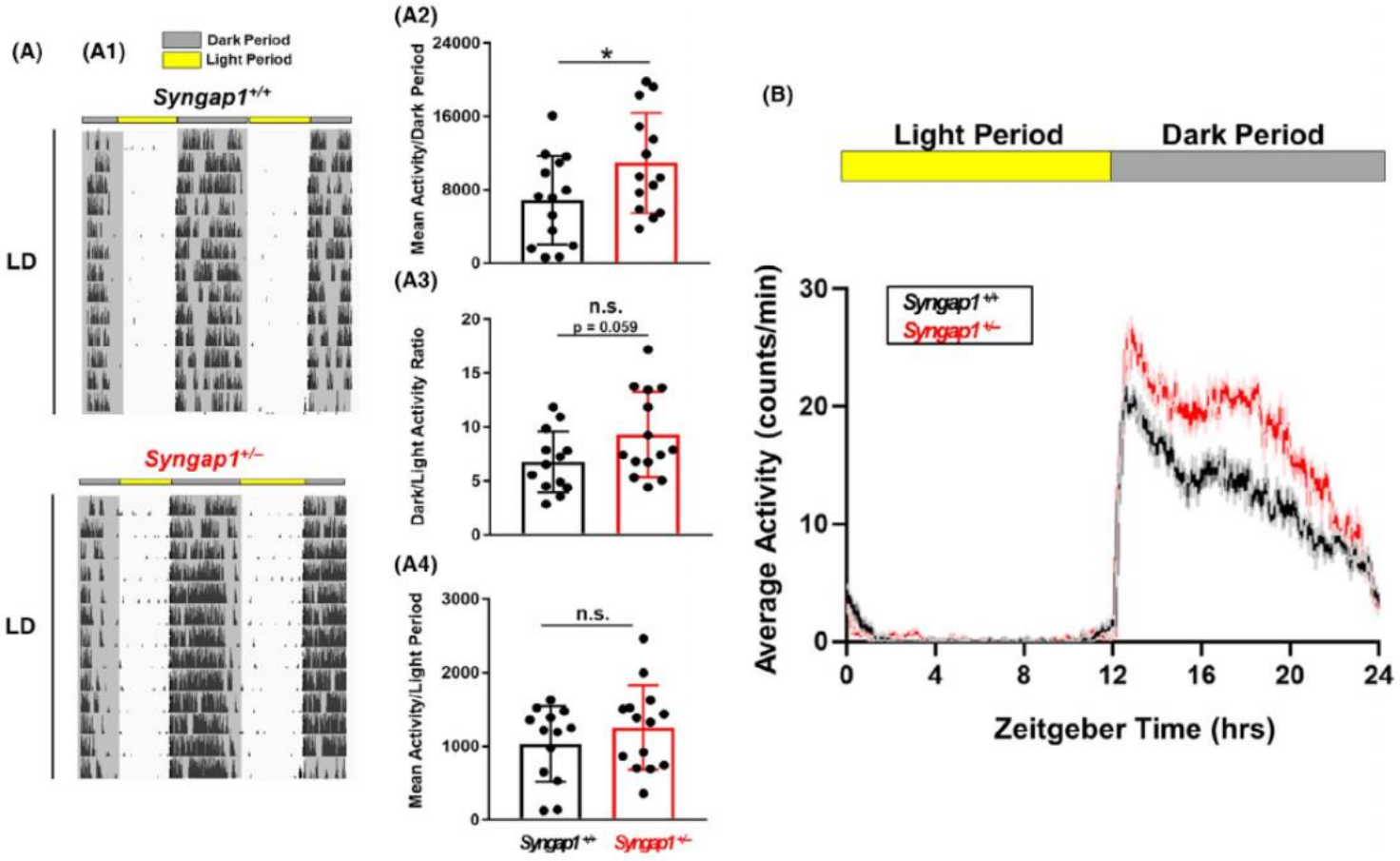

Figure 2.8 Circadian-gated locomotor activity in *Syngap1* $^{+/-}$ mice
(A: A1) Representative actograms of Syngap1 +/+ and Syngap1 +/− animals in free-running (DD) conditions. The mean ± SEM circadian period (tau) (A2) and activity (rotations per 24 hr period) (A3) are presented for each genotype. Mean tau and daily activity values for each animal are presented in scatter plot form in A2, and A3, respectively. (A4) Activity bouts per day during the rest period are presented as group means ± SEM; data for individual animals are presented in scatter plot form. (B: B1) Representative actograms of Syngap1+/+ and Syngap1+/− animals in constant light (LL). The group mean ± SEM circadian period (tau) (B2) and mean daily activity (rotations per day) (B3) in LL conditions for each genotype are shown. Mean tau and daily activity values for each animal are presented in scatter plot form in B2, and B3, respectively. (B4) Mean ± SEM percent total activity in LL condition relative to the LD condition is presented as both a group mean and scatter plot. Please see the Methods section for a description of the analysis approaches. All data presented in A and B were averaged from 7 to 14 animals per genotype; *: p < .05; n.s. = not significant; Student's t-test.

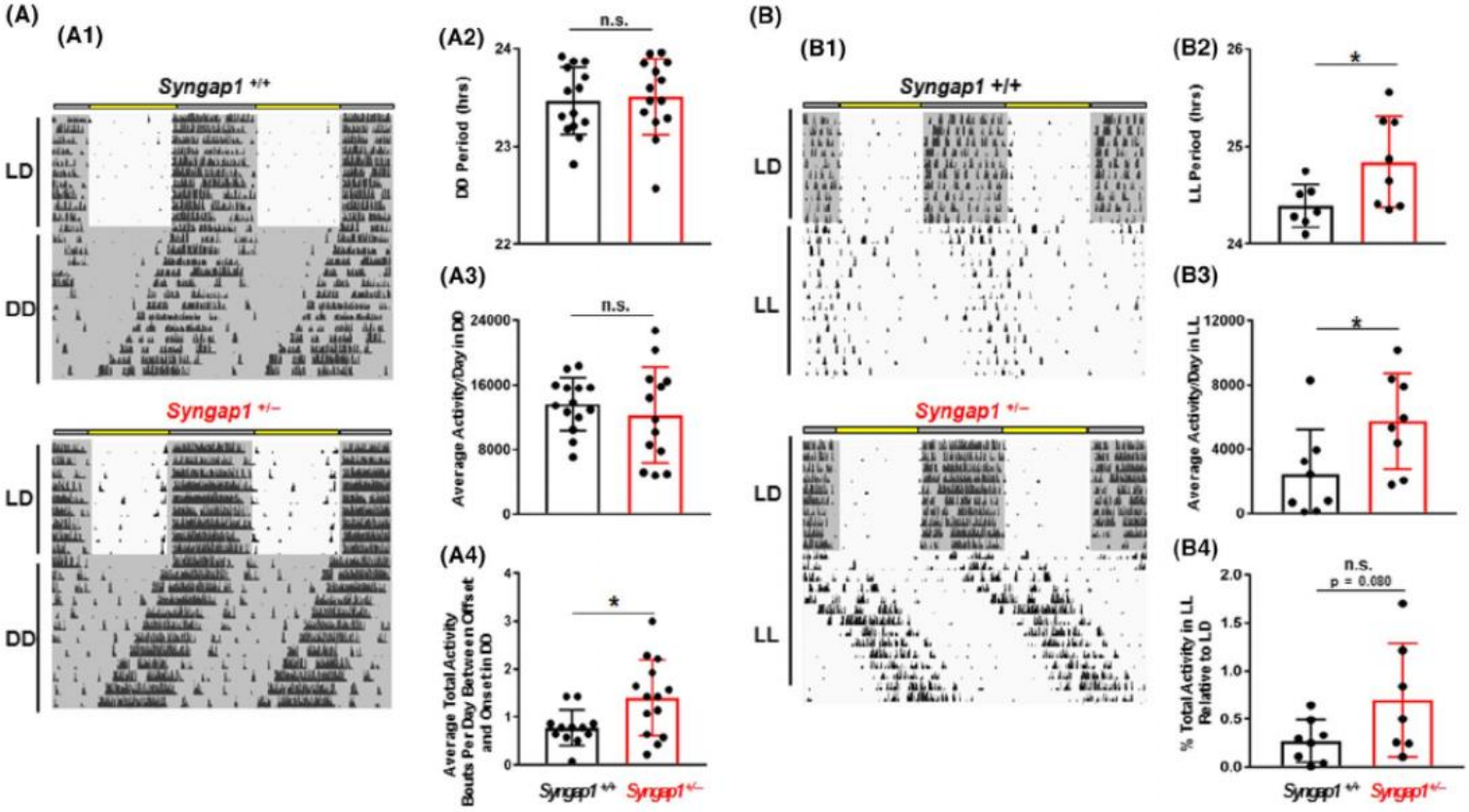

Figure 2.9 LL actograms in all *Syngap1* $^{+/+}$ and $^{+/-}$ mice
(A) LL wheel running actograms in all 8 *Syngap1* WT mice. Actograms represent wheel running activity from the first ~21 days in constant lighting (LL) conditions. (B) LL wheel running actograms in all 8 *Syngap1* Het mice. Actograms represent wheel running activity from the first ~21 days in constant lighting conditions. Note that the red boxes on the actograms represent a period of disrupted data collection.

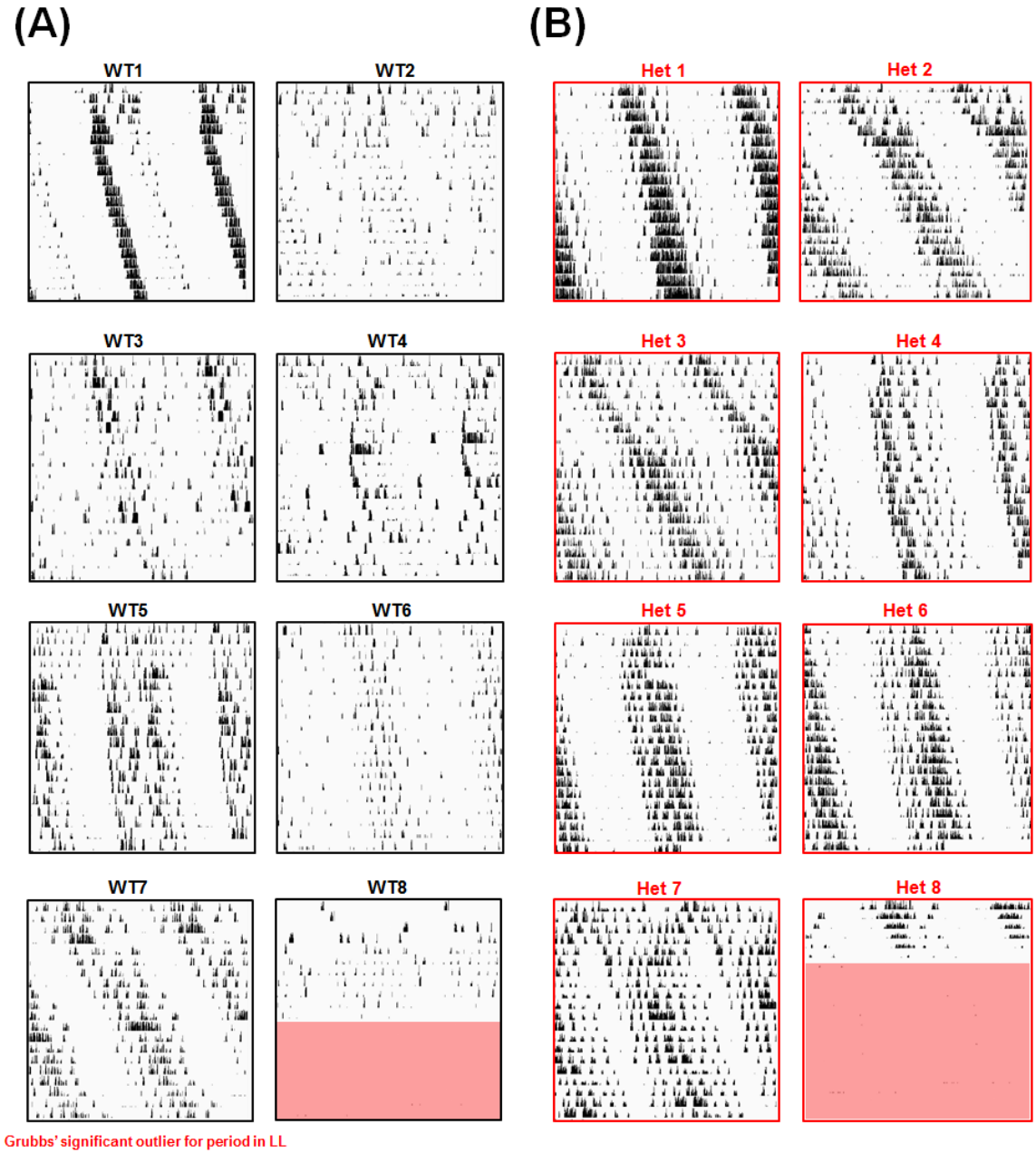

Figure 2.10 *Syngap1* regulates light-evoked ERK/MAPK activation and clock entrainment
Syngap1 regulates light-evoked ERK/MAPK activation and clock entrainment. (A-C: left panels) Representative low (top panels) and high (bottom panels) magnification images of pERK immunostaining in Syngap1 +/+ and Syngap1 +/− mice exposed to light (15 min; ~40 lux) or not exposed to light during the subjective day (CT6) (A), early subjective night (CT 15) (B) and late subjective night (CT 22) (C). Note that the red asterisk in the top panel approximates the location of the region depicted in the bottom panel. Scale bar = 200 µm for low magnification images and 100 µm for high magnification images. (A–C: right panels) Quantitative analysis of pERK immunostaining. For each circadian time, data were normalized to the control (i.e., no light) Syngap1 +/+ animal with the lowest pERK intensity, and the pERK intensity/value of this animal was set equal to 1. (D–F: Left panels) Representative actograms from Syngap1 +/+ and Syngap1 +/− animals that were dark-adapted at least 2 weeks before being pulsed with light (15 min; ~40 lux) at CT 6 (D), CT 15 (E) and CT 22 (F). Yellow arrows denote the time of the light pulse, and red regression lines were drawn both before and after the pulse to approximate the phase-shift. (D–F: Right panels) Group mean ± SEM phase-shifting effects of light for each time point; the phase-shifting effects for each animal are presented in scatter plot form. N = 5–6 animals per genotype/condition for the pERK light pulse experiments and N = 7–13 animals per genotype/condition for the wheel-running light pulse experiments. *: p < .05; **: p < .01; ***: p < .001; ****: p < .0001; n.s. = not significant; pERK light pulse experiment data were analyzed by two-way ANOVA followed by post hoc tests, and wheel running pulse experiments were analyzed using Student's t-test.

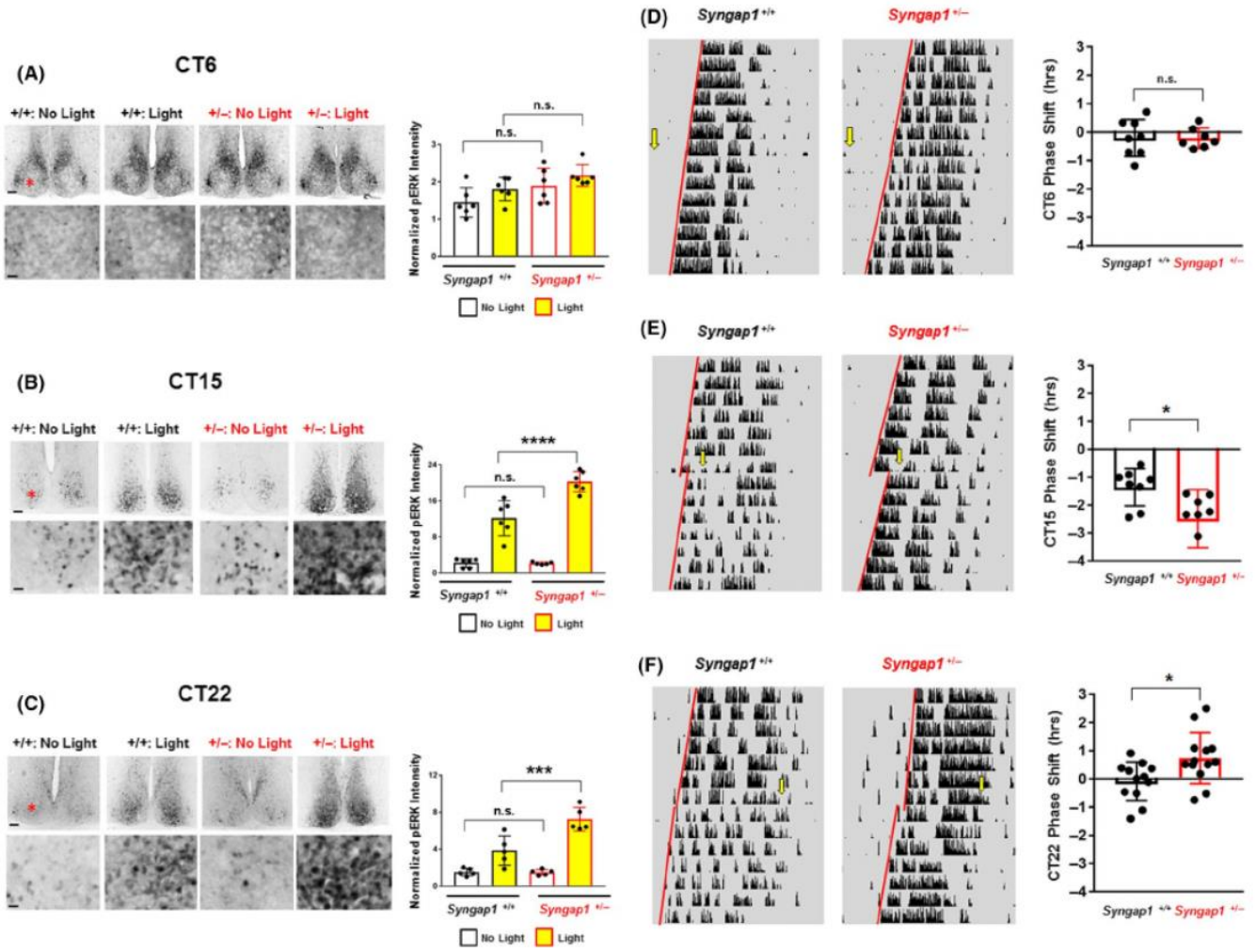

Figure 2.11 Potential mechanism by which SynGAP regulates light entrainment capacity in the SCN
In this model, photic input drives glutamate release from retinohypothalamic (RHT) nerve terminals, which triggers Gefs (guanine nucleotide exchange factors)-mediated exchange of GDP for GTP in Ras. In its activated, GTP-loaded, form, Ras stimulates MAPK pathway activation. By stimulating the conversion of GTP to GDP, SynGAP functions as a negative regulator of this glutamate/RAS/MAPK signaling cassette. This negative regulatory effect of SynGAP can be reduced via its phosphorylation by CaMKII, which leads to its dispersion from dendritic spines. In Syngap1 heterozygous mice, a reduced level of negative regulation of Ras GTP hydrolysis is predicted to trigger prolonged light-evoked Ras signaling, which in turn, would lead to enhanced MAPK activity (either peak levels or duration of activation). Potential mechanisms by which enhanced MAPK signaling leads to an increase in light-evoked clock entrainment are listed.

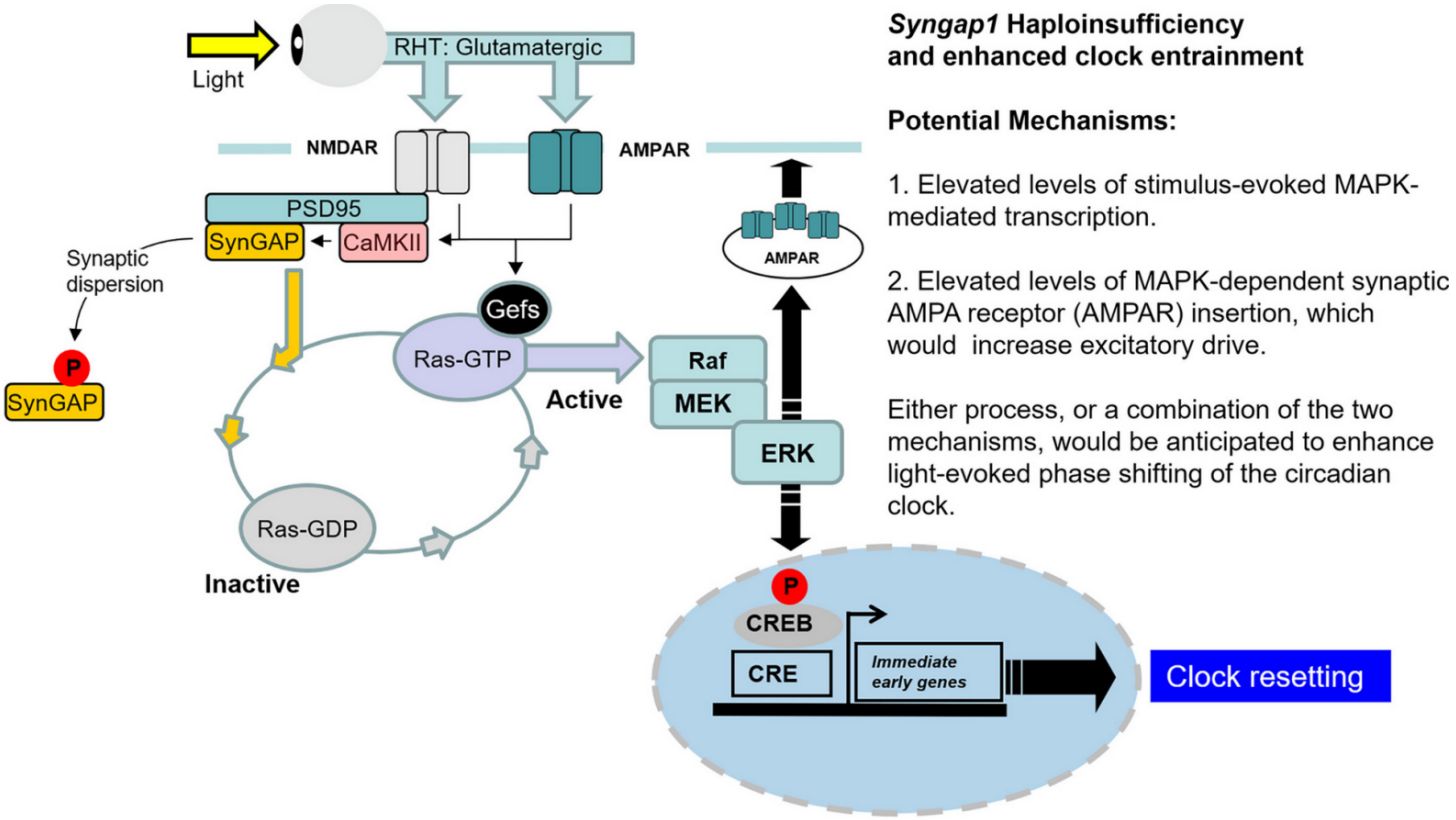

Table 2.1 MRD5 participant demographics
Note that demographic information from four participants is not listed.

Variables		*MRD5 Participants (N = 132)*
Race	White	119
	Non-white	13
	Not answered	0
Sex	Males	60
	Females	72
	Not answered	0
Current Age	0-5	62
	6-8	32
	9-11	17
	12-17	13
	18+	8
	Not answered	0
Diagnosis Age	0-5	75
	6-8	28
	9-11	14
	12-17	10
	18+	5
	Not answered	0
Education Level	Kindergarten or below	52
	1st - 6th	39
	7th - 12th	7
	No schooling	14
	Not answered	20
Mother Education	Below high school	3
	High school graduate/GED	14
	College graduate	61
	College but did not graduate	15
	Graduate/professional school	29
	Trade/vocational school	4
	Not answered	6
Father Education	Below high school	5
	High school graduate/GED	18
	College graduate	53
	College but did not graduate	10

	Graduate/professional school	30
	Trade/vocational school	10
	Not answered	6
Participant Employment Status		
	Student	60
	Not able to work	11
	Holds job	4
	Homemaker	1
	Not applicable	8
	Not answered	48
Family Income		
	Less than $10,000 (USD)	6
	$15,000 - $19,999	2
	$20,000-$24,999	2
	$25,000 - $29,999	6
	$30,000 - $34,999	1
	$35,000-$39,999	0
	$40,000 - $44,999	4
	$45,000 - $49,999	3
	$50,000 - $54,999	4
	$55,000-$59,999	0
	$60,000 - $74,999	5
	$75,000 - $84,999	5
	$85,000 - $99,999	14
	$100,000 - $149,999	16
	$150,000-$199,999	4
	$200,000-$249,999	6
	$250,000 and above	10
	Not answered	44

Table 2.2 Sleep issues reported in MRD5 participants
Data were collected from parent/guardian-reported questionnaires.

	0 – 5 years	6 – 8 years	9 – 11 years	12 – 17 years	18+ years	Age not reported	Total regardless of age
Total # of participants	62	32	17	14	8	3	136
# of participants reporting sleep issues	49	28	12	10	6	1	106
# of participants not reporting sleep issues	13	4	5	4	2	2	30
% of participants reporting sleep issues	79%	88%	71%	71%	75%	33%	78%

Table 2.3 Medications taken by MRD5 circadian/sleep participants
List of medications taken by MRD5 registry patients who answered circadian/sleep surveys/questionnaires. Also note that many participants were/are taking more than one listed medication.

Medication Types		*MRD5 Participants (N = 35)*
Antihypertensive/ADHD	Clonidine	4
	Guanfacine	1
	Amphetamine (unspecified)	1
Anticonvulsants/sedative	Sodium valproate	8
	Ethosuximide	3
	Lamotrigine	7
	Levetiracetam	6
	Dizapem	1
	Carbamazepine	1
	Clobazam	2
	Topirimate	1
	Clonazpam	2
Infections/ulcers	Amoxicillin	1
Antipsychotic	Repiridone	1
Stomach/GI	Omeprazole	1
	Miralax	1
Analgesic	Acetaminophen	1
Statin	Teva atorvastatine	1
Other	CBD	3
	THC	2
	Cobalt	1
Supplements	Maltofer	1
	Probiotics	1
Sleep aid	Melatonin	20
Asthma/Antihistamine	Hydroxyzine	1
	Montelukast sodium	1
Not reported/none		11

Table 2.4 Sleep disorders diagnosed in MRD5 circadian/sleep participants
7 MRD5 registry patients (who answered circadian/sleep surveys/questionnaires) reported a sleep diagnosis. Note that complete genetic reports (detailing the *Syngap1* gene variant) were available for 5 of the 7 participants diagnosed with a sleep disorder.

Participant # (De-identified from MRD5 Registry)	Age (years)	Sex	Reported Sleep Issues	Sleep Disorder Diagnosis	*Syngap1* Variant (from detailed genetic report)
29480	7	Male	Trouble falling asleep, insomnia, trouble remaining asleep, waking early, fragmented sleep	Irregular Sleep Wake Rhythm Disorder	c.3718 C > T (p.R1240X); nonsense
31414	4	Male	Trouble falling asleep, insomnia, trouble remaining asleep, waking early, fragmented sleep	Irregular Sleep Wake Rhythm Disorder	Not provided
31983	3	Female	Trouble falling asleep, insomnia, trouble remaining asleep, waking early, fragmented sleep	Delayed Sleep Phase Syndrome	c.2294+1G>T; nonsense
32387	Not reported	Not reported	Trouble falling asleep, insomnia, trouble remaining asleep, waking early, fragmented sleep	Irregular Sleep Wake Rhythm Disorder	c. 1167_1168delAG (p.Gly391Glnfs*27); frameshift
35323	9	Male	Trouble falling asleep, insomnia, trouble remaining asleep, waking early, fragmented sleep	Irregular Sleep Wake Rhythm Disorder	c.3415insA (p.Thr1140AspfsTer13) ; frameshift
38821	Not reported	Not reported	Trouble falling asleep, insomnia, trouble remaining asleep, waking early, fragmented sleep	Delayed Sleep Phase Syndrome	c.2294+1G>T; nonsense
40048	Not reported	Not reported	Falling asleep, insomnia, remaining asleep	Other (not specified)	Not provided

Figure 2.12 Increased incidences of sleep-related issues in MRD5 participants relative to typically-developing individuals
Data were collected from self-reported (or parent/guardian-reported) sleep/survey questionnaires (N = 35 MRD5 participants), with participant ages ranging from several months to 20 years of age. Average age reported for MRD5 participants was ~6.4 years. Data reflecting individuals with ASD (Autism Spectrum Disorder) and typically developing individuals were collected (and averaged) from the following sources: Polimeni et al 2005, Miano et al 2007, Cotton and Richdale 2006, Williams et al 2004, Krakowiak et al 2008, Liu et al 2006, Wiggs and Stores 2004. The ages for typically developing and individuals with ASD ranged from 2 to 19 years.

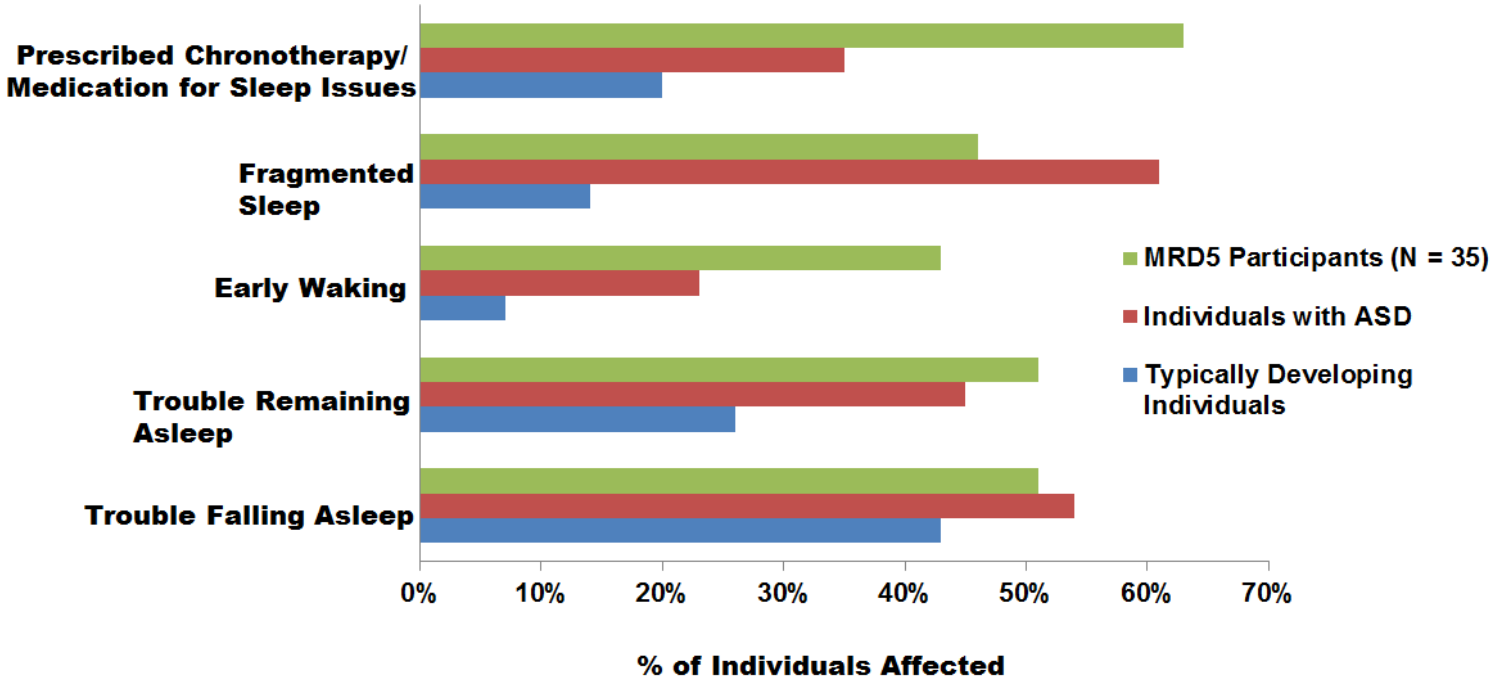

CHAPTER 3

miR-132 couples the circadian clock to daily rhythms of neuronal plasticity and cognition

Introduction

Work in many species has shown that the circadian timing system exerts a potent modulatory influence over both learning and memory (Fernandez et al., 2003; Holloway and Wansley, 1973; Monk et al., 1997; Wansley and Holloway, 1975); for reviews, see (Gerstner and Yin, 2010; Lyons, 2011; Schmidt et al., 2007; Smarr et al., 2014b). For example, in mammals, the efficacy of memory formation, acquisition, and recall vary depending on the time-of-day (Chaudhury and Colwell, 2002b; Davies et al., 1973; Kristin L Eckel-Mahan et al., 2008; Monk et al., 1997). Further, disruption of circadian timing in the suprachiasmatic nucleus (SCN), the locus of the master circadian clock, has profound effects on the acquisition and maintenance of learning and memory (Phan et al., 2011b; Ruby et al., 2008; Stephan and Kovacevic, 1978b; Tapp and Holloway, 1981).

In addition to the SCN, the role of ancillary clocks located in forebrain circuits has also been shown to exert circadian influence over cognition. For example, Snider et al showed deficits in circadian-gated learning in a mouse model where a key circadian gene, *Bmal1,* was deleted from forebrain excitatory neurons (Snider et al., 2016b). Likewise, Shimizu et al demonstrated that consolidation of long-term recognition memory is abrogated when the hippocampal clock is disrupted (Shimizu et al., 2016b). These

findings raise interesting questions about the molecular effectors that couple the circadian clock to rhythms of plasticity and memory in the hippocampus.

If one were to posit potential genetic/cellular signaling mechanisms by which the clock modulates cognition, a candidate gene would likely function at the interface of circadian timing and memory; hence this gene would be clock-regulated, and it would serve as a modulator of synaptic plasticity in the hippocampus. One gene that could fit these criteria is the microRNA, miR-132. (Vo et al., 2005) first identified miR-132, characterizing its inducible regulation and its marked effects on neurite outgrowth. Since this initial study, a large body of work has shown that miR-132 is inducibly expressed in vivo following a wide range of stimuli (Cheng et al., 2007a; Hansen et al., 2013; Hernandez-Rapp et al., 2015; Mellios et al., 2011; Nudelman et al., 2010). miR-132 also plays a role in shaping neuronal morphology and synaptic plasticity/transmission (Impey et al., 2010; Jasińska et al., 2016); for review, see (Aten et al., 2016)). Consistent with this, deletion of miR-132 attenuates activity-dependent dendritic growth and leads to a reduction in hippocampal dendritic length and spine density (Magill et al., 2010; Wayman et al., 2008) and a decrease in the amplitude of both evoked and spontaneous EPSCs (Luikart et al., 2011; Remenyi et al., 2013), whereas overexpression of miR-132 leads to an increase in spine density (Hansen et al., 2010) and an increase in paired-pulse facilitation and mEPSC amplitude (Edbauer et al., 2010; Lambert et al., 2010). In accordance with these observations, knockout of miR-132 leads to cognitive deficits (Hansen et al., 2016; Hernandez-Rapp et al., 2015), while moderate overexpression of transgenic miR-132 enhances cognition (Hansen et al., 2013).

With respect to circadian physiology, miR-132 expression is under the control of the circadian oscillator in the SCN, and photic entrainment cues trigger a marked increase in miR-132 levels (Cheng et al., 2007a). Additionally, miR-132 also varies over the diurnal cycle in the rat brain, with significant time-of-day expression differences found in the somatosensory cortex (Davis et al., 2011).

The noted studies raise the possibility that miR-132 could serve as a signaling intermediate through which the circadian timing system fine tunes learning and memory efficacy. Here, we used transgenic and knockout mouse lines and a series of molecular and behavioral approaches to examine the contribution of miR-132 to time-of-day dependent measures of cognition. We show that both the deletion of miR-132 and the transgenic expression of miR-132 to stable (noncircadian-regulated) levels disrupt the effect of the circadian system on learning and memory efficiency. These data suggest that the rhythmic expression of miR-132 modulates synaptic circuits that facilitate optimal cognitive performance across the circadian day.

Materials and Methods

miR-132 transgenic and knockout mouse lines

Generation of the CaMKII-Cre::miR-132/212$^{f/f}$ conditional forebrain neuron knockout (referred to as "cKO") mouse line was previously described by Hansen et al (Hansen et al., 2016). The miR-132/212$^{f/f}$ animals were provided to us by Dr. Simon Arthur, and the CaMKII-Cre line (Mayford et al., 1996) was acquired from Jackson Laboratory (Bar Harbor, ME, USA). To generate the CaMKII-tTA::miR-132:CaMKII-Cre::miR-132/212$^{f/f}$ mouse line (referred to as "Transgenic"), homozygous CaMKII-

Cre::miR-132/212$^{f/f}$ mice were crossed to a tetracycline-regulated bidirectional miR-132/cyan fluorescent protein (CFP) transgenic mouse line (driven by CaMKII::tTA); the details of this mouse line are provided in Hansen et al 2010 (Hansen et al., 2010). Female and male experimental CaMKII-tTA::miR-132:CaMKII-Cre::miR-132/212$^{f/f}$ animals were homozygous for the miR-132/212$^{f/f}$ locus and positive for Cre, tTA, and miR-132. Littermates negative for either the driver(s) (CaMKII-tTA and/or CaMKII-Cre) and/or the responder(s) (miR-132 and/or miR-132/212$^{f/f}$) served as control, WT-like mice (referred to as "WT"). All genotyping was performed as described previously (Hansen et al., 2016, 2010). Additionally, *BMAL1*$^{-/-}$ mice from the C57/Bl6 background were purchased from Jackson Laboratory (RRID:SCR_004633B6.129; Arntltm1Bra/J). *BMAL*$^{-/-}$ line genotyping was performed as described by Bunger et al (Bunger et al., 2000b). Animal care protocols and methods were approved by the Ohio State University's Institutional Animal Care and Use Committee.

Experimental animals were bred, housed, and maintained under standard 12 h/12 h light–dark (LD) conditions. Experiments performed under circadian time (CT) conditions are noted with the terminology "Circadian Day" or "Circadian Night." For these experiments, mice were dark-adapted (kept in constant darkness beginning at the normal lights-off time) for the noted periods. Any animal manipulations were performed under dim red light to avoid perturbation of the circadian clock. Under these conditions, CT0 denotes the beginning of the circadian day (when lights would have been turned on) and CT12 (when lights would have been turned off).

Fluorescence in situ hybridization

Tissue isolation and FISH against miR-132 was carried out as described previously (Hansen et al., 2013). Initially, brains were removed from mice at least 8 wk of age, tissue was cut into 500 μm coronal sections using a vibratome, and sections containing the dorsal hippocampus were fixed in 4% paraformaldehyde (PFA) for 4 h at 4°C. After fixing, tissue was cryoprotected overnight in 30% sucrose in PBS, and then thin cut (40 μm thick) using a freezing microtome. Next, free-floating sections were incubated with the nuclear/DNA stain DRAQ5 (1:10,000 dilution; BioStatus Limited, Cat# DR50050 RRID:AB_2314341) and then probed for miR-132 expression using fluorescein-conjugated locked nucleic acid (LNA) probes to mouse miR-132, or to a "scrambled" negative control probe that does not correspond to any known murine miRNA (Exiqon Corp). An anti-fluorescein Alexa 488 signal detection kit (Millipore, Cat# MAB045X RRID:AB_11214450) was used to amplify the fluorescein signal. Of note, 40× images were taken using a Zeiss 510 confocal microscope with LSM Software (LSM Image Examiner, RRID:SCR_014344) and MetaMorph analysis software (MetaMorph Microscopy Automation and Image Analysis Software, RRID:SCR_002368) was used to quantify the signals.

RT-PCR quantification of miR-132 expression levels

Total hippocampal RNA was isolated during the noted day and night time points, using methods described previously (Hansen et al., 2013). In brief, after RNA isolation, hippocampal cDNA was prepared using the miScript II Reverse Transcription kit (Qiagen). Amplification of cDNA was carried out using QuantiFast SYBR Green (Qiagen), and the miScript Primer System (Qiagen) was used to quantify miR-132 levels.

The following miR-132 primer sequence was utilized: 5′ UAACAGUCUACAGCCAUGGUCG (Qiagen, Cat# MS00001561). QuantiFast SYBR Green thermocycling conditions were previously described by Alemayehu et al 2013 (Alemayehu et al., 2013). Data from both time points were normalized to RNU6B_2 cDNA levels, and Double Delta CT was used for analysis.

Tissue processing and cresyl violet staining

A group of WT, cKO, and Transgenic animals was sacrificed, and brains were cut into 600 μm sections using a vibratome, fixed in 4% PFA (6 h at 4°C), and cryoprotected overnight in 30% sucrose in 1× PBS. After thin sectioning to 40 μm, sections were mounted onto gelatin-coated slides and dehydrated in alcohol (100%), incubated in a 0.1% cresyl violet solution in dH_2O (5 min), destained with 0.1% glacial acetic acid in 95% ethanol, cleared with xylenes, and coverslipped with DPX (Electron Microscopy Sciences).

Immunohistochemical labeling

Animals were sacrificed during day and night time points (CT4 and CT15), and tissue was fixed and cut using the methods noted above. Forty micrometer sections were washed in 1% Triton X-100 in PBST (3 times, 5 min each) and then incubated in 0.3% hydrogen peroxide in 1× PBST (20 min). Next, sections were blocked in 10% normal goat serum (NGS) in 1× PBST for 1 h and incubated in primary antibody overnight at 4°C in rabbit polyclonal anti-Sirt1/Sir2α (1:1000 dilution; Millipore, Cat# 09-845 RRID:AB_1587512), rabbit monoclonal anti-MeCP2 (1:3000 dilution; Cell Signaling Technology, Cat# 3456S RRID:AB_2143849), or rabbit polyclonal anti-NeuN (1: 2000

dilution; Millipore, Cat# MAB377 RRID:AB_2298772). The next day, sections were washed in PBST and incubated in biotin-conjugated goat anti-rabbit IgG secondary antibody (1:500 dilution; Vector Laboratories, Cat# BA-1000 RRID:AB_2313606) for 2 h at room-temperature. Next, tissue was processed using the ABC labeling method (Vector Laboratories Cat# PK-6100 RRID:AB_2336819) and the signal was visualized using nickel intensified diaminobenzidine labeling (Vector Laboratories Cat# SK-4100 RRID: AB_2336382). Finally, sections were mounted on gelatin-coated slides, washed in dH_2O (2×, 5 min each), cleared using xylene, and coverslipped with Permount Mounting Medium (Fisher Chemical). Bright field images were captured with a 16-bit digital camera (Micromax YHS 1300; Princeton Instruments) on a Leica DMIR microscope with Metamorph software (MetaMorph Microscopy Automation and Image Analysis Software, RRID:SCR_002368). For quantification of MeCP2, Sirt1 and NeuN labeling, images of the CA1, CA3, and GCL were traced digitally from 2 to 4 hippocampi per animal. Intensity levels for each section were background subtracted and analyzed using ImageJ software (ImageJ, RRID:SCR_003070). Values for each animal were averaged and displayed as the mean ± SEM for each noted region of the hippocampus.

Western blotting

The Western blotting protocol has previously been described (Hansen et al., 2010). Animals were sacrificed at CT4 and CT15 as noted above. Hippocampal tissue was collected and lysed in 125 μL of radioimmunoprecipitation assay buffer. Next, protein (10 μg/lane) was loaded into a 12% SDS–Page gel and transferred onto polyvinylidene difluoride membranes (Immobilon-P; EMD Millipore). Upon transfer,

membranes were blocked in 10% milk (in PBST or TBST) and incubated overnight at 4°C with the rabbit MeCP2 antibody (1:3000; Cell Signaling Technology, Cat# 2507 RRID:AB_561221) and rabbit Sirt1 (1:1000; Millipore, Cat# 09-845 RRID:AB_1587512). All antibodies were diluted in 5% NGS in PBST or 5% BSA in TBST. On the following day, membranes were incubated in 10% milk (in PBST or TBST) with an anti-rabbit IgG (goat) horseradish peroxidase-conjugated antibody (1:2000; PerkinElmer). Of note, since comparisons were only made within genotype (i.e., density of WT bands at CT4 versus CT15), each membrane contained protein for one specific genotype (WT, cKO, or Transgenic) for profiling of both timepoints (CT4 and CT15). Additionally, all membranes were also probed for mouse β-actin (1:200,000; PhosphoSolutions Cat# 125-ACT RRID:AB_2492035). The following day, membranes were incubated in 10% milk (in PBST or TBST) with an anti-mouse IgG (goat) horseradish peroxidase-conjugated antibody (1:2000; PerkinElmer Cat# NEL750001EA RRID:AB_2617185). A luminescent signal was generated using the Western Lightning Plus-ECL, Enhanced Chemiluminescence Substrate (PerkinElmer), and captured using BioBlue Lite Western Blot film (Alkali Scientific). PBST or TBST washes (three times, 5 min each) were carried out between each antibody incubation step. Photoshop CS6 (Adobe Photoshop, RRID:SCR_014199) was used for densitometric band analysis. To this end, the band intensity of MeCP2 and/or Sirt1 bands were digitally traced, background subtracted, and divided by the β-actin signal from the same lane. The mean signal for each genotype/time point was averaged from 3 to 4 animals, and the experiment was replicated at least one time per condition.

Behavioral assays: vision assessment

Animals used in each of the following behavioral assays were screened for proper vision by reaching for the surface before their vibrissae made contact with the table. Based on this assay, no vision issues were noted with any of the mouse lines.

Circadian activity analysis

Circadian activity rhythm analysis was carried out as described previously by Snider et al (Snider et al., 2016b). In brief, WT, cKO, and Transgenic animals were singly housed in cages with running wheels, and locomotor activity was collected via a magnet-actuated sensor. Animals were entrained to a 12 h/12 h LD light cycle for 10 d. Mice were then transitioned to total dark conditions (DD) for 17 d to assess free-running rhythms. Finally, to profile photic resetting abilities, mice were exposed to white light (40 lux, 15 min) at CT15 and then were allowed to free-run for six more days. VitalView software (VitalView Software, RRID:SCR_014497) was used to collect wheel-running data. The overall activity, circadian period, and phase delay were calculated based on readouts from ActiView software (Respironics Corp. Bend OR).

Novel object location

The NOL task was adapted from Takahashi et al (Takahashi et al., 2013b) and has been recently described by our laboratory (Snider et al., 2016b). In short, animals on a 12 h/12 h LD cycle were dark-adapted. From this point on, all habituation, exploration, and testing trials were conducted under dim red light (~5 lux). The following day, animals were habituated (two consecutive days) to an arena with shapes serving as contextual cues. Object shapes are described as in Snider et al (Snider et al., 2016b) and

were randomly distributed among cohorts. Exploration of the two objects and testing of the NOL occurred at CT4 or CT15 (24 h after the second day of habituation). During exploration, mice were allowed to explore two objects in the arena for a total of 5 min. Animals were then returned to their cages for 30 min (70% ethanol was used to clean the chamber in order to extinguish the odor from the previous mouse). During the test trial (which began 30 min after the exploration trial), mice explored the objects in the familiar and NOL. These objects were the same objects as those used in the initial exploration trial; however, one object (the familiar location) was in the same location as the exploration trial, while the other object (the novel location) was moved to a different location in the arena. Animals were then returned to their original 12 h/12 h LD cycle for 8 d. Next, animals were again dark-adapted and underwent 2 d of habituation. The following day, exploration and testing occurred as described above, except at the opposite time of day (i.e., an animal was tested for the first time at CT4 and tested a second time at CT15). A different set of arena contextual cues and objects was used to avoid any confounding effects of the mice having previously been exposed to a particular object. For analysis, the amount of time exploring each object was manually scored. "Exploration" was defined as the animals' nose being within 2 cm of the object, and the movement of the animal had to represent a distinct deflection from the original path. If an animal was touching or standing on the object, it must also be actively sniffing or exploring the object to constitute "exploration." Of note, animals that spent less than five total seconds of exploration during the test phase of the experiment were excluded from formal analysis (a total of two WT, one cKO, and two Transgenic animals in the no-

doxycycline experiment and a total of four WT, one cKO, and three Transgenic animals in the doxycycline experiment). Total distance moved and total seconds immobile were scored using Noldus Ethovision XT version 11.5 (EthoVision XT, RRID:SCR_000441).

For the NOL assay, half of the animals were tested first during the circadian day and half were tested first during the circadian night, with a 10 d interval separating the two testing trials. Here it is important to note that prior work from our laboratory and from other laboratories has shown that NOL can be repeated with the same subjects with no confounding effects of prior exposure to the arena and objects during the second test (Besheer et al., 1999; Graciarena et al., 2010; Snider et al., 2016b). Further, a regression analysis of our NOL data confirmed this. To this this end, we used regression analysis of the DI, which validated that no significant confounding effect (in any genotype) existed when animals were tested at both timepoints (R^2 = 0.032, P = 0.450 for WT animals, R^2 = 0.102, P = 0.227 for cKO animals, and R^2 = 0.109, P = 0.182 for Transgenic animals; data not shown). Thus, NOL performance was not dependent on the sequential nature or the temporal order of testing.

Contextual fear conditioning

Contextual fear conditioning experiments were adapted from previously published papers (Chaudhury and Colwell, 2002b; Kristin L. Eckel-Mahan et al., 2008). Animals were individually housed in ventilated cages 1 wk before the start of the experiment. Four days prior to training, animals were handled each day (1 min per day) during different, randomly chosen times of the 24 h period, as described in detail by Chaudhury and Colwell (Chaudhury and Colwell, 2002b). Two days prior to training,

animals were dark-adapted, and from this point on, animals were only exposed to dim red light (~5 lux) during the training and twice daily recall paradigms. The Passive/Active Avoidance Box Pacs-30 (Columbus Instruments) was used to administer the mild footshock. Contextual patterns and shapes were placed on three of the four walls of the chamber so that the animals could associate the context with the shock. For these experiments, we chose to train (shock) all of the animals at CT4. The decision to train during the early subjective day is based on the work of Eckel-Mahan et al who showed that contextual fear memory is impaired when animals are trained at night (Kristin L. Eckel-Mahan et al., 2008). Thus, on the day of training (at CT4) mice were placed in the chamber and were given 3 min to acclimate to the surroundings. Two consecutive 0.1 mA footshocks (each lasting 1 sec in duration) were given to the animals, and freezing behavior was monitored for an additional 2 min after the shock. Of note, we chose to administer a 0.1 mA shock, as pilot data revealed that the diurnal rhythm of contextual fear recall was abolished with higher-intensity shocks (data not shown). This 0.1 mA intensity was similar to the intensity reported in similar contextual fear conditioning paradigms (Alexander et al., 2009; Chaudhury and Colwell, 2002b). After the 5-min trial was completed, mice were placed back into their cages. Seventy percent ethanol was used to clean the chamber in order to extinguish the odor from the previous mouse. The first retrieval test was carried out 24 h after training, and all animals were repeatedly tested every 12 h for five continuous days. For the context-only control experiment, the same protocol, as described above, was used, except the animals did not receive a footshock. Freezing behavior and distance moved were scored by Noldus Ethovision software

(EthoVision XT, RRID:SCR_000441). The same freezing parameters were used for both the contextual fear experimental paradigm and for the context-only control paradigm. The percent freezing for each trial was determined by dividing the total cumulative freezing time (generated by Noldus software) by the total amount of time the mouse was allowed to explore the arena.

Regulation of transgenic miR-132 expression via doxycycline treatment

To reduce transgenic miR132 expression, doxycycline (0.40 μg/mL) was administered to the drinking water of a subset of the mice assayed in the NOL paradigm (Fig. 3.3E–G) and to all mice profiled using the contextual fear training paradigm (Fig. 3.4). Doxycyline dosing and the effects on transgenic miR-132 expression are described in our prior study (Hansen et al., 2013). Doxycycline water was changed every 3 days. Of note, doxycycline supplemented water was only administered for behavioral assays; animals sacrificed for immunolabeling/immunoblotting, and/or RT-PCR experiments did not receive doxycycline.

Experimental design and statistical analysis

All statistics were done using IBM SPSS Statistics 22 (SPSS, RRID:SCR_002865) and GraphPad Prism 3.0 (Graphpad Prism, RRID: SCR_002798), and all data are represented as the mean ± the SEM. For all data sets, statistical significance was set at $*P < 0.05$, as denoted in the figures and figure legends. Comparisons between two groups were performed using Student's two-tailed *t*-tests (unless otherwise stated), while comparisons (not dependent on the time-of-day) between the three noted genotypes were made using a one-way ANOVA. Further, Two-way

ANOVA analysis was used to analyze differences between genotype and the time-of-day, as noted in the text. Selective Bonferroni post hoc tests were conducted in PRISM 3.0 in order to examine the time-of-day difference of miR-132 in each noted brain region (see Fig. 3.1E). Repeated-measures ANOVA analysis was used for experiments in which the same mouse was run through a behavioral assay for more than one trial (i.e., the NOL and Contextual Fear Conditioning paradigms). For these experiments, CT4 and CT15 were used as the repeated measures and genotype was noted as the between-subjects factor. Bonferroni post hoc corrections were made for within-genotype time-of-day comparisons. Grubb's test was conducted on data sets within each group, and animals that were found to be statistically significant outliers ($P < 0.05$) were removed from analysis. miR-132 expression levels probed during the circadian day and the circadian night in WT, cKO, and Transgenic animals were not normally distributed ($P < 0.02$ for both timepoints; Shapiro–Wilks test of normality). Thus, fold changes obtained from qPCR data were log transformed before analysis (as in (Snider et al., 2016b)).

For the NOL paradigm, the DI was calculated as described previously by Snider et al (Snider et al., 2016b). Time-of-day differences were analyzed by repeated-measures ANOVA with Bonferroni post hoc analysis. Additionally, regression analysis was conducted in PRISM to ensure that prior exposure did not confound the results of the experiment (i.e., testing each mouse in the NOL paradigm once at CT4 or CT15, and a second time—10 d later—at the opposite timepoint). Further, to determine whether animals displayed above-chance discrimination, a one sample *t*-test was conducted for each genotype, at each separate time point (CT4 and CT15).

For all immunohistochemical labeling, differences between time points in each region of the brain were statistically analyzed using the Student's *t*-tests. Of note, expression level comparisons were only made within genotype (i.e., WT CT4 versus WT CT15) and not across genotypes (i.e., WT CT4 versus Transgenic CT4). Similarly, for Western blotting, relative band intensity was only measured within genotype; thus, Student's *t*-tests were used for analysis.

Results

Endogenous miR-132 expression is higher during the circadian night

Previous work has demonstrated that miR-132 expression is under the control of the circadian timing system in the SCN, with peak expression occurring during the subjective day (Cheng et al., 2007a). Given that circadian rhythms have been detected in the forebrain, we examined whether miR-132 could also be expressed in a time-of-day-dependent manner within the hippocampus. To this end, C57Bl/6 mice were entrained to a 12 h light–dark cycle, and were then dark-adapted for 2 days (to remove the entraining effects of light) before being sacrificed during either the circadian day (CT 6) or the circadian night (CT 15). Subsequently, hippocampal tissue was processed for miR-132 expression using fluorescence in situ hybridization (FISH) (Fig. 3.1A–3.1E). Representative images (Fig. 3.1A–3.1C) and quantitative analysis (Fig. 3.1E) revealed that miR-132 expression was significantly higher during the circadian night (CT15) (Hansen, 2015) (Fig. 3.1E, overall the time-of-day effect on brain regions $F_{(1,32)} = 20.107$, $P < 0.001$; interaction $F_{(2,32)} = 1.500$, $P = 0.241$; two-way ANOVA). Specifically, miR-

132 was significantly higher at night in the GCL and CA3 (Fig. 3.1E, $t_{(9)} = 3.796$, $P = 0.004$ for GCL and $t_{(9)} = 2.625$, $P = 0.028$ for CA3; selective Bonferroni post hoc test).

Next, we examined the circadian profile of miR-132 expression in the hippocampus. Thus, WT mice were dark-adapted for 2 days, and tissue was isolated at 4 h intervals over the circadian cycle. Quantitative RT-PCR revealed an oscillation in miR-132 expression, with peak expression occurring during the early subjective night (CT14) and nadir occurring during the early subjective day (CT2) (Fig. 3.1F; $F_{(5,44)} = 12.94$, $P = 0.024$; Kruskal–Wallis one-way ANOVA). Specifically, Dunn's Multiple Comparison Test revealed a significant difference in miR-132 expression between CT2 and CT14 (Fig. 3.1F, $t_{(15)} = -24.39$, $P < 0.01$). Further, to determine whether this oscillation is under the influence of the circadian clock, miR-132 expression was examined in tissue isolated from *BMAL1*$^{-/-}$ mice. BMAL1 is an essential component of the molecular circadian clock, and as such *BMAL1*$^{-/-}$ mice do not exhibit clock-gated molecular or behavioral rhythms (Bunger et al., 2000b). Using the approximate peak and nadir of miR-132 expression in WT mice as a reference point, we did not detect a time-of-day difference in miR-132 expression in hippocampal tissue from *BMAL1*$^{-/-}$ mice (Fig. 3.1G; $t_{(5)} = 0.864$; Student's *t*-test). Together these data indicate a clock-driven miR-132 rhythm in the hippocampus.

miR-132 knockout and miR-132 transgenic mice

Prior studies from our laboratory demonstrated that cognitive capacity is tightly regulated by miR-132 (Hansen et al., 2013, 2010). This observation, coupled with the observed rhythm in hippocampal miR-132 expression, led us to test the role of miR-132

in time-of-day learning and memory. To this end, we utilized two genetically modified mouse lines: one in which miR-132 is deleted, and a second line, where miR-132 time-of-day expression is suppressed. In the first line, a Cre/lox strategy was used to conditionally delete the miR-132/212 locus from excitatory forebrain neurons, including those of the cortex and hippocampus (miR-132/212$^{f/f}$ conditional knockout; Fig. 3.2A, hereafter referred to as the "cKO" line: Fig. 3.2B, Animal #2). Prior work with this line confirmed the selective loss of miR-132 from forebrain excitatory neurons (Hansen et al., 2016). In the second mouse line, we sought to test the cellular and behavioral effects that constitutive, noncircadian-gated, expression of miR-132 would have on time-of-day-dependent learning and memory. Thus, we crossed the miR-132/212$^{f/f}$ conditional knockout (cKO) line to a tetracycline-inducible transgenic miR-132 mouse line. The tetracycline inducible (i.e., "Tet-off") miR-132 transgenic line (previously described by Hansen et al (Hansen et al., 2010) was generated by crossing a CaMKII-tTA driver line with a line expressing miR-132 (and cyan fluorescent protein) under the control of the TRE promoter. Therefore, crossing of the CaMKII-Cre::miR-132/212$^{f/f}$ (cKO) line to the CaMKII-tTA::miR-132-CFP transgenic line generated a four transgene mouse line: CaMKII-tTA::miR-132:CaMKII-CRE::miR-132/212$^{f/f}$ (Fig. 3.2A, hereafter referred to as the "Transgenic" miR-132 line: Fig. 3.2B, Animal #3). This unique animal model allowed us to selectively delete endogenous miR-132 and transgenically express miR-132 in the same population of excitatory forebrain neurons. Of note, cKO and transgenic mice were generated in the expected Mendelian distribution with normal sex ratios, and no anatomical abnormalities were detected. Cresyl violet labeling revealed no obvious gross

morphological differences in the hippocampus of cKO and Transgenic animals compared to WT animals (Fig. 3.2C). Control animals (hereafter referred to as "WT") were either negative for all four noted transgenes (as depicted in Fig. 3.2B, Animal #1), or they were positive for the driver (CaMKII-Cre or CaMKII-tTA) or the responder transgene (miR-132 or miR-132/212$^{f/f}$).

In order to assess hippocampal miR-132 expression, quantitative RT-PCR was performed on the three noted mouse lines at CT4 (circadian day) and CT15 (circadian night). Consistent with the data shown in Figure 3.1, WT animals showed significantly higher miR-132 expression at night (Fig. 3.2D, $t_{(9)} = 2.560$, $P = 0.031$; Student's *t*-test); in contrast, a time-of-day difference in cKO and Transgenic animals was not detected (Fig. 3.2D). The low level of miR-132 detected in cKO animals likely results from interneuron and nonneuronal cell populations. Importantly, expression of the reference snRNA that was used for normalization (RNU6B) was not altered between circadian day and night conditions (data not shown). Together, these results suggest that the WT rhythmic profile of miR-132 is eliminated in miR-132 cKO and Transgenic animals.

Next, we examined circadian wheel running activity of WT, cKO, and Transgenic mice in order to determine whether the SCN clock machinery was significantly affected by the noted genetic manipulations. Double plotted actograms of WT, cKO, and Transgenic mice are presented (Fig. 3.2E). All circadian wheel running data were analyzed by one-way ANOVA. The circadian period (tau) under DD conditions was similar for all genotypes (Table 3.1; $F_{(2,13)} = 2.087$, $P = 0.170$), and the overall activity (rotations per day) in LD and in DD was similar for all three genotypes

(Table 3.1; $F_{(2,13)} = 0.876$, $P = 0.442$) and ($F_{(2,13)} = 2.139$, $P = 0.164$). Additionally, a light pulse (40 lux, 15 min) administered during the early subjective night (CT15), elicited phase delaying responses in all three lines. The Transgenic animals exhibited an attenuated phase shift relative to the two other lines, however this difference did not reach statistical significance (Table 3.1; $F_{(2,13)} = 3.217$, $P = 0.079$). Together, these experiments show that key functional features of the SCN are retained in miR-132 cKO and Transgenic animals.

Impairments in time-of-day dependent novel object location memory in mice with forebrain miR-132 dysregulation

We next sought to examine the effects of miR-132 dysregulation on time-of-day dependent measures of learning and memory. To this end, we utilized the novel object location (NOL) task—a hippocampal-dependent memory test (Barker and Warburton, 2011; Chao et al., 2016) with an efficiency that has previously been shown to be influenced by circadian time (McGowan and Coogan, 2013; Snider et al., 2016b; Takahashi et al., 2013b). The NOL task examines the ability of a mouse to remember the location of an object after moving one of the two objects in the arena. Thus, the more time spent exploring the moved object (compared to the object in the familiar location), the better the memory recall (paradigm shown in Fig. 3.3A).

To determine time-of-day performance in the NOL task, mice were tested at circadian day (CT4) and circadian night (CT15) time points. For this experiment, mice on a 12 h/12 h LD schedule were dark-adapted (DD) for 2 d and were subsequently tested under dim red light (~5 lux). The red light condition allowed animals to use

visual/contextual cues, while not affecting the circadian clock timing system (Figueiro and Rea, 2010; Hattar et al., 2003; Zhang et al., 2014). Interestingly, WT animals exhibited time-of-day differences in NOL discrimination, while miR-132 cKO and Transgenic animals did not. Indeed, an interaction at the level of genotype that depended on time-of-day was detected (Fig. 3.3B, interaction $F_{(2,28)} = 5.011$, $P = 0.001$; repeated-measures ANOVA). In particular, when comparing within genotype, WT animals displayed a significantly higher discrimination index (DI) when tested at night compared to when tested during the day (Fig. 3.3B, $t_{(9)} = 3.497$, $P = 0.020$; Bonferroni post hoc test). On the other hand, cKO and Transgenic animals showed no such differences (Fig. 3.3B, $t_{(9)} = 0.978$, P = 1.000 for cKO mice and $t_{(10)} = 0.776$, $P = 1.000$ for Transgenic mice; Bonferroni post hoc test). Additionally, statistical analyses were performed to determine whether the DI for each group (at each time point) was significantly greater than chance levels. Only WT animals demonstrated greater-than-chance discrimination for the novel location at night (Fig. 3.3B, $t_{(9)} = 3.47$, $P = 0.005$; one sample *t*-test). Finally, no significant effect of time-of-day or genotype on total distance moved (Fig. 3.3C) or total exploration time (Fig. 3.3D) was observed (assessed via repeated-measures ANOVA).

Previous work from our laboratory has shown that overexpression of miR-132 (greater than approximately threefold over basal levels) can impair learning and memory(Hansen et al., 2013, 2010). Given that the Transgenic animals displayed an approximately sevenfold increase in miR-132 during the day, and a ~3.5-fold increase relative to endogenous miR-132 levels at night (Fig. 3.2D), we wanted to determine

whether time-of-day-dependent cognitive deficits revealed in the NOL assay in the miR-132 Transgenic animals could be attributed to the high, supra-physiological, levels of transgenic miR-132. Thus, we administered 0.4 μg/mL doxycycline to the drinking water of a separate cohort of mice, and tested the animals in the NOL task 3 wk later. Of note, 0.4 μg/mL doxycycline treatment was previously shown to reduce transgenic miR-132 expression to a level that is approximately equivalent to WT (i.e., endogenous) miR-132 expression levels in the hippocampus (Hansen et al., 2013). Remarkably, Transgenic animals maintained on doxycycline did not exhibit time-of-day-dependent differences in NOL discrimination (Fig. 3.3E). We again found an interaction at the level of genotype that depended on the time point of testing (Fig. 3.3E, interaction $F_{(2,18)} = 3.594$, $P = 0.0176$; repeated-measures ANOVA). When comparing within genotype, WT animals displayed a significantly higher DI at night compared to during the day (3.3E, $t_{(5)} = 3.974$, $P = 0.0078$; Bonferroni post hoc test). However, cKO and Transgenic animals did not show a significant difference (Fig. 3.3E, $t_{(8)} = 1.512$, $P = 0.523$ for cKO mice and $t_{(5)} = 0.272$, $P = 1.000$ for Transgenic mice; Bonferroni post hoc tests). Again, only WT animals demonstrated greater-than-chance discrimination for the novel object at night (Fig. 3.3E, $t_{(5)} = 4.504$, $P = 0.006$; one sample *t*-test). Finally, no significant effect of time-of-day or genotype on total distance moved or total exploration time (assessed via repeated-measures ANOVA) was observed (Fig. 3.3F-3.3G). Together, these results indicate that the daily rhythm in miR-132 facilitates both the formation of NOL memory and regulates its strength as a function of time-of-day.

Disruption of circadian-gating of contextual fear memory recall in miR-132 cKO and Transgenic mice

Next, we tested whether miR-132 influences time-of-day-dependent memory recall. This approach is in line with previous studies showing that the strength of memory recall is influenced by the time-of-day (Chaudhury and Colwell, 2002b; Kristin L. Eckel-Mahan et al., 2008). For this experiment, mice were initially handled once a day under LD conditions (for two consecutive days). Next, they were transferred to darkness (DD), where they were handled once per day for an additional 2 days. The 2 days of handling in DD, the training trial, and all retrieval trials were conducted under dim red light (~5 lux), allowing the animals to use visual/contextual cues without influencing the circadian timing system, as described in the NOL section above.

On the day of training, mice received a conditioning footshock during the early subjective day (CT4; Fig. 3.4A, Day 7). Memory retrieval (based on the percent time an animal was immobile/freezing) was then tested 24 h after conditioning and then probed every 12 h thereafter for 5 days (Fig. 3.4A; days 8 through 12). Mice were maintained on drinking water supplemented with 0.4 μg/mL doxycycline (from 3 wk prior to the beginning of the experiment until the completion of the experiment). A graphical representation of the daily recall profile of contextual fear memory for all three genotypes is shown in Figure 3.4B. We report that WT mice showed a daily oscillation in contextual fear memory recall; thus, over the first 3 days of testing, WT mice consistently exhibited more efficient recall during the subjective day. In contrast, daily oscillations in contextual fear memory recall were not consistently observed in miR-132 cKO and Transgenic

animals. Specifically, a significant effect of genotype (Fig. 3.4C, $F_{(2,24)} = 3.609$, $P = 0.043$; repeated-measures ANOVA) and a trend between genotype and freezing level that is dependent on time-of-day was observed (Fig. 3.4C, interaction $F_{(2,24)} = 3.156$, $P = 0.061$; repeated-measures ANOVA). WT mice showed higher daytime freezing compared to nighttime freezing (Fig. 3.4C, $t_{(9)} = 5.476$, $P < 0.001$; Bonferroni post hoc test), whereas miR-132 cKO and Transgenic mice showed no significant time-of-day-dependent differences in memory recall (Fig. 3.4C, $t_{(10)} = 2.122$, $P = 0.180$ for cKO mice and $t_{(5)} = 2.559$, $P = 0.153$ for Transgenic mice, Bonferroni post hoc tests). The abrogation of a circadian rhythm in memory recall in the knockout and transgenic animals supports the idea that the rhythmic expression of miR-132 gates time-of-day-dependent contextual fear memory recall.

To control for the effects of doxycycline treatment, we also examined time-of-day contextual fear memory recall in mice that were not treated with doxycycline; consistent with the doxycycline-treated paradigm, we found that only WT mice exhibited a significant time-of-day contextual fear memory recall (data not shown). Further, to test whether the observed reduction in freezing during subjective night in WT animals was a result of a circadian rhythm in fear memory, or a result of an innate increase in an animal's activity, we subjected a second cohort of animals to a context-only paradigm (data not shown). In this experiment, the animals were “trained” and tested in the same shock-box as the mice that underwent contextual fear conditioning; however, the context-only mice did not receive a footshock when they were exposed to the arena. As expected, all groups (WT, cKO, and Transgenic) displayed a mild, nonsignificant, overall increase

in average freezing percentage during subjective day time points compared to subjective night time points, and no significant interaction was observed between genotypes that was dependent on the time-of-day (interaction $F_{(2,13)} = 2.32$, $P = 0.0814$; repeated-measures ANOVA). Additionally, while context-only WT animals froze an average of 1.8 sec more during the day than the night, fear conditioned WT animals froze an average of 12.7 sec more during the day than the night. These data suggest that the increase in freezing observed in WT animals during the subjective day is due to a circadian rhythm in fear memory retrieval and is not simply the result of the animals' increase in activity during the night time point domain.

Hippocampal time-of-day-dependent expression changes in miR-132 target genes

MicroRNAs function via the suppression of translation and/or the degradation of target mRNA. Given the marked effects on time-of-day-dependent memory recall in the miR-132 cKO and Transgenic lines, we examined whether miR-132 affects the time-of-day expression of putative target genes that affect synaptic plasticity and/or cognition. To this end, we profiled the expression of MeCP2 and Sirt1.

For the analysis of MeCP2, hippocampal tissue was profiled at CT4 and CT15 via immunohistochemical labeling and Western blotting (Fig. 3.5). Quantitative immunohistochemical analysis revealed a significant time-of-day variation in MeCP2 expression within the CA1 (Fig. 3.5B, $t_{(10)} = 2.762$, $P = 0.017$; Student's *t*-test) and the GCL (Fig. 3.5B, $t_{(10)} = 2.309$, $P = 0.044$; Student's *t*-test) of WT mice, with higher levels observed during the circadian night. Interestingly, time-of-day-dependent differences in MeCP2 expression within the CA1, GCL, and CA3 were not detected in miR-132 cKO or

Transgenic mice (Fig. 3.5B, $P > 0.3$ for all brain regions in both genotypes, Student's *t*-tests). Western analysis of hippocampal lysates from WT animals showed a mean increase in MeCP2 expression during the subjective night, although significance was not reached (Fig. 3.5D, $t_{(4)} = 1.229$, $P = 0.287$; Student's *t*-test). Significant time-of-day differences in band intensity were not detected in miR-132 cKO or Transgenic mice (Fig. 3.5D, $P > 0.30$ for both genotypes, Student's *t*-tests). As a loading control, all Western blots were probed for β-actin. Importantly, previous studies have reported that β-actin expression is not under the control of the circadian clock (Kristin L. Eckel-Mahan et al., 2008; Gerstner et al., 2014; Jang et al., 2015).

Here, it is also worth noting that expression level comparisons for the noted target genes were only made within a genotype (e.g., WT circadian day versus WT circadian night), as immunohistochemical labeling and Western blotting experiments were run independently for each genotype. Hence, though one would expect for MeCP2 (and Sirt1) levels to be highest in the miR-132 cKO animals and lowest in the miR-132 Transgenic animals (given that they are miR-132 targets), we did not make across-genotype comparisons.

Next we examined Sirt1 (Fig. 3.6), an NAD-dependent deacetylase that has been reported to modulate synaptic plasticity and memory (Gao et al., 2010). In WT mice, immunohistochemical labeling detected higher Sirt1 expression within the CA1 cell layer during the circadian night compared to during the circadian day (Fig. 3.6B, $t_{(6)} = 2.973$, $P = 0.025$; Student's *t*-test). In contrast, significant time-of-day expression within the CA1 cell layer (or CA3 and GCL) was not detected in cKO or Transgenic mice (Fig.

3.6B, $P > 0.30$ for all brain regions analyzed in both genotypes, Student's *t*-tests). As a complement to the IHC analysis, Western blotting of hippocampal lysates revealed significant time-of-day expression of Sirt1, with higher expression during the circadian night (Fig. 3.6D, $t_{(5)} = 3.907$, $P = 0.011$; Student's *t*-test). In contrast, significant time-of-day expression in the miR-132 cKO or Transgenic animals was not observed (Fig. 3.6D; $P > 0.30$, Student's *t*-tests).

As a control, we profiled the time-of-day expression of the neuronal-enriched protein NeuN (Fig. 3.7A; (Mullen et al., 1992)). Given that NeuN is not a target of miR-132 and has not been reported to be regulated by the circadian clock (Campos et al., 2015), we did not anticipate time-of-day-gated NeuN expression. In WT mice, the expression of NeuN was not significantly different between CT4 and CT15 in the CA1, CA3, or GCL (Fig. 3.7B). Further, the expression of NeuN was not significantly affected in either the miR-132 cKO or the Transgenic lines (Fig. 3.7B). Together these data indicate that the effects of miR-132 are specific, and as such, add support to the idea that the rhythmic expression of miR-132 plays a key role in shaping the functionality of forebrain circuits that underlie cognition.

Finally, we examined time-of-day expression of MecP2 and Sirt1 in *BMAL1*$^{-/-}$ animals (Fig. 3.7C-3.7F). *BMAL1*$^{-/-}$ is a critical component of the circadian clock timing mechanism, and its germline deletion results in a complete loss of circadian timekeeping capacity (Bunger et al., 2000b). Interestingly, significant time-of-day differences in MeCP2, and Sirt1 in the CA1, GCL, and CA3 were not observed in the *BMAL1*$^{-/-}$ background (Fig. 3.7D and 3.7F; $P > 0.30$ for all three brain regions profiled for both

proteins, Student's *t*-tests). These data provide support for the idea that the circadian timing system drives a rhythm of miR-132, which in turn imparts rhythmicity to target genes and cognition.

Discussion

Here, we provide evidence that miR-132 serves as a conduit through which the biological clock confers daily rhythms on cellular plasticity and cognition in forebrain circuits. With respect to the miR-132 rhythm in the hippocampus, our data are in line with several studies that have found time-of-day expression differences in miR-132 within the murine cortex (Davis et al., 2011) and the SCN (Cheng et al., 2007a). Interestingly, a time-of-day difference in hippocampal miR-132 expression was not detected in *BMAL1*$^{-/-}$ mice, indicating that miR-132 is a clock-regulated gene. Consistent with this idea, Cheng et al found that the disruption of the circadian clock transcription/translation feedback led to a suppression of rhythmic miR-132 expression in the SCN. However, it should be noted that our assessment of miR-132 levels in the *BMAL1*$^{-/-}$ mice was conducted at two time points (CT4 and CT15), approximating the time points in which miR-132 was low or high in WT animals. Though unlikely, it is possible that there may be a shift in the phase of the rhythm in miR-132 in the *BMAL1*$^{-/-}$ mouse lines that evaded our detection; as such, more extensive circadian profiling would be needed to confirm a total loss of the miR-132 hippocampal rhythm in *BMAL1*$^{-/-}$ animals.

It is worth noting that miR-132 does not appear to be under the *direct* control of the E-Box dependent core clock timing mechanism wherein heterodimers of *CLOCK* and

BMAL1 promote the transcription of *cryptochrome* and *period* genes (Cheng et al., 2007a). Consistent with this, the promoter/regulatory region of miR-132 does not contain an E-box element (Cheng et al., 2007a). Rather, the rhythmic expression of miR-132 is likely to be driven by the CREB/CRE transcriptional pathway. In support of this hypothesis, multiple CRE-motifs have been identified within the regulatory region of the miR-132/212 gene cluster (Remenyi et al., 2010; Vo et al., 2005). Further, the disruption of CREB-mediated transcription has been shown to suppress inducible miR-132 expression in neurons (Remenyi et al., 2010; Vo et al., 2005).

Interestingly, within the SCN, circadian-gated, CRE-mediated, gene expression has been reported by several laboratories (Obrietan et al., 1999; O'Neill et al., 2008). Further, time-of-day changes in CREB activity have been reported in multiple forebrain regions (Cirelli and Tononi, 2000; Graves et al., 2003; Guzman-Marin et al., 2006), thus raising the prospect that rhythmic miR-132 expression in the forebrain is mediated via a circadian clock-driven, CREB-dependent, transcriptional pathway.

In the NOL task, we found that cKO and Transgenic animals exhibited time-of-day-dependent learning deficits, suggesting that peak cognitive performance requires rhythmic miR-132 expression. It should be noted that the NOL memory impairments observed in miR-132 cKO animals are similar to recent studies showing that both forebrain miR-132 cKO animals and miR-132 germline knockout animals exhibit marked deficits in Novel Object Recognition (Hansen et al., 2016; Hernandez-Rapp et al., 2015). Further, with regard to the time domain-specific efficacy observed in the NOL task in WT animals, studies from several laboratories have shown that rodents display better

discrimination at night and very low to negligible discrimination during the day (Hansen et al., 2016; Takahashi et al., 2013b). It was somewhat unexpected that both constitutive expression and targeted deletion of miR-132 disrupted discriminatory capacity; hence neither line scored better than chance during either the circadian day or circadian night. The reasons for these similar effects resulting from two profoundly different transgenic manipulations are not clear. It is worth noting, however, that Transgenic animals displayed increased orientation toward the NOL (during both the subjective day and night; Fig. 3.3B), but these values did not reach statistical significance; a larger sample size may have been needed to disentangle a potential phenotypic effect.

Turning to the contextual fear conditioning paradigm, we found that both the loss of miR-132 expression in the knockout animals and constitutive expression in the Transgenic animals led to a disruption of time-of-day gated memory recall. This finding contrasts with the recall rhythm in WT mice, which persisted for 4 days after training. Of note, this rhythm is consistent with work from several papers which found that fear memory recall varies as a function of the time-of-day, with better retrieval occurring during the day (Chaudhury and Colwell, 2002b; Kristin L. Eckel-Mahan et al., 2008). Here, however, it should be noted that we cannot definitively conclude that the superior day-time retrieval in WT mice (or lack thereof in cKO and Transgenic mice) is strictly a time-of-day effect, as we have not controlled for the potential influence of time-stamping in our experiments. Along these lines, several groups (using a variety of memory retention paradigms) have shown that regardless of the time-of-day in which training occurs, memory retention is optimal 24 h later (or multiples of 24 h after training)

(Chaudhury and Colwell, 2002b; Holloway and Wansley, 1973; Ralph et al., 2002; Wansley and Holloway, 1975, p. 1978) Hence, since we trained our mice at only one timepoint (CT4), it is possible that our behavioral findings may also be attributed to a miR-132-dependent time-stamping phenomenon. Indeed, additional experiments aiming to tease apart the role of miR-132 and its function in time-of-day memory retrieval and/or time-stamping would be of merit. Finally, one interesting observation from our contextual fear conditioning studies was that miR-132 cKO mice exhibited a higher level of freezing than WT mice, which could be interpreted as more efficient memory retrieval. However, our NOL data reported here, as well as prior work from our laboratory and the Hébert laboratory, found that the disruption of miR-132 results in diminished cognitive capacity (Hansen et al., 2013, 2010; Hernandez-Rapp et al., 2015). Potential explanations for this discord may be related to the differences inherent to the contextual fear conditioning assay compared to spatial learning assays used to detect cognitive deficits (i.e., novel object recognition, NOL and Barnes maze). Along these lines, contextual fear training would be expected to require the involvement of fear circuits to a much greater extent than the novel object recognition, NOL and Barnes maze assays (Fendt and Fanselow, 1999; Moser et al., 2008). As such, the relatively high level of cKO freezing detected in the contextual fear conditioning assay may be related to an elevated anxiety response: a topic that we are currently pursuing.

Prior hippocampal gene profiling work from our laboratory found that miR-132 affects the expression of hundreds of functionally diverse gene transcripts (Hansen et al., 2016). Hence, it is reasonable to expect that the behavioral effects that we report here for

cKO and Transgenic mice may result from a complex interplay of genes (i.e., direct targets) and gene networks (i.e., indirect targets) that are affected by miR-132. Given this complexity, attempts to identify a target gene(s) through which miR-132 disrupts time-of-day learning would have been technically challenging. Thus, rather than attempting to identify a behavioral link between miR-132 and a target, we chose to focus on the cellular functional effects of miR-132 rhythms by analyzing two genes that are (1) well-characterized miR-132 targets, (2) reported to exhibit diurnal oscillations, and that (3) affect cognition. To this end, we examined MeCP2 and Sirt1.

MeCP2 is a chromatin-associated protein targeted by miR-132 that functions as a potent transcriptional regulator (Alvarez-Saavedra et al., 2011, 2011; Chahrour et al., 2008; Hansen et al., 2010; Klein et al., 2007). Loss-of-function mutations in MeCP2 have been shown to result in Rett syndrome (Amir et al., 1999) a developmental disorder that results in marked deficits in learning and memory tasks (Moretti et al., 2006; Pelka et al., 2006); for review, see (Na et al., 2012). Initially, we detected a significant time-of-day-dependent MeCP2 expression profile within the hippocampus of WT mice. Consistent with this finding, a number of profiling studies performed on both brain and peripheral tissues have reported an oscillatory profile at the level of mRNA and protein (Hoogerwerf et al., 2007); Mouse 1.OST Lung Affymetrix: Circadian Expression Profiles Data Base (CircaDB) (Martínez de Paz et al., 2015; Pizarro et al., 2013b). Given the profound effects that MeCP2 has on synaptic plasticity and dendritic complexity and cognition (Na et al., 2012), it is reasonable to postulate that MeCP2 could contribute to the circadian clock-mediated, miR-132-dependent, modulation of learning and memory.

Interest in the NAD-deacetylase Sirt1 was piqued by work showing that Sirt1 knockout mice display impairments in both short- and long-term associative memory tasks and show deficits in synaptic plasticity and dendritic branching/arborization (Codocedo et al., 2012; Michán et al., 2010). Further, regarding its post-transcriptional regulation, (Strum et al., 2009) and (Zhang et al., 2014) identified Sirt1 as a direct target of miR-132, and both the MicroRNA.org and miRanda algorithms detect robust hybridization capacity between miR-132 and *Sirt1* (Betel et al., 2008; Peterson et al., 2014).

Our analysis indicates that rhythmic Sirt1 hippocampal expression is driven by miR-132. The temporal profile of Sirt1 expression in WT mice reported here is consistent with the work of Rawashdeh et al (Rawashdeh et al., 2014b) who reported peak protein levels of hippocampal Sirt1 during the night domain and (Asher et al., 2008) who reported peak levels of Sirt1 protein from the mouse liver at ZT16. Interestingly, CREB protein levels have been shown to be significantly reduced in mutant mice lacking brain-specific Sirt1 catalytic activity (Gao et al., 2010). Given the tight regulation of miR-132 by CREB, one could propose a complex interplay wherein Sirt1 regulates plasticity and cognition across the circadian day, in part, through a miR-132-CREB-mediated mechanism.

With respect to the peak in the time-of-day protein expression profiles of MeCP2 and Sirt1 reported here, one may have expected for these gene products to be lower at night (given that they are direct targets of miR-132—which was highest at night). However, at the level of protein expression/regulation, the kinetics of a wide array

of processes impacts the functional effects of microRNA. Along these lines, in addition to the kinetic rates of miRNA-mediated mRNA decay and translational repression (Morozova et al., 2012), simple mRNA stability and translation rates, as well as protein half-lives, impact the temporally delimited effects of miRNAs. Hence, within a circadian timeframe, it is conceivable for the peak expression times of MeCP2 and Sirt1 to temporally overlap with the peak in miR-132 expression.

Together, these data suggest that the rhythm of miR-132 expression regulates learning and memory as a function of the time-of-day. In addition, the results presented here raise interesting questions regarding the potential role of miR-132 in an array of time-of-day-delineated processes, including synaptic scaling and homeostatic plasticity; to these ends, additional studies are highly merited.

Acknowledgements

We thank Dr. Katelin Hansen for her expertise in performing the *in situ* hybridization experiment.

Figure 3.1 Time-of-day miR-132 expression in the hippocampus
miR-132 expression in the CA1 (*A*), GCL (*B*), CA3 (*C*), was examined by FISH in WT animals during the circadian day (CT6) and the circadian night (CT15) time points. Scale bar = 50 μm for CA1, GCL, and CA3. (*D*) FISH profiling of a control, scrambled miRNA probe: note the lack of cellular labeling. (*E*) Quantification of the relative intensity of miR-132 expression in the noted brain regions during the circadian day and the circadian night. Data were analyzed by two-way ANOVA, n = 5–6 animals per group. CA1 miR-132 mean intensity during the circadian night was set equal to a value of one, and the remaining brain regions were normalized to this condition. Data are displayed as the mean ± standard error (SEM); (*) $P < 0.05$; (**) $P < 0.01$; (n.s.) not significant ($P > 0.05$). (*F*) Total hippocampal RNA was isolated from WT mice sacrificed every 4 h across the 24-h circadian cycle, and miR-132 cDNA was probed via real-time PCR. Relative miR-132 abundance at CT2 was set equal to a value of one. Significance was examined via Kruskal Wallis Test, n = 7–8 animals per group. Data are displayed as the mean ± SEM for each timepoint. (*G*) Total hippocampal RNA was isolated from *BMAL1*$^{-/-}$ animals sacrificed at CT4 and CT15. Relative miR-132 abundance at CT4 was set equal to a value of one, and miR-132 expression at CT15 was normalized to this value. Significance was examined via Student's *t*-test, n = 3–4 animals per timepoint. Note that the in situ hybridization data from this figure (panels A-E) was adapted from '*Hansen, K. "MiR-132 as a Dynamic Regulator of Neuronal Structure and Cognitive Capacity." (2015; PhD Dissertation; The Ohio State University).'*

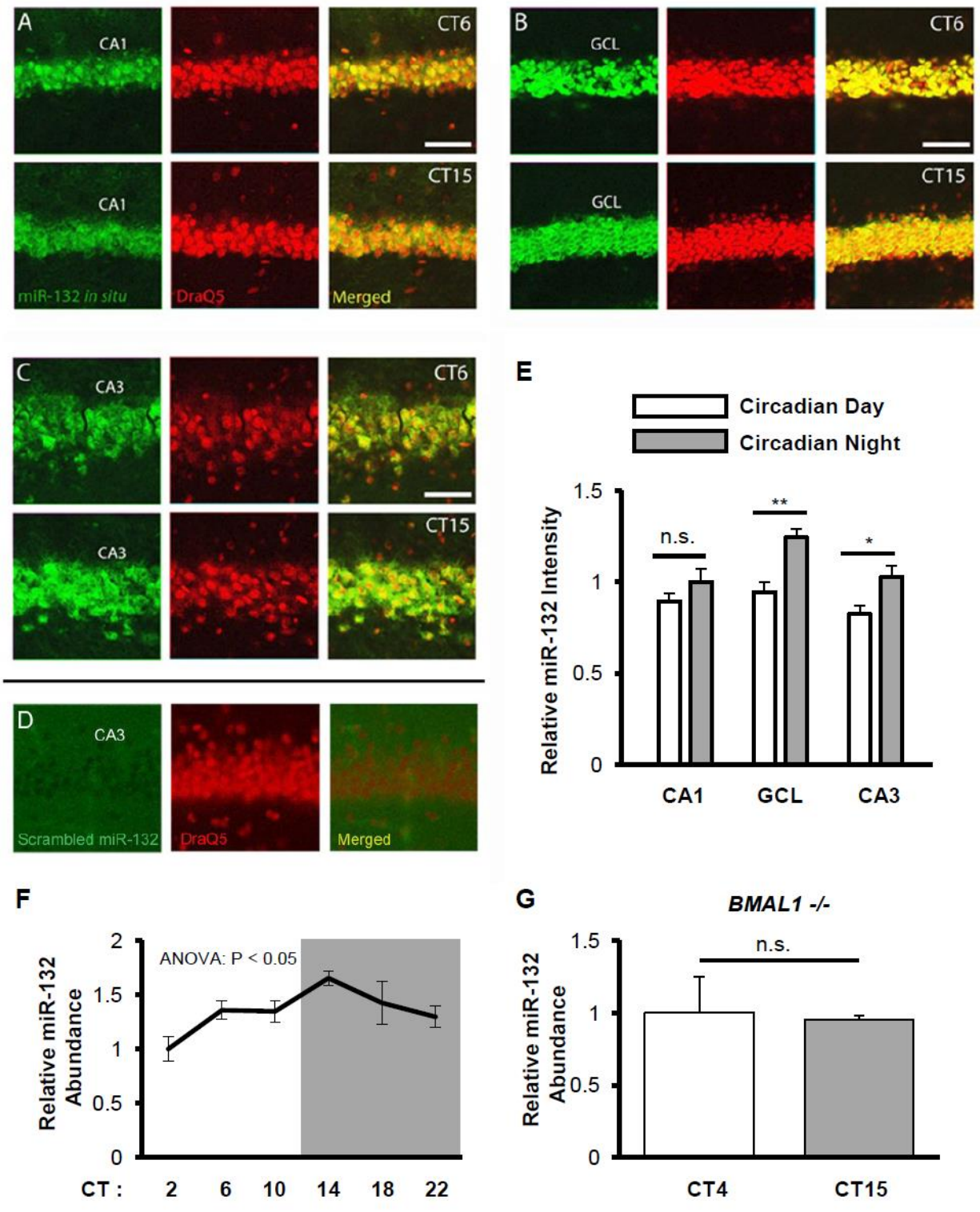
A
CA1
CT6
CA1
CT15
miR-132 in situ
DraQ5
Merged
B
GCL
CT6
GCL
CT15
C
CA3
CT6
CA3
CT15
D
CA3
Scrambled miR-132
DraQ5
Merged
E
Circadian Day
Circadian Night
Relative miR-132 Intensity
1.5
1
0.5
0
n.s.
**
*
CA1
GCL
CA3
F
Relative miR-132 Abundance
2
1.5
1
0.5
0
ANOVA: P < 0.05
CT :
2
6
10
14
18
22
G
BMAL1 -/-
Relative miR-132 Abundance
1.5
1
0.5
0
n.s.
CT4
CT15

Figure 3.2 miR-132 knockout and transgenic mouse models and circadian phenotyping
(*A*) Schematic depiction of CaMKII-Cre::miR-132/212$^{f/f}$ (denoted as "cKO") and CaMKII-tTA::miR-132:CamKII-Cre::miR-132/212$^{f/f}$ ("Transgenic") mice. (*B*) PCR-based genotyping results for the miR-132 cKO and Transgenic mice. Of note, mouse #2 represents a miR-132 cKO animal—positive for both the CaMKII-Cre driver and the miR-132/212$^{f/f}$ transgene. Mouse #3 represents a miR-132 Transgenic animal—positive for both the tTA and miR-132 transgenes, in addition to the CaMKII-Cre driver and the miR-132/212$^{f/f}$ transgene. (*C*) Representative hippocampal tissue stained with cresyl violet. Of note, no gross morphological differences in cKO and Transgenic animals were detected; scale bar = 150 μm for low-magnification images and 50 μm for high-magnification images. (*D*) To profile miR-132 expression levels, total hippocampal RNA from WT, cKO, and Transgenic animals was isolated, reverse transcribed and probed via real-time PCR. Relative miR-132 abundance (in WT animals) during the circadian night was set equal to a value of one. Time-of-day comparisons were analyzed by Student's *t*-test, $n = 3–5$ animals per group. Data are displayed as the mean ± SEM; (*) $P < 0.05$; (n.s.) not significant ($P > 0.05$). (*E*) Double-plotted wheel running actograms of WT, cKO, and Transgenic mice. White and black horizontal bars across the tops of the plots represent the light and dark (LD) periods, respectively; DD (shown on the Y-axis) refers to the time when mice were housed in constant darkness. Yellow arrows indicate a light pulse (15 min, 40 lux) given at CT15 to induce a phase delay.

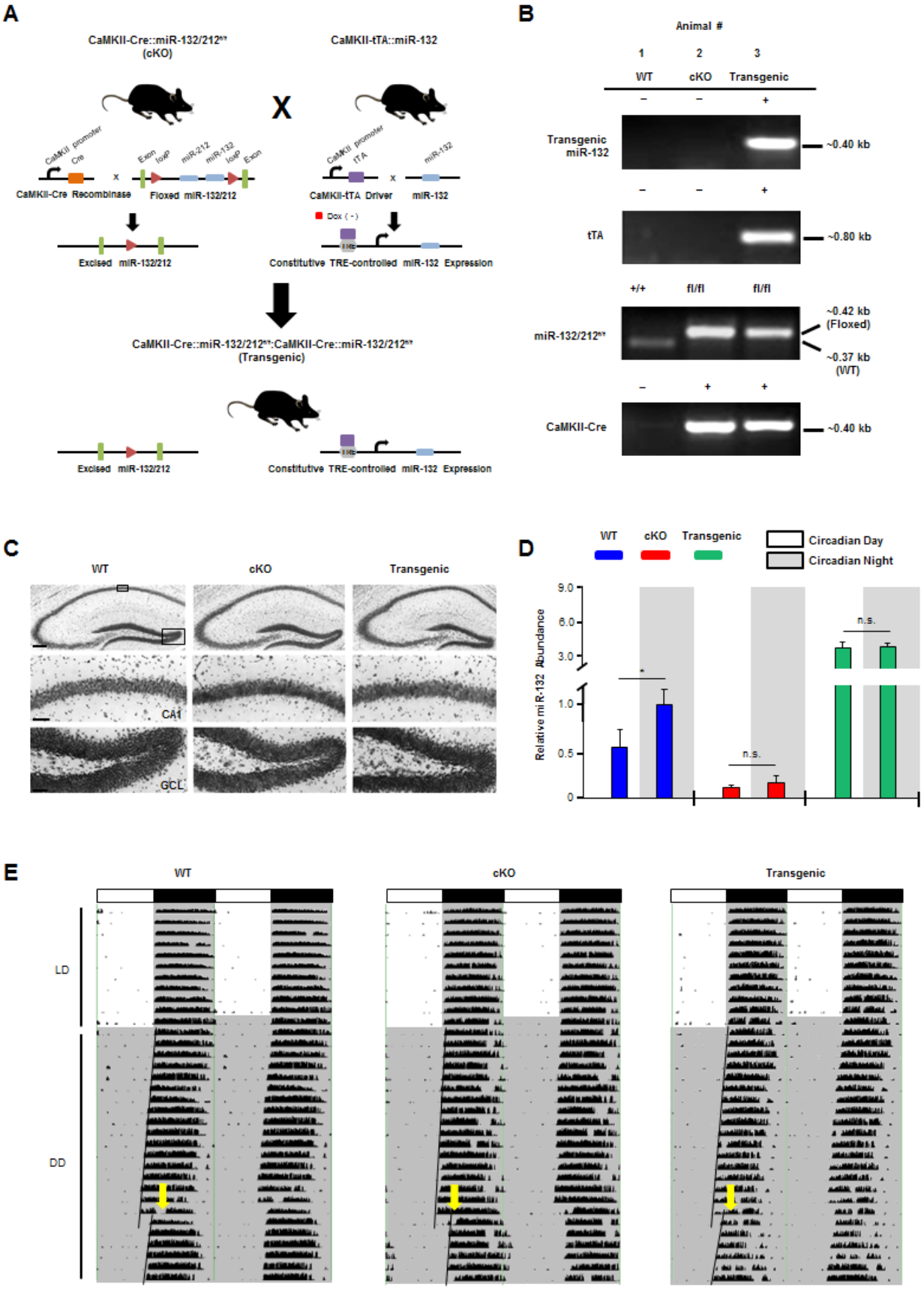
A
CaMKII-Cre::miR-132/212fl/fl
(cKO)
CaMKII-tTA::miR-132
X
CaMKII promoter
Cre
CaMKII-Cre Recombinase
Exon
loxP
miR-212
miR-132
loxP
Exon
Floxed miR-132/212
CaMKII promoter
tTA
CaMKII-tTA Driver
miR-132
Dox (-)
TRE
Excised miR-132/212
Constitutive TRE-controlled miR-132 Expression
CaMKII-Cre::miR-132/212fl/fl:CaMKII-Cre::miR-132/212fl/fl
(Transgenic)
Excised miR-132/212
Constitutive TRE-controlled miR-132 Expression
B
Animal #
1
2
3
WT
cKO
Transgenic
–
–
+
Transgenic miR-132
~0.40 kb
–
–
+
tTA
~0.80 kb
+/+
fl/fl
fl/fl
miR-132/212fl/fl
~0.42 kb (Floxed)
~0.37 kb (WT)
–
+
+
CaMKII-Cre
~0.40 kb
C
WT
cKO
Transgenic
CA1
GCL
D
WT
cKO
Transgenic
Circadian Day
Circadian Night
Relative miR-132 Abundance
9.0
6.0
3.0
1.0
0.5
0
*
n.s.
n.s.
E
WT
cKO
Transgenic
LD
DD

Table 3.1 Tabular representation of the circadian period (tau), the overall activity in LD and DD, and the mean phase delay after a light pulse at CT15 for the three noted mouse lines
Wheel running activity (denoted as rotations per day) was averaged over 7 days in both LD and DD conditions. Data were analyzed with a one-way ANOVA; N = 4-6 mice per group. No parameters were significantly different across genotypes. Data are presented as the mean ± SEM.

Parameter (mean ±SE)	WT	cKO	Transgenic	*P Value*
Circadian period (τ) in DD (hr)	23.57±0.05	23.49±0.02	23.47±0.02	0.170
Overall activity in LD (rotations/day)	16450.56±1159.33	18921.60±1028.67	17899.20±1512.84	0.442
Overall activity in DD (rotations/day)	11895.84±3064.06	18167.04±2962.17	19252.80±1238.92	0.164
Photic phase delay at CT15 (hr)	117.49±23.61	151.60±17.78	71.06±4.10	0.079

Figure 3.3 Time-of-day-dependent learning assayed using the NOL task
(*A*) Outline of the experimental design. (*B*) Discrimination indices of WT, cKO, and Transgenic mice were profiled (in the absence of doxycycline treatment) during the circadian day and the circadian night, recorded as [(novel object exploration time-familiar object exploration time)/(total exploration time)]. Significant time-of-day differences were tested using the repeated-measures ANOVA with Bonferroni post hoc correction for within genotype comparisons; $n = 8–10$ animals per group. The dashed line indicates 30% more time spent exploring the NOL compared to the familiar object location. Only WT animals (tested during the circadian night) demonstrated above-chance NOL discrimination, analyzed with a one-sample *t*-test. Total distance moved (*C*) and total exploration time (*D*) did not differ between WT, cKO, and Transgenic animals, and did not differ in any genotype depending on time-of-day, assessed via Repeated-Measures ANOVA. (*E*) Discrimination indices of WT, cKO, and Transgenic animals (maintained on 0.4 μg/mL doxycycline water) profiled during both time points, as described in *B*. Only WT animals (tested at night) demonstrated above-chance NOL discrimination. Total distance moved (*F*) and total exploration time (*G*) did not differ between genotypes or time-of-day after doxycycline treatment, assessed via Repeated-Measures ANOVA; $n = 6–9$ animals per group. Data are presented as mean ± SEM. (*) $P < 0.05$; (**) $P < 0.01$; (n.s.) not significant ($P > 0.05$).

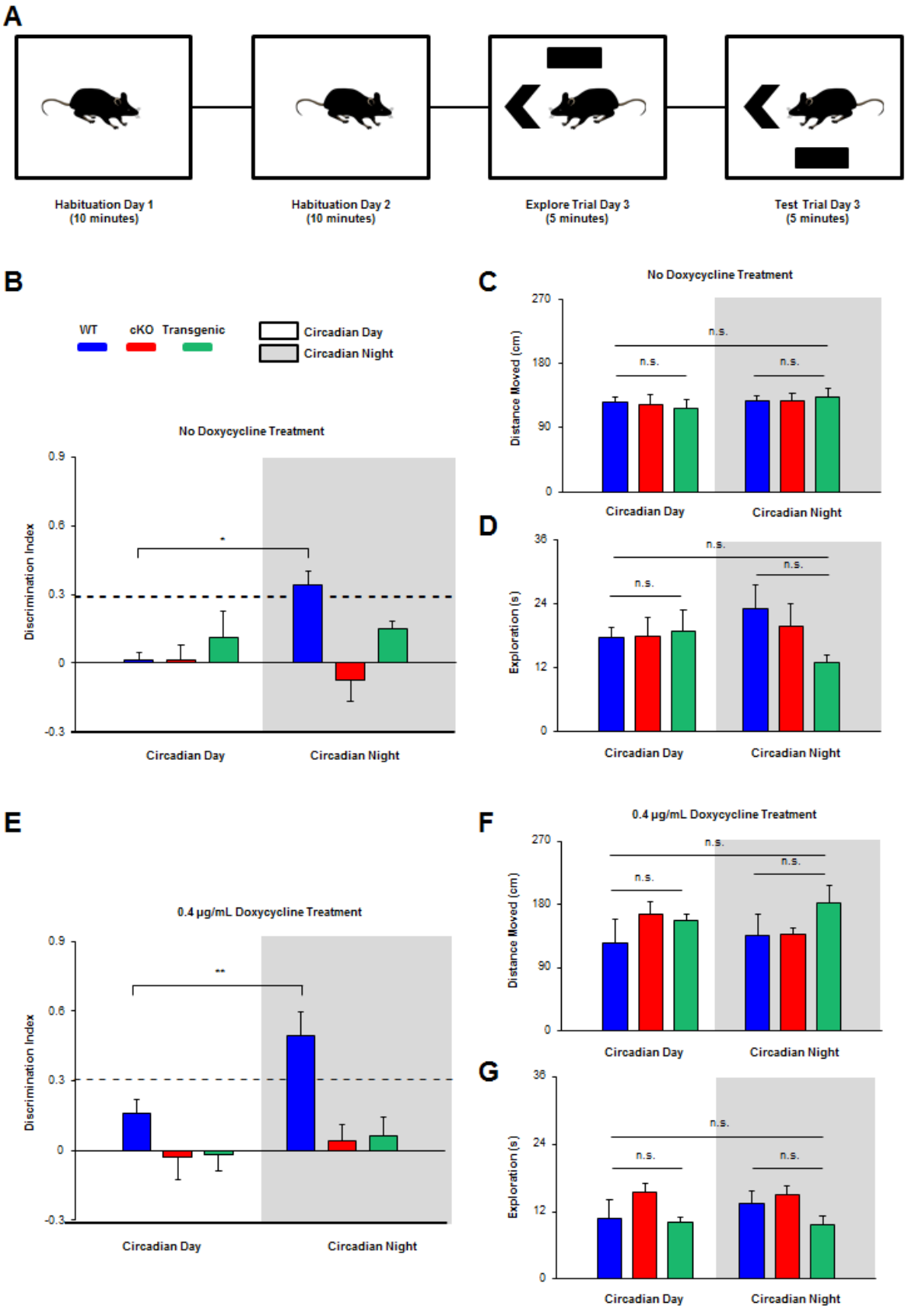
A
Habituation Day 1
(10 minutes)
Habituation Day 2
(10 minutes)
Explore Trial Day 3
(5 minutes)
Test Trial Day 3
(5 minutes)
B
WT
cKO
Transgenic
Circadian Day
Circadian Night
No Doxycycline Treatment
Discrimination Index
0.9
0.6
0.3
0
-0.3
*
Circadian Day
Circadian Night
C
No Doxycycline Treatment
Distance Moved (cm)
270
180
90
0
n.s.
n.s.
n.s.
Circadian Day
Circadian Night
D
Exploration (s)
36
24
12
0
n.s.
n.s.
n.s.
Circadian Day
Circadian Night
E
0.4 µg/mL Doxycycline Treatment
Discrimination Index
0.9
0.6
0.3
0
-0.3
**
Circadian Day
Circadian Night
F
0.4 µg/mL Doxycycline Treatment
Distance Moved (cm)
270
180
90
0
n.s.
n.s.
n.s.
Circadian Day
Circadian Night
G
Exploration (s)
36
24
12
0
n.s.
n.s.
n.s.
Circadian Day
Circadian Night

Figure 3.4 Time-of-day-dependent contextual fear memory recall
(*A*) Outline of the experimental design. After 2 days of dark-adaptation (days 5–6) mice were trained to associate a context box with a mild footshock. Beginning 24 h after training, mice were placed in the box every 12 h during circadian day and circadian night time points to profile their freezing behavior (i.e., memory retrieval). Of note, from day 5 onward, experimental manipulations were conducted under dim red light. Gray boxes represent circadian day time points (retrieval at CT4) and black boxes represent circadian night time points (retrieval at CT15). Mice were maintained on doxycycline drinking water (0.4 µg/mL) for 3 wk prior to fear conditioning (and throughout the fear conditioning experiment). (*B*) Graphical representation of the percentage of time spent freezing for WT, cKO, and Transgenic mice. 24, 48, 72, 96, and 120 h (post-training) represent day contextual fear retrieval time points, while 36, 60, 84, 108, and 132 h represent night retrieval time points. (*C*) Comparison of the freezing percentage (averaged over the first three respective day time points and the first three night time points) revealed a significant difference in WT animals, but not in cKO or Transgenic animals; analyzed using repeated-measures ANOVA with Bonferroni post hoc correction for within genotype comparison by TOD; n = 6–10 mice per group. Data are presented as mean ± SEM. (**) P < 0.01; (n.s.) not significant (P > 0.05).

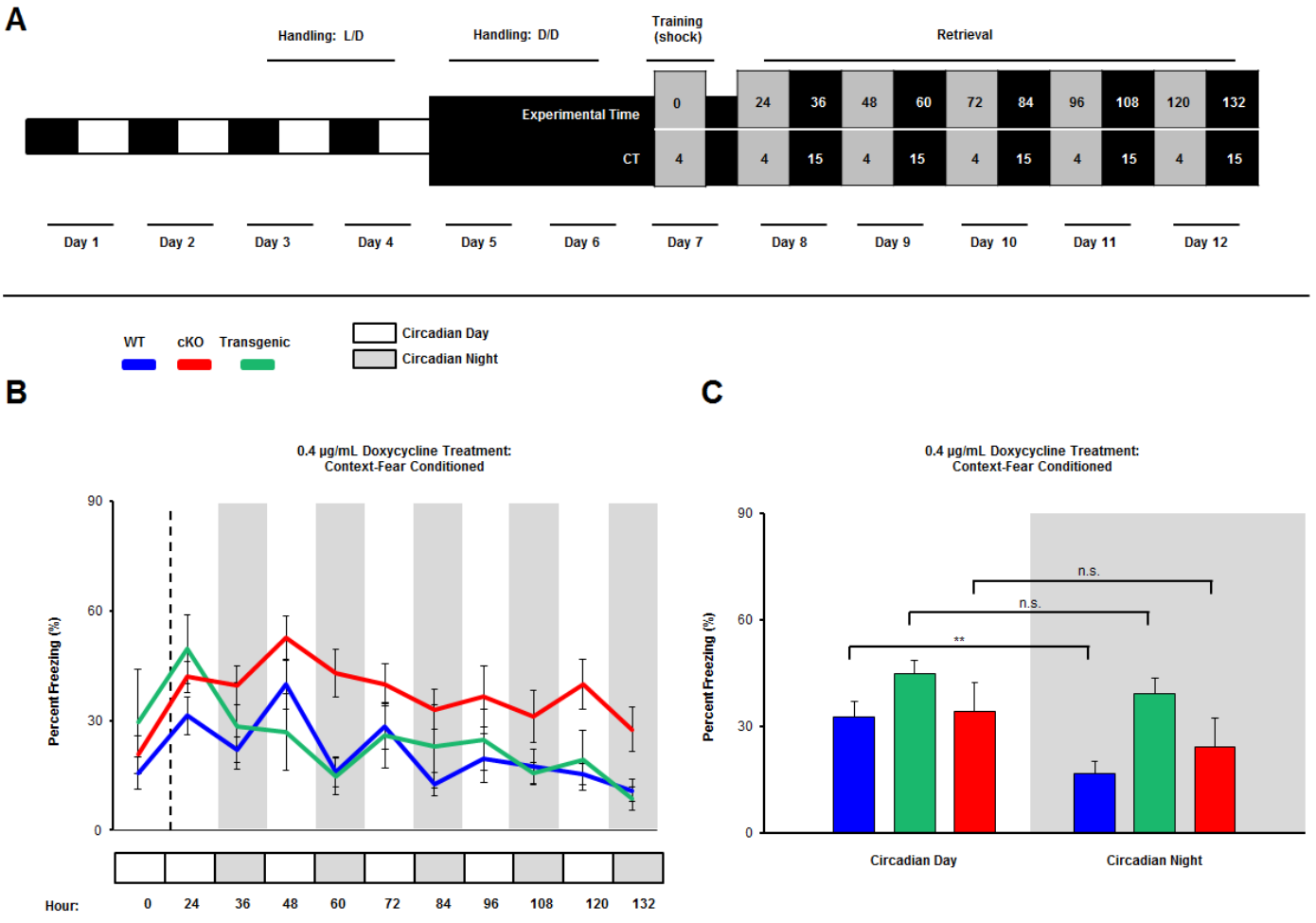

Figure 3.5 Clock-gated and miR-132-regulated MeCP2 expression in the hippocampus
(*A*) Low and high magnification representative images of MeCP2 immunohistochemical labeling in WT, cKO, and Transgenic animals sacrificed during the circadian day and the circadian night; scale bar = 50 μm for low-magnification images and 30 μm for high-magnification images. Boxed regions in the low magnification images approximate the locations from which the high magnification images were acquired. (*B*) Immunolabeling quantification for the CA1, GCL, and CA3. Within-genotype time-of-day differences were statistically analyzed using the Student's *t*-test, $n = 5–6$ mice per condition. For each genotype, MeCP2 expression is presented as relative intensity values, with the highest of the six expression levels set to a value of one. (*C*) Representative Western blot images of hippocampal MeCP2 expression in WT, cKO, and Transgenic animals sacrificed during the circadian day and the circadian night. Each time point was run as an experimental replicate (one mouse/lane, two lanes per condition). For each genotype, the time point (day or night) with the highest relative band intensity was set equal to a value of one. (*D*) Quantitative densitometric analysis of MeCP2 hippocampal protein levels relative to the control protein, β-actin; significance was assessed via the Student's *t*-test, $n = 3–4$ animals per group. The experiment was replicated at least one time per condition. Of note, immunolabeling and Western blotting for each genotype was performed on separate occasions, thus comparisons were only made within genotype (i.e., WT day versus WT night), and not across genotypes. Data are presented as mean ± SEM. (*)$P < 0.05$; (n.s.) not significant ($P > 0.05$).

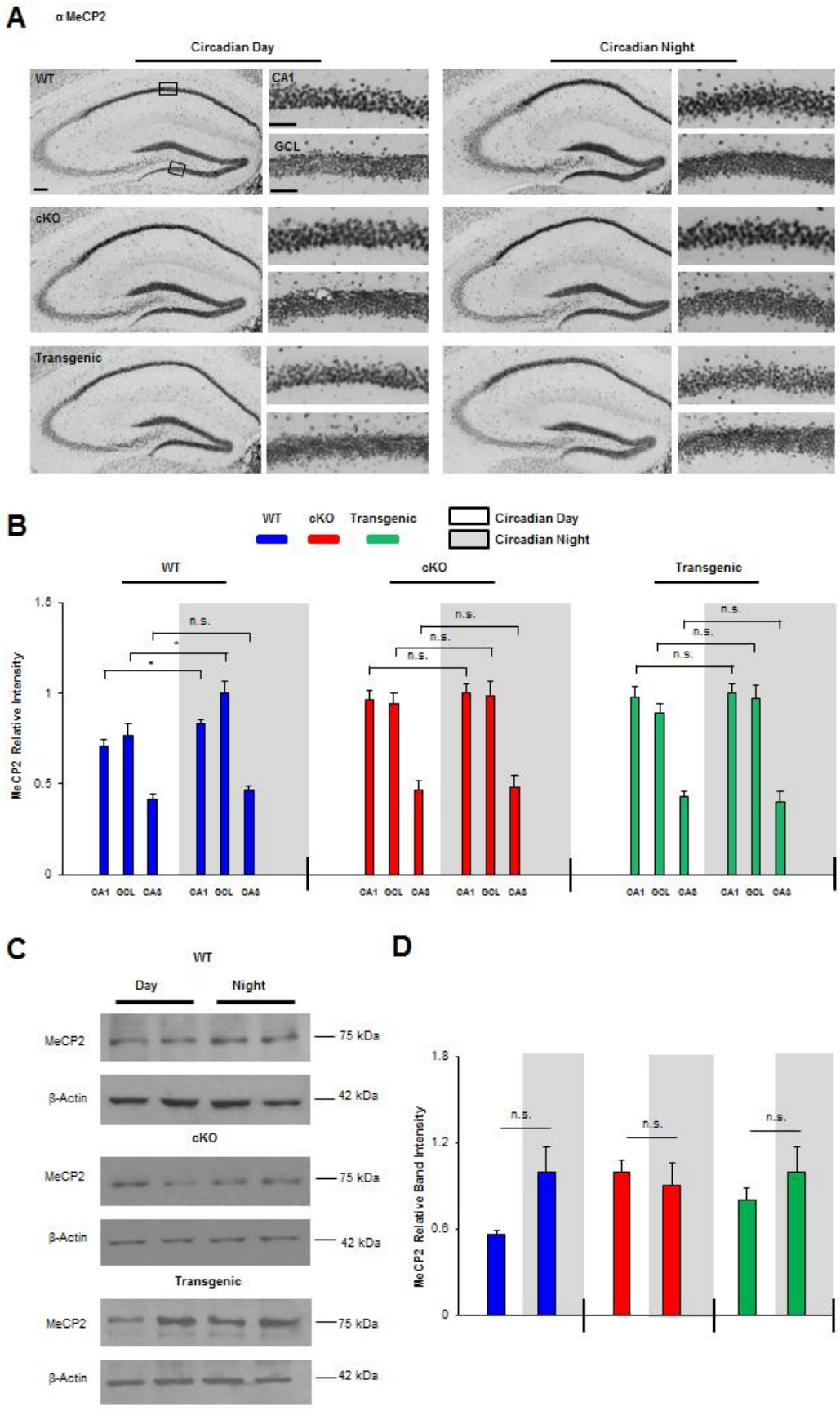
A
α MeCP2
Circadian Day
Circadian Night
WT
CA1
GCL
cKO
Transgenic
B
WT
cKO
Transgenic
Circadian Day
Circadian Night
MeCP2 Relative Intensity
1.5
1
0.5
0
n.s.
*
CA1 GCL CA3
C
WT
Day
Night
MeCP2
β-Actin
75 kDa
42 kDa
cKO
Transgenic
D
MeCP2 Relative Band Intensity
1.8
1.2
0.6
0

Figure 3.6 Clock-gated and miR-132-regulated Sirt1 expression in the hippocampus
(*A*) Representative low and high magnification images of hippocampal Sirt1 immunostaining in WT, cKO, and Transgenic animals sacrificed during the circadian day and the circadian night. Scale bar = 50 μm for low-magnification images and 30 μm for high-magnification images. Boxed regions in the low magnification images approximate the locations from which the high magnification images were acquired. (*B*) Quantification of Sirt1 expression in the CA1, GCL, and CA3. Statistical comparisons of time-of-day expression were performed using the Student's *t*-test, $n = 4–6$ animals per condition. For each genotype, Sirt1 expression is presented as relative intensity values, with the highest of the six expression levels set to a value of one. (*C*) Representative Western blot images of hippocampal Sirt1 expression in WT, cKO, and Transgenic animals sacrificed during the circadian day or night. Each time point was run as an experimental replicate (one mouse/lane, two lanes per condition). For each genotype, the time point (day or night) with the highest relative band intensity was set equal to a value of one. (*D*) Quantitative ratiometric densitometric analysis of Sirt1/β-actin protein levels; significance was assessed using the Student's *t*-test, $n = 3–4$ animals per group. The experiment was replicated at least one time per condition. A significant time-of-day difference in band intensity was observed for the WT animals, but no significant differences were observed in cKO or Transgenic animals. Expression level comparisons for immunolabeling and Western blotting were only made within genotype. Data are presented as mean ± SEM. (*) $P < 0.05$. (n.s.) not significant ($P > 0.05$).

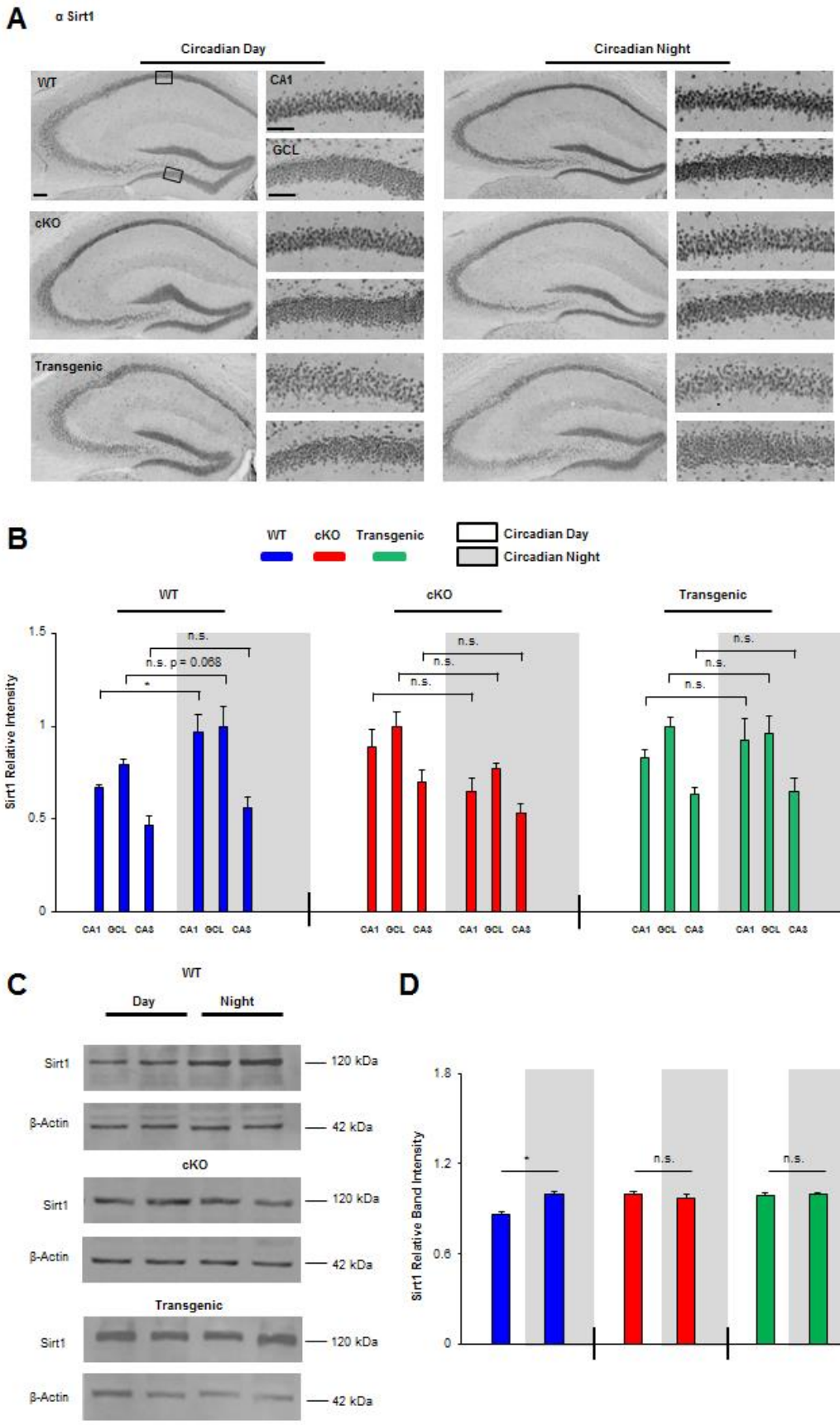
A
α Sirt1
Circadian Day
Circadian Night
WT
CA1
GCL
cKO
Transgenic
B
WT
cKO
Transgenic
Circadian Day
Circadian Night
Sirt1 Relative Intensity
1.5
1
0.5
0
n.s.
n.s. p = 0.068
*
CA1 GCL CA3
C
WT
Day
Night
Sirt1
120 kDa
β-Actin
42 kDa
cKO
Transgenic
D
Sirt1 Relative Band Intensity
1.8
1.2
0.6
0

Figure 3.7 Profiling hippocampal TOD expression: NeuN, and MeCP2/Sirt1 in *BMAL1*$^{-/-}$ mice. (*A*) Representative immunohistochemical labeling for NeuN in WT, cKO, and Transgenic animals sacrificed during the circadian day and the circadian night. Scale bar = 30 μm. (*B*) Immunolabeling quantification; no time-of-day differences in NeuN expression were observed in any genotype. Significance assayed using the Student's *t*-test; $n = 4–6$ mice per group. In each of the three noted mouse lines, the hippocampal region with the highest NeuN intensity was set equal to a value of one. (*C*) Representative immunolabeling for MeCP2 in *BMAL1*$^{-/-}$ mice; animals were profiled during the circadian day and the circadian night. (*D*) Quantification of MeCP2 expression did not detect a time-of-day difference in any hippocampal region. Data were analyzed by Student's *t*-test; $n = 4$ mice per time point. (*E*) Representative Sirt1 immunolabeling in *BMAL1*$^{-/-}$ animals. (*F*) Quantification of Sirt1 expression did not detect a time-of-day difference in any hippocampal region. Data were analyzed by Student's *t*-test; $n = 4$ mice per time point. Data are presented as mean ± SEM. (n.s.) not significant; $P > 0.05$.

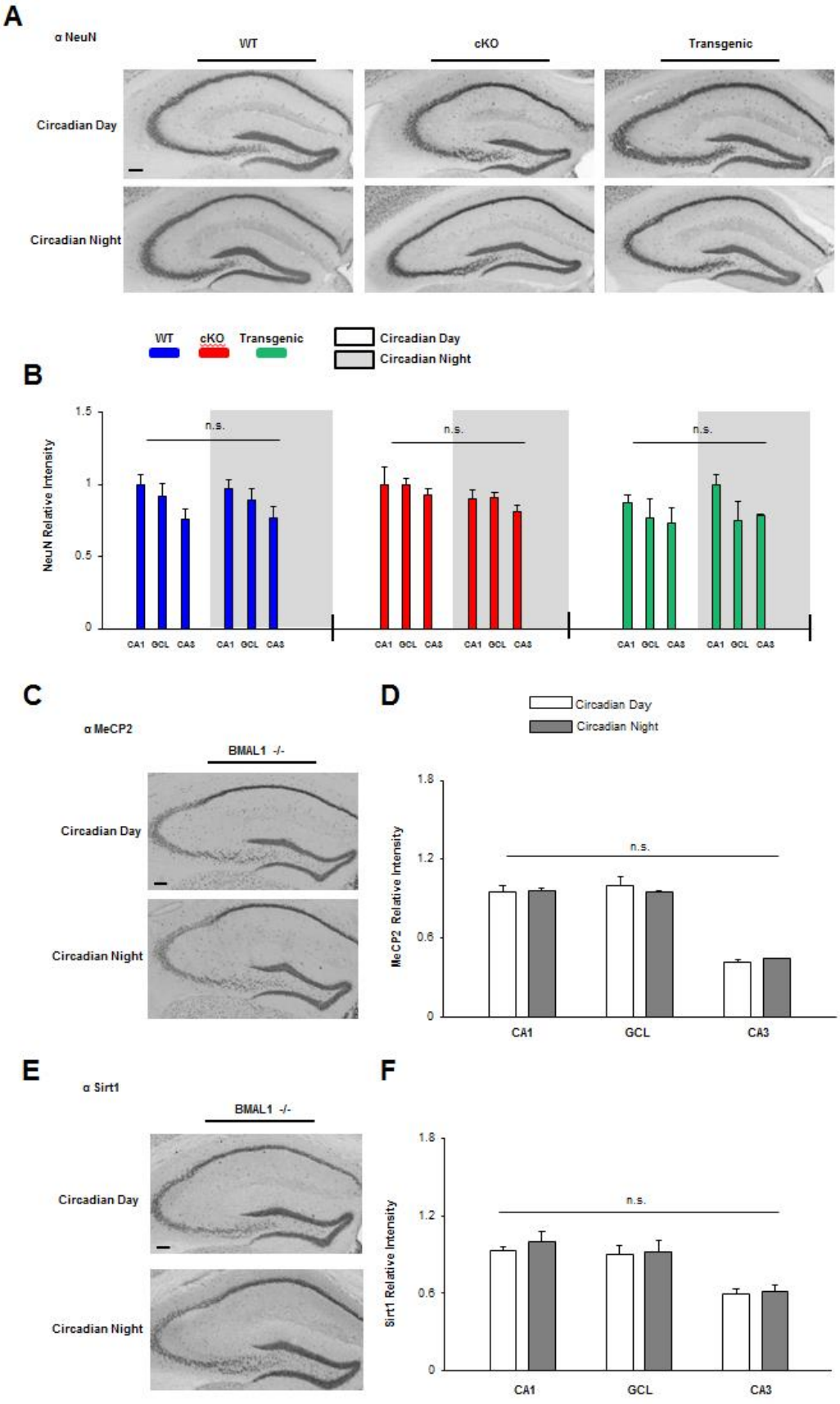
A
α NeuN
WT
cKO
Transgenic
Circadian Day
Circadian Night
WT
cKO
Transgenic
Circadian Day
Circadian Night
B
NeuN Relative Intensity
1.5
1
0.5
0
n.s.
n.s.
n.s.
CA1 GCL CA3 CA1 GCL CA3
CA1 GCL CA3 CA1 GCL CA3
CA1 GCL CA3 CA1 GCL CA3
C
α MeCP2
BMAL1 -/-
Circadian Day
Circadian Night
D
Circadian Day
Circadian Night
MeCP2 Relative Intensity
1.8
1.2
0.6
0
n.s.
CA1
GCL
CA3
E
α Sirt1
BMAL1 -/-
Circadian Day
Circadian Night
F
Sirt1 Relative Intensity
1.8
1.2
0.6
0
n.s.
CA1
GCL
CA3

CHAPTER 4

miR-132/212 is induced by stress and its dysregulation triggers anxiety-related behavior

Introduction

Anxiety disorders are a class of neuropsychiatric ailments that often result from and/or are influenced by both genetic and epigenetic factors (Nugent et al., 2011; Poulton et al., 2008; Smoller, 2016). Along these lines, gene expression can alter anxiety onset/severity through mechanisms that include DNA and histone modifications and non-coding RNA regulation (for review, see (Issler and Chen, 2015; McEwen et al., 2012; Nieto et al., 2016). As for the latter case, microRNAs are small, non-coding RNA molecules that modulate essential physiological processes, such as cellular homeostasis and immune/stress responsiveness (for review, see (Haramati et al., 2011; Leung and Sharp, 2010, 2007; Mendell and Olson, 2012; Wiegand et al., 2017). Indeed, the ability of miRNAs to fine-tune gene expression positions them as excellent candidates for regulating stress and anxiety behaviors (Andolina et al., 2016; Cohen et al., 2017; Hollins and Cairns, 2016; Issler and Chen, 2015; Leung and Sharp, 2010; Malan-Müller et al., 2013; Mannironi et al., 2018, 2013; O'Connor et al., 2012; Volk et al., 2014).

Among these miRNAs is brain-enriched miR-132 (Vo et al., 2005). A large body of work has characterized the miR-132/212 locus as a synaptic activity-dependent regulator of gene expression and plasticity within the CNS (Cheng et al., 2007a; Jimenez-Mateos et al., 2011; Mellios et al., 2011; Nudelman et al., 2010). With respect to its role

in synaptic physiology, miR-132 has been shown to regulate hippocampal neuronal spine density, dendritic arborization, and long-term potentiation (Hansen et al., 2010; Nudelman et al., 2010; Tognini et al., 2011; Wayman et al., 2008).

Recently, miR-132 has been shown to function as a modulator of cognitive capacity. Along these lines, transgenic overexpression of miR-132 was found to reduce spatial and recognition memory (Hansen et al., 2010; Scott et al., 2012), while the targeted deletion of the miR-132/ 212 locus led to deficits in learning and memory (Hansen et al., 2016; Hernandez-Rapp et al., 2015). Interestingly, dysregulation of miR-132/ 212 expression has been reported in patients with schizophrenia and bipolar disorder (Kim et al., 2010; Perkins et al., 2007). Further, miR-132 is increased in patients with depression (Li et al., 2013), as well as in animal models that exhibit non-learned helplessness (Smalheiser et al., 2011). Several groups have also reported a correlation between stress and miR-132 expression. For example, Meerson et al showed that miR-132 is induced in the hippocampal CA1 region following chronic immobilization stress (Meerson et al., 2010), while Shaltiel et al demonstrated that predator scent and footshock stress leads to long lasting increases in hippocampal miR-132 and concomitant decreases in miR-132 target genes (Shaltiel et al., 2013). Likewise, miR-132 is significantly increased in the prefrontal cortex of maternally separated rat pups (Uchida et al., 2010) and has been shown to modulate stress-induced chemokine production (Strum et al., 2009).

These studies, coupled with our recent observation that miR-132/ 212 conditional KO mice displayed a heightened level of freezing behavior in the contextual

fear conditioning paradigm (Aten et al., 2018a), led us to test the relationship between the dysregulation of miR-132/212 and the appearance of anxiety-like behavior. Here, using RT-qPCR, we show that miR-132 and miR-212 are induced after both acute and chronic stress paradigms. Further, utilizing forebrain miR-132/212 knockout and transgenic targeting approaches, we demonstrate that the dysregulation of miR-132/212 expression leads to anxiety-related behaviors. Collectively, these data indicate that the miR-132/212 locus contributes to the manifestation of anxiety-like behavioral states.

Materials and Methods

miR-132 transgenic and miR-132/212 knockout mice

The CaMKII-Cre::miR-132/212$^{f/f}$ conditional forebrain neuron knockout (referred to as 'miR-132/212 cKO') mouse line was previously described by our lab (Hansen et al., 2016). The miR-132/212$^{f/f}$ animals were provided by Dr. J. Simon C. Arthur (University of Dundee, Scotland), and the CaMKII-Cre line (Tsien et al., 1996) was purchased from Jackson Labs (Stock number: 005359: Bar Harbor, ME, USA). Generation of the CaMKII-tTA::miR-132:CaMKII-Cre::miR-132/212$^{f/f}$ mouse line (referred to as 'miR-132 transgenic') was recently reported by Aten et al (Aten et al., 2018a). In brief, miR-132 transgenic animals were created by breeding homozygous CaMKII-Cre::miR-132/212$^{f/f}$ (miR-132/212 cKO) mice with a tetracycline-regulated bidirectional miR-132/cyan fluorescent protein (CFP) transgenic mouse line driven by CaMKII::tTA. Thus, miR-132 transgenic mice were homozygous for the miR-132/ 212$^{f/f}$ locus and positive for Cre, tTA, and miR-132 transgenes. This 'Tet-off' transgenic animal model allowed for selective deletion of endogenous miR-132/212 and transgenic

over-expression of miR-132 within the same population of excitatory forebrain neurons. For all experiments with transgenic and knockout mice, control (referred to as 'WT') animals were littermates that were negative for either the driver and/or responder genes. Genotyping for both the miR-132/212 cKO and miR-132 transgenic lines was previously described by our lab (Aten et al., 2018a; Hansen et al., 2010, 2016).

All mice utilized for experiments were bred, housed, and maintained under standard 12 h/12 h Light/Dark (LD) conditions and had *ad libitum* access to food and water. All behavioral and molecular experiments took place from the mid-to late-day light period. Experimental animals were screened, as described in Hansen et al (Hansen et al., 2013), to ensure that they did not have any vision deficits. Of note, for experiments examining miR-132 and miR-212 expression after stress paradigms (Fig. 4.1 and Fig. 4.3) only male WT mice (8–12 weeks of age) were utilized to eliminate potential sex-specific effects. However, given the limited number of miR-132/212 cKO and miR-132 transgenic mice available, both males and females were used for behavioral and molecular experiments (Fig. 4.6-4.11); a sex-parsed presentation of data for WT, miR-132/212 cKO, and miR-132 transgenic anxiety behavioral experiments are provided in Fig. 4.8. The Ohio State University Institutional Animal Care and Use Committee approved all protocols and methods, and all experiments were in accordance with the National Institutes of Health guide for the care and use of Laboratory animals.

Doxycycline treatment

In a subset of animals (Fig. 4.7), temporal modulation of tetracycline-inducible miR-132 transgene expression was accomplished via the administration of doxycycline

(0.40 μg/mL) to the drinking water. Using this technique, as previously described (Aten et al., 2018a; Hansen et al., 2013), we were able to reduce the expression of the miR-132 transgene (see Fig. 4.11). For the elevated plus and open field experiments, all animals (WT and miR-132 transgenic) were given this doxycycline dose for three weeks prior to the start of the experiment, and the animals remained on doxycycline throughout the duration of the experiment(s). Doxycycline water was changed every three days. Consistent with our previous data (Aten et al., 2018a; Hansen et al., 2013), no significant effect of doxycycline was observed in control, WT animals (i.e. animals that were not positive for both the tTA and miR-132 driver/responder transgenes; data not shown).

Acute multimodal stress paradigm

Our acute stress test was adapted from recently published papers (Chen et al., 2010; Zimprich et al., 2014). Male WT mice (8–12 weeks of age) were divided into two groups (control and stress) and were given 30 min to acclimate to the testing room before the experiment began. For the acute stress paradigm, mice were placed in ventilated 50 mL conical tubes. Next, the tubes were secured on an orbital shaker in a brightly lit (~400 lux) room, with loud music. Stressed animals were maintained in ventilated conicals for 5 h. Control animals remained in their respective cages for the 5 h period. After cessation of the stress paradigm, control and stressed animals were divided into three cohorts: one cohort was used for RT-qPCR analysis (Fig. 4.1B-4.1E), another for behavioral analysis (Fig. 4.2A-4.2D), and a final group for immunohistochemical analysis (Fig. 4.2E-4.2F). For RT-qPCR analysis of miR-132 and miR-212 expression, stressed and control mice were sacrificed 30 min after the stress session ended (approximately 5.5 h after stress

onset). The timing of sacrifice was chosen as it reflects the kinetics for inducible miR-132 expression(Nudelman et al., 2010; Vo et al., 2005). For the behavioral analysis, stressed animals were given a 20 min resting period after the cessation of the multimodal stress paradigm before the open field test was conducted. This 20 min rest period was based on work by Zimprich et al, which demonstrated that this delay period between the acute stressor and examination of the stress response was required to eliminate the confounding effects of a transient bout of grooming behavior (Zimprich et al., 2014). Finally, animals (stressed and control) were killed immediately after the stress session ended for immunohistochemical profiling of cFos. The specific timecourse/protocol for each of the three mentioned experiments is described in separate sections below.

Chronic restraint stress paradigm

The chronic restraint paradigm was adapted from recently published papers (Jeong et al., 2013; Meerson et al., 2010). In brief, stressed WT mice (males only) were restrained in ventilated 50 mL conical tubes for 2 h each day for a 15 day period. After each stress session, mice were placed back into their home cages. Control mice were handled daily while the stressed animals were restrained. Mice were also weighed every five days in order to assess body weight during the stress paradigm. Animals were sacrificed on day sixteen—24 h after the last restraint session—for RT-qPCR profiling of miR-132 and miR-212 expression (Fig. 4.3A-4.3E). Post-mortem adrenal glands, thymus, and spleen were dissected from both control and stressed animals and were weighed to test the efficacy of the stress chronic restraint stress paradigm (Fig. 4.4).

RT-qPCR quantification of miR-132 and miR-212 expression levels in the hippocampus and amygdala

WT animals were killed 30 min after the cessation of the acute multimodal stress paradigm and 24 h after the last chronic stress session; tissue processing and RNA isolation were performed using methods described previously for the hippocampus (Aten et al., 2018a), and the amygdala (Zapala et al., 2005). RNA was reverse transcribed using the miScript II Reverse Transcription kit (Qiagen). The miScript Primer System (Qiagen) was used to quantify miR-132 and miR-212 levels: miR-132 primer sequence: 5′ UAACAGUCUACAGCCAUGGUCG (Qiagen, Cat# MS00001561); miR-212 primer sequence: 5'UAACAGU CUCCAGUCACGGCCA (Qiagen, Cat# MS00024570). For RT-qPCR, QuantiFast SYBR Green thermocycling conditions were used, following methods previously described (Alemayehu et al., 2013; Aten et al., 2018a). Data were normalized to RNU6B_2 levels, and fold change was calculated using Double Delta CT analysis.

Elevated plus maze

The elevated plus maze was run under dim white light (~50 lux). The maze dimensions and structure were previously described by our lab (Snider et al., 2016b). During the experiment, mice were placed in the center of the plus-shaped maze, facing an open arm and were given 5 min to explore. 70% ethanol was used to clean the maze between each trial. The total number of open arm transitions, cumulative open arm duration, and latency to enter an open arm was scored using Noldus Ethovision XT version 11.5 (EthoVision XT).

For the behavioral experiments depicted in Fig. 4.6-4.7, all mice (WT, miR-132/212 cKO, and miR-132 transgenic) were first run through the elevated plus maze. Two days later, the same animals were subjected to the open field test.

Open field assay

For examination of anxiety-like behavior in the three noted mouse lines (WT, miR-132/212 cKO, and miR-132 transgenic), the open field test was conducted under dim white light (~50 lux). Mice were placed in the arena and were given 5 min to explore. The bottom surface and the walls of the arena were wiped with 70% ethanol between each trial. Total time spent in the center of the arena, number of crosses into the center of the arena, and cumulative freezing time was scored by Noldus EthoVision XT version 11.5 (EthoVision XT).

To confirm hypothalamic pituitary adrenal (HPA) axis activation in WT mice after the acute multimodal stress paradigm, the same open field protocol was used as described above. Three common readouts of acute stress-responsivity were measured: number of rears, distance traveled, and velocity (Zimprich et al., 2014). Note that number of rears was manually scored. A rear was defined as a mouse positioning itself on its hind legs, with its front legs off the ground.

Tissue processing for immunolabeling

Mice were sacrificed via rapid cervical dislocation, and brains were cut into 600 μm sections using a vibratome. Next, sections were fixed in 4% paraformaldehyde diluted in 1X phosphate-buffered saline (PBS) for 6 h (4 °C) and then cryoprotected via

overnight incubation in 30% sucrose (in 1X PBS). In preparation for immunolabeling, sections were thin-cut to 40 μm on a freezing microtome.

Immunohistochemistry

Sections were incubated for 20 min in 0.3% hydrogen peroxide in 0.1% Triton X-100 in PBS (PBST). Next, tissue was blocked for 1 h in 10% normal goat serum, followed by incubation at 4 °C (for 8 h) with one of the following antibodies: rabbit anti-cFos (1:2000 dilution; Millipore, Cat# ABE457), rabbit anti-Sirt1/Sir2α (1:1000 dilution; Millipore, Cat# 09–845), or rabbit anti-Pten (1:100 dilution; Cell Signaling Technology, Cat # 9188P).

On the second day, sections were incubated in biotin-conjugated goat anti-rabbit IgG secondary antibody (1:1000 dilution; Vector Laboratories, Cat# BA-1000) for 2 h at room-temperature. Next, sections were processed using the ABC labeling method (Vector Laboratories Cat# PK-6100) and horseradish peroxidase enzymatic activity was visualized using nickel intensified diaminobenzidine labeling method (Vector Laboratories Cat# SK-4100). Of note, sections were washed three times (5 min/wash) in PBST between each labeling step. Finally, sections were mounted on gelatin-coated slides, washed in dH2O, and coverslipped with Permount Mounting Medium (Fisher Chemical). Bright field images were captured with a 16-bit digital camera (Micromax YHS 1300; Princeton Instruments) on a Leica DMIR microscope with Metamorph software (MetaMorph Microscopy Automation and Image Analysis Software). For the quantification of cFos labeling, digital images of the PVN, BNST, medial septum, central amygdala, and dorsal CA1 of the hippocampus were traced digitally from 1–3 sections

per animal. Intensity levels for each section were background subtracted and quantitatively analyzed using ImageJ software. Mean intensity values for regions of interest were generated for each animal and the group average was displayed as the mean ± the standard error (SEM) for each noted brain region. For the quantification of Sirt1 and Pten labeling, digital images of the amygdala and the CA1, CA3, and GCL hippocampal subfields were acquired, and intensity values and quantitation methods were performed as described for c-Fos labeling.

Experimental design and statistical analysis

Statistics were performed using GraphPad Prism 7.0 (Graphpad Prism) software. All data are presented as the mean ± SEM. As denoted in the figure legends, significance for all experiments was set at $*p < 0.05$. Comparisons between two groups were performed using Student's two-tailed t-tests, while comparisons between three or more groups were made using a one-way ANOVA. Bonferroni post-hoc tests were conducted to show an interaction obtained from significant ANOVA results. To determine if there were significant interactions between two independent variables on the dependent variable, a two-way ANOVA was performed. Additionally, Grubb's test was conducted on data sets within each group, and animals that were found to be statistically significant outliers ($p < 0.05$) were removed from analysis. Grubb's test was used to exclude two control animals from the acute stress RT-qPCR data set and one WT animal from the Pten immunolabeling analysis. Further, for behavioral experiments, one WT animal, two cKO, and one transgenic animal used in the no-doxycycline anxiety

paradigms were also found to be significant outliers, while one WT and one transgenic animal in the doxycycline behavioral experiments were significant outliers.

Results

Hippocampal and amygdalar miR-132 and miR-212 are upregulated after acute stress

Extensive work in several brain regions has characterized miR-132 as an activity-inducible gene (Cheng et al., 2007a; Hansen et al., 2013; Hernandez-Rapp et al., 2015; Mellios et al., 2011; Nudelman et al., 2010; Tognini et al., 2011). With these observations in mind, we aimed to test whether miR-132 is induced after an acute stress paradigm (Fig. 4.1B-4.1C). RT-qPCR analysis revealed that a 5-h long acute multimodal stress paradigm led to a two-fold increase in hippocampal miR-132, relative to control animals (Fig. 4.1B, $t_{(17)} = 2.270$, $p = 0.0365$; Student's t-test); in the amygdala, stress also led to a two-fold relative increase in miR-132 expression (Fig. 4.1C, $t_{(16)} = 3.423$; $p = 0.0035$; Student's t-test). Interestingly, miR-212 hippocampal and amygdalar expression was also increased (> two-fold in the hippocampus and > four fold in the amygdala) in acutely stressed animals (Fig. 4.1D, $t_{(17)} = 3.583$, $p = 0.0023$ for hippocampus and Fig. 4.1E, $t_{(15)} = 4.881$, $p = 0.00032$ for amygdala; Student's t-tests). Together, these results demonstrate the inducible nature of the miR-132/212 locus after an acute stress paradigm.

To test the efficacy of the noted multimodal stress paradigm, a separate cohort of stressed and non-stressed animals was subjected to the open field test 20 min after the cessation of the stress paradigm (Fig. 4.2A). As expected, compared to control animals, mice that were exposed to the stress paradigm displayed behaviors associated with an elevated level of stress responsivity (Zimprich et al., 2014); hence, the stress paradigm

led to a significant increase in the number of rears (Fig. 4.2B, $t_{(9)} = 2.283$, $p = 0.0483$; Student's t-test), an increase in the total distance moved (Fig. 4.2C, $t_{(9)} = 2.378$, $p = 0.0414$; Student's t-test), and an increase in the mean velocity (Fig. 4.2D, $t_{(9)} = 2.376$, $p = 0.0415$; Student's t-test). An additional set of mice was sacrificed after termination of the stress paradigm, and tissue from these animals was processed for cFos induction—a readout of stress-induced neuronal activation (Cullinan et al., 1995; Hoffman et al., 1993; Senba et al., 1993) (Fig. 4.2E-4.2F). Similar to recently published results (Maras et al., 2014), the 5 h acute multimodal stress paradigm increased cFos counts in the paraventricular nucleus (PVN), bed nucleus of the stria terminalis (BNST), medial septum, and amygdala (Fig. 4.2F, $F_{(4, 36)} = 16.5$, $p < 0.0001$; two-way ANOVA). Specifically, cFos expression in the PVN, BNST, medial septum, and amygdala was significantly higher in stressed mice compared to control mice (Fig.4.2F $t_{(8)} = 7.389$, $p < 0.001$ for PVN; $t_{(8)} = 6.105$, $p = 0.0015$ for BNST, $t_{(8)} = 4.762$, $p = 0.0070$ for medial septum, and $t_{(5)} = 8.721$, $p = 0.0015$ for central amygdala; Bonferroni post-hoc tests). cFos expression in the dorsal CA1 of stressed mice also showed a trending relative increase, though significance was not reached (Fig. 4.2F $t_{(7)} = 3.388$, $p = 0.0580$; Bonferroni post-hoc test). Collectively, these data indicate that our multimodal stress paradigm elicits the expected behavioral and molecular responses.

Amygdalar miR-132 and miR-212 are upregulated after chronic restraint stress

Given our acute stress results, we aimed to determine whether miR-132/212 induction in the hippocampus and amygdala is specific to acute stress exposure, or if chronic stress also leads to its induction. To this end, we exposed WT mice to 2 h of

restraint stress (or brief handling for control animals) each day, for a 15 day period, before sacrificing the animals on day 16 (Fig. 4.3A). Interestingly, no significant difference was observed in hippocampal miR-132 expression between control and chronically stressed mice (Fig. 4.3B $t_{(16)} = 0.5149$, $p = 0.6136$; Student's t-test), while amygdalar miR-132 was increased ~ three-fold (Fig. 4.3C $t_{(16)} = 2.254$, $p = 0.0386$; Student's t-test). The chronic stress paradigms also led to an increase in miR-212 in the amygdala, but not in the hippocampus (Fig. 4.3D $t_{(16)} = 1.036$, $p = 0.3156$ for the hippocampus and Fig. 4.3E $t_{(16)} = 3.687$, $p = 0.0020$ for the amygdala; Student's t-test).

A hallmark of chronic stress in mice is a decrease in body weight gain (Krahn et al., 1990). To confirm the effectiveness of the chronic stress paradigm, mice were weighed every five days. Consistent with previous findings (Jeong et al., 2013; Voorhees et al., 2013; Yoon et al., 2014), after 15 days of chronic restraint, body weight gain was significantly reduced in stressed mice compared to control mice (Fig. 4.4A $F_{(3, 60)} = 4.416$, $p = 0.0072$; two-way ANOVA). Specifically, body weight was lower in stressed mice on day 16 (Fig. 4.4A $t_{(15)} = 3.238$, $p = 0.0220$; Bonferroni post-hoc test). Adrenal glands, thymus, and spleens were also weighed post-mortem, as a measure of stress reactivity (Blanchard et al., 1993; Engler et al., 2005). Again, consistent with previous findings (Stankiewicz et al., 2014; Voorhees et al., 2013), after 15 days of restraint, stressed mice had increased adrenal mass (Fig. 4.4B, $t_{(15)} = 5.661$, $p < 0.0001$; Student's t-test), decreased thymic mass (Fig. 4.4C, $t_{(15)} = 3.524$, $p = 0.0031$; Student's t-test), and a trend toward increased spleen weight (Fig. 4.4D, $t_{(14)} = 1.835$, $p = 0.0879$; Student's t-test). Together, these support the effectiveness of the chronic restraint paradigm.

Basal anxiety is affected by the dysregulation of miR-132 in forebrain excitatory neurons

Given our finding that stress paradigms trigger the upregulation of miR-132/212 in brain regions that underlie stress and anxiety responsiveness, we examined whether anxiety levels are affected by the dysregulation of miR-132/212. To this end, we employed a combination of conditional miR132/212 gain- and loss-of-function mouse lines. As detailed in the Methods section and in our recent paper (Aten et al., 2018a), the miR-132/212 loss-of-function mouse line (hereafter referred to as the 'miR-132/212 cKO' mouse line; Fig. 4.5A) uses a Cre/lox gene deletion strategy to eliminate the miR-132/212 locus from excitatory forebrain neurons—including neurons of the hippocampus, amygdala, and cortex. For the gain-of-function mouse line (hereafter referred to as the 'miR-132 transgenic' mouse line; Fig. 4.5B), a tetracycline/doxycycline-controlled CaMKII-tTA::TRE-miR-132 transgenic line (previously described by our lab (Hansen et al., 2010) was crossed with the miR-132/212 cKO mouse line. Transgenic expression of miR-132 was targeted to the same excitatory neuronal cell populations in which the miR-132/212 gene locus was deleted. Importantly, in the absence of doxycycline treatment, transgenic miR-132 is expressed at supraphysiological levels (Aten et al., 2018a), and thus by applying doxycycline to the drinking water, this 'Tet-off' mouse line can be used to examine the effects of titered miR-132 expression. Using the elevated plus maze paradigm (Fig. 4.6A), we found that the number of open arm transitions (a measure that is often used as a read-out of anxiety-like behavior; (Walf and Frye, 2007), was significantly affected by the gain- and loss-of miR-132/ 212 expression (Fig. 4.6B; $F_{(2,33)} = 7.753$; $p = 0.0021$; one-way ANOVA). In specific, both miR-132/212 cKO and miR-

132 transgenic animals displayed significantly fewer transitions into the open arms of the elevated plus maze compared to control animals (Fig. 4.6B; $t_{(19)} = 2.793$, $p = 0.0348$ for miR-132/212 cKO to WT comparison and $t_{(20)} = 2.984$, $p = 0.0219$ for miR-132 transgenic to WT comparison; Bonferroni post-hoc tests). Moreover, the cumulative duration spent in the open arms of the maze was significantly different between genotypes (Fig. 4.6C; $F_{(2,33)} = 5.202$, $p = 0.0113$; one-way ANOVA). While miR-132 transgenic animals spent significantly less time in the open arms compared to WT animals (Fig. 4.6C; $t_{(21)} = 2.704$, $p = 0.0399$; Bonferroni post-hoc test), no significant differences were found between WT animals and miR-132/212 cKO animals (Fig. 4.6C; $t_{(22)} = 1.850$, $p = 0.2334$; Bonferroni post-hoc test). Further, a significant genotypic difference in the latency to open arms was also observed (Fig. 4.6D; $F_{(2,33)} = 5.630$, $p = 0.0082$; one-way ANOVA). miR-132 transgenic animals took significantly more time, on average, to enter the open arms of the maze compared to WT mice (Fig. 4.6D; $t_{(21)} = 3.636$ $p = 0.0045$; Bonferroni post-hoc test) while the latency for miR-132/212 cKO animals to enter open arms did not vary significantly from WT animals (Fig. 4.6D; $t_{(22)} = 1.239$ $p = 0.6852$; Bonferroni post-hoc test).

To complement our elevated plus maze data, we also explored the anxiety phenotype of miR-132/212 cKO and miR-132 transgenic mice using the noted open field assay (Fig. 4.6E). We found significant genotype-dependent differences in the total time spent in the center of the field, (Fig. 4.6F; $F_{(2,33)} = 4.337$, $p = 0.0218$; one-way ANOVA). Specifically, miR-132 transgenic animals spent less time in the center of the field compared to WT mice (Fig. 4.6F; $t_{(20)} = 2.616$ $p = 0.0498$; Bonferroni post-hoc test),

whereas mean time spent in the center by miR-132/212 cKO mice did not significantly differ from WT mice (Fig. 4.6F; $t_{(23)} = 1.676$ $p = 0.322$; Bonferroni post-hoc test). Further, the number of crossings into the center of the open field arena also varied by genotype (Fig. 4.6G; $F_{(2,33)} = 10.038$, $p < 0.0001$; one-way ANOVA). miR-132 transgenic animals crossed into the center of the arena fewer times than WT animals (Fig. 4.6F; $t_{(21)} = 4.103$ $p = 0.0015$; Bonferroni post-hoc test), while the number of center crosses for miR-132/212 cKO mice did not significantly differ from WT animals (Fig. 4.6G; $t_{(24)} = 0.066$; Bonferroni post-hoc test). Finally, a main effect of genotype on the overall immobility of animals in the open field test was observed (Fig. 4.6H; $F_{(2, 33)} = 4.043$, $p = 0.0269$; one-way ANOVA). The total time spent freezing was significantly higher in miR-132 transgenic animals compared to WT animals (Fig. 4.6H; $t_{(20)} = 3.016$, $p = 0.0198$; Bonferroni post-hoc test). The total immobility time was not significantly different between WT and miR-132/212 cKO mice (Fig. 4.6H; $t_{(24)} = 1.54$ $p = 0.4110$). Together, the elevated plus maze and open field assay data indicate that the dysregulation of miR-132/212 led to anxiety-like behaviors.

Doxycycline mitigates the anxiety phenotype in miR-132 transgenic mice

To further test the relationship between miR-132 and anxiety-like behaviors, we examined whether the anxiety phenotype in miR-132 transgenic animals could be suppressed via doxycycline administration. To this end, naïve miR-132 transgenic mice and WT mice (mice that were negative for either the driver and/or responder genes) were maintained on drinking water containing 0.4 μg/mL doxycycline for three weeks and then tested using the elevated plus maze (Fig. 4.7A). Of note, our prior work has shown that

treatment with 0.4 μg/mL of doxycycline reduces transgenic miR-132 over-expression to physiological levels (Hansen et al., 2013). Remarkably, we found that doxycycline mitigated the anxiety phenotype of miR-132 transgenic mice. Thus, no significant difference in the number of open arm transitions was observed between WT and miR-132 transgenic mice (Fig. 4.7B $t_{(30)} = 0.3511$, $p = 0.7280$; Student's t-test). Further, the amount of time spent in the open arms and the latency to an open arm of the maze did not differ between WT and miR-132 transgenic mice (Fig. 4.7C $t_{(30)} = 0.2203$, $p = 0.8271$ and Fig. 4.7D $t_{(30)} = 0.5122$, $p = 0.6122$; Student's tests). Similarly, in the open field test, we found that the anxiety phenotype was absent in the miR-132 transgenic mice upon administration of 0.40 μg/mL of doxycycline (Fig. 4.7E). No significant difference in the time spent in the center, the number of crosses, or the total seconds immobile was observed between WT and miR-132 transgenic mice (Fig. 4.7F $t_{(33)} = 1.131$, $p = 0.2661$ for center time; Fig. 4.7G $t_{(35)} = 1.049$, $p = 0.30313$ for center crosses and Fig. 4.7H $t_{(33)} = 0.3999$, $p = 0.6918$ for immobility time Student's t-test). Further, an analysis of elevated plus maze performance and open field activity between WT mice (Fig. 4.6) and WT mice maintained on doxycycline (Fig. 4.7) did not detect significant differences in any of the reported measures (data comparison not shown). Altogether, these data support the link between miR-132 and the induction of anxiety-like behavior.

Here, we note that both male and female WT, miR-132/212 cKO, and miR-132 transgenic animals were used in the above behavioral experiments. Hence, the results presented above (from Figs. Figs.4.6-4.7) include both male and female pooled data sets. Given that sex differences in rodent anxiety paradigms have been reported (for review,

see (Donner and Lowry, 2013; Kokras and Dalla, 2014), the noted data sets were also analyzed as separate female and male cohorts (see Fig. 4.8). In both the elevated plus maze experiments and in the open field experiments (both no-doxycycline and doxycycline conditions), we found no significant interaction between genotype and sex in any reported measure (Fig. 4.8A-4.8F; 4.8I-4.8J and 4.8L; $p > 0.05$; two-way ANOVA). However, in the no-doxycycline open field experiment, we did observe a significant effect of sex in the total duration spent in the center and in the number of center crosses (Fig. 4.8G $F_{(1,\ 29)} = 8.652$; $p = 0.0064$ for center duration and Fig. 4.8H $F_{(1,30)} = 8.703$; $p = 0.0061$ for center crosses). Additionally, in the doxycycline open field experiment, we noted an effect of sex in the number of center crosses (Fig. 4.8K $F_{(1,\ 33)} = 6.163$; $p = 0.0183$). Further, paralleling our pooled results, in each parameter measured (in both the no-doxycycline elevated plus and open field experiments), we did find a significant effect of genotype (Fig. 4.8A-4.8C; 4.8G-4.8I; $p < 0.05$ for each parameter tested; two-way ANOVA). This genotypic effect was not observed in animals treated with doxycycline (Fig. 4.8D-4.8F; 4.8J-4.8L; $p > 0.05$ for each parameter tested; two-way ANOVA).

Altered expression of miR-132 target genes in miR-132/212 cKO and miR-132 transgenic mice

Given the significant alterations in baseline anxiety in miR-132 transgenic mice, and that miRNAs repress the translation of mRNA targets, we examined the expression of Sirt1 and Pten—two miR-132/ 212 targets that are expressed within the hippocampus and amygdala (Lachyankar et al., 2000; Ramadori et al., 2008; Zakhary et

al., 2010) and that influence synaptic plasticity and anxiety (Gao et al., 2010; Kwon et al., 2006; Libert et al., 2011; Lugo et al., 2014; Michán et al., 2010).

Marked Sirt1 immunohistochemical (IHC) labeling was observed throughout the hippocampus and amygdala of WT mice (Fig. 4.9A). Interestingly, quantitative densitometric analysis of the IHC labeling revealed a significant effect of genotype on the expression of Sirt1 (Fig. 4.9B $F_{(2, 35)} = 5.247$, $p = 0.0043$; two-way ANOVA). Specifically, Sirt1 expression was significantly higher in the GCL of WT mice compared to miR-132 transgenic mice (Fig. 4.9B $t_{(7)} = 2.827$, $p = 0.023$; Bonferroni post-hoc test), and in the GCL of miR-132/212 cKO mice compared to miR-132 transgenic mice (Fig. 4.9B $t_{(8)} = 3.785$, $p = 0.0017$; Bonferroni post-hoc test). Additionally, expression of Sirt1 in the amygdala of miR-132/212 cKO mice was significantly higher relative to expression in miR-132 transgenic mice (Fig. 4.9B $t_{(8)} = 3.325$, $p = 0.0062$; Bonferroni post-hoc test). Sirt1 expression within the CA1 and lateral amygdala showed a trending increase in miR-132/212 cKO mice relative to miR-132 transgenic mice, though significance was not reached after Bonferroni correction (Fig. 4.9B $t_{(8)} = 2.465$, $p = 0.0563$ for hippocampus and Fig. 4.9B $t_{(8)} = 2.401$, $p = 0.0654$ for lateral amygdala). Notably, we also show that Sirt1 levels were increased in miR-132/212 cKO mice compared to WT mice, and that miR-132 transgenic mice on doxycycline showed increased Sirt1 expression relative to those not on dox (Fig. 4.11A-4.11B).

Turning to Pten (Fig. 4.10), we found a significant effect of genotype on the expression of Pten within the forebrain (Fig. 4.10B $F_{(2, 40)} = 11.66$, $p = 0.0001$; two-way ANOVA). In particular, Pten expression within the CA1 was significantly lower in miR-

132 transgenic mice relative to miR-132/212 cKO mice (Fig. 4.10B $t_{(8)} = 3.318$, $p = 0.0058$; Bonferroni post-hoc test). Further, in the CA3 and GCL subregions of the hippocampus, a trend was observed, wherein Pten expression was higher in miR-132/212 cKO animals relative to miR-132 transgenic animals, though significance was not reached (Fig. 4.10B $t_{(8)} = 2.448$, $p = 0.0566$ for GCL and $t_{(8)} = 2.37$, $p = 0.0681$ for CA3; Bonferroni post-hoc tests). Additionally, a trending increase in PTEN expression was also noted in the GCL of miR-132/212 cKO animals relative to WT animals, though the data did not pass Bonferroni correction (Fig. 4.10B $t_{(9)} = 2.23$, $p = 0.0944$). Further, we also show that Pten levels were increased in miR-132/212 cKO animals, and that miR-132 transgenic mice on dox showed increased Pten expression relative to those not on dox (Fig. 4.11C-4.11D).

Discussion

The over-arching goal of this project was to elucidate the role of the miR-132/212 locus in the regulation of stress responsiveness and anxiety. Here, we demonstrate that both miR-132 and miR-212 are induced in two stress-responsive regions—the hippocampus and amygdala—after an acute stress paradigm and in the amygdala after a chronic stress paradigm. Further, we show that dysregulation of forebrain miR-132/212 expression alters baseline anxiety levels. Taken together, these data suggest that the miR-132/212 locus modulates stress- and anxiety-like behavior.

Induction of the miR-132/212 locus after acute and chronic stress

With respect to the multimodal stress results, to our knowledge, this is the first study to show induction of miR-132 after an acute stress paradigm. The rather rapid (less

than 6 h after stress onset) induction of miR-132 is not surprising given its highly inducible nature and classification as an early response miRNA (Lagos et al., 2010). Along these lines, WIbrane et al noted an upregulation of both mature miR-132 and miR-212 just 2 h after the onset of LTP within the dentate gyrus of rats (Wibrand et al., 2010). Similarly, increased miR-212 expression has yet to be reported after an acute stressor, though its induction is not unexpected given that it is expressed from the same primary transcript as miR-132 (Vo et al., 2005).

Interestingly, our findings that the miR-132/212 locus is induced in the hippocampus and amygdala following acute stress and only in the amygdala following chronic stress—mirror the biphasic effects that are observed in many stress-related disorders. Indeed, acute stress often enhances synaptic transmission in forebrain regions, leading to increases in dendritic spine density within the hippocampus (Komatsuzaki et al., 2012; Shors et al., 2001), while repeated or chronic stress often reduces transmission and promotes dendritic retraction in the hippocampus (Magariños et al., 1996; Vyas et al., 2002; Watanabe et al., 1992), but not in the amygdala (Musazzi et al., 2015; Rosenkranz et al., 2010).

In line with the idea that acute stress facilitates synaptic transmission, the transgenic upregulation of miR-132 in hippocampal neurons increases dendritic spine density (Hansen et al., 2010) and enhances dendritic morphogenesis (Wayman et al., 2008). Given our observed induction of miR-132/212 within the hippocampus after acute stress, but not after chronic stress, it would be interesting to examine whether increases in dendritic spine density after acute stress are miR-132/212 dependent, and whether

decreases in spine density after chronic stress are miR-132/212 independent. Consistent with the latter idea, Yi et al reported a marked downregulation in miR-132 expression within the hippocampus following a chronic unpredictable stress paradigm (Yi et al., 2014), coinciding with the atrophy of dendrites and loss of synapses that is often observed during chronic stress paradigms as part of the biphasic action of stress (Musazzi et al., 2015).

Turning to the amygdala, both acute and chronic stress lead to increases in basolateral amygdalar neuron dendritic length/arborization (Cui et al., 2008; Hill et al., 2011; Kim et al., 2014; Mitra et al., 2005; Vyas et al., 2002). These neurons are also more hyperactive (Correll et al., 2005; Padival et al., 2013; Rosenkranz et al., 2010; Zhang and Rosenkranz, 2012) and have a greater number of NMDA receptors compared to non-stressed, control animals (Lei and Tejani-Butt, 2010). Consistent with this, imaging studies have shown that the amygdala and insula are hyperactive in patients with social anxiety and specific phobia disorder (Etkin, 2012; Etkin and Wager, 2007), and in patients who are ‘anxiety-prone’(Stein et al., 2007). Given that bouts of both brief and prolonged stress increase the dendritic complexity of amygdalar neurons, and that we found miR-132/212 to be induced after both acute and chronic stress paradigms, one may postulate that miR-132 and miR-212 could be contributing to the observed increased physiological drive of amygdalar neurons after both transient and long-lasting stress. Hence, future studies aimed at examining if and how the miR-132/212 locus is involved in the molecular network that leads to changes in dendritic morphology and synaptic activity within the amygdala after stress, are highly merited.

Bidirectional miR-132 dysregulation increases anxiety-related behaviors

Our data showing an upregulation of the miR-132/212 locus after stress prompted us to turn to the question of whether this locus contributes to anxiety-like behavior. Interestingly, we found that miR-132 transgenic mice displayed a heightened anxiety phenotype in both the elevated plus maze and open field paradigms. To our surprise, miR-132/212 cKO mice also exhibited anxiety behaviors, albeit to a lesser degree than the miR-132 transgenic animals. Of note, this phenotype in the miR-132/212 cKO animals is in line with a prior study, which showed that miR-132/212 germline knockout mice spent slightly more time freezing in the open field test and less time in the open arms of the elevated plus maze, though significance was not reached (Hernandez-Rapp et al., 2015). On the surface, the observation that both miR-132/ 212 gain- and loss-of-function facilitate anxiety-like behaviors could be viewed as counter-intuitive. However, it should be noted that prior work from our lab has revealed that both miR-132 over-expressing mice and miR-132/212 cKO mice display cognitive deficits in several learning and memory paradigms (Hansen et al., 2016, 2013, 2010). Thus, in many respects, the anxiety phenotype that we observed after both knocking out and over-expressing miR-132, parallels the noted cognitive effects. Hence, these results suggest that tight regulation of miR-132 (and perhaps miR-212) is also necessary for maintenance of 'normal' basal anxiety levels. Consistent with this hypothesis, by titering transgenic miR-132 expression to physiological levels, we found that the anxiety phenotype was abolished in miR-132 transgenic animals. Further, given that the miR-132/212 locus is tightly regulated by the CREB/CRE transcriptional pathway (Vo et al., 2005), it is

interesting to note that there also appears to be an optimal range of CREB activity that is required for the maintenance of 'normal' anxiety, as both knockdown and over-expression of CREB has been show to increase anxiogenic behaviors (Valverde et al., 2004; Vogt et al., 2014; Wallace et al., 2004).

The idea that there exists an optimal range of miR-132 (and perhaps miR-212) expression, below or above which anxiety-related behaviors are increased, is in line with several studies related to the role of forebrain excitatory/inhibitory (E/I) balance. Intriguingly, many groups have posited that anxiety disorders emerge and/or are potentiated by the dysregulation of E/I balance within the molecular network that comprises the limbic system (Ferraguti, 2018; Nuss, 2015; Tovote et al., 2015). In support of this idea, synaptic transmission is reduced in the hippocampus and cortex of miR-132/212 knockout animals (Luikart et al., 2011; Remenyi et al., 2013), while mEPSC amplitude and frequency are increased and synaptic depression is decreased after miR-132 over-expression (Edbauer et al., 2010; Lambert et al., 2010). Whether miR-132/212 regulates E/I balance in limbic brain regions remains an intriguing avenue for future study.

Here it should be noted that in the CNS, miR-132 is expressed at a much higher level than miR-212 (Remenyi et al., 2016); our unpublished data). This observation combined with the fact that miR-132 and miR-212 share a common seed sequences (and thus, are predicted to have a good degree of functional redundancy), led us to focus our transgenic over-expression approach solely on miR-132. The combination of findings showing that 1) transgenic miR-132 elicits anxiety-like behavior, and 2) that this

phenotype is reversed with doxycycline treatment provides solid support for the idea that elevated levels of miR-132 (and possibly miR-212) couple stress to the manifestation of anxiety-like behavior. Here, one caveat regarding the transgenic miR-132 mouse line should be noted: tonically high levels of transgenic miR-132 are expressed via the CaMKII-tTA driver through late stage development and into maturity. As such, there may be long-term compensatory processes that could contribute to the anxiety-like phenotype. Approaches in which transient induction of transgenic miR-132 expression is initiated (via withdrawal of doxycycline from the drinking water after maturation) would be needed to obviate these issues. Similarly, deletion of the miR-132 locus (via the same CaMKII promotor construct), could also result in compensatory processes; additional experiments that employ inducible gene deletion approaches in mature animals (e.g., via the use of a tamoxifen-inducible CRE) would provide an excellent, further, test of the data reported here.

Altered expression of miR-132/212 target genes

The anxiety-like phenotype of miR-132 transgenic and miR-132/ 212 cKO mice reported here likely results from alterations in the expression patterns of both direct and indirect targets of miR-132/212. Notably, prior gene profiling methods have found that the deletion or over-expression of miR-132/212 leads to changes in the expression of hundreds of genes (Hansen et al., 2016; Mazziotti et al., 2017). Given the complexity of the miR-132/212-gated transcriptome, we chose to examine the expression levels of two miR-132/212 targets that have been shown to affect anxiety-like behavior: Sirt1 and Pten. Sirt1 is a NAD-deacetylase that has been characterized as a direct target of miR-132

(Gong et al., 2016; Miyazaki et al., 2014; Strum et al., 2009; Zhang et al., 2014). Though not yet validated, Sirt1 and miR-212 also show strong hybridization capacity (microRNA.org). Of relevance to this study, Sirt1 has been shown to mediate anxiety behavior and exploratory drive (Libert et al., 2011). Indeed, knocking down or over-expressing Sirt1 leads to anxiogenic behaviors (Kim et al., 2016; Libert et al., 2011). Though miR-132-mediated actuation of anxiety-like behavior likely involves multiple gene targets, it is interesting to note that Sirt1 expression was reduced in the hippocampus and amygdala of miR-132 transgenic mice. Further, consistent with data obtained from our chronic stress qPCR results (Fig. 4.3B-4.3C), Sirt1 protein was decreased in the amygdala of chronically stressed WT mice, whereas it remained unchanged within the hippocampus. Taken together, these data raise the prospect that miR-132 regulation of Sirt1 may play a role in stress-induced anxiety.

We next examined the expression of Pten, a key regulator of the PI3K/AKT/mTOR signaling pathway. With respect to its post-transcriptional regulation, Pten has been validated as a target of miR-132 by multiple groups (Hanin et al., 2018; Wong et al., 2013; Zhang et al., 2019). Additionally, miR-212 and Pten also show a robust predicted hybridization capacity (microRNA.org). Our interest in Pten was heightened by data showing that Pten conditional knockout mice display social deficits and anxiety-like behavior (Kwon et al., 2006; Zhou et al., 2009) and that knockdown of Pten also decreases amygdalar spine density and increases mEPSC frequency and amplitude (Haws et al., 2014), suggestive of a role for its regulation of synaptic activity in limbic regions. Intriguingly, our immunohistochemical data revealed a decrease in

Pten in the CA1 of miR-132 transgenic animals. Given these results, a deeper understanding of the cellular signaling events that regulate Pten expression at baseline and after stress, may be of merit.

Finally, we should reiterate that while altered expression of either Sirt1 or Pten could significantly affect molecular/cellular signaling pathways that modulate anxiety states, we are not attributing the anxiety phenotype of the miR-132/212 cKO or miR-132 transgenic mice to the singular dysregulation of either target gene. However, in line with the idea of miRNA-target signaling regulation, the results that we present here suggest that dysregulation of the miR-132/212 locus leads to profound changes in gene expression that underlie stress and anxiety behavior.

Conclusions

Our data reveal a novel role for the miR-132/212 locus in the regulation of stress response and anxiety. Given that dysregulation of this locus is associated with a number of neurological diseases (see(Wanet et al., 2012) for review), these findings raise compelling questions about the molecular underpinnings of miR-132/212 signaling and the importance of this locus in the etiology and regulation of other psychiatric and mood related disorders. Indeed, new genome editing technologies, novel small-molecule delivery techniques, and recent advances in exosomal non-coding RNA, may be utilized to characterize miRNAs as both biomarkers and/or therapeutic targets for several psychiatric conditions. To this end, additional work investigating the miR-132/212 locus and its molecular interactions in other psychopathologies is highly merited.

Acknowledgements

The authors thank Dr. Kate Karelina for her input on experimental design.

Figure 4.1 miR-132 and miR-212 are upregulated in the hippocampus and amygdala after acute multimodal stress

(A) Acute multimodal stress experimental design: WT animals were subjected to 5 h of acute multimodal stress, wherein mice were placed in restraint tubes which rocked on a laboratory shaker for 5 h. Loud music was also played in the room. After the paradigm, animals were then used for tissue isolation, open field testing, or immunohistochemistry. (B) RT-qPCR for miR-132 was performed on RNA samples isolated from the hippocampus (B) and amygdala (C) of control and acutely stressed mice. Similarly, hippocampal miR-212 (D) and amygdalar miR-212 (E) expression was probed via RT-qPCR. miR-132 and miR-212 expression in control animals was set equal to a value of one, and miR-132 and miR-212 expression in stressed mice was normalized to this value. Significance was examined with Student's t-test for each brain region, and data are presented as the mean ± SEM. *: $p < 0.05$; **: $p < 0.01$; ***: $p < 0.001$. N = 9–10 mice per group.

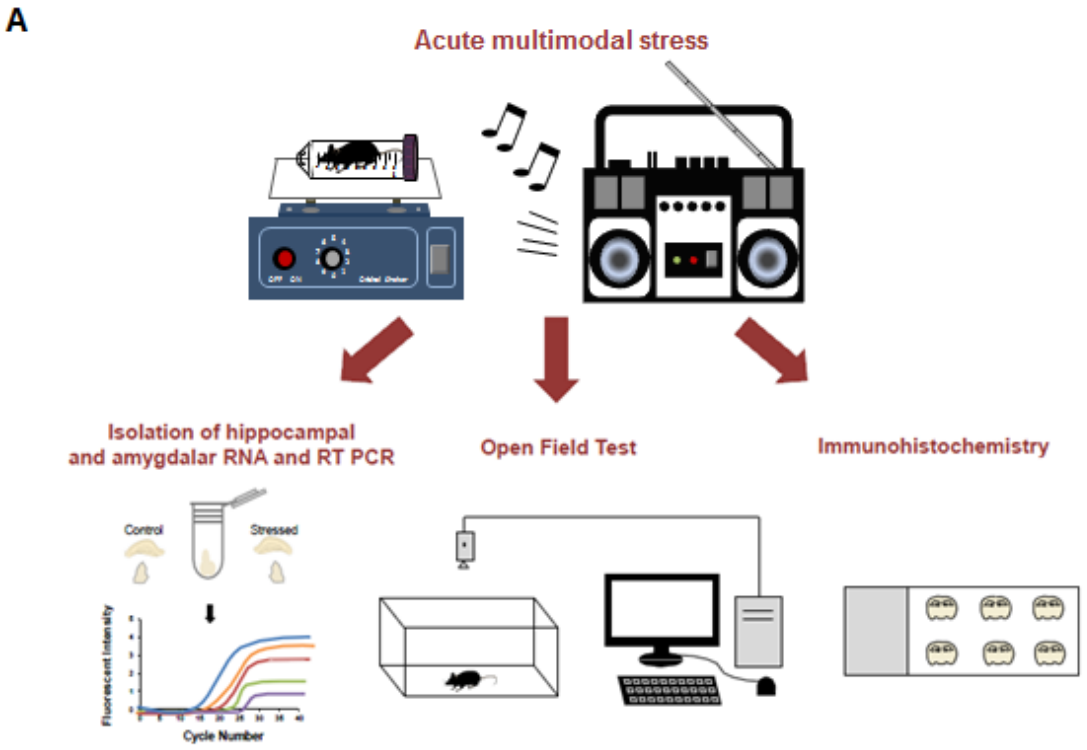
A
Acute multimodal stress
Isolation of hippocampal and amygdalar RNA and RT PCR
Open Field Test
Immunohistochemistry
Control
Stressed
Fluorescent Intensity
Cycle Number

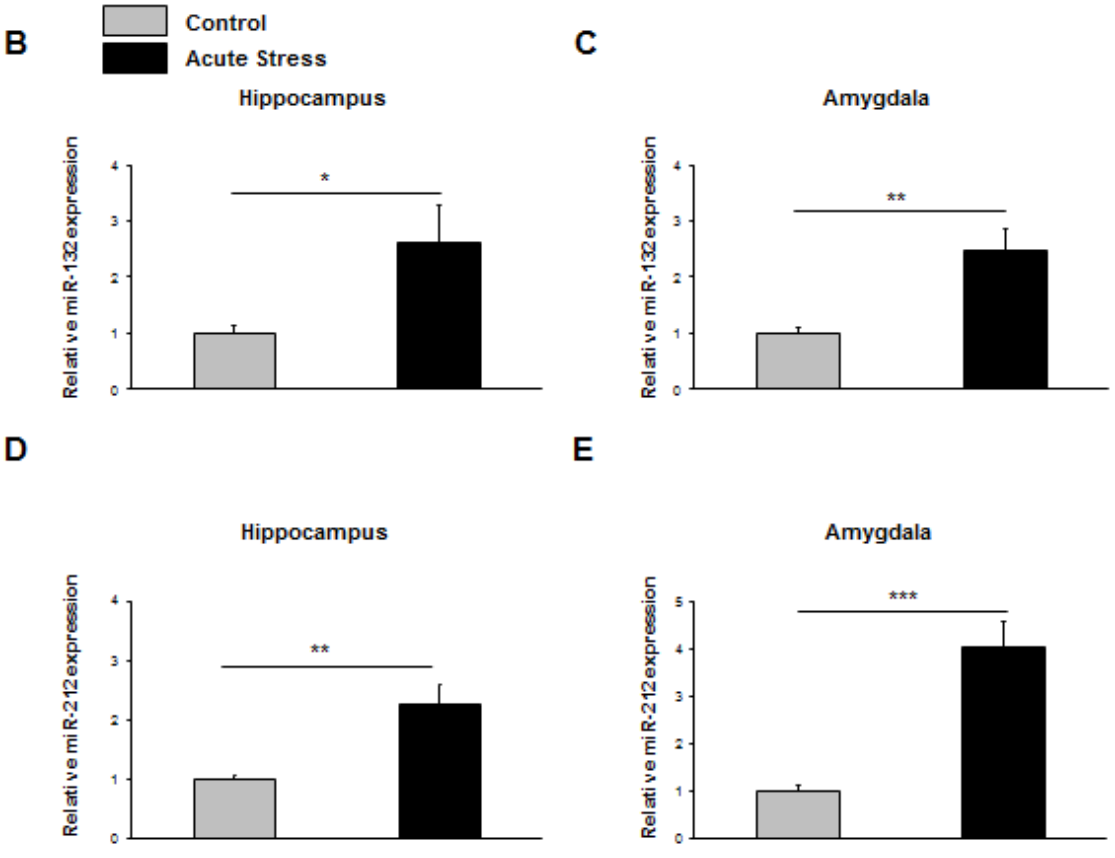
B
Control
Acute Stress
Hippocampus
Relative miR-132 expression
*
C
Amygdala
**
D
Hippocampus
Relative miR-212 expression
**
E
Amygdala
***

Figure 4.2 Effects of acute multimodal stress paradigm
(A) Representative open field test locomotor traces and heat maps from control mice and mice subjected to the acute stress paradigm. Compared to non-stressed control animals, in the open field test, stressed mice exhibited an increase in the average number of rears (B), the average distance traveled (C), and the average velocity (D). Data were analyzed by Student's t-tests and are presented as the mean $\pm$ SEM. * $p < 0.05$; n = 5-6 mice per group. (E) cFOS immunohistochemical labeling in the paraventricular nucleus (PVN), bed nucleus of the stria terminalis (BNST), medial septum (MS), lateral amygdala, and dorsal CA1 of the hippocampus of control and stressed animals. (F) The total number of cFOS positive cells was increased in stressed mice compared to control mice. Scale bar = 100 μm for 10X images (PVN and CA1) and 50 μm for 6X images (BNST, medial septum, and central amygdala). Data were analyzed by two-way ANOVA and are presented as the mean $\pm$ SEM. **: $p < 0.01$; ***: $p < 0.001$; ****: $p < 0.0001$; n.s.: not significant ($p > 0.05$). N = 3-5 mice per group. Abbreviations: 3V-Third ventricle; LV-lateral ventricle; cc-corpus callosum; LS-lateral septum; MS-medial septum; ac-anterior commissure; CeA-central amygdala; LA-lateral amygdala; BLA-basolateral amygdala; sr-stratum radiatum; so-stratum oriens.

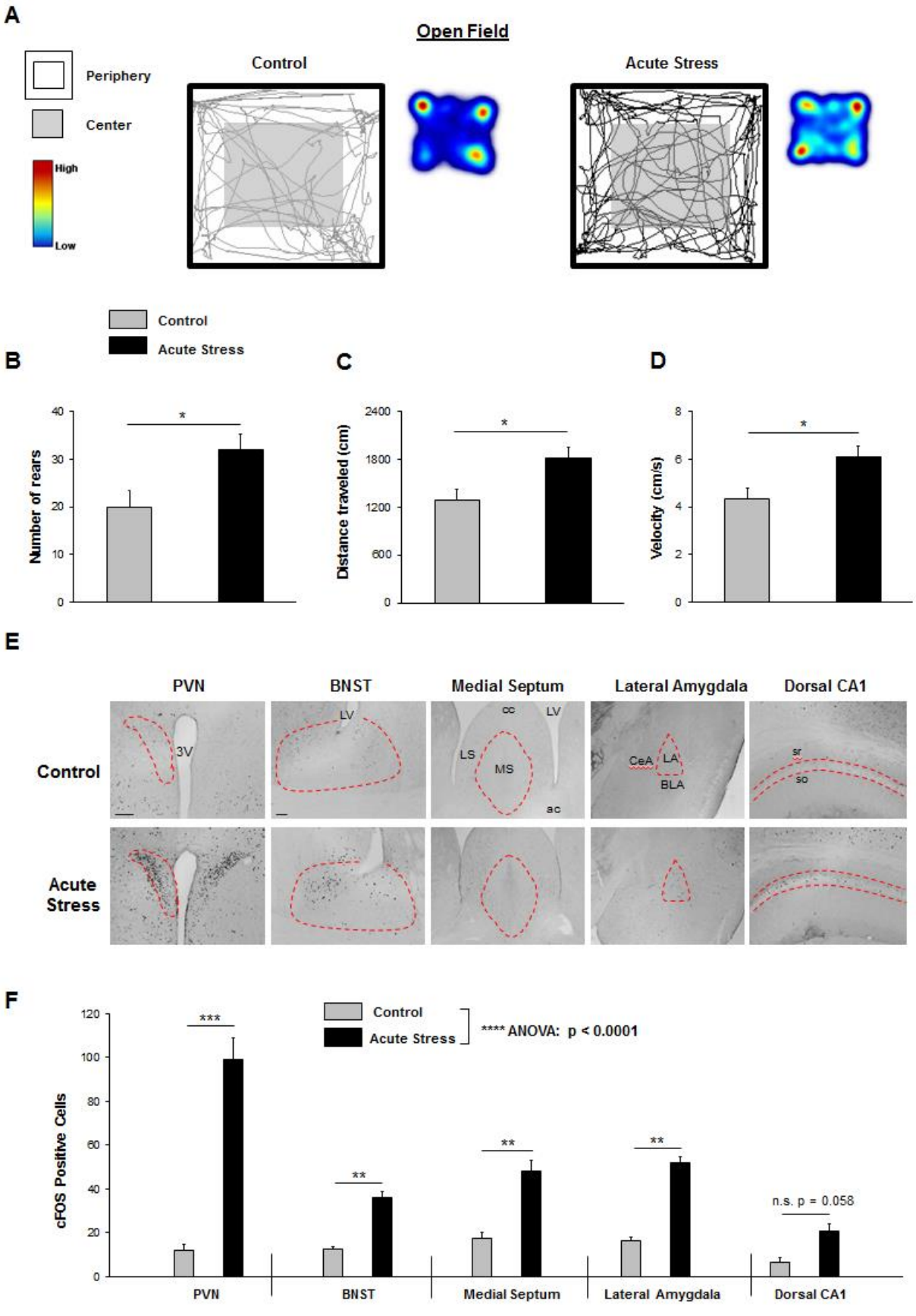
A
Open Field
Periphery
Center
High
Low
Control
Acute Stress
Control
Acute Stress
B
Number of rears
C
Distance traveled (cm)
D
Velocity (cm/s)
E
PVN
BNST
Medial Septum
Lateral Amygdala
Dorsal CA1
Control
Acute Stress
3V
LV
cc
LV
LS
MS
ac
CeA
LA
BLA
sr
so
F
Control
Acute Stress
**** ANOVA: p < 0.0001
cFOS Positive Cells
n.s. p = 0.058
PVN
BNST
Medial Septum
Lateral Amygdala
Dorsal CA1

Figure 4.3 miR-132 and miR-212 are upregulated in the hippocampus and amygdala after chronic stress

(A) Chronic restraint stress experimental design: WT animals were subjected to 2 h of restraint each day, throughout the 15 day paradigm. On day 16, RNA was isolated from both chronically stressed and control mice and hippocampal (B) and amygdalar (C) miR-132 expression was examined using RT-qPCR. Similarly, hippocampal (D) and amygdalar miR-212 (E) expression was probed via RT-qPCR. miR-132 and miR-212 expression in control animals was set equal to a value of one, and miR-132 and miR-212 expression in stressed mice was normalized to this value. Significance was examined with Student's t-test for each brain region, and data are presented as the mean ± SEM. *: $p < 0.05$; **: $p < 0.01$; n.s: not significant ($p > 0.05$). N = 9–10 mice per group.

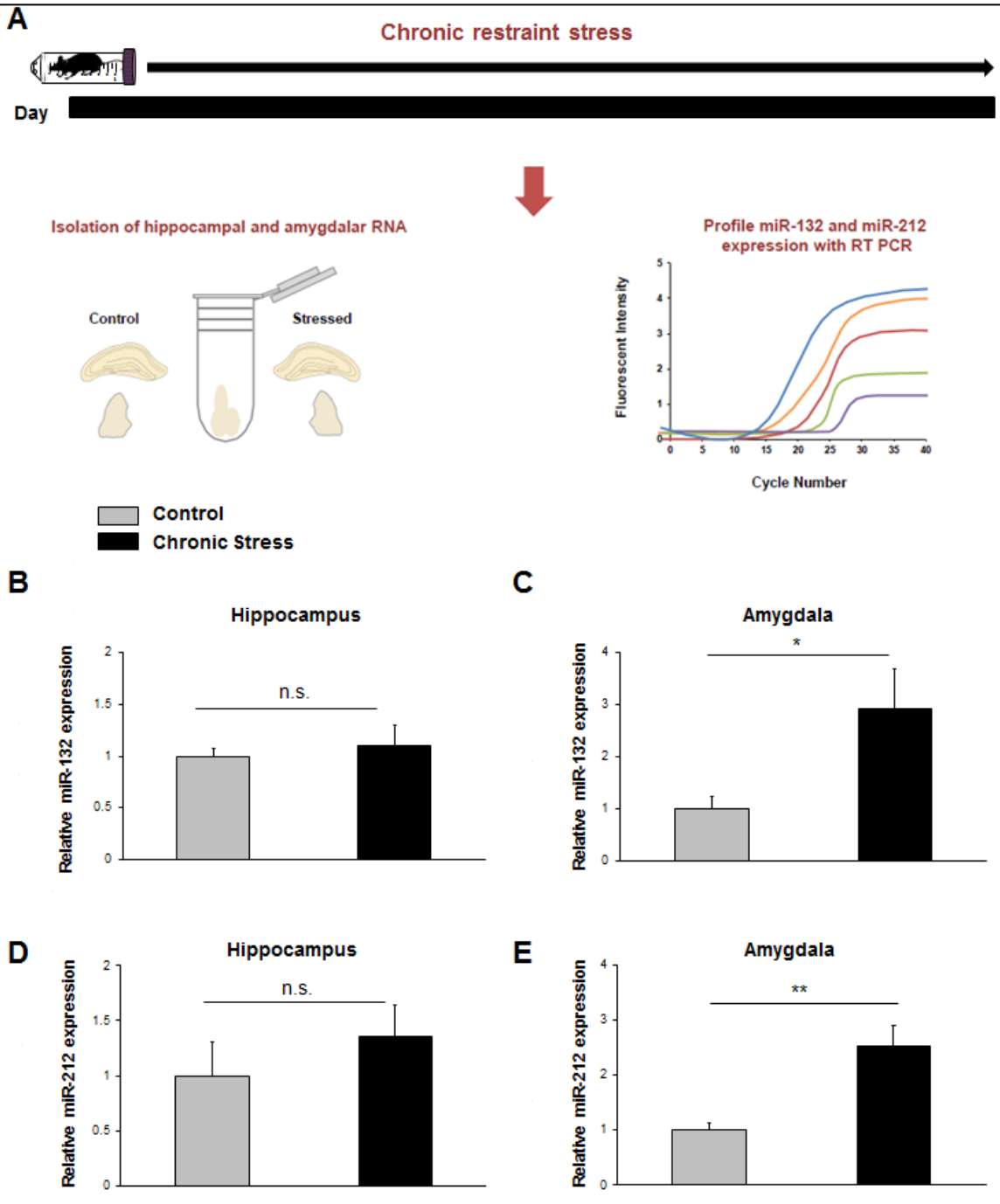

Figure 4.4 Effects of chronic restraint stress on body and organ weights
(A) Graphical representation of mean body weight in control and chronically stressed WT mice. Data were collected at 5 day intervals throughout the 15 day stress paradigm. Animals were weighed one final time on day 16—24 hours after the last restraint session. (B) Adrenal gland weight per one gram of body weight in control and stressed mice. Both right and left adrenal glands were weighed. (C) Thymus weight per one gram of body weight in control and stressed mice. (D) Spleen weight (both right and left) per one gram of body weight in control and stressed mice. Data were analyzed by Student's t-tests and are presented as the mean ± SEM. **: $p < 0.01$; ****: $p < 0.0001$; n.s.: not significant ($p > 0.05$). N = 8-9 mice per group.

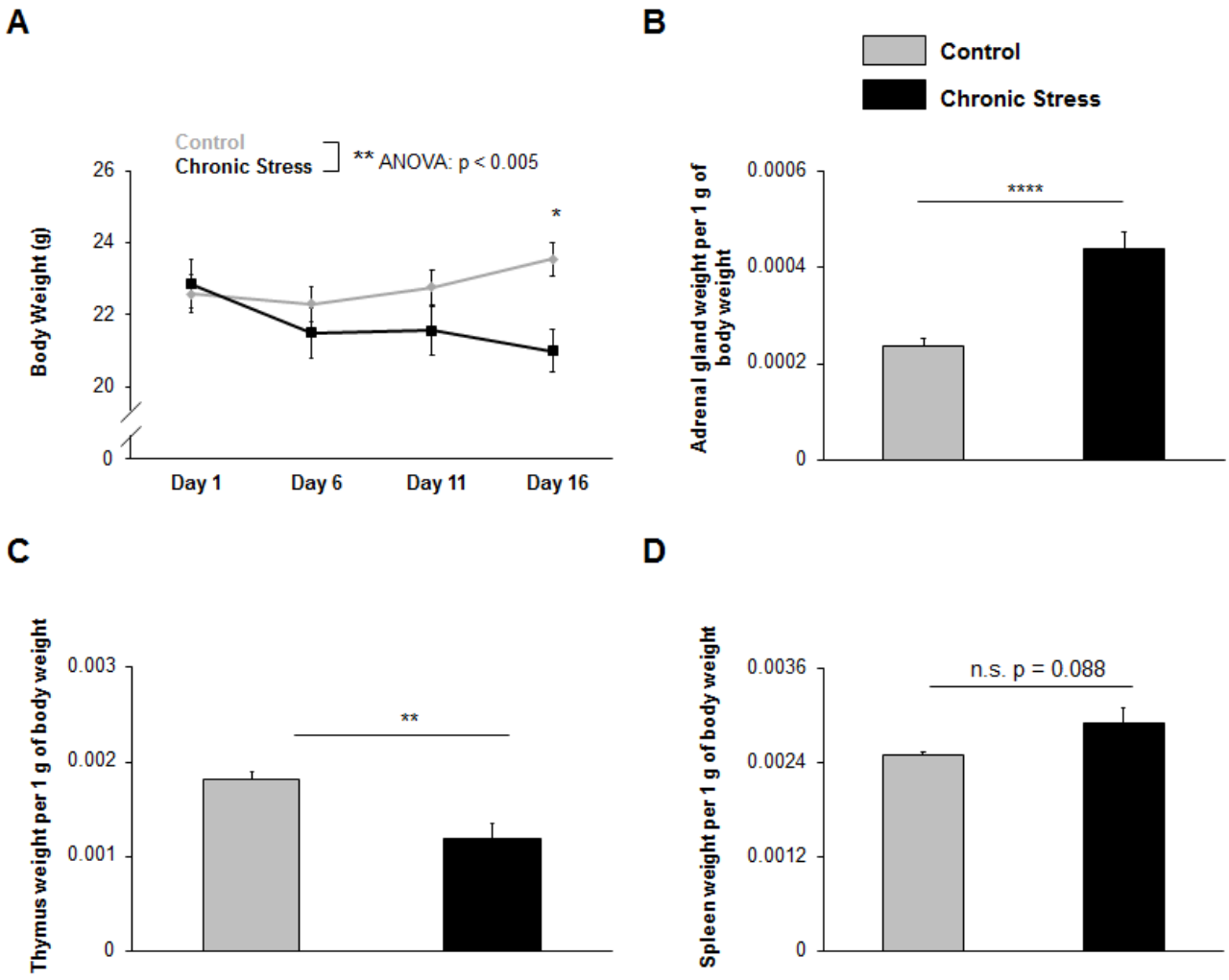

Figure 4.5 miR-132/212 conditional knockout and miR-132 transgenic mouse models
(A) Schematic depiction of the miR-132/212 conditional knockout mouse models (CaMKII-CremiR-132/212$^{f/f}$ (denoted as 'miR-132/212 cKO' in red lettering)). A Cre/lox strategy was used to delete the miR-132/212 locus from excitatory forebrain neurons in these animals. (B) Representation of the breeding strategy used to generate the CaMKII-tTA::miR-132:CamKII-Cre::miR-132/212$^{f/f}$ ('miR-132 Transgenic') mice, as depicted in green lettering. The miR-132/212$^{f/f}$ conditional knockout (cKO) line was crossed to a tetracycline-inducible transgenic miR-132 mouse line (denoted as 'miR-132 Over-expression' in black lettering). This tetracycline inducible ('Tet-off') transgenic mouse line was created by crossing a CaMKII-tTA driver mouse with a mouse expressing miR-132 under the control of the TRE promoter. Hence, crossing the miR-132/212 cKO line to the CaMKII-tTA::miR-132-CFP transgenic line, generated a quadruple transgenic mouse line: CaMKII-tTA::miR-132:CaMKII-CRE::miR-132/212$^{f/f}$ ('miR-132 Transgenic'). This animal allowed for selective deletion of endogenous miR-132 and the transgenic expression of miR-132 within the same population of excitatory neurons of the forebrain. The schematic was adapted from Aten et al. (2018a).

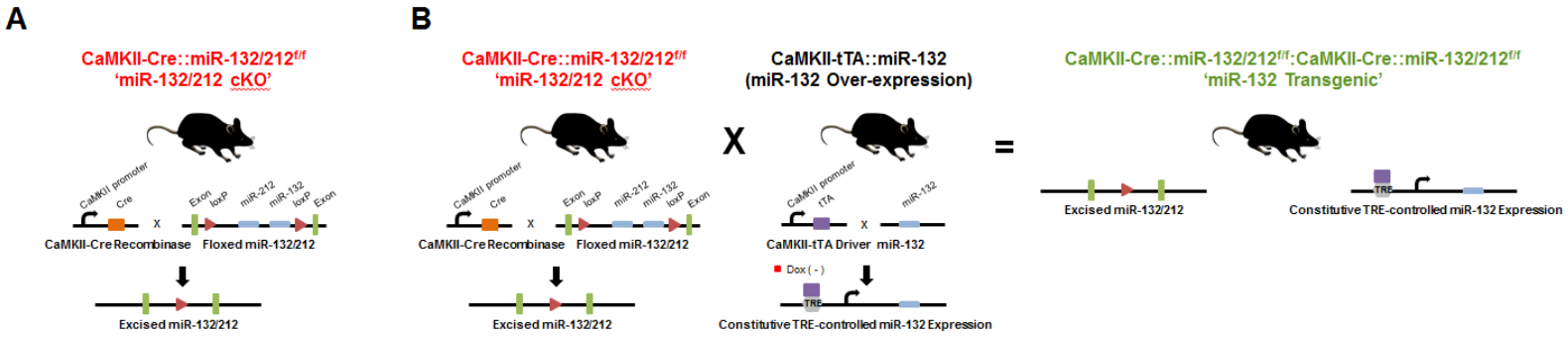

Figure 4.6 Profiling anxiety phenotype in miR-132/212 cKO and miR-132 transgenic animals with elevated plus maze and open field assay
(A) Representative elevated plus maze locomotor traces and heat maps from WT (blue), miR-132/212 cKO (red), and miR-132 transgenic animals (green). (B) miR-132/212 cKO and miR-132 transgenic animals exhibited significantly fewer open arm transitions in the elevated plus maze compared to WT mice. Mean time spent in open arms (C) and mean latency to open arms (D) were significantly different between WT and miR-132 transgenic animals. (E) Representative open field test locomotor traces and heat maps from WT, miR-132/212 cKO, and miR-132 transgenic animals. (F) Total duration in the center of the open field was significantly different between miR-132 transgenic and WT mice. (G) Number of crosses into the center was significantly reduced in miR-132 transgenic mice compared to WT mice. (H) Total immobility was significantly different between WT and miR-132 transgenic mice. Data were analyzed by one-way ANOVA with Bonferroni post-hoc tests. Data are presented as the mean ± SEM. *: $p < 0.05$; **: $p < 0.01$; n.s.: not significant ($p > 0.05$). N = 9–13 mice per group.

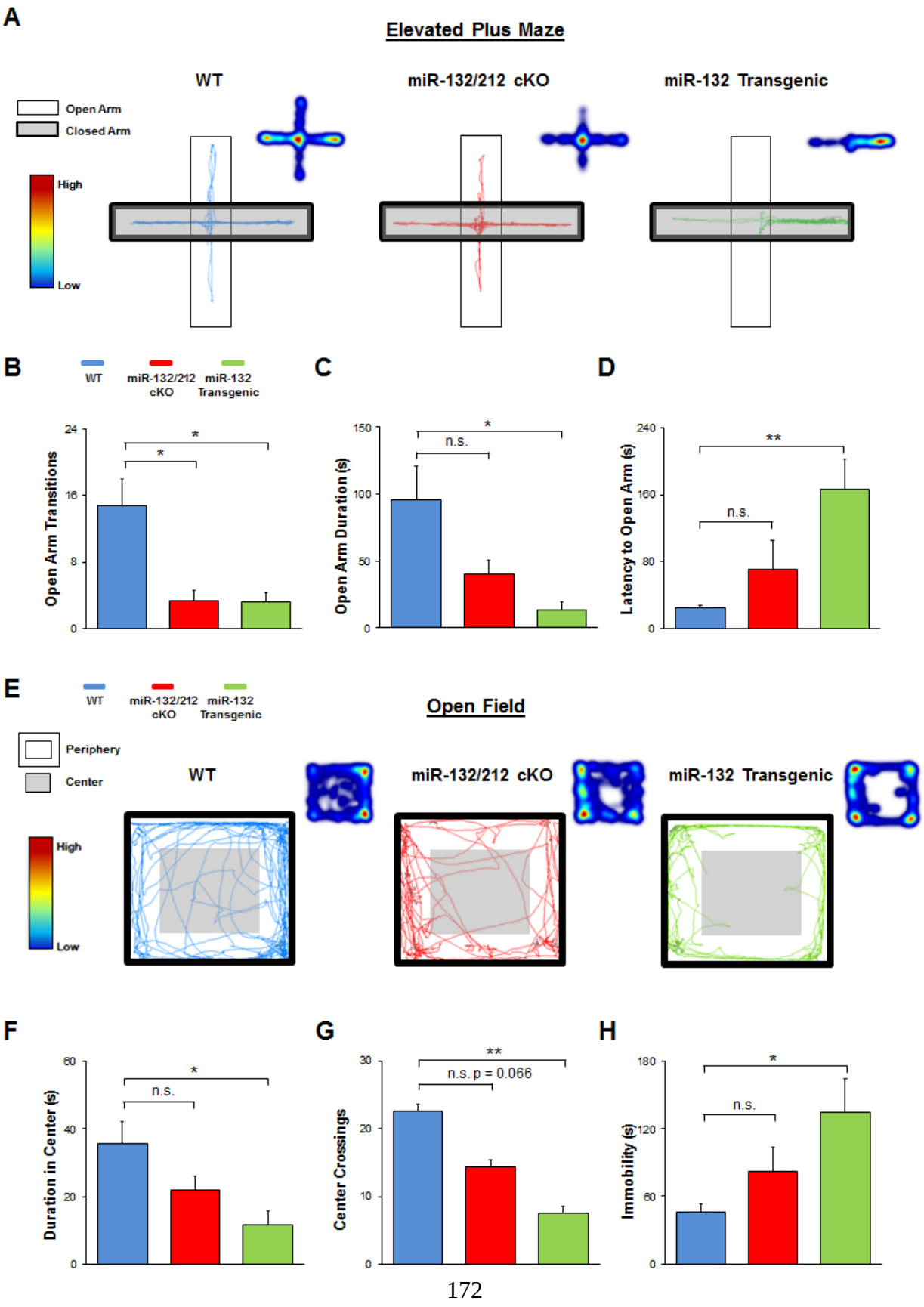
A
Elevated Plus Maze
WT
miR-132/212 cKO
miR-132 Transgenic
Open Arm
Closed Arm
High
Low
B
C
D
WT
miR-132/212 cKO
miR-132 Transgenic
Open Arm Transitions
Open Arm Duration (s)
Latency to Open Arm (s)
n.s.
E
Open Field
Periphery
Center
F
G
H
Duration in Center (s)
Center Crossings
Immobility (s)
n.s. p = 0.066

Figure 4.7 Profiling anxiety phenotype in miR-132 transgenic animals treated with doxycycline
(A) Representative elevated plus maze locomotor traces and heat maps from WT (blue) and miR-132 transgenic animals (green). Note that both WT and miR-132 transgenic animals were given a 0.4 μg doxycycline dose in their drinking water for three weeks prior to testing (and throughout the testing period). No differences in open arm transitions (B), open arm cumulative duration (C), or latency to open arm (D) were observed between WT and miR-132 transgenic animals in the elevated plus maze. (E) Representative open field locomotor traces and heat maps from WT and miR-132 transgenic animals. No significant differences in duration in the center of the arena (F), center crossings (G), or time spent immobile (H) were observed between WT and miR-132 transgenic animals in the open field test. Data were analyzed by Student's t-tests and are presented as the mean ± SEM. n.s.: not significant ($p > 0.05$). N = 15–20 mice per group.

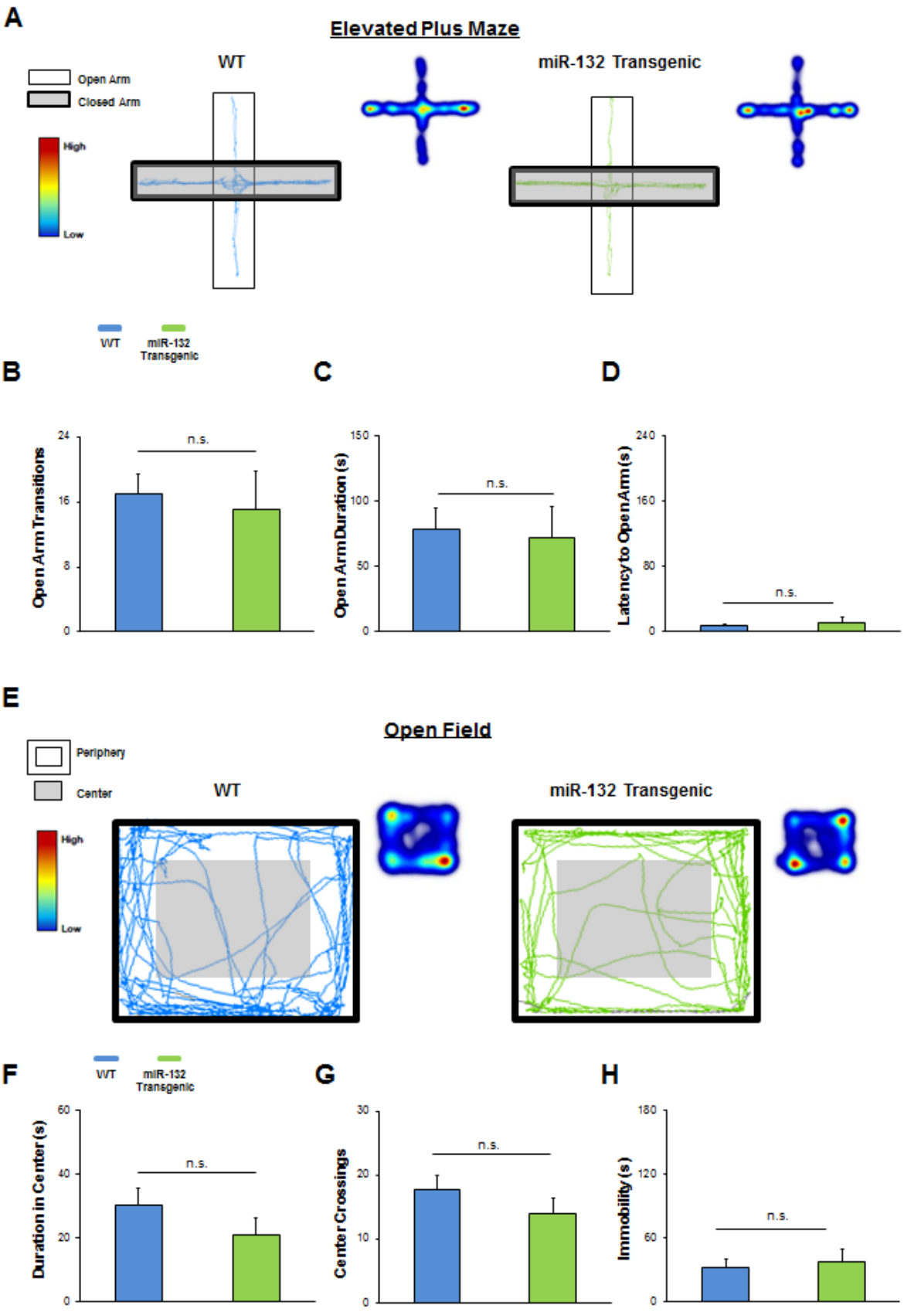
A
Elevated Plus Maze
WT
miR-132 Transgenic
Open Arm
Closed Arm
High
Low
WT
miR-132 Transgenic
B
C
D
Open Arm Transitions
24
16
8
0
n.s.
Open Arm Duration (s)
150
100
50
0
n.s.
Latency to Open Arm (s)
240
160
80
0
n.s.
E
Open Field
Periphery
Center
WT
miR-132 Transgenic
High
Low
F
G
H
WT
miR-132 Transgenic
Duration in Center (s)
60
40
20
0
n.s.
Center Crossings
30
20
10
0
n.s.
Immobility (s)
180
120
60
0
n.s.

Figure 4.8 Sex-parsed graphical representations of elevated plus maze and open field assay data in WT, miR-132/212 cKO, and miR-132 transgenic animals

Data displaying sex-delineated graphs of WT (blue), miR-132/212 cKO (red), and miR-132 transgenic animals (green) in the open field assay. Note that these data sets are reflective of the pooled data sets (combined male and female) presented in figures 3 and 4. Male and female gender symbols are located under each bar graph. In the elevated plus maze no-doxycycline experiment (top row), no significant effect of gender was found in the number of open arm transitions (A), total open arm duration (B), or latency to open arm (C). Similarly, in the doxycycline elevated plus experiment (second row from the top), no significant gender effect was observed in the number of open arm transitions (D), total open arm duration (E), or latency to open arm (F). In the no-doxycyline open field experiment (second row from the bottom), a significant effect of gender was observed in the total duration in the center of the field (G), and the number of center crosses (H). No effect on gender was observed on total immobility time (I). In the doxycyline open field experiment (bottom row), no significant gender effect was found in the center duration time (J). However, a significant effect of gender was noted in the number of center crosses (K). Finally, no effect of gender was observed in total immobility time (L). Note that the ANOVA genotype-gender interaction statistical significance parameters are not displayed on the graphs, as there were no significant interactions in any reported measure. Statistical significance parameters are only noted for the gender effects. Data were analyzed by two-way ANOVA and are presented as the mean $\pm$ SEM. *: $p < 0.05$; **: $p < 0.01$. N = 5-11 mice per group.

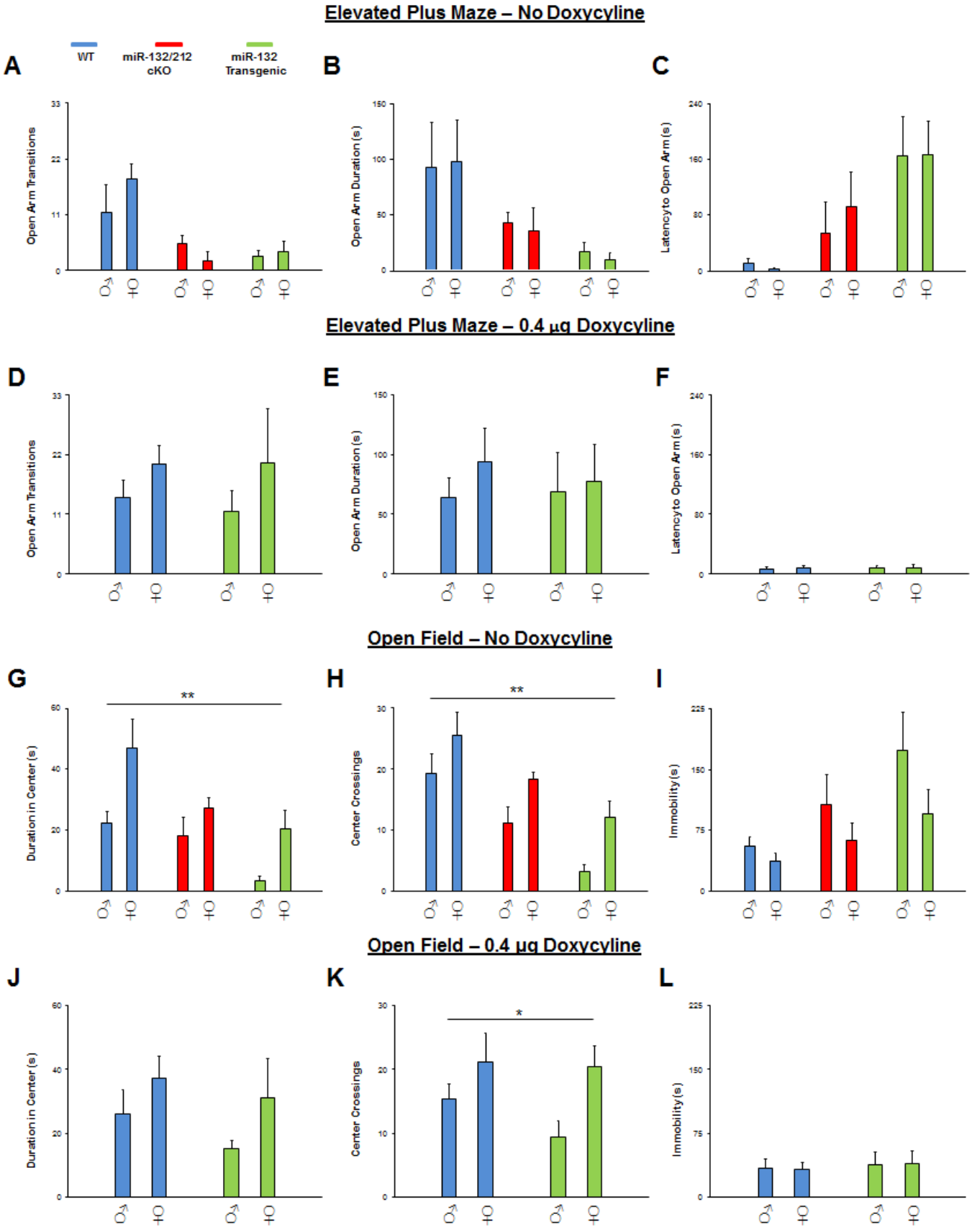
Elevated Plus Maze – No Doxycyline
WT
miR-132/212 cKO
miR-132 Transgenic
A
B
C
Open Arm Transitions
Open Arm Duration (s)
Latency to Open Arm (s)
Elevated Plus Maze – 0.4 µg Doxycyline
D
E
F
Open Field – No Doxycyline
G
H
I
**
**
Duration in Center (s)
Center Crossings
Immobility (s)
Open Field – 0.4 µg Doxycyline
J
K
L
*

Figure 4.9 Profiling Sirt1 expression in miR-132/212 cKO and miR-132 transgenic mice
(A) Representative immunohistochemical labeling for Sirt1 in the hippocampus and amygdala of WT (blue), miR-132/212 cKO (red), and miR-132 transgenic mice (green). The boxed regions in the lowmagnification images approximate the locations of the regions that are depicted in the high-magnification panels (to the right for the hippocampus, and inset for the amygdala). (B) Quantification of Sirt1 immunolabeling in three hippocampal regions (the CA1, CA3, and GCL) and in the lateral amygdala. Note the increased expression of Sirt1 in the miR-132/212 cKO animals. Scale bar = 50 μm for the low magnification images (i.e., whole hippocampus and amygdala) and 30 μm for high magnification images (i.e., CA1 cell layer and GCL-lower blade). Data were analyzed by two-way ANOVA with Bonferroni post-hoc correction and are presented as the mean ± SEM. *: $p < 0.05$; **: $p < 0.01$; n.s.: not significant ($p > 0.05$). N = 3–5 mice per genotype.

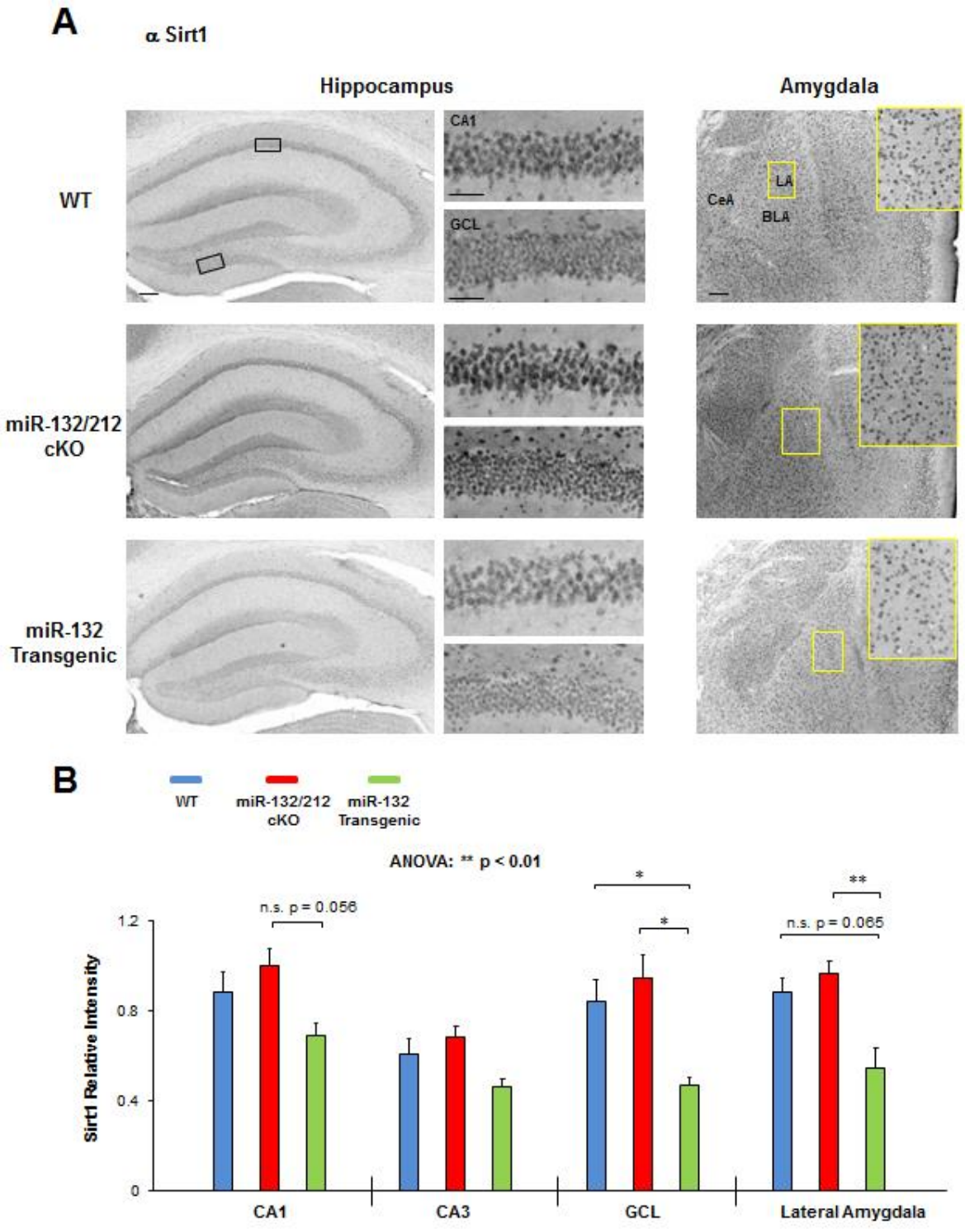
A
α Sirt1
Hippocampus
Amygdala
WT
CA1
GCL
CeA
LA
BLA
miR-132/212
cKO
miR-132
Transgenic
B
WT
miR-132/212
cKO
miR-132
Transgenic
ANOVA: ** p < 0.01
n.s. p = 0.056
*
*
**
n.s. p = 0.065
Sirt1 Relative Intensity
1.2
0.8
0.4
0
CA1
CA3
GCL
Lateral Amygdala

Figure 4.10 Profiling PTEN expression in miR-132/212 cKO and miR-132 transgenic mice
(A) Representative immunohistochemical labeling for PTEN in the hippocampus and amygdala of WT (blue), miR-132/212 cKO (red), and miR-132 transgenic animals (green). The boxed regions in the low-magnification images approximate the locations of the regions that are depicted in the high-magnification panels (to the right for the hippocampus, and inset for the amygdala). (B) Quantification of PTEN immunolabeling in the hippocampus and amygdala. Note the increased expression of PTEN within the miR-132/212 cKO mice. Scale bar = 50 μm for the low magnification images (i.e., whole hippocampus and amygdala) and 30 μm for the high magnification images (i.e., CA1 cell layer and GCL-lower blade). Data were analyzed by two-way ANOVA with Bonferroni post-hoc correction and are presented as the mean ± SEM. **: $p < 0.01$; n.s.: not significant ($p > 0.05$); N = 3–6 mice per genotype.

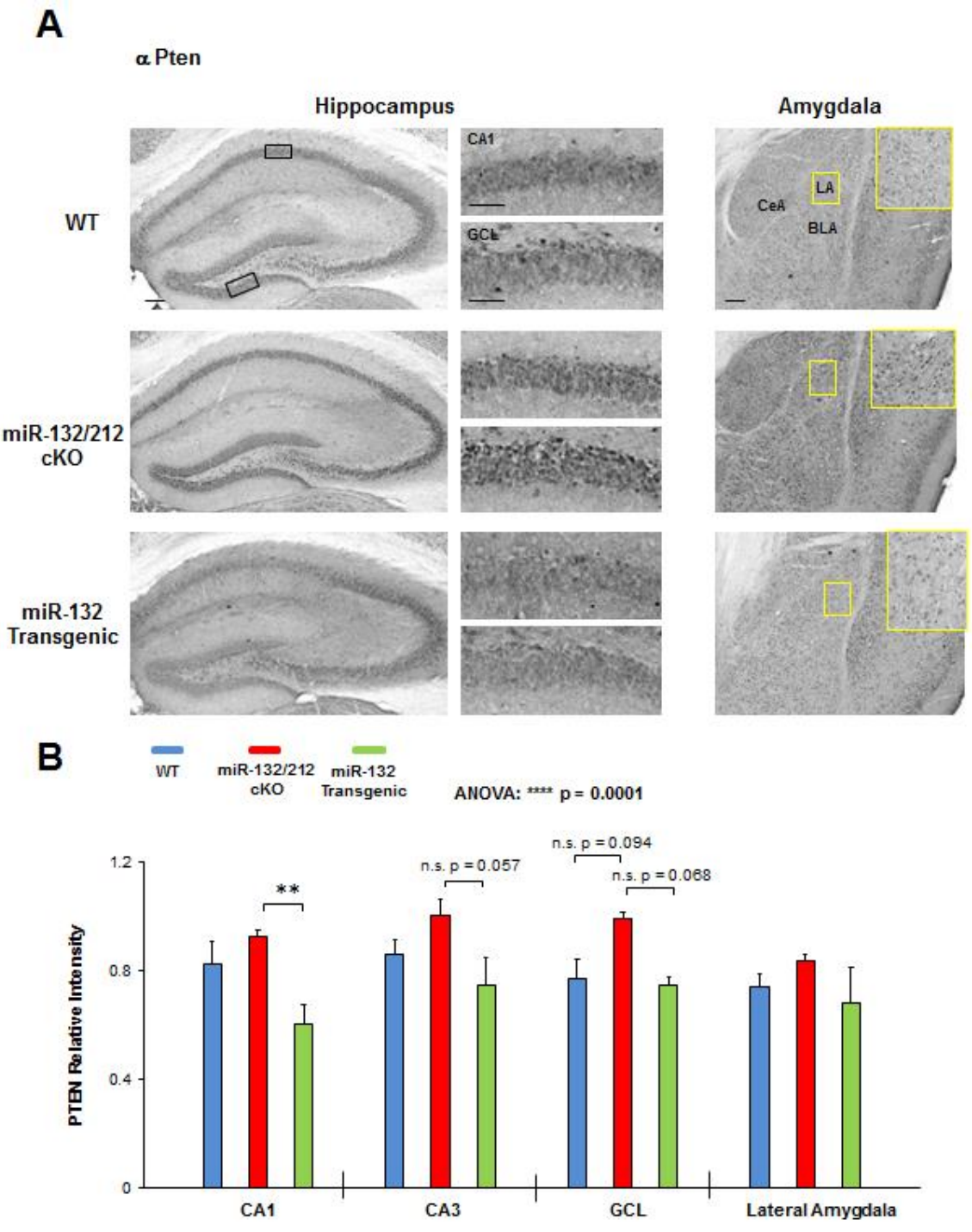
A
α Pten
Hippocampus
Amygdala
CA1
GCL
CeA
LA
BLA
WT
miR-132/212
cKO
miR-132
Transgenic
B
WT
miR-132/212
cKO
miR-132
Transgenic
ANOVA: **** p = 0.0001
n.s. p = 0.094
n.s. p = 0.057
n.s. p = 0.068
**
PTEN Relative Intensity
1.2
0.8
0.4
0
CA1
CA3
GCL
Lateral Amygdala

Figure 4.11 Expression of Sirt1 and Pten within the forebrain of WT, miR-132/212 cKO, and miR-132 transgenic animals

Representative 10X immunofluorescent images of Sirt1 in the hippocampus (A) and amygdala (B). Representative 10X immunofluorescent images of Pten in the hippocampus (C) and amygdala (D). Immunolabeling in miR-132 transgenic animals maintained on doxycycline is also shown (bottom row). Note the increased and decreased target gene expression in miR-132/212 cKO and miR-132 transgenic animals, respectively, relative to WT mice. Also note the decreased expression of CFP in the miR-132 transgenic animals maintained on doxycycline, in addition to the subtle increase in Sirt1 and Pten expression in miR-132 transgenic animals on doxycycline relative to miR-132 transgenic animals not maintained on doxycycline. CFP is a marker for the miR-132 transgenic mouse line, and as such, immunofluorescence was not observed in WT and miR-132/212 cKO animals. Scale bar = 300 μm for both hippocampal and amygdalar images. Abbreviations: CA1-cornu ammonis 1 hippocampal subfield; GCL-granule cell layer; LA-lateral amygdala; BLA-basolateral amygdala; CeA-central amygdala.

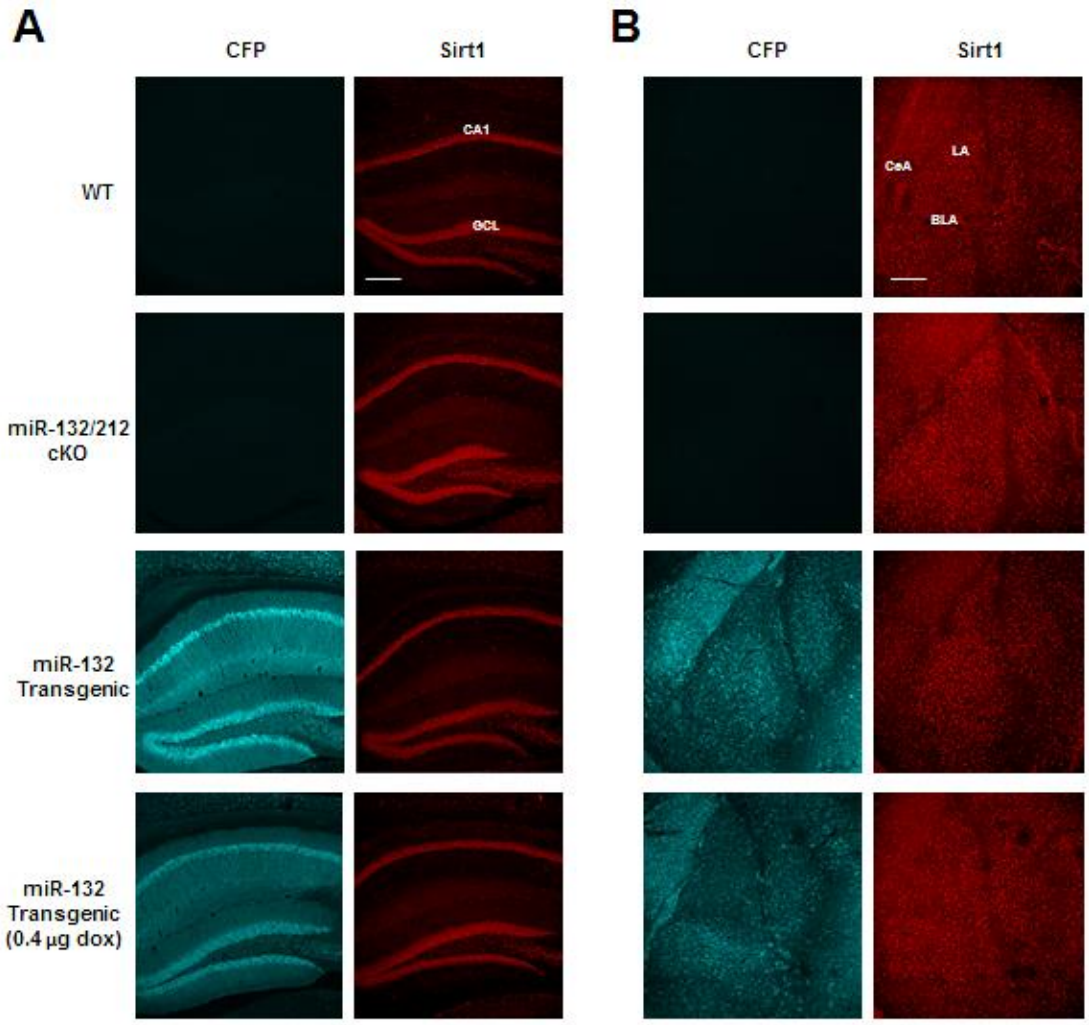

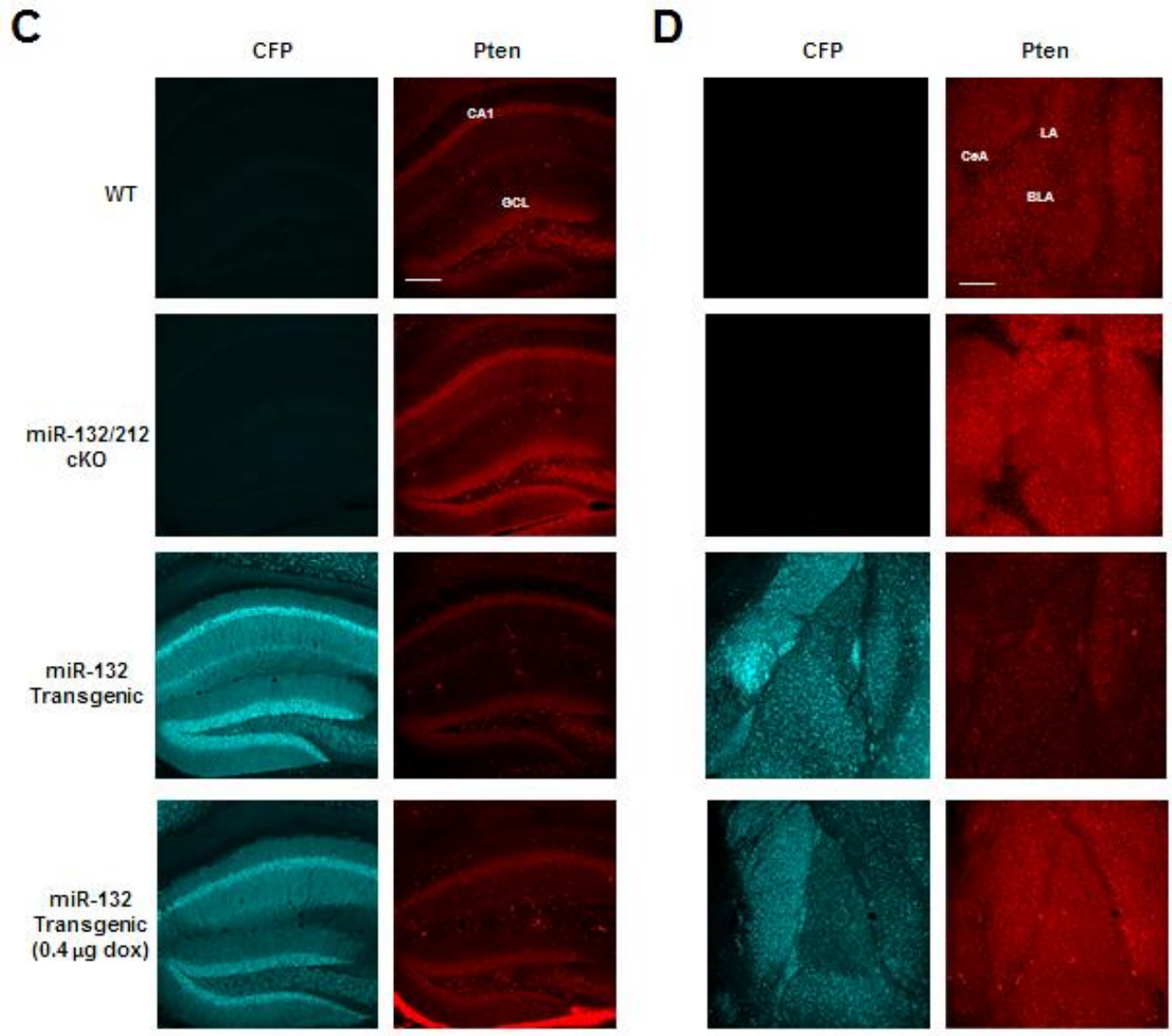
C
CFP
Pten
CA1
GCL
WT
miR-132/212
cKO
miR-132
Transgenic
miR-132
Transgenic
(0.4 μg dox)
D
CFP
Pten
LA
CeA
BLA

CHAPTER 5

Profiling circadian clock timing after unpredictable chronic mild stress

Introduction

Nearly every aspect of mammalian physiology and behavior is shaped by a ~24 hour (circadian) rhythm. Importantly, this biological timekeeping process—formed by a transcription/translation feedback loop—is intrinsic and self-sustaining, functioning to adjust the body to geophysical time, even in the absence of external timing cues (as reviewed in (Buhr and Takahashi, 2013; Ko and Takahashi, 2006)).

For years it was believed that circadian timekeeping capacity was restricted to the SCN—a bilateral structure located within the hypothalamus that serves to synchronize oscillators in the brain (and in peripheral organs) to the daily light/dark cycle. However, recent work has revealed that the SCN also functions in coordination with oscillators located in forebrain regions, which coincides with the fact that circadian clock gene expression and circadian oscillatory capacity exists in several regions throughout the brain—including areas of the hippocampus, cortex, and amygdala (Abe et al., 2004; Al-Safadi et al., 2014; Chun et al., 2015; Kristin L Eckel-Mahan et al., 2008; Harbour et al., 2013; Jilg et al., 2010; Lamont et al., 2005)—regions that underlie both cognition, mood, and stress response (Drevets et al., 2008; Lucassen et al., 2014; Petersen and Sporns, 2015). Further, circadian gating of cellular excitability/output from several other brain regions (including the habenula, raphe nuclei, and locus coeruleus) has also been reported (Albrecht and Stork, 2017; Aston-Jones et al., 2001; Baño-Otálora and

Piggins, 2017; González and Aston-Jones, 2006; Smarr et al., 2014a)—providing further support that the circadian timing system modulates synaptic plasticity, cognitive efficiency, and the release of hormones that may mediate affective behavior(s).

These observations, coupled with the fact that dysregulation of circadian timing is highly prevalent in individuals with neuropsychiatric disorders such as Major Depressive Disorder (Germain and Kupfer, 2008b; Turek, 2007), merit a deeper understanding of the relationship between clock timing and depression. Along these lines, a large body of work has suggested that stress, anxiety, and sleep disruption contribute to mood disorders via dysregulation of the circadian cycle (reviewed in (Edgar and McClung, 2013; Germain and Kupfer, 2008a; Kronfeld-Schor and Einat, 2012; McClung, 2007)). However, there is conflicting work regarding the role of SCN disruption in the development of depression-like behavior, with some studies reporting that master clock dysfunction protects against stress-induced depressive-like behavior and others showing that SCN clock dysregulation actually elicits depressive-like behaviors (Landgraf et al., 2016b; Tataroğlu et al., 2004).

Furthermore, it remains to be determined whether chronic stress (and associated depressive-like behavior) leads to circadian dysfunction within the master clock (the SCN) or within ancillary clocks located within limbic regions of the forebrain. Additionally, although circadian disruption has been shown to affect mood, the precise role that forebrain clocks play in eliciting depressive-like behaviors remains unknown. Indeed, to date, there is yet to be a definitive understanding of the cellular- and systems-level relationship between clock dysregulation and mood disorders. Along these lines, it

is unclear whether circadian clock dysregulation arises in the SCN, in 'mood circuits' that underlie depression, or in both the SCN and in mood circuits. Hence, the goal of this work was to gain a deeper understanding of circadian circuits after chronic stress. Using an innovative *Per1*-Venus circadian clock reporter mouse combined with immunofluorescent labeling, organotypic slice culture, and a multitude of behavioral paradigms, we were able to resolve clock timing in individual cells in order to characterize rhythms after chronic stress. We found that a six-week Unpredictable Chronic Mild Stress (UCMS) paradigm leads to a damping of Venus expression within the hippocampus and other limbic regions, while Venus expression within the SCN remained relatively unchanged. This observation was complemented by the fact that working and intermediate term time-of-day dependent memory was abrogated in UCMS-exposed animals, while circadian wheel running activity remained largely intact. Overall, the results from this study provide new insights into the relationship between circadian clock gene expression and depressive-like behavior-- potentially opening the door for the development of chronotherapeutic approaches that may be used to treat neuropsychiatric disorders.

Materials and Methods

Per1-Venus transgenic clock reporter mice

All animals used in this study were male and female WT (C57Bl/6) animals bred in-house, or *Per1*-Venus transgenic clock reporter mice (also bred in-house) which allow for the visualization of the core clock gene, *Period1*, transcription (Cheng et al., 2009a). Note that for all immunofluorescent-based experiments, only *Per1*-Venus mice

were used so that clock gene expression could be visualized. Animals were fed ad libitum and were maintained on a standard 12:12 LD cycle unless otherwise noted. All procedures were approved by the Institutional Animal Care and Use Committee of Ohio State University.

Unpredictable Chronic Mild Stress (UCMS) paradigm

Key to the experiments detailed below is the implementation of the unpredictable chronic mild stress (UCMS) paradigm that has been used extensively in rodents to model pathophysiological processes (i.e. anhedonia, altered grooming, learned helplessness) that are believed to underlie depression (Banasr et al., 2007; Farooq et al., 2012; Frisbee et al., 2015; Mineur et al., 2006; Nollet et al., 2012; S. Zhu et al., 2014). Our UCMS protocol models approaches previously outlined (Li et al., 2011; Logan et al., 2015; Monteiro et al., 2015; Willner, 1997). To this end, animals were exposed to two unpredictable stressors per for a six week period. Stressors were applied at random times throughout the circadian cycle to avoid confounds related to habituation. Following the UCMS paradigm, depression and anxiety-like behaviors were measured using the open field test, elevated plus maze, tail suspension test, forced swim test, and sucrose splash test (Castagné et al., 2011; Darcet et al., 2014; Isingrini et al., 2010a; Lister, 1987; Seibenhener and Wooten, 2015; Yankelevitch-Yahav et al., 2015). Body weight and coat state was also monitored weekly.

Open field test

The open field test was adapted from our previous study (Aten et al., 2019). In brief, mice were placed in the corner of the open field arena, and they were permitted to

explore the arena for a period of 5 minutes. During this time Noldus Ethovision software was used to score the total time spent in the center of the arena in addition to the total number of center crosses.

Elevated plus maze

The elevated plus maze protocol was adapted for our previous study (Aten et al., 2019). In brief, mice were placed in the center of an elevated maze that consisted of 2 open and 2 closed arms. Each mouse was then given a period of 5 minutes to explore the maze. Noldus Ethovision software was used to record the latency to enter the open arm of the arena and the total time spent in the open arms.

Tail suspension test

The tail suspension test was adapted as described in a comprehensive review (Cryan et al., 2005). In brief, mice were hung upside down (by their tails) for a period of 6 minutes, during which time the latency to immobility and the total time spent immobile, were recorded by an experimenter. Note that immobility was defined as no obvious movement (i.e. freezing behavior) for a period of two seconds.

Forced swim test

In addition to the tail suspension test, depressive-like behaviors were also assessed with the forced swim test, using an adapted protocol recently described (Shepard et al., 2016). A large glass beaker was filled with water (24–25 °C), and each animal was placed in the water for 6 minutes. Latency to immobility (i.e. freezing) and total time spent immobile were recorded by an experimenter. After each trial, mice were dried with a paper towel and were placed back in their home cages which rested on a heating pad.

Sucrose splash test

The sucrose splash test was used as an index of self-care and motivational behavior and has been pharmacologically validated and demonstrates that UCMS decreases grooming behavior (Ducottet et al., 2004; Santarelli et al., 2003; Surget et al., 2008). This paradigm was adapted from Isingrini et al wherein the dorsal coat of each mouse was squirt with three 'sprays' of a viscous, 10% sucrose solution (while in the home cage) (Isingrini et al., 2010b). This solution dirties the fur and causes most mice to begin grooming behavior. After the squirts, the latency to groom and total number of grooming episodes were recorded for a 5 minute period. Grooming was defined as a mouse that was licking his/her dorsal coat in an attempt to clean off the sucrose solution.

Coat/fur state scoring and monitoring of body weight

Coat/fur states were recorded on a weekly basis, as were animal body weights (Isingrini et al., 2010b). These parameters were recorded until the end of the UCMS protocol. The coat state evaluation consisted of the scoring of fur in eight different body regions: the head, neck, tail, dorsal coat, ventral coat, forelimbs, hindlimbs, and genital area. For each body area, a score of 1 to 4 was attributed (1 being very clean and 4 signifying bald patches and an extremely dirty/scruffy coat). The total score was then added and the average score (from each body region) was then taken.

Note that any animal that displayed a sharp reduction in total body weight (more than 15%) was removed from the UCMS experiment.

T-maze

For the T-maze assay (testing working memory capacity) animals were placed in the 'start arm' of the maze for ~60 seconds. Note that a wooden barrier was placed in the center of the alternate arms. After 60 seconds, the mice were then allowed to freely explore the maze for a period of 7 minutes, and the number of correct alternations were scored by an experimenter (blind to conditions). Note that a correct alternation was defined as the mouse entering one arm, going back to the 'start arm' and then entering the opposite arm.

Novel object location

The NOL paradigm was adapted from our recent study (Snider et al., 2016b). Animals were dark-adapted for one day and habituation trials occurred on the following two days. On the third day, object exploration and novel location testing occurred during the circadian day (CT4) or circadian night (CT15). Mice explored the two objects for 5 minutes and were returned to their home cages. Next, during the 5 minute testing period, mice explored the same objects; however, one object was moved to a novel location. The number of seconds spent exploring each object was scored, and the discrimination index was calculated.

Contextual fear conditioning

The CFC paradigm was adapted from our recent study (Aten et al., 2018a). In brief, mice underwent two days of dark adaption and were then trained to associate a context box with a footshock (the training period). 24 hr later, mice were placed in the box every 12 h during both the circadian day and night timepoints to profile freezing behavior.

Profiling circadian wheel running activity

Circadian wheel running profiling was performed as recently described by our lab (Aten et al., 2021; K. L. Wheaton et al., 2018). In brief, mice were placed in large cages equipped with running wheels and were maintained in a 12:12 light:dark cycle. After approximately 45 days in LD, mice were then transferred to total darkness (DD) to monitor free-running activity. Further, to examine light entrainment properties in control and stressed mice, a 15 minute light pulse was administered at CT15. The circadian period (tau), total day and night activity, and phase shift (photic delay) were examined using ClockLabs and ActiView software.

Tissue processing

Unless otherwise noted, animals were sacrificed at ~CT4 (circadian day) or CT15 (circadian night). Animals were sacrificed via cervical dislocation/decapitation, and 600 um thick brain sections were cut in aCSF using a Leica vibratome. Tissue was then fixed for 6 hours in 4% PFA and cryoprotected in 30% sucrose overnight before thin-sectioning to ~40 um thick sections on a freezing microtome.

Immunofluorescent staining, imaging, and analysis

For immunofluorescent experiments, tissue was labeled according to a previous study (Aten et al., 2018b). To increase visualization of the Venus transgene, after washing and blocking steps, brain sections containing the SCN, hippocampus, amygdala, and/or habenula were incubated in chicken anti-GFP primary antibody (1:2000 dilution; Abcam, Cat # ab13970). For co-labeling experiments, a rabbit anti Sox9 antibody (1:2000 dilution; Abcam, Cat # ab5535) or a rat anti GFAP antibody (1:30,000 dilution;

Invitrogen, Cat # 13-0300) was also used. The next day (after washes), sections were incubated for 2 hours in Alexa Fluor 488 goat anti-chicken IgY and/or Alexa 594 goat anti-rat IgY, and/or Alex Fluor 647 goat anti-rabbit IgY (all at 1:2000 dilution; Invitrogen). Finally, sections were incubated for 10 min in either hoescht or Draq5 (1:5000 dilution) for 10 min in PBST before mounting/coverslipping.

10X, 20X, and 40 or 63X (oil) images were acquired using a Lecia TSC SP8 confocal microscope. Acquisition parameters were held constant for all conditions/groups.

For regional analysis of Venus intensity/expression, an entire ROI was drawn around the pyramidal cell layer of the CA1 region of the hippocampus, or the SCN and values for this ROI were background subtracted from surrounding stratum oriens sub-region or lateral hypothalamus. 1-2 sections were analyzed per animal, and the mean intensity value (from each mouse) was taken for analysis. For single-cell analysis of the Venus transgene, an ROI was drawn around each DraQ5 or Hoescht positive cell within the CA1, SCN, lateral amygdala, or habenula. An ROI was also drawn in tissue surrounding these brain regions order to background subtract. The average Venus fluorescent intensity (taken from hundreds of cells from control or stressed animals) was then depicted on a scatterplot in order to demonstrate the heterogeneity of the Venus transgene.

Organotypic SCN slice culture

SCN organotypic slice culture was performed on slices from both control and stressed animals according to a recently published paper (K. L. Wheaton et al., 2018). In brief, WT and stressed *Per1*-Venus mice were sacrificed at ~CT6. Brains were placed in aCSF and 180 um thick coronal sections containing the SCN were collected using a Leica vibratome. The SCN sections were then placed into dissection media (aCSF containing 1% penicillin/streptomycin—Gibco 5140122, 0.06% nystatin—N1638 Sigma, and 0.1 uM MK801—0924 Tocris). The SCN was then isolated via trimming of the surrounding lateral hypothalamic tissue, and it was placed on a filter in a 35 mm dish. The slices were maintained in tissue culture media containing 0.5 nM Glutamax, 1% penicillin/streptomycin, 0.1 uM MK-801, 2% B-27, 0.06% nystatin, and 5% horse serum in Neurobasal. These slices were kept at 35C in a CO2 incubator and media was changed approximately two hours after culturing.

Next, slices were sealed and were placed on an incubator on top of an inverted Leica SP8 confocal. Images through the SCN were collected each hour over a ~4 day period. Mean Venus expression values for the whole SCN were analyzed during each hour of the experiment. Note that an ROI was drawn around the SCN in addition to a separate region (just lateral to the SCN) in order to background subtract and generate a normalized Venus value for each hour of the experiment. This process was performed for slices from 9-10 control and stressed animals. The mean circadian period and amplitude of the SCN were then plotted during hours 24-144 of the experiment.

Results

Expression of Per1-Venus throughout the brain

To begin, we first confirmed that the *Per1*-Venus transgene would express in both the SCN and in other limbic regions. As expected, the Venus fluorescent signal was easily resolved using standard confocal-based microscopy (Cheng et al., 2009b) and its expression could be observed throughout the brain (Fig. 5.1A-5.1B).

To confirm the efficacy of the stress paradigm, animal body weights were recorded each week. Though no significant interaction was observed between stress condition and week (Fig. 5.1C $F_{(5, 269)} = 1.942$; $p = 0.0877$; ANOVA), an effect of stress condition on weight was observed (Fig. 5.1C $F_{(5, 269)} = 4.726$; $p = 0.0004$; ANOVA). Further, we found a significant reduction in the latency to immobility and in total time spent immobile in the forced swim test (Fig. 5.1D $t_{(83)} = 3.203$; $p = 0.0019$; unpaired t-test for latency to immobility and $t_{(83)} = 4.733$; $p < 0.0001$; unpaired t-test for total immobility, respectively). To profile self-care related behaviors, we then used the sucrose splash test. In UCMS-exposed mice, we observed a significant increase in the latency to groom and in the number of grooming episodes (Fig. 5.1F $t_{(43)} = 4.866$; $p < 0.0001$; unpaired t-test for latency and $t_{(44)} = 4.868$; $p < 0.0001$; unpaired t-test for number of grooming episodes).

6 week UCMS paradigm induces depression and anxiety-like behaviors

Turning to anxiety-related tasks, in stressed mice, we observed a significant increase in the latency to enter an open arm and in the total open arm time (Fig. 5.1G $t_{(40)} = 2.482$; $p = 0.0174$; unpaired t-test for latency to open arm and $t_{(48)} = 1.396$; $p = 0.17$;

unpaired t-test for total open arm time). Finally, in the open field test, in stressed mice, we observed a significant decrease in the amount of time spent in the center of the arena in addition to a trending decrease in the number of center crosses (Fig. 5.1H $t_{(96)} = 2.141$; $p = 0.0348$; unpaired t-test for time spent in center and $t_{(98)} = 1.701$; $p = 0.0921$; unpaired t-test for center crosses). Taken together, these data show that we were, indeed, able to obtain depressive-like behaviors in mice exposed to a six week UCMS paradigm.

Alterations in Per1-Venus expression in forebrain regions

We then asked whether Venus expression might be altered in forebrain regions after the six week UCMS paradigm. To begin, we sacrificed mice (control and stressed) during both the circadian day (~CT6) and circadian night (CT18) (Fig. 5.2A). Although there was no significant interaction between stress condition and time-of-day (Fig. 5.2B $F_{(1, 17)} = 0.878$; $p = 0.362$; two-way ANOVA), we did observe a significant effect of stress on Venus expression (Fig. 5.2B $F_{(1, 17)} = 13.19$; $p = 0.0021$; two-way ANOVA). Specifically, we found a significant reduction in Venus expression in stressed mice during the circadian day (Fig. 5.2B $p = 0.036$; Tukey multiple comparison test).

Given this finding, we then sought to examine cellular-level Venus expression. Thus, high-magnification/resolution images were acquired from Venus mice (control and stressed) and individual cells were traced throughout the CA1 region of the hippocampus (Fig. 5.2C). Upon pooling cells from 4 stressed and 4 control animals, we observed a significant decrease in the Venus fluorescent intensity in stressed mice (Fig. 5.2D $t_{(1197)} = 15.7$; $p < 0.0001$; t-test). Further, when the average Venus intensity (per animal) was correlated with average fur state, we observed a trending indirect correlation (Fig. 5.2E;

R = 0.422; p = 0.0581), suggesting that animals with higher Venus intensities displayed lower fur state scores (i.e. cleaner fur). Finally, single cell analysis of two other limbic regions—the lateral amygdala and medial habenula—revelaed a significant decrease in Venus intensity in UCMS-exposed animals (Fig. 5.2F $t_{(1198)} = 6.322$; $p < 0.0001$; t-test for amygdala and Fig. 5.2G $t_{(1210)} = 11.5$; $p < 0.0001$; t-test for habenula). Frequency distribution plots (Fig. 5.2F and 5.2G—bottom panels) also revealed an increase in the number of 'lower' Venus intensity cells in stressed mice relative to control mice. Taken together, these data suggest that the UCMS paradigm dampens Venus expression within limbic regions.

Per1-Venus expression is increased in the hippocampal astrocytes from UCMS mice

While the experiment above demonstrates that the UCMS paradigm does, indeed, alter forebrain circadian clock timing, we did not distinguish which cell types were affected by chronic stress. Given that *Per1*-Venus is expressed in astrocytes (Fig. 5.3A—note the colocalization of Venus with astrocytic markers GFAP and Sox9), we wanted to investigate whether UCMS alters clock gene expression within astrocytes. Hence, we labeled tissue from both control and stressed mice with Venus and Sox9 (Fig. 5.3B and 5.3C). Interestingly, we noted that astrocytes from mice exposed to chronic stress displayed higher levels of Venus in the stratum oriens and stratum radiatum relative to control animals (Fig. 5.3D-left panel- $t_{(209)} = 6.177$; $p < 0.0001$; t-test for stratum oriens and Fig. 5.3D-right panel-$t_{(188)} = 4.083$; $p < 0.0001$; t-test for stratum radiatum). Together, these data suggest that *Per1*-Venus expression is altered in astrocytes within the CA1 region of the hippocampus.

UCMS alters time-of-day dependent working and intermediate-term memory

Given our observation that the six week UCMS paradigm alters Venus expression within limbic regions, coupled with the fact that mice lacking a functional forebrain 'clock' display memory deficits (Snider et al., 2016b), we posited whether the UCMS protocol might alter time-of-day dependnent cognition. To begin, we used the t-maze paradigm to assay working term memory (Fig. 5.4A). Paralleling a finding in hamsters (Ruby et al., 2013), we found that control animals displayed better working memory (i.e. an increase in correct arm alternations) during the nighttime compared to the day (Fig. 5.4B; $t_{(79)} = 2.314$; $p = 0.0233$; t-test). Mice exposed to UCMS, however, displayed no time-of-day difference in correct alternations (Fig. 5.4B; $t_{(81)} = 0.3581$; $p = 0.7212$; t-test). These data suggest that UCMS alters working-term time-of-day dependent cognition.

In the NOL task—a paradigm that has been shown to be clock-gated (Snider et al., 2016a) (Fig. 5.4C)—we found a significant interaction between time-of-day and stress condition (Fig. 5.4D $F_{(1, 30)} = 12.47$; $p = 0.0014$; two-way ANOVA). More specifically, we found that a significant difference between the day discrmination index versus the night discrmination index in control animals (Fig. 5.4D; adjusted $p = 0.0467$; Tukey post-hoc test). In UMCS mice; however, no significant differences were observed (Fig. 5.4D; adjusted $p = 0.1383$; Tukey post-hoc test). These data suggest that UCMS alters intermediate term NOL, time-of-day dependent memory.

Finally, as a longer term memory readout, we used the contextual fear conditioing paradigm (Fig. 5.4E). Notably, our lab has previously shown that this task is

time-of-day dependent, with increased freezing (i.e. better memory recall) observed during the circadian day (Aten et al., 2018a). Interestingly, we found no significant interaction between stress condition and time-of-day on contextual fear memory (Fig. 5.4F; $F_{(1, 58)} = 0.0553$; $p = 0.8149$; two-way ANOVA). Furthermore, both groups showed heightened freezing levels during the circadian day. Given that freezing percentage was not altered, these data suggest that longer-term memory capacity is not altered by the six week stress paradigm.

Unaltered Per1-Venus expression in SCN of UCMS-exposed animals

Given our observation that *Per1*-Venus expression was dampened within forebrain regions after chronic stress, we next sought to determine whether this same phenomenon would be observed within the master clock. To this end, control and stressed Venus animals were sacrificed every four hours across the circadian cycle, and SCN tissue was immunolabeled for the Venus transgene (Fig. 5.5A). Whole SCN analysis revealed no significant interaction between stress condition and Venus expression across the day and nighttime domains (Fig. 5.5B; $F_{(5 , 37)} = 0.2477$; $p = 0.9383$; two-way ANOVA). Similarly, high magnification/resolution images of the SCN core (of both control and stressed animals) were acquired on a confocal microsocpe in order to determine whether Venus heterogeneity may be altered (Fig. 5.5C). We found no significant difference in Venus fluorescent intensity values between the two groups (Fig. 5.5D; $t_{(1047)} = 1.245$; $p = 0.2133$l; t-test). These Venus fixed-tissue results suggest that *Per1* is not altered within the SCN of chronically stressed animals.

SCN organotypic culture reveals similar period and amplitude in slices from control and UCMS animals

To validate the fixed SCN tissue results, we then profiled the circadian period and amplitude in SCN organotypic slices from control and stressed animals (Fig. 5.6A). Along these lines, control and stressed animals were sacrificed during the early day, and the SCN were sliced and subsequently cultured and placed on an incubator-stage on an inverted confocal. After four days profiling Venus rhythms (every hour) (Fig. 5.6B), we noted no significant differences in the amplitude of the rhythms (Fig. 5.6C; $t_{(17)} = 0.1613$; $p = 0.8738$; t-test). Similarly, the period for slices from both control and stressed animals was similar (23.1 for control and 23.11 for stressed, respectively; Fig. 5.6C; $t_{(17)} = 0.05695$); $p = 0.9631$; t-test). These data, coupled with the fixed tissue results suggest that Venus expression within the SCN remains largely unchanged after stress.

Light entrainment capacity is intact in UCMS-exposed animals

In order to obtain a behavior readout of our cellular-level analysis of clock timing in the SCN after UCMS, we next profiled circadian wheel running activity and light entrainiment capacity (Fig. 5.7A—see actograms). To this end, control and stressed animals were placed into large cages equipped with running wheels. Note that stressed animals received daily 'stressors' while on the running wheels. Analysis revealed no significant effect of stress on the period (tau) (Fig. 5.7B; $t_{(25)} = 0.038$; $p = 0.9700$; t-test). We did, however, observe a trending decrease in day activity (during LD conditions) in stressed animals (Fig. 5.7B; $t_{(28)} = 1.845$; $p = 0.0756$; t-test) and a significant decrease in

night activity (during LD conditions) (Fig. 5.7B; $t_{(28)} = 4.96$; $p < 0.0001$; t-test). This decrease in activity can also be observed in the plotted activity profiles (Fig. 5.7C).

Finally, in order to assay light re-entrainment capacity, we administered a light pulse at CT15 (in order to induce a phase delay) in animals housed in constant dark (DD) conditions. We found no significant differences in phase delay in stressed mice (Fig. 5.7B; $t_{(25)} = 0.253$; $p = 0.8024$; t-test). Together, thse data reveal that, in addition to cellular level clock timing remaining intact within the SCN, circadian-related behavioral output also remains intact upon stress.

Discussion

Work from several labs has shown that forebrain regions (hippocampus, cortex, amygdala, etc.) exhibit circadian clock gene expression and oscillatory capacity (Dibner et al., 2010; Guilding and Piggins, 2007). However, the cellular-level effects of chronic stress on circadian oscillations within these limbic areas remain unknown. The purpose of the experiments in this study was to create a detailed cellular/systems-level representation of clock timing in brain circuits underlying depression. Here, we used control and chronically stressed *Per1*-Venus circadian clock reporter mice in combination with immunofluorescent labeling, organotypic slice culture, and multiple behavioral paradigms. We found that Venus expression was dampened in limbic regions, while expression (and rhythms) within the SCN were largely intact. Further, our working and intermediate-term cognitive tasks revealed time-of-day dependent deficits in mice exposed to UCMS, while circadian/activity behavioral paradigms were largely unchanged.

A mechanistic understanding of the cellular, systems, and behavioral-level relationship between circadian clock dysfunction and mood disorders remains largely unknown. Indeed, this question has been difficult to interrogate due to the lack of reporter-based animal models and other resources that enable one to depict clock timing capacity with single-cell resolution in monoaminergic and serotonergic circuits ('mood' ciruits). However, here, we utilized our innovative transgenic clock reporter line to answer these questions.

Our profiling of Venus expression within both the SCN and within limbic regions suggests that *Per1* expression dampens as a result of chronic stress. Although we did not tease apart the precise mechanism of this circadian disruption, the fact that Venus rhythms (and expression) within the SCN remained unchanged, while they were seemingly damped in limbic regions, suggests circadian disruption associated with depression-like behaviors likely resides within forebrain mood circuits. To this end, one may surmise that chronic stress may lead to an uncoupling of oscillators within the master clock from those oscillators within ancillary brain regions (i.e. in mood circuits that may be involved in the etiology of depression-like behavior).

One could further predict that this uncoupling (of SCN from forebrain oscillators) is followed by individual (i.e. cellular-level) uncoupling of these ancillary oscillators. Hence, this individual and network-level dysfunction could result in a lack of circadian-gated output from mood regions. To this end, one possibility is that chronic stress leads to cellular-level incoherence, and thus, clock-gated output may become disrupted. In turn, this disruption may decrease the activity of the circadian

transcription-translation feedback loop, subsequently damping and/or desynchronizing cellular oscillations within the forebrain. This phenomenon may explain both the depressive-like behaviors and the cognitive behavioral manifestations that we observed (with respect to the alterations in time-of-day dependent T-maze and NOL memory).

This idea—that chronic stress-induced perturbations in forebrain circadian oscillator populations are responsible (at least in part) for the behavioral manifestations of depression—is not entirely unfounded. Indeed, using *period2*-luciferse clock reporter mice and RNA-based profiling methods, several labs have reported that depression-like behaviors are associated with alterations in clock timing within mood circuits and/or the master clock (Christiansen et al., 2016; Landgraf et al., 2016a; Logan et al., 2015; Savalli et al., 2015). However, these referenced studies were limited by technical aspects of their reporter mouse model and entire brain-region RNA isolation approaches, wherein whole-brain region analysis (of a collection of cellular oscillators) was used as a readout of circadian functionality. Because cellular-level resolution was unattainable in these studies, the mechanism of this reported circadian disruption is not entirely clear. Along these lines, clock dysregulation could have resulted from either a damping or a desynchronization of cellular oscillators (or from a combination of both noted mechanisms).

Here, we should reiterate that the hypothesis that we are positing here does not require SCN dysfunction after chronic stress—which is in line with our results suggesting that Venus expression/rhythmicity within the SCN remains intact in chronically stressed animals. Rather, it is these forebrain clocks that become unable to effectively

communicate with the SCN, which may serve as a 'trigger' in the development of depressive-like behaviors. In many respects, this idea is in line with work indicating that the etiological underpinnings of depression results from an excitatory/inhibitory imbalance of the connectivity within mood-modulating circuits (Gabbay et al., 2013; Greicius et al., 2007; Kaiser et al., 2016, 2015; Marchetti et al., 2012; Peng et al., 2012; Ressler and Mayberg, 2007; Whitfield-Gabrieli and Ford, 2012). Here, we should also mention that our profiling of circadian-gated locomotor activity revealed a significant decrease in activity in mice exposed to chronic stress. This finding is similar to that in a recently published report (DeVallance et al., 2017). However, it should be noted that this reduction in activity does not mean that the master clock is 'dysfunctional'—as our examination of circadian period/tau and entrainment capacity were no different in UCMS mice compared to control mice.

Finally, with respect to cell-type specificity of the observed Venus dysregulation within limbic circuits, we were somewhat surprised to find that Venus expression was actually increased within hippocampal astrocytes obtained from chronically stressed animals. Although we did not profile other cell types (i.e. excitatory/inhibitory neurons, oligodendrocytes, microglia, etc), the find that hippocampal astrocytes showed *increased* Venus expression was in contrast to the finding that Venus expression was dampened (as a whole) within other cells. While the reason behind this increase in astrocytic Venus expression is not clear, these data suggest that, perhaps, chronic stress causes astrocytes to oscillate/express in a different phase compared to other cell types. Given that astrocytes have recently been reported to serve as key players in the clock timekeeping

process (Brancaccio et al., 2019, 2017), if true, this finding could be critical to the development of chronotherapies that may be used to treat depression, as it suggests that circadian dysfunction in both neurons *and* astrocytes plays a role in the development of depression-like behaviors.

In total, this study reveals that a six week chronic stress paradigm leads to altered *Per1*-Venus clock gene expression within limbic regions of the brain. Given that *Per1* is highly expressed within 'mood-regulating' regions of the brain and that *Per1* is a known IEG, our results suggest that it may be well positioned to contribute to the cellular-level changes that may occur in response to the administration of antidepressants. Indeed, future studies that focus on how circadian clock gene expression (particularly *Period1*) is altered by antidepressant therapies, are of high merit.

Acknowledgements

I thank Dr. Kari Hoyt for her expertise in the analysis of the SCN organotypic slice culture.

Figure 5.1 *Per1*-Venus transgenic clock reporter mouse and validation of chronic stress paradigm
(A) Our transgenic circadian clock reporter mice express the *Per1*-Venus fluorescent transgene throughout the brain. (B) Coronal brains sections were cut, and tissue sections were immunolabeled at ~500 um intervals. Note that we have labeled several limbic brain regions in red: Nucleus Accumbens, Prefrontal Cortex, Ventral Tegmental Area, Raphe Nucleus, Habenula, Hippocampus. (C) Graphical representation of mean body weight in control and UCMS-exposed animals throughout the 6-week long UCMS experiment. (D) Latency to immobility (top) and total time immobile (bottom) in the forced swim test. (E) Latency to immobility (top) and total time immobile (bottom) in the tail suspension test. (F) Latency to groom (top) and number of grooming episodes (bottom) in the sucrose splash test. (G) Latency to open arm (top) and total open arm time (bottom) in the elevated plus maze. (H) Center duration (top) and center crosses (bottom) in the open field test. Data are presented as mean $\pm$ SEM. n = 16-27 animals per group. *: $p < 0.05$; **: $p < 0.01$; ****: $p < 0.0001$; n.s.: not significant ($p > 0.05$).

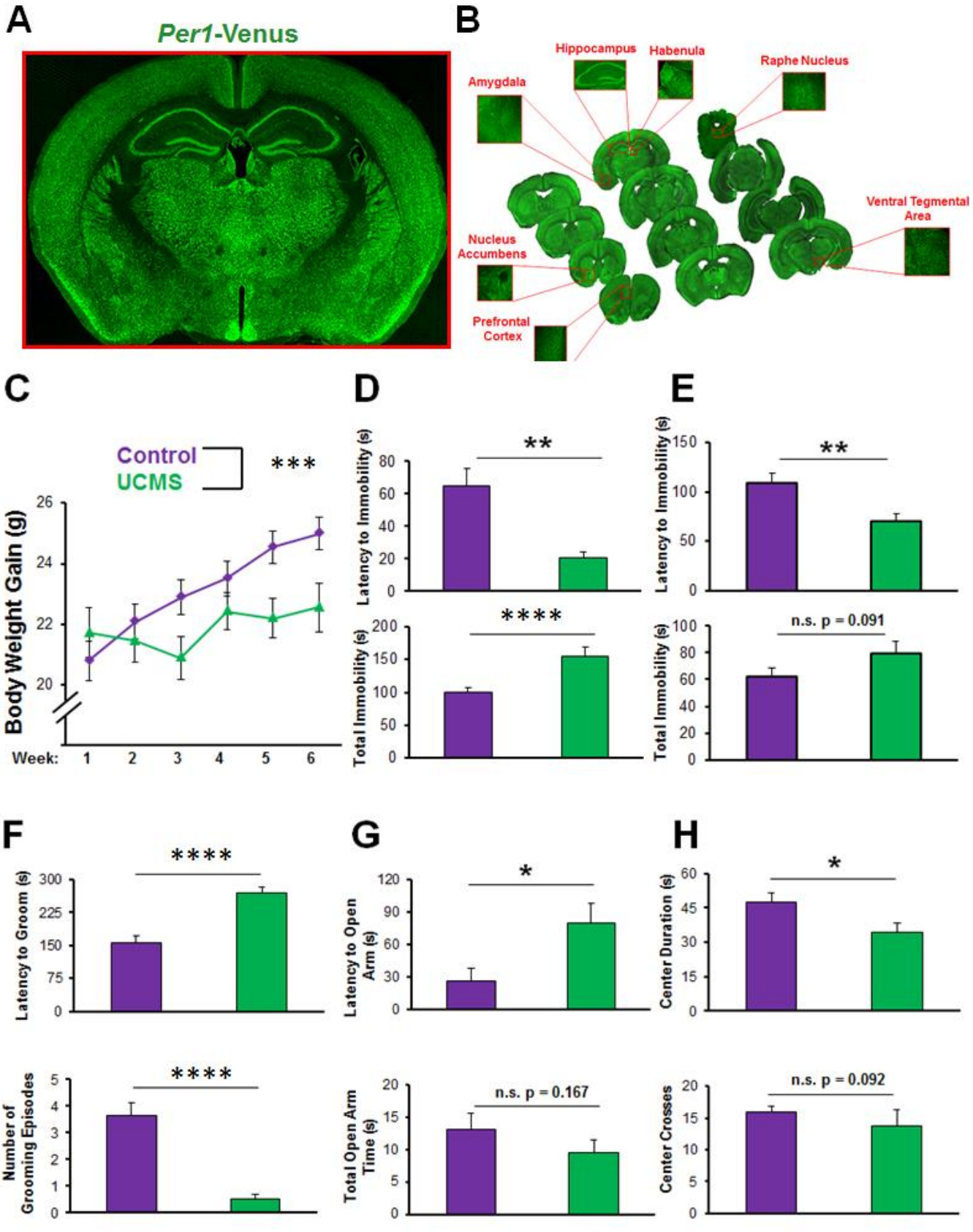
A
Per1-Venus
B
Hippocampus
Habenula
Raphe Nucleus
Amygdala
Ventral Tegmental Area
Nucleus Accumbens
Prefrontal Cortex
C
Control
UCMS
***
Body Weight Gain (g)
Week:
D
**
Latency to Immobility (s)
****
Total Immobility (s)
E
**
Latency to Immobility (s)
n.s. p = 0.091
Total Immobility (s)
F
****
Latency to Groom (s)
****
Number of Grooming Episodes
G
*
Latency to Open Arm (s)
n.s. p = 0.167
Total Open Arm Time (s)
H
*
Center Duration (s)
n.s. p = 0.092
Center Crosses

Figure 5.2 *Per1*-Venus expression in the forebrain after UCMS
(A) Expression of Venus in the CA1 of the hippocampus during the circadian day (CT6) and circadian night (CT18) in control and UCMS-exposed animals. Scale bar = 60 um (B) Quantification of whole-CA1 venus intensity. A TOD difference was observed in control animals, but not in stressed animals. Also note the reduced Venus expression in UCMS-exposed animals during the circadian day. N = 4-5 animals per condition; Analyzed with an ANOVA. (C) At the individual cell level, a heterogeneous expression pattern of Venus is observed. (D) Note the reduction in Venus fluorescent intensity in the UCMS-exposed animals. Each dot on the graph represents Venus values for a single cell (n = 600 CA1 cells analyzed for each group: control and UCMS—collected from 4 control and 4 UCMS animals during the circadian day). (E) Venus fluorescent intensity is negatively correlated with coat state/fur rating. Animals were assigned a 'fur rating' with lower values indicative of being 'well groomed,' as outlined in Logan et al 2015 and Mineur et al 2006. Each dot on the graph represents the average Venus intensity (from the CA1 cell layer) for each animal. (F) Scatterplot depiction of Venus intensity values taken from 600 cells from six animals in each group at CT6 (top panel) within the lateral amygdala and Venus intensity distribution from those same cells within the lateral amygdata (bottom panel). (G) Scatterplot depiction of Venus intensity values taken from 300 cells from six animals in each group at CT6 (top panel) within the medial habenula and Venus intensity distribution from those same cells within the habennula (bottom panel). Data are presented as mean $\pm$ SEM. *: $p < 0.05$; ***: $p < 0.001$.

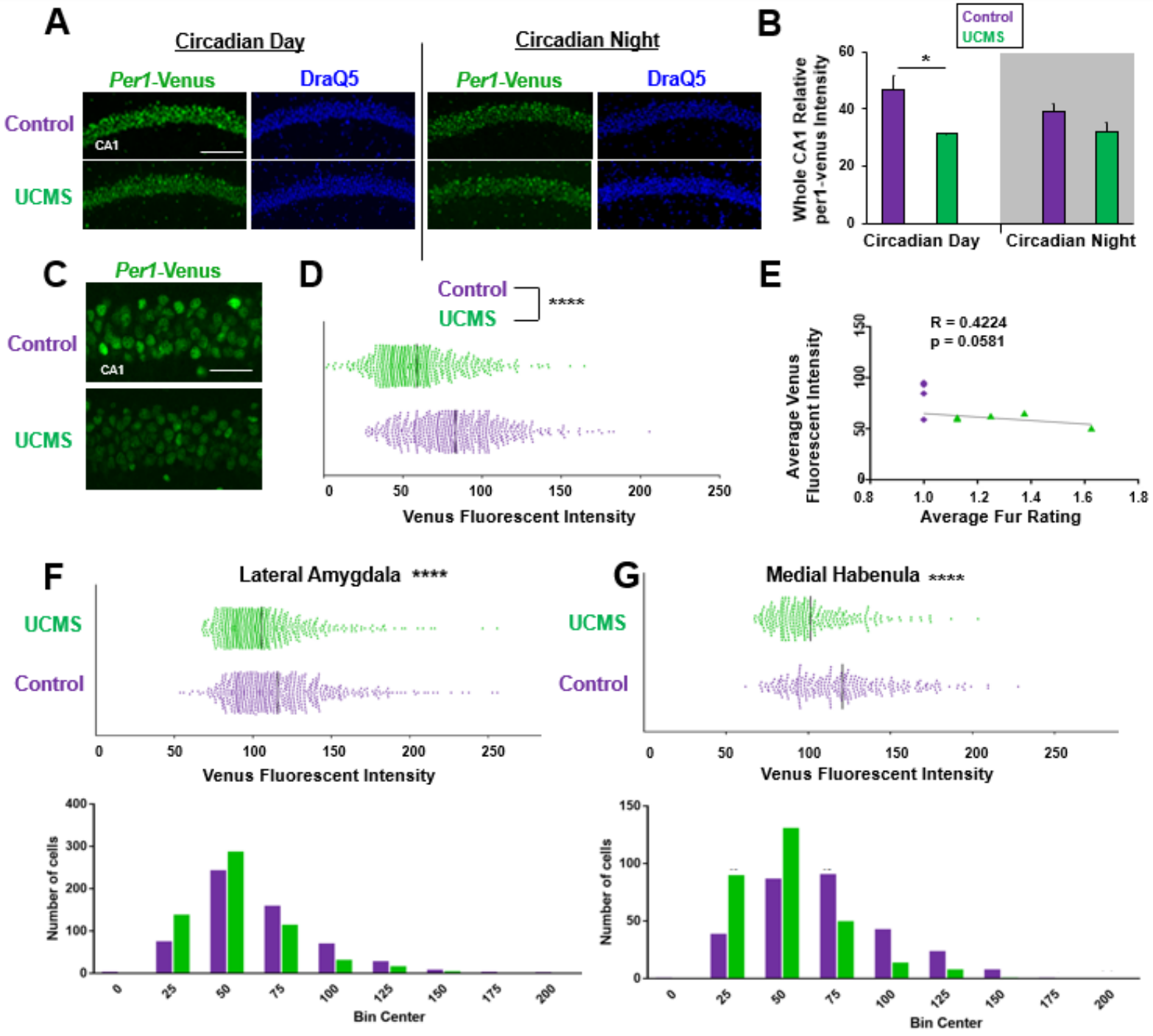
A
Circadian Day
Circadian Night
Per1-Venus
DraQ5
Per1-Venus
DraQ5
Control
UCMS
CA1
B
Control
UCMS
Whole CA1 Relative per1-venus Intensity
60
40
20
0
*
Circadian Day
Circadian Night
C
Per1-Venus
Control
UCMS
CA1
D
Control
UCMS
****
0
50
100
150
200
250
Venus Fluorescent Intensity
E
R = 0.4224
p = 0.0581
Average Venus Fluorescent Intensity
150
100
50
0
0.8
1.0
1.2
1.4
1.6
1.8
Average Fur Rating
F
Lateral Amygdala ****
UCMS
Control
0
50
100
150
200
250
Venus Fluorescent Intensity
Number of cells
400
300
200
100
0
0
25
50
75
100
125
150
175
200
Bin Center
G
Medial Habenula ****
UCMS
Control
0
50
100
150
200
250
Venus Fluorescent Intensity
Number of cells
150
100
50
0
0
25
50
75
100
125
150
175
200
Bin Center

Figure 5.3 *Per1*-Venus is expressed in astrocytes and astrocytic *Per1*-Venus is increased after stress (A) Expression of Venus and its co-localization with astrocytes (Sox9 and GFAP) in the CA1 region of the hippocampus. Orange arrows denote colocalization. Scale bar = 75 um. (B) Representative image of Venus expression in Sox9 positive cells from a control mouse. Note that ROIs on the right panel depict the same cells that are circled in white in the lower magnification image. Scale bar = 60 um for low magnification images and 20 um for higher magnification images of Venus ROIs. SO = stratum oriens and SR = stratum radiatum. (C) Representative image of Venus expression in Sox9 positive cells from a stressed mouse. Note that ROIs on the right panel depict the same cells that are circled in white in the lower magnification image. (D) Graphical representation of the fluorescent intensity of Venus positive astrocytes in the stratum oriens (left panel) and stratum radiatum (right panel) of control and stressed mice. Note that data was collected from 4 animals per condition (105 total cells coming from control and 106 total cells coming from stressed mice for stratum oriens analysis, and 86 total cells and 104 total cells coming from the stratum radiatum of control and stressed animals). Data are presented as mean $\pm$ SEM. ****: $p < 0.0001$.

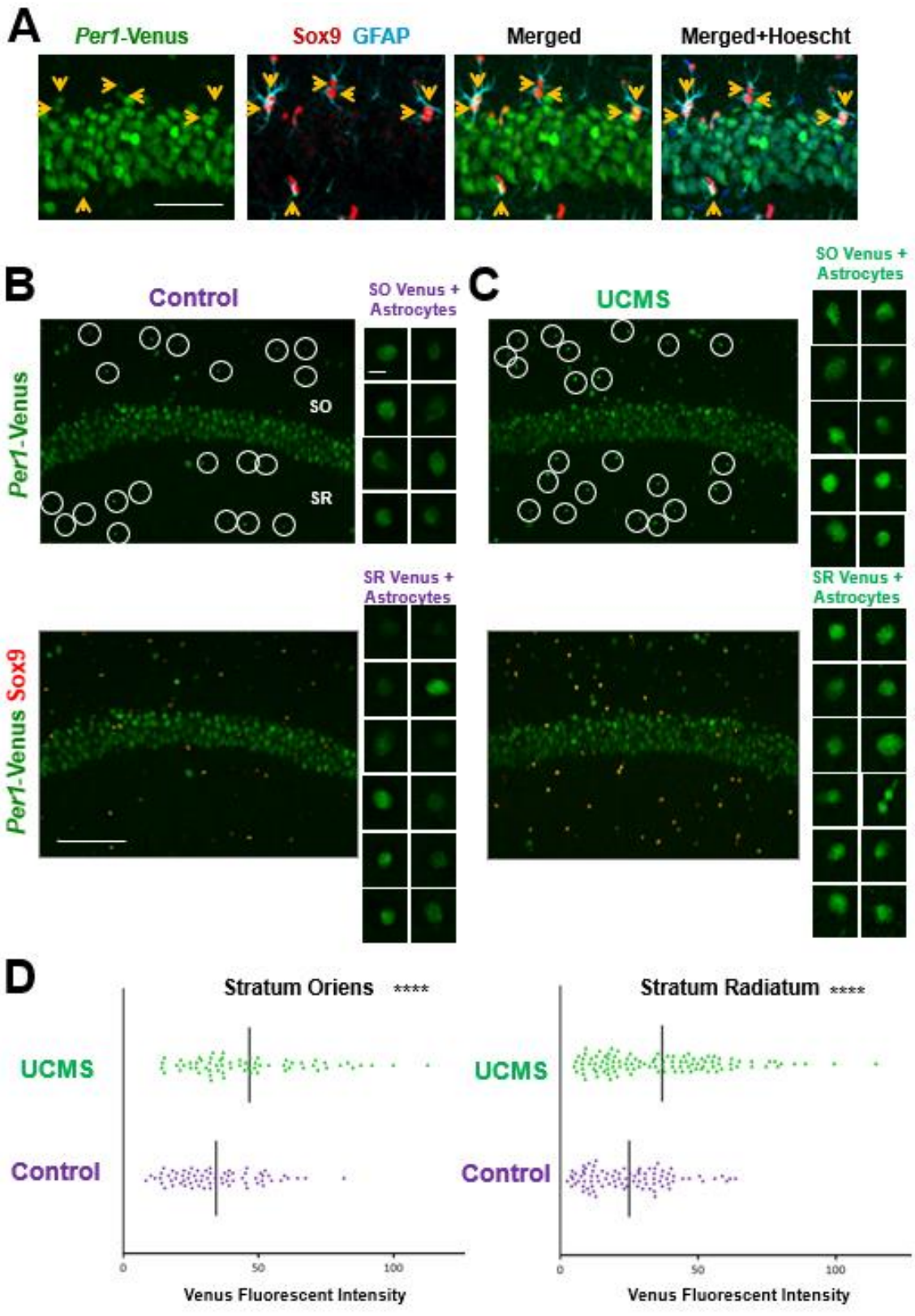
A
Per1-Venus
Sox9 GFAP
Merged
Merged+Hoescht
B
Control
SO Venus + Astrocytes
Per1-Venus
SO
SR
SR Venus + Astrocytes
Per1-Venus Sox9
C
UCMS
SO Venus + Astrocytes
SR Venus + Astrocytes
D
Stratum Oriens ****
Stratum Radiatum ****
UCMS
Control
0
50
100
Venus Fluorescent Intensity

Figure 5.4 Profiling time-of-day dependent memory after UCMS
(A)T-maze paradigm: Animals were placed in the start arm of the maze for ~60 seconds and were then allowed to freely explore the maze for 7 minutes. Correct alternations were scored during this 7 min trial, and a correct alternation was defined as the animal entering one arm, going back to the start arm, and entering the opposite arm. The schematic was created using BioRender software. (B) Statistical representation of the T-maze results during both the circadian day and night timepoints. N = 39-40 animals per condition and data is presented as mean $\pm$ SD. (C) Novel Object Location paradigm: Animals were dark adapted for one day, and habituation trials occurred on the following two days. On the third day, object exploration and novel location testing occurred during the circadian day (CT4) or night (CT15). (D) Graphical representation of NOL results. Note that a significant time-of-day difference for discrimination index was observed in control mice but not in UCMS mice. (E) Contextual fear conditioning paradigm: after dark adaptation, mice were trained to associate a context box with a footshock (training). 24 h after training, mice were placed in the box every 12 h during circadian day and night timepoints to profile freezing behavior. (F) Graphical representation of freezing percentage (averaged across the first three day timepoints and the first three night timepoints). N = 16 animals per group. Data are presented as mean $\pm$ SEM. *: $p < 0.05$; n.s. = not significant.

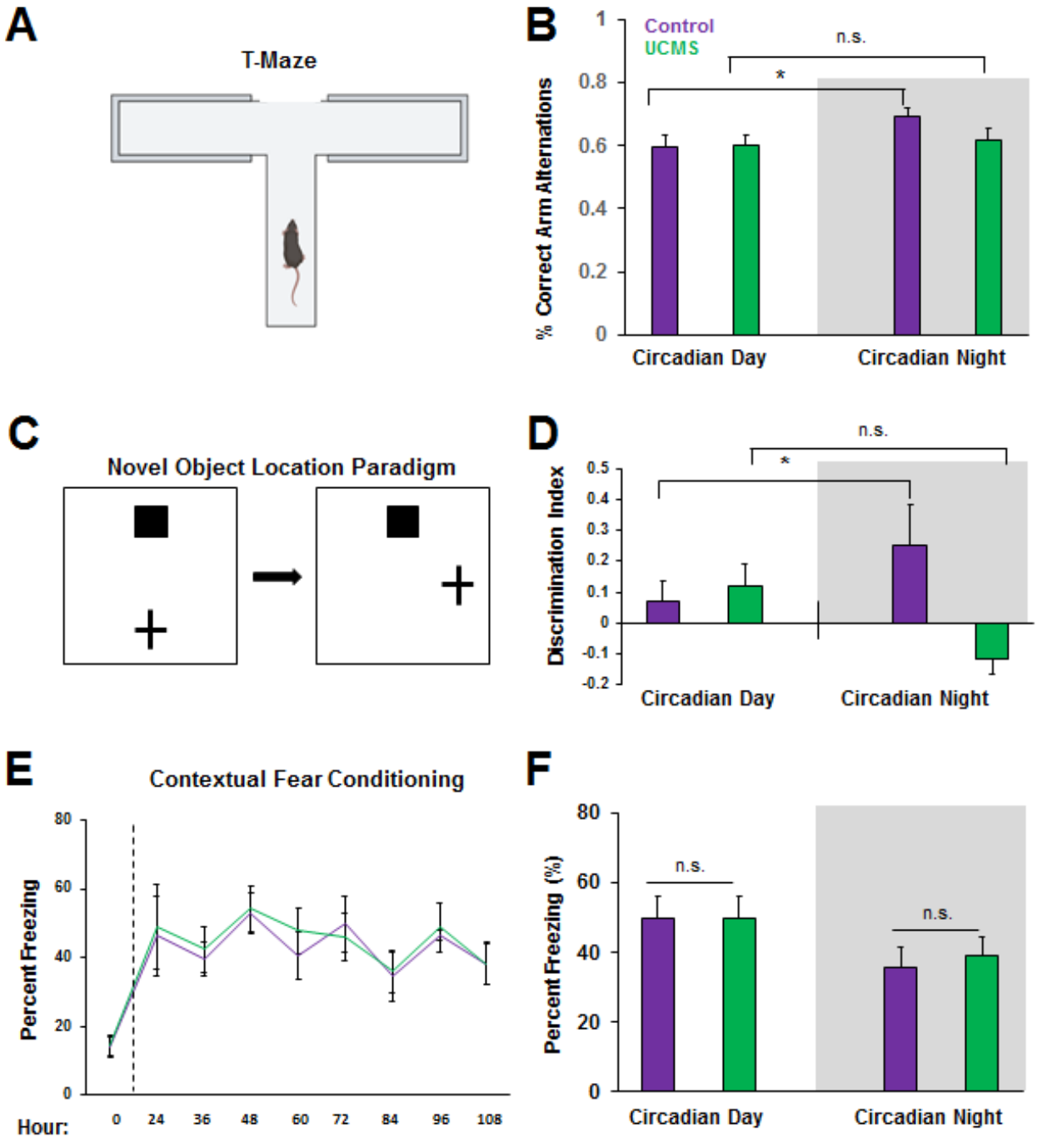
A
T-Maze
B
Control
UCMS
n.s.
*
% Correct Arm Alternations
1
0.8
0.6
0.4
0.2
0
Circadian Day
Circadian Night
C
Novel Object Location Paradigm
D
n.s.
*
Discrimination Index
0.5
0.4
0.3
0.2
0.1
0
-0.1
-0.2
Circadian Day
Circadian Night
E
Contextual Fear Conditioning
Percent Freezing
80
60
40
20
0
Hour:
0
24
36
48
60
72
84
96
108
F
Percent Freezing (%)
80
60
40
20
0
n.s.
n.s.
Circadian Day
Circadian Night

Figure 5.5 Expression of *Per1*-Venus in the SCN in control and UCMS-exposed mice
(A) Representative images of Venus expression in the SCN across the circadian day in control (top) and UCMS-exposed (bottom) animals. (B) Quantification of whole-SCN Venus intensity. A marked TOD difference, with peak at CT10, was observed in control and stressed animals. N = 3-5 animals per condition. (C) At the individual cell level, a heterogeneous expression pattern of Venus is observed. (D) No differences in Venus fluorescent intensity were observed between control and UCMS exposed animals. Each dot on the graph represents Venus values for a single cell (n = 600 SCN cells analyzed for each group: control and UCMS—collected from 4 control and 4 UCMS animals during the circadian day). Data are presented as mean ± SEM. n.s. = not significant.

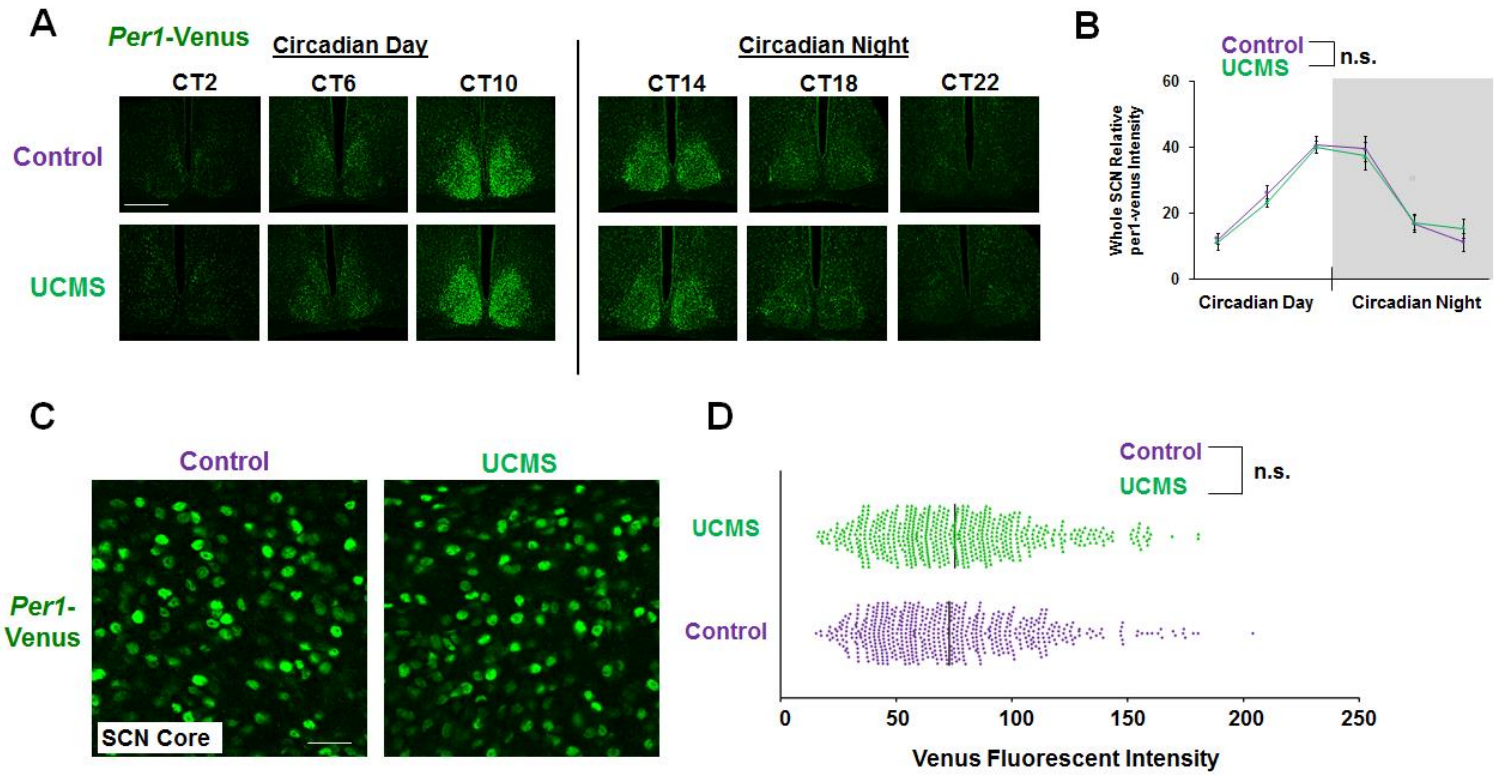

Figure 5.6 Venus organotypic slice culture in control and UCMS-exposed mice
(A) Representative traces from organotypic slices from control (top) and UCMS (bottom) mice containing the SCN were cultured and images were acquired for every hour for ~4 consecutive days. The images shown in the figure were taken at 4 h intervals. (B) Graphical representation of the de-trended traces from control and stressed mice. (C) Statistical representation of the period (left panel) and amplitude (right panel) from the slice analysis. N = 9-10 animals per group. Data are presented as mean ± SEM and were analyzed with Student's t-test. n.s. = not significant.

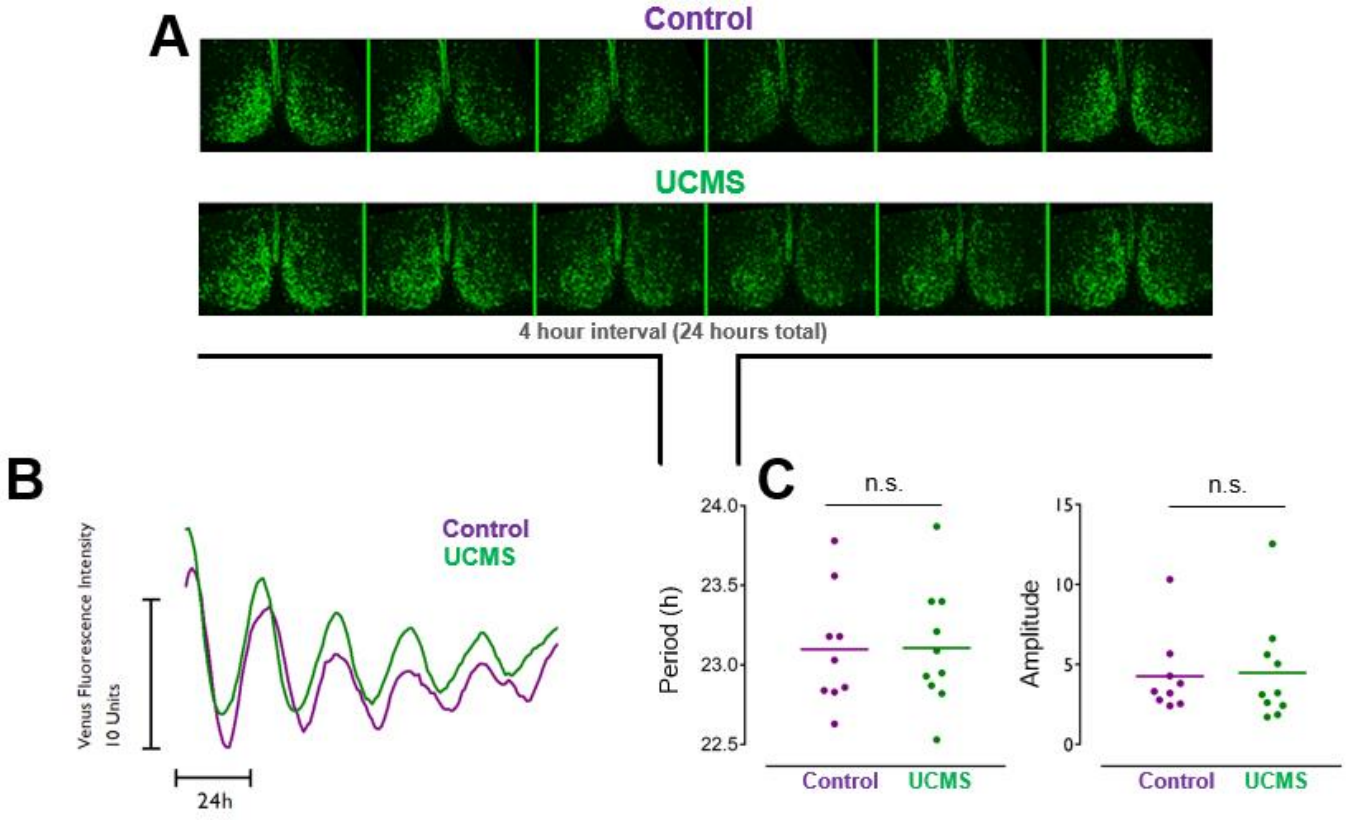

Figure 5.7 Profiling wheel running activity in control and UCMS-exposed animals
(A) Representative wheel running plots (actograms) of individual control (left) or UCMS exposed (right) animals maintained in a 12:12 light:dark (LD) cycle. Note that each row represents a 24 hour period (double plotted), and black notches indicate a 5-minute bin of wheel running activity. After approximately 45 days in LD, mice were transferred to total darkness (DD) to monitor free-running activity. Further, to examine light entrainment properties of UCMS exposed mice, a 15 minute (40 lux) light pulse was given at CT15 (yellow arrows) in order to induce a phase delay. (B) Tabular representation of wheel running statistical analyses in control and chronically stressed animals. Note that only nighttime activity was significantly different between control and UCMS mice (student's t-tests). Data was collected from 13-16 mice per group. (C) Average daily activity profiles of control and UCMS mice, averaged from 4-5 animals per group. Data are presented as mean ± SEM and were analyzed with Student's t-test. n.s. = not significant.

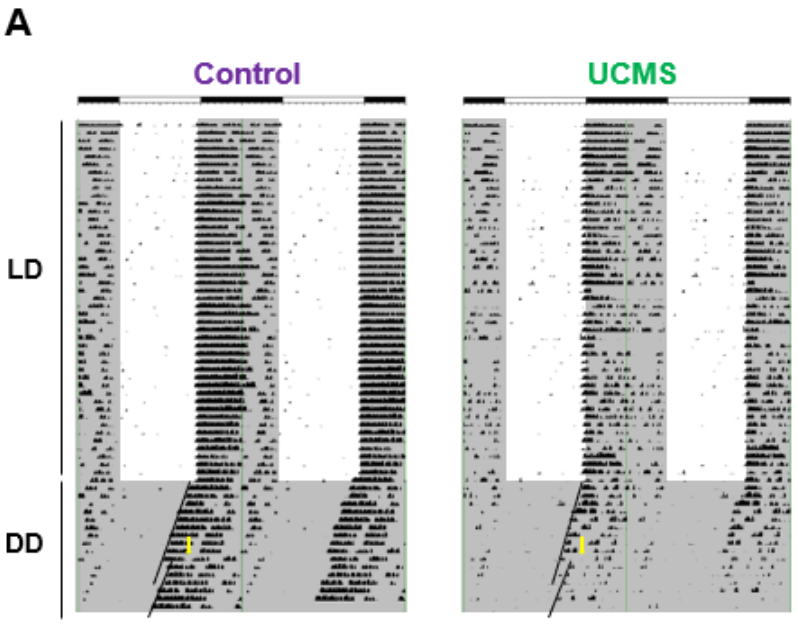

B

Parameter (mean ±SE)	Control	UCMS	*P* Value
Circadian period (τ) in DD (hr)	23.50±0.09	23.50±0.04	0.970
Day activity in LD (rotations/day)	863.80+312.90	236.60+59.26	0.076
Night activity in LD (rotations/day)	11886+1048	5855±499.7	**** < 0.0001
Photic phase delay at CT15 (min)	115.60±12.47	120.50±14.65	0.802

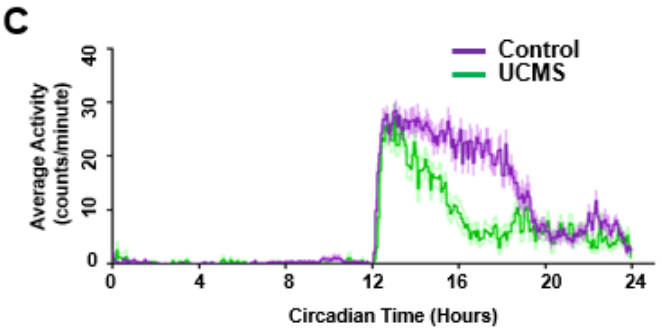

CHAPTER 6

Anatomical and functional impairment of the astrocyte syncytial network following unpredictable chronic mild stress

Introduction

The lifetime incidence of Major Depressive Disorder (MDD) in adults is over 20% (Hasin et al., 2018). Indeed, depression is one of the leading causes of disability around the world with over 4% of the global population (or over 320 million people) afflicted by the disorder (Friedrich, 2017). Notably, chronic exposure to stressful situations or life events is thought to be a major player in the development of depression (Hammen, 2005; Yang et al., 2015). From a basic research perspective, while much literature over the years has elucidated the synaptic dysfunctions/neuronal perturbations that are often associated with chronic stress and depressive-like behaviors (Duman, 2009; Duman and Aghajanian, 2012; Liu et al., 2017), there is still much to be learned about the role of astrocytes in depressed states.

Astrocytes are star-shaped glial cells that are connected via gap junctions to form an extensive network within the CNS. These gap junctions help to mediate intercellular communication by providing continuity between the cytoplasm of adjacent cells (Bennett et al., 2003). Hence, gap junctions are critical components in the establishment of a functional astrocyte syncytium whereby these intercellular channels allow for astrocytes to be electrically coupled such that they are in a state of ‘syncytial isopotentiality’—a phenomenon recently discovered by Ma et al (Kiyoshi and Zhou, 2019; Ma et al., 2016). This ability of astrocytes to remain electrically coupled to

neighboring cells (wherein the cells can equalize their membrane potentials to comparamble levels throughout the brain) allows them to function as a single unit and maintain homeostasis. Hence, it is reasonable to postulate that altered gap junction coupling may lead to the manifestation of many behaviors that are often observed in individuals with neurological disease/disorders—such as depression.

Accumulating evidence has suggested that astrocyte (dys)function may be key in the development of depressive-like behaviors observed in animal models of stress.Along these lines, a reduction in astrocyte process length and/or volume has been observed after chronic stress paradigms (Naskar and Chattarji, 2019; Tynan et al., 2013; Walker et al., 2013). Further, using sequencing-based approaches, several recent studies have shown that acute and chronic stress lead to alterations in gene expression associated with astrocyte plasticity, in addition to alterations in the expression of connexin subunits—proteins that comprise gap junctions (Murphy-Royal et al., 2020; Simard et al., 2018). These studies revealed important information about the morphological and transcriptomic changes that occur within astrocytes and accompany chronic stress. However, whether astrocyte *network* anatomy and function are altered in response to chronic stress is not yet known. To this end, until recently, techniques that accurately measure the strength of astrocytic gap junction coupling throughout the brain have been lacking, thus making it difficult to discern astrocyte network functionality.

Here, we used an *Aldh1l1*-eGFP astrocyte reporter mouse line and a six week unpredictable chronic mild stress (UCMS) model of depression to examine how astrocyte network anatomy and function change in response to stress. Using immunofluorescence

and tissue clearing techniques, we found that astrocytes in the hippocampus and/or PFC display a reduction in process length/area in addition to an increase in the distance between neighboring astrocytes after chronic stress. Further, using a novel electrophysiology (i.e. patch clamp approach), we demonstrate that chronic stress leads to a decrease in astrocyte syncytial coupling. These findings suggest that alterations in gap junction coupling between astrocytes may contribute (at least in part) to the behavioral manifestations that are often observed in individuals with MDD.

Materials and Methods

Mice

All experiments were performed in BAC *Aldh1l1*-eGFP transgenic adult (i.e. at least six weeks of age) animals. These mice have been described in our previous papers (Kiyoshi et al., 2018; Yang et al., 2011a; Zhong et al., 2016). All mice were housed in a 12:12 LD cycle and were given ad libitum access to water and food.

Unpredictable Chronic Mild Stress (UCMS) paradigm

The unpredictable chronic mild stress (UMCS) paradigm has been used to model depression in human subjects, and our specific model is adapted from previously published papers (Li et al., 2011; Logan et al., 2015; Monteiro et al., 2015; Willner, 1997). In brief, animals were exposed to two to three unpredictable mild stressors per day for a period of six weeks. The stressors were performed at random times throughout the day to avoid habituation. Every animal within the ‘stress’ group was exposed to the same stressors. Anxiety and depression-related behaviors were then profiled using the open

field test, tail suspension test, and sucrose splash test. Body weight and coat state was also monitored each week.

Coat state scoring

The fur/coat state of each mouse was monitored weekly by an individual blind to stress condition. This scoring system was adapted from previously described coat rating scales/protocols (Dominguez et al., 2019; Frisbee et al., 2015; Nguyen et al., 2020). In brief, the coat for each mouse was assigned a score ranging from 1 to 4, and this score was determined by assigning individual scores to 8 total body regions: head, neck, dorsal coat, ventral coat, tail, forelimbs, hindlimbs, and genital region. The final score was then calculated as the sum of the score for each body part divided by 8 (the number of body regions). The scoring system for fur state is noted below for reference:

1: coat is extremely shiny and smooth; no bald patches or discoloration

2: coat is largely smooth, but a few ‘spikey’ patches can be noted

3: small ‘bald’ patches are noticeable and slight discoloration is also apparent

4: several bald patches can be noted; fur is not shiny and discoloration and/or many ‘spikey’ fur patches are obvious

Open field test

The open field test was was adapted from a recently published paper (Aten et al., 2019) and was conducted under dim white light. In brief, animals were placed in the arena and were given 10 minutes to explore. A video camera was used to record each trial. The bottom surface and the walls of the arena were wiped with ethanol between

trials.The number of center entries and the total time spent in the center of the arena were analyzed by an experimenter blind to stress condition.

Tail suspension test

The tail suspension test was adapted from a protocol described by (Cryan et al., 2005). Briefly, mice were hung upside down for a 6 minute period, and a video camera recorded each trial. The total time spent immobile (i.e. freezing) and the latency to the first immobile episode was recorded by an experimenter blind to stress condition.

Sucrose splash test

The sucrose splash test (a readout of self care) was adapted from a previously published paper (Isingrini et al., 2010b). While in the home cage, the dorsal coat of each mouse was sprayed with three ‘squirts’ of 10% sucrose solution, which dirties the fur and causes the animals to initiate grooming behavior. A video camera then recorded the grooming behavior (which was defined as the mouse licking his/her dorsal coat to clean off the sucrose). The number of grooming bouts and the total time spent grooming during the 5 minute period were subsequently analyzed.

Tissue processing for immunofluorescence

Tissue was processed using methods adapted from previously published papers (Aten et al., 2021, 2019, 2018a). Along these lines, mice were sacrificed via rapid cervical dislocation, and brains were cut into ~600 μm thick sections (hippocampus and PFC) on a vibratome. Sections were then fixed in 4% PFA—which was diluted in 1X PBS—for 6 h at 4C. Sections were then cryoprotected overnight in 30% sucrose solution (in 1X PBS). ~30 um thick sections were then cut on a freezing microtome.

Immunofluorescent staining, imaging, and analysis

Labeling of tissue for immunofluorescence experiments was adapted from a protocol published in a recent study (Aten et al., 2018b). For visualization of the *Aldh1l1*-eGFP transgene expression throughout the brain (serial sections), 30 um thick tissue sections were mounted onto a slide (i.e. no primary antibody was applied), and images were acquired.

To visualize *Aldh1l1*-eGFP expression with the astrocytic marker GFAP and the neuronal marker NeuN, brain sections were washed/permeabalized in PBST, blocked in 3% bovine serum alum (BSA)/PBST for 1 hour at room termperature before overnight incubation in the following primary antibodies: to enhance the GFP transgene, chicken anti-GFP (1:40,000; Aves Cat # GFP-1010), rat anti-GFAP (1: 20,000 Invitrogen, Cat # 13-0300), and guinea pig anti-NeuN (1:5,000 Millipore Sigma, Cat # ABN90). The next day (after washes), sections were incubated for 2 hours in Alexa Fluor 488 goat anti-chicken IgY, Alexa 594 goat anti-rat IgY, and anti-guinea pig Cy5 respectively (1:1500 each diluted in PBST). Tissue was then incubated in hoescht (1:3000 diluted in PBST) for 10 min before being washed, mounted, and coverslipped with Fluoromount G. 20X images were then acquired on a Leica SP8 confocal to visualize colocalization (or lack thereof, in the case of NeuN and the *Aldh1l1*-eGFP transgene).

For *Aldh1l1*-eGFP immunofluorescence for astrocyte morphological analysis within the PFC and hippocampus, a staining protocol was adapted from a recently described paper (Huang et al., 2020). Two sections per mouse were stained using a protocol similar to that described above. However, after washing and blocking steps,

sections were incubated in chicken anti-GFP (1:800; Aves Labs Cat# GFP-1010). The next day, sections were incubated in 1:2000 Alexa Fluor 488 goat-anti chicken IgY (1:2000 dilution in PBST). Sections were then mounted and coverslipped in Fluoromount G. 40x (oil) images (layer II of the PFC and stratum radiatum region of the CA1) were acquired using a Leica SP8 confocal with the following parameters held constant for each condition (stress and control). 1024 x1024 scan format, 1 um step size (bit depth of 12), 16 line average, 300 Hz scan speed, 1.0 AU pinhole, and 1.0 zoom. For analysis of astrocyte morphology, Imaris v9.1 (Bitplane) was utilized. Note that entire astrocytes were analyzed (i.e. partial astrocytes wherein somas were not within the z-stack range were not analyzed) (Lanjakornsiripan et al., 2018). Further, astrocytes chosen for analysis were clearly defined (i.e. not joined together). An experimenter blinded to conditions validated the criteria automated by Imaris. 3D surface rendering was then performed using the Imaris surface module. The selected astrocytes were then color-coded (in a heatmap fashion) according to the surface area of the entire astrocyte. The Imaris Filament module was also used to analyze astrocyte process length. Along these lines, the astrocytic branches were outlined using Autopath with starting point and seed point held constant between conditions (control and stress). Data were then extracted and input into Prism software for statistical analysis.

For connexin 30 and 43 staining, a similar immunofluorescence protocol was used as described above. After washing and blocking steps, sections (2 per mouse per region: hippocampus and PFC) were incubated in rabbit anti-connexin 30 (Intritogen Cat 71-2200; 1:1000 dilution in PBST) and mouse anti-connexin 43 (ThermoFisher Cat13-

8300; 1:500 dilution in PBST). Note that GFP primary antibody was not used to amplify the *Aldh1l1*-eGFP transgene signal in these sections. The following day, sections were washed and incubated in anti-mouse Cy5 (1:1000 dilution in PBST) and anti-rabbit Cy3 (1:1000 dilution in PBST). Sections were then washed and incubated in hoescht (1:3000 dilution in PBST) before being mounted and coverslipped. 40X oil z stack images were acquired on a Leica SP8 confocal using the following imaging paramters, which were held constant between stress condition: 1.0 zoom, 1.0 AU pinhole, 1024x1024 scan format, 200 Hz scan speed, 2 um step size (bit depth of 12). All z-stack images were then imported into ImageJ for analysis of connexin 30/43 immunreactive puncta per area.

Tissue processing for CUBIC tissue clearing

Control and stressed animals were injected with 8% chloral hydrate in 0.9% saline. Once anesthetized, transcardial perfusion was performed with a rate of flow ~3 mL/min. Note that animals were first perfused with PBS followed by a 4% PFA/PBS solution. Brains were then extracted, cut to ~2 mm thick sections using a mouse brain matrix, and finally post-fixed for ~9 hours in 4% PFA/PBS at 4C. Brains were covered and stored at 4C until CUBIC clearing was performed.

CUBIC tissue clearing, immunofluorescent staining, imaging, and analysis

CUBIC tissue clearing was adapted from methods previously described (Kiyoshi et al., 2018; Susaki et al., 2015, 2014; Tainaka et al., 2014). To begin, 2 mm thick perfused coronal brain sections were cut to ~400 um on a microtome. Sections were then incubated in CUBIC reagent-1 for two days at room temperature (covered; on a laboratory shaker/rocker). Brain slices were subsequently blocked in a solution

containing 5% normal donkey serum (NDS) and 0.1% Triton X-100 in PBS for 1 day at room temperature. Next, sections were incubated in primary antibody (1:1000 anti-guinea pig NeuN Millipore Sigma, Cat # ABN90) for two days at room temperature in 10% NDS and 0.05% Triton X-100 in PBS. Next, brain slices were washed in PBS (3 washes; 3 hrs/wash) and incubated in secondary antibody (anti-guinea pig Cy5; 1:1000 dilution in 10% NDS, 0.05% Triton-X 100 PBS). Sections were then placed back into CUBIC reagent-1 for 1 day before imaging.

CUBIC images were acquired on a Leica SP8 confocal (~2 sections per mouse per region). The following imaging settings were held constant between stress condition: 10X magnification; 2.0 zoom; 1.0 AU pinhole; 512x512 scan format; 400 scan speed; 1 um thick step size. Tissue was imaged to ~300 um in depth.

Astrocyte cell density in control and UCMS CUBIC samples was analyzed using LASX software wherein the physical length (X, Y, and Z) was used to determine the volume of each ROI within the CUBIC-cleared image. The image was then imported into ImageJ, and the number of *Aldh1l1* eGFP positive cells was manually counted/tagged by an experimenter blind to stress condition in order to obtain a readout of astrocyte density per ROI volume. A similar protocol was performed in the acquired images in order to obtain neuronal cell density (NeuN positive cells were used to ascertain neuron density within the ROI volume).

For interastrocyte distance analysis, the pixel size for each image was first obtained using LASX software. Images were then imported into ImageJ, wherein a line

was manually drawn beween astrocytes and tagged. The length (i.e. distance) between astrocytes (analyzed from 20 cells per image) was recorded.

Finally, analysis of the number of nearest neighbors was performed in ImageJ. Reference cells were chosen (at least 25 stacks from the beginning of the image), and the number of neighboring astrocytes (within 25 um from the reference cell) were tagged. Note that the number of nearest neighbors was calculated from three reference cells per image.

Electrophysiology

Brain slice recordings were performed according to our previously published papers (Du et al., 2018; Kiyoshi et al., 2018; Wang et al., 2020). In brief, after tissue processing, coronal hippocampal and PFC slices (from both control and stressed mice) were placed in a recording chamber (RC-22; Warner Instruments) and were subsequently mounted on a BX51WI microscope (Olympus) that was equipped with infrared differential interference (IR-DIC). Slices were then perfused with oxygenated aCSF.

Pipettes used for recording were fabricated from borosilicate capillaries (Warner Instruments) by utilizing a Flaming/Brown Micropipette Puller (Sutter Instrument). Note that the standard K+ pipette solution contained 140 mM KCl, 0.5 mM CaCl2, 1 mM MgCl2, 5 mM EDTA, 10 mM Hepes, 3 mM Mg-ATP, and 0.3 mM Na2-GTP. In the K+ free-Na+ pipette solution, the KCl was substituted with 140 mM NaCl.

Patch clamp (whole cell) recordings were conducted with a MultiClamp 700B amplifer and pClamp 9.2 software system (Molecular Devices). Also note that at least a 2 GΩ seal resistance was needed before membrane rupture into the whole-cell

configuration. Further, all electrophysiological experiments were performed at room temperature.

Statistics

Statistics were performed using GraphPad Prism 7.0 software, and data are presented as the mean ± SEM. However, as noted above, patch clamp recording data was analyzed using Clampfit 9.0. As noted in the legends, significance for experiments was set at $*p < 0.05$. Further, statistical comparisons between two groups were done using Student's t-tests, while comparisons between more than three groups/conditions/timepoints were done using an ANOVA. Further, post-hoc tests were conducted to show an interaction obtained from significant ANOVA results. Finally, Grubb's test was performed on each data set to test whether statistically significant outliers were found in each group.

Also note that a 'Z-emotionality score' was calculated based upon the open field, tail suspension, and sucrose splash test results. This emotionality score was adapted from a previously published paper (Shepard et al., 2016), and it was conducted because multiple behavioral testing paradigms in rodents may produce variability between testing. To do this, a Z-score was first determined for each parameter within each behavioral test using the following equation, wherein X refers to the data for the individual parameter within each test, μ refers to the mean for the control group, and σ refers to the standard deviation of the control group.

$$Z = (X - \mu) / \sigma$$

A Z-score for each behavioral test was then calculated by taking the average of each parameter for each paradigm, and the overall emotionality score was calculated by taking the average Z-score values across the behavioral tests.

Results

Expression of astrocytic Aldh1l1-eGFP transgene throughout the brain

To begin, we first confirmed that the *Aldh1l1*-eGFP transgene is expressed within the PFC and the hippocampus (two regions implicated in the etiology of depression) and that the transgene is specifically expressed within astrocytes. Indeed, serial sections acquired throughout the coronal aspect of the brain revealed the expression of the transgene in both noted regions (Fig. 6.1A). Further, co-labeling experiments with the neuronal marker NeuN and astrocytic marker GFAP revealed that the transgene is only found within astrocytes, and not neurons, as expected (Fig. 6.1B).

Six weeks of UCMS elicits depression-and anxiety-like behaviors in Aldh1l1-eGFP mice

To determine whether chronic stress influences astrocyte network anatomy and functionality, we turned to an unpredictable chronic mild stress (UCMS) paradigm that has been widely used in rodents to model depression (Li et al., 2011; Logan et al., 2015; Monteiro et al., 2015; Willner, 1997) (Fig. 6.1C; Table 6.1). Following the six-week UCMS paradigm, body weight and coat state in addition to depression and anxiety-like behaviors were measured. Similar to a previously published report (S. Zhu et al., 2014), we found that our chronic stress paradigm led to a reduction in body weight gain across the six week period (Fig. 6.1D). Specifically, we found a significant interaction between

stress condition and body weight gain over time (Fig. 6.1D; $F_{(5, 125)} = 4.066$; $p = 0.0019$; Repeated Measures ANOVA). Post-hoc tests revealed a significant reduction in body weight in stressed animals at week 3, week 4, and week 6 (Fig. 6.1D; $p = 0.0001$, $p = 0.0223$, and $p = 0.0227$, respectively). Similarly, we found a significant increase in coat/fur state score (Fig. 6.2A) in UCMS mice (Fig. 6.1E; $F_{(5, 125)} = 12.45$; $p < 0.0001$; Repeated Measures ANOVA). Specifically, post hoc tests revealed a significant increase in coat score during weeks 3-6 (Fig. 6.1E; $p = 0.0122$ for week 3, $p < 0.0001$ for week 4, $p < 0.0001$ for week 5, and $p < 0.0001$ for week 6). Together, these data suggest that the UCMS paradigm leads to worsened fur state and a decrease in body weight gain.

Turning to the open field test, we found that that chronic stress led to a decrease in the number of center entries in the arena (Fig. 6.1F; $t_{(24)} = 2.6265$; $p = 0.0148$; t-test) and the total time spent in the center of the arena (Fig. 6.1F; $t_{(24)} = 5.272$; $p < 0.0001$; t-test). Additionally, chronic stress led to a trending increase in the total time spent immobile in the tail suspension test (Fig. 6.1G; $t_{(25)} = 1.981$; $p = 0.0587$; t-test). The latency to first immobility was also decreased in stressed animals (Fig. 6.1G; $t_{(25)} = 2.069$; $p = 0.0491$; t-test). Finally, in the sucrose splash test, we found a decrease (albeit non-significant) in the number of grooming bouts in stressed mice (Fig. 6.1H; $t_{(21)} = 1.91$; $p = 0.0699$; t-test) and a significant decrease in the time spent grooming (Fig. 6.1H; $t_{(21)} = 3.078$; $p = 0.0057$; t-test).

The depressive-like behaviors in UCMS-exposed animals were also observed from analysis of z-scores within the respective paradigms. For example, we found a significant increase in the open field, tail suspension, and sucrose splash z-scores in

stressed animals (Fig. 6.2B-6.2D; $t_{(24)} = 4.017$; $p = 0.0005$; t-test for open field; $t_{(25)} = 2.247$; $p = 0.0337$; t-test for tail suspension; and $t_{(21)} = 2.702$; $p = 0.0134$; t-test for sucrose splash). Furthermore, the z-emotionality score (a readout of the combined behavioral results) (Fig. 6.2E) revealed a significant increase in stressed animals (Fig. 6.2F; $t_{(25)} = 4.798$); $p < 0.0001$; t-test). Taken together, these combined behavioral results reveal that our chronic stress paradigm was effective in eliciting depressive and anxiety-like behaviors.

UCMS leads to changes in astrocyte morphological complexity

To begin to profile changes in astrocyte anatomy after stress, we first asked whether individual astrocytes display morphological alterations after the chronic stress paradigm. To answer this question, we sacrificed control and stressed animals, collected hippocampal and PFC tissue, and immunolabeled for the *Aldh1l1*-eGFP transgene. We then conducted high magnification/high resolution confocal microscopy to map (in detail) changes within astrocyte process length and area (Fig. 6.3A-6.3B). Using filament tracing, we found that chronic stress led to a reduction in total astrocyte process length within both the hippocampus and the PFC (Fig. 6.3C1). Indeed, our analysis revealed a difference in process length within the hippocampus (Fig. 6.3C1; $t_{(5)} = 3.844$; $p = 0.0121$; t-test) and a significant difference between process length in the PFC (Fig. 6.3C1; $t_{(9)} = 3.475$; $p = 0.0070$; t-test). Furthermore, correlation between total hippocampal astrocyte process length and Z-emotionality score revealed a trending negative correlation (Fig. 6.3C2; $r = -0.4323$; $p = 0.1663$; one-tailed Pearson analysis) and a significant negative correlation between total PFC astrocyte process length and emotionality score (Fig.

6.3C2; r = -0.7124; p = 0.0069; one-tailed Pearson analysis). Turning to surface area analysis, we found a significant decrease in average astrocyte surface area in chronically stressed animals (Fig. 6.3D1). Analysis revealed a significant decrease in hippocampal astrocytic surface area after stress (Fig. 6.3D1; $t_{(10)} = 4.433$; p = 0.0013; t-test). Note that significance within the PFC was not reached (Fig. 6.3D1; $t_{(10)} = 1.02$; p = 0.3316; t-test). Additionally, correlation between average astrocyte surface area within the hippocampus and Z-emotionality score revealed a significant negative correlation (Fig. 6.3D2; r = -0.7707; p = 0.0017; one-tailed Pearson analysis) though a significant correlation was not observed between average PFC area and emotionality score (Fig. 6.3D2; r = -0.1733; p = 0.2951; one-tailed Pearson analysis). Taken together, these data suggest that at the *individual* cell level, the six week chronic stress paradigms leads to changes in astrocyte morphology.

UCMS leads to increase in interastrocyte distance within the hippocampus and PFC

Given the anatomical changes in *individual* astrocytes after chronic stress, we then asked whether astrocyte *network* anatomy might be altered after chronic stress. Hence, control and UCMS mice were sacrificed via cardiac perfusion, and thick hippocampal (stratum radiatum) and PFC (layer II) brain slabs were collected. Tissue sections were then placed in CUBIC tissue clearing reagent and were subsequently imaged using confocal microscopy (Fig. 6.4A-6.4B). After imaging, astrocyte cell density, interastrocyte distance, and the number of nearest neighbors (Fig. 6.4C) were then analyzed in both hippocampal and PFC sections. The inerastrocyte distance was measured as described in our recently published paper (Kiyoshi et al., 2018). Along these

lines, the distance was measured between nearest neighbors at the center of the cell body. Note that a randomly selected cell was used as the reference cell, and neighboring cells were defined as astrocytes that were next to the reference cell (with no blood vessel in between). Interestingly, our analysis of interastrocyte distance revealed that the distance between both hippocampal and PFC astrocytes was significantly increased by chronic stress (Fig. 6.4E; $t_{(12)} = 2.856$; $p = 0.0145$; t-test for hippocampus and Fig. 6.4E; $t_{(10)} = 3.812$; $p = 0.0.0034$; t-test for PFC).

UCMS does not alter astrocyte or neuron density or number of nearest neighbors

We next tested whether astrocyte density and number of nearest neighboring astrocytes was altered by UCMS. Our analysis revealed that chronic stress did not change the density of astrocytes within either brain region (Fig. 6.4D; $t_{(12)} = 0.7034$; $p = 0.4953$; t-test within the hippocampus and Fig. 6.4D; $t_{(11)} = 0.4409$; $p = 0.6679$; t-test for PFC). Furthermore, we also immunolabeled for NeuN in our CUBIC (i.e. brain-cleared) sections (Fig. 6.5A-6.5B). Our analysis of NeuN density revealed no significant difference in neuron density between control and stressed animals (Fig. 6.5C; $t_{(11)} = 0.1411$; $p = 0.8903$; t-test for hippocampus and Fig. 6.5C; $t_{(10)} = 1.493$; $p = 0.1664$; t-test for PFC). Together, these results suggest the neither astrocyte nor neuron density are altered by stress.

Finally, our previously published papers found that within the murine hippocampus, interastrocytic electrical coupling and having at least 7-9 nearest neighbor (astrocytes) are key factors that underpin strong syncytial coupling (Kiyoshi et al., 2018; Ma et al., 2016). Given this, we were interested in determining whether chronic stress

may alter the number of nearest neighboring astrocytes (Fig. 6.4C3). Interestingly, we found no significant difference between the number of nearest neighbors and stress condition (Fig. 6.4F; $t_{(12)} = 0.6384$; $p = 0.5352$; t-test for hippocampus and Fig. 6.4F; $t_{(11)} = 0.389$; $p = 0.7047$; t-test for PFC). Thus, while six weeks of chronic stress alters interastrocyte distance, it does not appear to alter the number of nearest neighboring astrocytes.

UCMS leads to weakened astrocyte gap junction coupling

We next asked whether the network-level anatomical differences in stressed animals (i.e. the increased interastrocyte distance) may lead to differences in the strength of synctytical isopotentiatlity within these limbic (i.e. hippocampus and PFC) regions. To test this idea, we used a K+-free/Na+ pipette solution to substitute the endogenous K+ content in whole-cell recording which in theory should subsequently leads to a Vm depolarization (toward 0 mV) as anticipated from the Nernst equation. Notably, we have shown that the Vm (recorded with [Na+]P from astrocytes in situ wherein the cells are coupled) does not obey the Nerstian prediction, and instead, the Vm remains at quasi-physiological conditions level at the steady state (Vm, ss) (Kiyoshi et al., 2018; Ma et al., 2016). In our [Na+]P recording of both hippocampal and PFC astrocytes (from control and stressed mice), the Vm, I (indicative of the resting membrane potential), revealed no significant differences between the groups (Fig. 6.6A; $t = -1.269$; $p = 0.231$; unpaired t-test for hippocampus and Fig. 6.6A; $t = 0.354$; $p = 0.726$; unpaired t-test for PFC). However, the membrane potential in stressed animals showed more depolarization relative to control animals (indicated by the shift in Vm,ss toward more positive values)

(Fig. 6.6B). Indeed, within the hippocampus, the Vm,ss in astrocytes recorded from control animals was –72.26 mV, while that of UMCS astrocytes was -57.89 mV, and statistical analysis revealed a significant difference between the readings (Fig. 6.6C; t = 2.401 ; p = 0.045 ; unpaired t-test). Notably, a trending difference in the PFC was also observed (Fig. 6.6C; t = -2.037; p = 0.060 ; unpaired t-test). Indeed, a depolarizing shift in the Vm, ss in several recordings from UCMS mice (from astrocytes in both the hippocampus and PFC) was noted (Fig. 6.7A and 6.7B). Taken together, these data suggest that six weeks of stress leads to a reduction in syncytial coupling strength.

UCMS does not alter the number of connexin 30/43 immunoreactive puncta within the hippocampus or PFC

Because our novel electrophysiological approach allowed us to determine that UCMS reduces the strength of astrocyte gap junction coupling, we next wanted to test whether the expression of connexin 30 and 43—two of the major proteins that from gap junctions (Nielsen et al., 2012)—are altered after stress. To this end, control and UCMS-exposed animals were sacrificed, and hippocampal and PFC brain sections were collected and stained for connexin 30 and 43 expression (Fig. 6.8A-6.8B). Analysis of connexin 30 puncta revealed no significant difference in immunoreactivity in either the hippocampus or the PFC after stress (Fig. 6.8C; $t_{(10)} = 0.8296$; p = 0.4261 for hippocampus and $t_{(10)} = 0.8638$; p = 0.4079 for PFC; t-tests). The same finding was observed with respect to connexin 43 puncta. Indeed, we found no significant effect of stress on connexin 43 immunoreactivity in either the hippocampus or the PFC (Fig. 6.8D; $t_{(10)} = 0.2755$; p = 0.7886 for hippocampus and $t_{(10)} = 1.275$; p = 0.2313 for PFC; t-tests). Together, these

results suggest that connexin 30 and 43 total protein levels are not altered by our UCMS paradigm.

Discussion

Here, we expand upon previous studies—providing data showing that astrocyte morphology is altered after chronic stress. In addition to morphological changes at the individual cell level, we also show that astrocyte network anatomy and syncytical coupling strength are altered as a result of chronic stress.

High magnification/resolution confocal imaging revealed that our six week UCMS paradigm led to a marked reduction in total astrocyte process length and surface area (Fig. 6.3), without changing the total number of astrocytes (or neurons) (Fig. 6.4 and 6.5). These findings are in line with studies published by Simard et al and Tyan et al who used chronic stress paradigms to profile cortical astroglial cells (Simard et al., 2018) (Tynan et al., 2013). Additionally, we were able to correlate these two morphological readouts (process length and surface area) with the emotionality score of each experimental animal. Here, we sould note that while we only examined the stratum radiatum and PFC (layer II) in our study, the astrocytic process atrophy that we observed in these regions is likely to be circuit specific. Indeed, the study performed by Tynan et al found no evidence of atrocytic atrophy within the motor cortex (Tynan et al., 2013)—a region that is not typically thought to be especially significant in the etiology of mood-related disorders.

With respect to understanding the implications of the individual astrocyte morphological changes observed after stress, here it should be mentioned that extensive

dendritic atrophy (and dendritic spine loss) has been observed within the PFC after chronic stress (Izquierdo et al., 2006; Radley et al., 2004; Shansky et al., 2009). Paralleling these animal studies, human imaging studies have also reported significant reductions in the volume of grey matter within the PFC in patients with a history of depression (Drevets et al., 1997; Hastings et al., 2004). Hence, while neuronal alterations/dysfunction may be a key contributer in the etiology of mood-related disorders, the precise mechanism(s) that underpin these changes are not yet known. The fact that astrocytes (within these same brain regions) also show atrophy of their process, coupled with emerging evidence suggesting that astrocytes are key players in controlling synapse formation and function (Chung et al., 2015), and that astrocytes closely associate with synapses (Ventura and Harris, 1999a) raises the prospect that astrocytes may actually be initating neuronal/synaptic dysfunction when mood disorders first arise. Given this, studies that examine whether astrocyte dysfunction proceeds (and hence significantly contributes to) neuronal dysfunction during chronic stress, are of high merit.

Turning to network-level profiling, to our knowledge, we are the first to report that astrocyte syncytial anatomy changes as a result of chronic stress. Indeed, we observed that the interastrocyte distance (i.e. the distance between two neighboring astrocytes), was increased in both the PFC and the hippocampus after chronic stress (Fig. 6.4). In control animals, the average interastrocyte distance within the hippocampus stratum radiatum subregion was ~40 um—consistent with our previously published paper (Kiyoshi et al., 2018). However, the average distance was found to be just over 45 um in stressed animals. A similar observation was also observed within the PFC. At first glance,

one may postulate that an increased astrocyte density and/or shorter inerastrocytic distance may make for an increase in the strength of astrocyte network coupling. While this may be the case in our current study (i.e. the increased interastrocyte distance after stress may play an underlying role in the strength of network coupling), it is important to note that at baseline conditions (i.e. no stress), in our previously published report, we did not observe a definitive correlation between syncytial anatomy and strength of syncytial isopotentiality (Kiyoshi et al., 2018). As such, caution should be taken when positing that the altered interastrocyte distance in stressed animals plays a causative role in the weakened coupling strength observed using our novel electrophysiological K^+-free/Na^+-containing recording pipette solution (Ma et al., 2016).

With that said; however, it was interesting to note that our electrophysiological recordings did show a weakening in syncytial coupling strength in stressed mice (Fig. 6.6). This innovative technique, which serves to create a 'reporter astrocyte' that can provide a readout of network coupling (Kiyoshi et al., 2018; Ma et al., 2016) suggests that not only individual astrocyte anatomy/morphology, but also network level coupling is impaired by chronic stress. Notably, we only profiled hippocampal and PFC subregions in our recording experiments (paralleling our morphological data). It would be interesting to test whether other mood-related regions—such as the habenula, amygdala, and nucleus accumbens—regions known to be involved in the etiology of depression-like behaviors and/or altered by stress (Browne et al., 2018; Campioni et al., 2009; Cerniauskas et al., 2019; Zhang et al., 2018)—show similar impairments in response to stress. Furthermore,

whether this weakened coupling strength is specific to limbic circuits remains to be determined.

Given our observations that network-level anatomical and electrophysiolgical differences were observed after stress and that vertebrate gap junctions are comprised of connexin proteins (Nielsen et al., 2012), we were somewhat surprised that our analysis did not reveal any effect of stress on connexin 30/43 immunoreative puncta density (Fig. 6.8). Notably, these results are in contrast to a recently published paper that found a reduction in the density of connexin 30 and 43 positive puncta in the cortex in rats exposed to a chronic stress paradigm (Miguel-Hidalgo et al., 2018). While the differential results may be attributed to differences in species and/or brain region analyzed, another study found that acute stress induces the opening of connexin 43 channels within astrocytes and that this opening is potentiated by chronic stress (Orellana et al., 2015). Thus, the regulation of gap junction coupling by connexins is likely quite complex.

Our current study did not investigate the mechanism(s) underlying the weakened gap junction coupling observed after chronic stress, or the functional ramifications of this weakened coupling on interastrocyte communication. However, placed within a mechanistic model, one of the most reasonable explanations for the data reported here is that the weakened syncytial coupling results from alterations in calcium signaling within the astrocyte network. No study (to our knowledge) has examined whether chronic stress alters both spontaneous and/or evoked calcium events within astrocyte microdomains. However, a recently published study demonstrated that acute stress leads to astrocyte atrophy and prolongs spontaneous calcium events within

astrocytes (Murphy-Royal et al., 2020). Interestingly, one of the key features of astrocytes is their ability to respond to stimuli (endogenous or exogenous) to generate calcium increases that subsequently couple to downstream cellular signaling processes to regulate animal physiology and behavior (for an excellent review, see (Guerra-Gomes et al., 2018). Hence, this calls into question the idea that calcium may serve as a potential regulator of astrocyte syncytial isopotentiality in both healthy and diseased states—a topic that is currently under investigation in our lab. Indeed, one may posit that chronic stress leads to a reduction in intracellular calcium levels which, in turn, weakens gap junction coupling strength and causes hypotrophy within individual astrocytes. Future studies that examine astrocytic calcium signaling after chronic stress—and how such signaling may regulate the state of syncytial coupling—are of high merit.

In total, these studies reveal that a six week UCMS paradigm alters not only astrocyte morphology, but also astrocyte network coupling. These observations suggest that other neuropsychiatric conditions may change the spatial organization of the astrocyte network and alter coupling strength. Hence, our study reveals important insights related to how depression disruptsastrocyte network communication.

Acknowledgements

I thank Dr. Yixing Du for her expertise in performing the electrophysiological experiments. I also thank Olivia Taylor and Courtney Dye for their assistance with Imaris astrocyte morphology analysis.

Figure 6.1 *Aldh1l1*-eGFP mouse and Unpredictable Chronic Mild Stress paradigm
(A) Coronal mouse brain sections from one *Aldh1l1*-eGFP. 30 μm thick tissue sections were mounted on slides at ~500 μm intervals to demonstrate transgene expression throughout the rostral-caudal and dorsal-ventral axis of the brain. Abbreviations: PrL = prelimbic cortex. (B) 20X representative images of the *Aldh1l1*-eGFP transgene in both the prefrontal cortex (left panel) and hippocampus (right panel). Note that *Aldh1l1*-eGFP positive cells co-localize with the astrocytic marker GFAP, but not with the neuronal marker NeuN. Scale bar: 50 μm. Abbreviations: SO = stratum radiatum; Pyr = pyramidal cell layer; SR = stratum radiatum (C) Schematic outline of the six-week Unpredictable Chronic Mild Stress (UCMS) paradigm. (D) Percent change in weight over the six-week UCMS paradigm in control (black line) and UCMS (red line) mice. Data were analyzed using ANOVA, followed by post-hoc tests. (E) Graphical representation of coat/fur state across the six-week UCMS paradigm. Data were analyzed using ANOVA, followed by post-hoc tests. (F) Graphical representation of number of center entries (left panel) and total time spent in the center or the arena (right panel) in the open field test. Data were analyzed using Student's t-test. (G) Graphical representation of the amount of time spent immobile (left panel) and the latency to the first immobility (right panel) in the tail suspension test. Data were analyzed using Student's t-test. (H) Graphical representation of the number of total grooming bouts (left panel) and the amount of time spent grooming (right panel) in the sucrose splash test. Data were analyzed using Student's t-test. * : $p < 0.05$; ** : $p < 0.01$; *** : $p < 0.001$; **** : $p < 0.0001$; n.s. = not significant. N = 11-14 animals per condition.

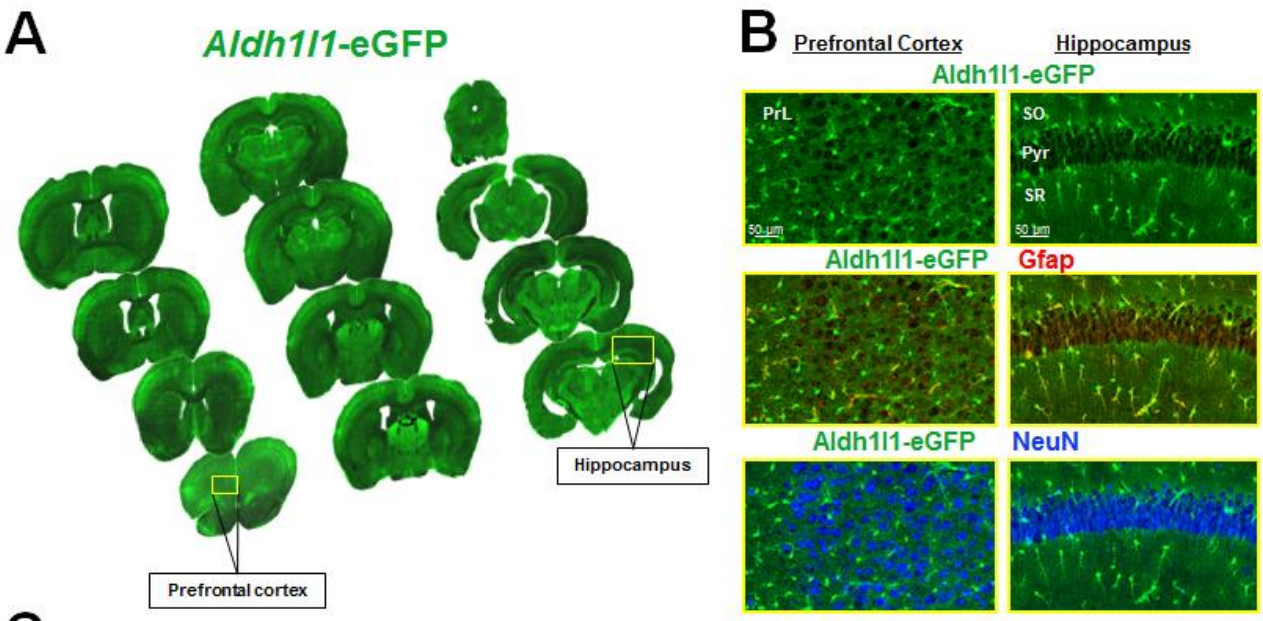
A
Aldh1l1-eGFP
Hippocampus
Prefrontal cortex
B
Prefrontal Cortex
Hippocampus
Aldh1l1-eGFP
PrL
SO
Pyr
SR
50 µm
Aldh1l1-eGFP
Gfap
Aldh1l1-eGFP
NeuN

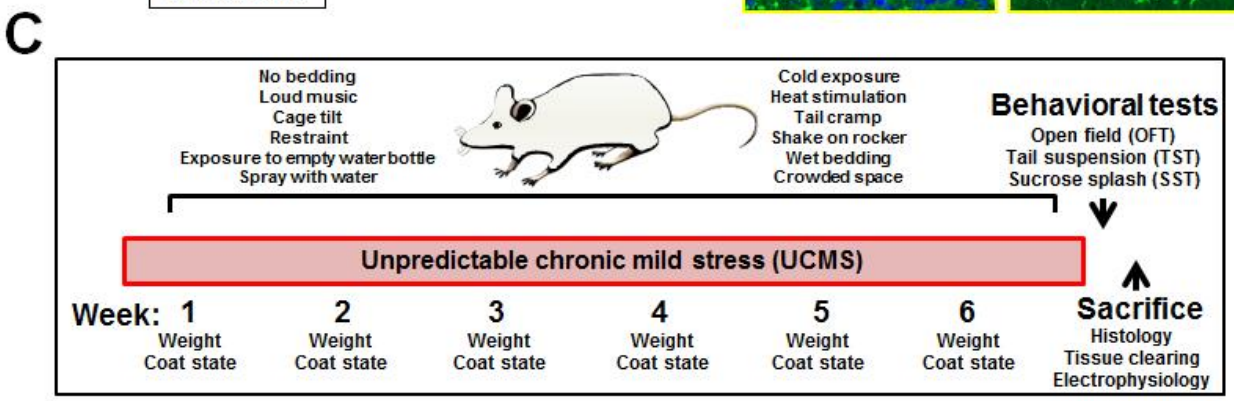
C
No bedding
Loud music
Cage tilt
Restraint
Exposure to empty water bottle
Spray with water
Cold exposure
Heat stimulation
Tail cramp
Shake on rocker
Wet bedding
Crowded space
Behavioral tests
Open field (OFT)
Tail suspension (TST)
Sucrose splash (SST)
Unpredictable chronic mild stress (UCMS)
Week: 1 2 3 4 5 6
Weight
Coat state
Sacrifice
Histology
Tissue clearing
Electrophysiology

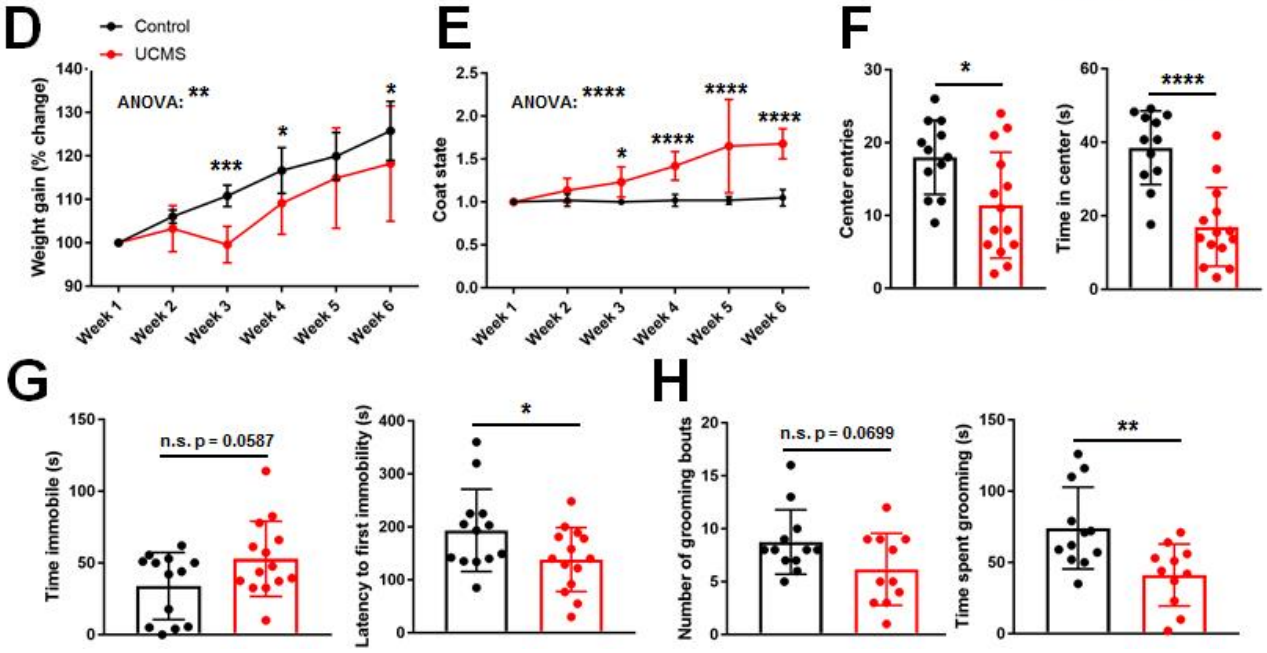
D
Control
UCMS
Weight gain (% change)
ANOVA: **
E
Coat state
ANOVA: ****
F
Center entries
Time in center (s)
G
Time immobile (s)
n.s. p = 0.0587
Latency to first immobility (s)
H
Number of grooming bouts
n.s. p = 0.0699
Time spent grooming (s)
Week 1
Week 2
Week 3
Week 4
Week 5
Week 6

Table 6.1 Example six-week UCMS schedule
Mice were exposed to 2-3 stressors each day for a period of six consecutive weeks. Of note, to prevent animals from habituating to the daily stressors, these stressors were performed at different times throughout the day (i.e. in the morning, afternoon, evening, and overnight).

Sunday	Monday	Tuesday	Wednesday	Thursday	Friday	Saturday
Tail cramp (1 min)	Restraint (2 hrs)	Wet bedding (3 hrs)	Shake on rocker (1 hr)	No bedding (4 hrs)	Loud music (3 hrs)	Spray with water (5 min)
Heat stimulation (10 min)	Loud music (3 hrs)	45º cage tilt (7 hrs)	Cold exposure (30 mn)	Heat stimulation (10 min)	Crowded space (1 hr)	Tail cramp (1 min)
	Exposure to empty water bottle (overnight)		Spray with water (5 min)	Restraint (2 hrs)		45º cage tilt (overnight)

Figure 6.2 Coat state images and Z-scores following UCMS paradigm
(A) Representative images of coat/fur state in control (left) and UCMS (right) following the six-week paradigm. (B-D) Z-score of control and UCMS mice in the open field test (left), tail suspension test (middle) and sucrose splash test (right). Data were analyzed using Student's t-test. (E) Schematic depiction of the Z-emotionality score in control and UCMS mice. Note that this Z-emotionality parameter reflects the combined Z-scores from all three noted behavioral tests (open field, tail suspension, and sucrose splash). Please see the methods section for details. (F) Graphical representation of the Z-emotionality score in control and UCMS mice. Data were analyzed using Student's t-test. * : $p < 0.05$; *** : $p < 0.001$; **** : $p < 0.0001$. N = 11-14 animals per condition.

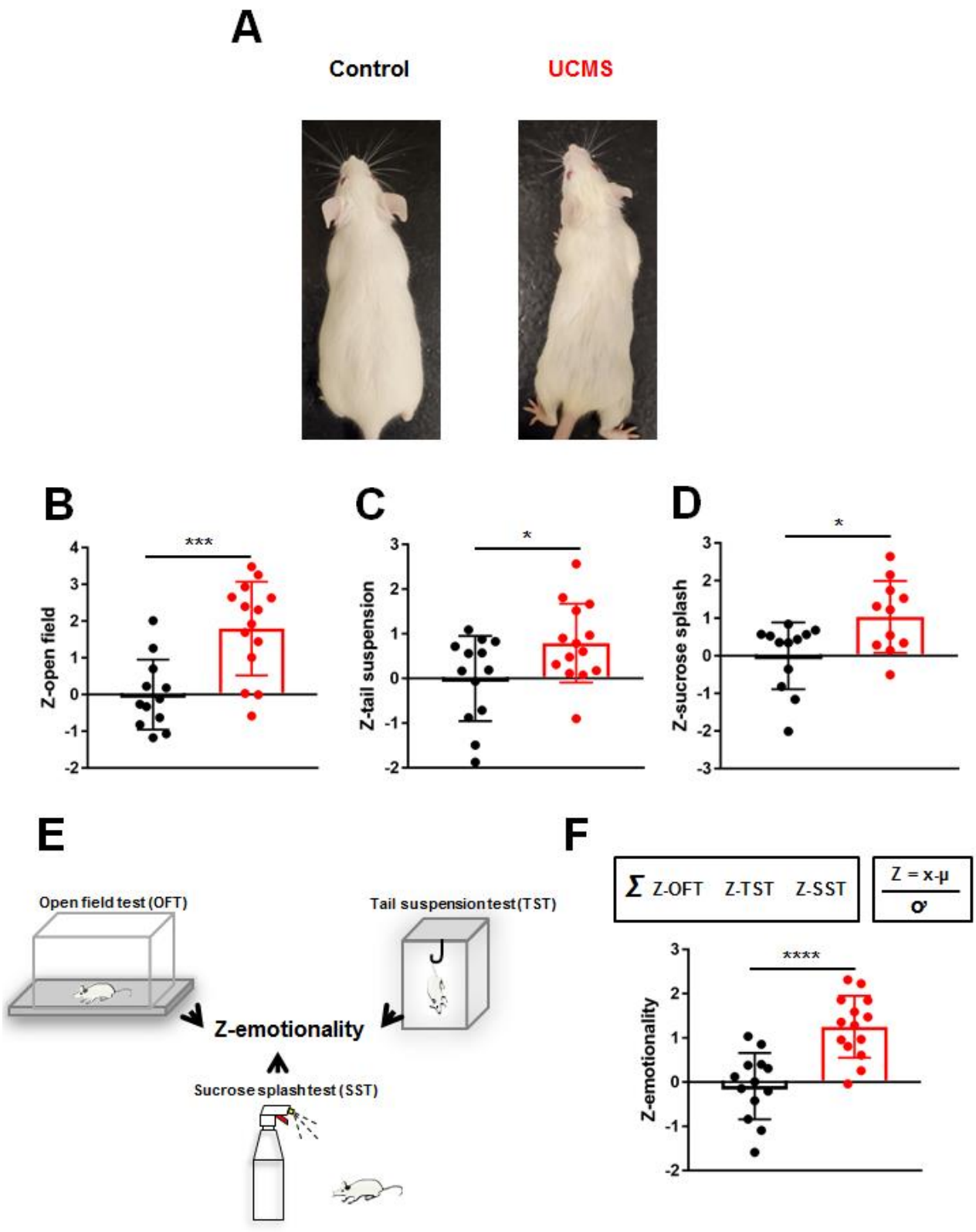
A
Control
UCMS
B
***
Z-open field
C
*
Z-tail suspension
D
*
Z-sucrose splash
E
Open field test (OFT)
Tail suspension test (TST)
Z-emotionality
Sucrose splash test (SST)
F
Σ Z-OFT Z-TST Z-SST
Z = x-μ / σ
****
Z-emotionality

Figure 6.3 Changes in astrocyte morphology after UCMS
(A1-A2) Representative 40X confocal images of *Aldh1l1*-GFP transgene in hippocampus of a control (left panel) and stressed animal (right panel). The regions boxed in white reflect the same areas depicted in 'A3-A4'. (A3-A4) Imaris filament tracing of astrocyte processes from a control (left panel) and UCMS (right panel) animal. (A5-A6) Imaris 3D-surface rendering of the same astrocytes depicted in 'A1-A4'. Note the relative increased area of astrocytes in the control section relative to the UCMS section. (B1-B2) Representative 40X confocal images of *Aldh1l1*-GFP transgene in the PFC of a control (left panel) and stressed animal (right panel). The regions boxed in white reflect the same areas depicted in 'B3-B4'. (B3-B4) Imaris filament tracing of astrocyte processes from the PFC of a control (left panel) and UCMS (right panel) animal. (B5-B6) Imaris 3D-surface rendering of the same astrocytes depicted in 'B1-B4'. (C1) Graphical analysis of Imaris filament tracing in hippocampal and PFC astrocytes from control animals (black) and UCMS animals (red). The average total astrocyte process length for each animal (analyzed from 3-4 images) is represented by each dot. Data were analyzed using Student's t-test. *: $p < 0.05$; ** : $p < 0.01$. N = 3-6 animals per stress condition. (C2) Graphical representation of correlations between average astrocyte process length (from hippocampal astrocytes: left panel and PFC astrocytes: right panel) and Z-emotionality behavioral scores. Correlations were analyzed using mice from both control (black dots) and UCMS (red dots) mice. A one-tailed Pearson analysis (using the 'R correlation coefficient') was used. N = 3-6 animals per condition. (D1) Graphical analysis of average astrocyte area (using Imaris 3D surface rendering) in hippocampal and PFC astrocytes from control animals (black) and UCMS animals (red). The average total astrocyte process area for each animal (analyzed from 3-4 images) is represented by each dot. Data were analyzed using Student's t-test. ** : $p < 0.01$; n.s. = not significant. N = 6 animals per stress condition. (D2) Graphical representation of correlations between average astrocyte process area (from hippocampal astrocytes: left panel and PFC astrocytes: right panel) and Z-emotionality behavioral scores. Correlations were analyzed using mice from both control (black dots) and UCMS (red dots) mice. A one-tailed Pearson analysis (using the 'R correlation coefficient') was used. N = 6 animals per condition.

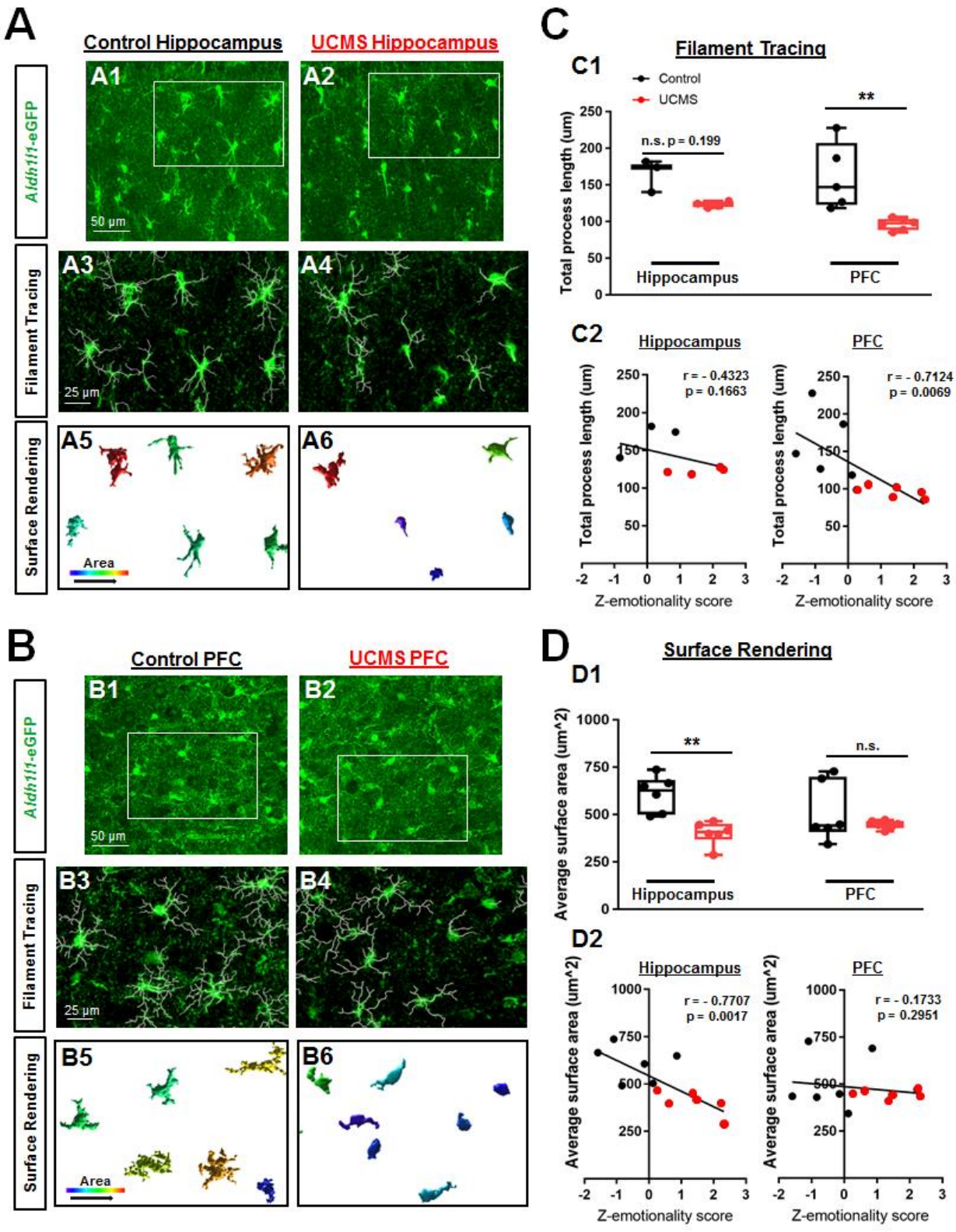
A
Control Hippocampus
UCMS Hippocampus
Aldh1l1-eGFP
Filament Tracing
Surface Rendering
A1
A2
A3
A4
A5
A6
50 μm
25 μm
Area
B
Control PFC
UCMS PFC
B1
B2
B3
B4
B5
B6
C
Filament Tracing
C1
Control
UCMS
n.s. p = 0.199
**
Total process length (um)
Hippocampus
PFC
C2
Hippocampus
PFC
r = - 0.4323
p = 0.1663
r = - 0.7124
p = 0.0069
Z-emotionality score
D
Surface Rendering
D1
n.s.
Average surface area (um^2)
D2
r = - 0.7707
p = 0.0017
r = - 0.1733
p = 0.2951

Figure 6.4 CUBIC tissue clearing in hippocampus and PFC of *Aldh1l1*-eGFP animals reveals alterations in interastrocyte distance after UCMS
(A1-A2) Representative 10X CUBIC tissue clearing in the hippocampus of a control (left panel) and UCMS (right panel) animal. Note that the red box in the larger panels approximate the locations of the zoomed-in images on the right. (B1-B2) Representative 10X CUBIC tissue clearing in the PFC of a control (left panel) and UCMS (right panel) animal. (C1) Representation of astrocyte syncytial cell density analysis, interastrocyte distance (C2), and nearest neighbors (C3). (D) Graphical representation of the density of *Aldh1l1*-eGFP positive cells in the hippocampus (left) and PFC (right) of control and stressed animals. Data was analyzed from 6-7 animals per condition using Student's t-test. (E) Graphical representation of the interastrocyte distance (i.e. the distance between astrocytes) in the hippocampus (left) and PFC (right) of control and stressed animals. (F) Graphical representation of the number of neighboring astrocytes nearest to the reference cell/astrocyte. Data was analyzed from 6-7 animals per condition using Student's t-test.*: $p < 0.05$; ** : $p < 0.01$; n.s. = not significant.

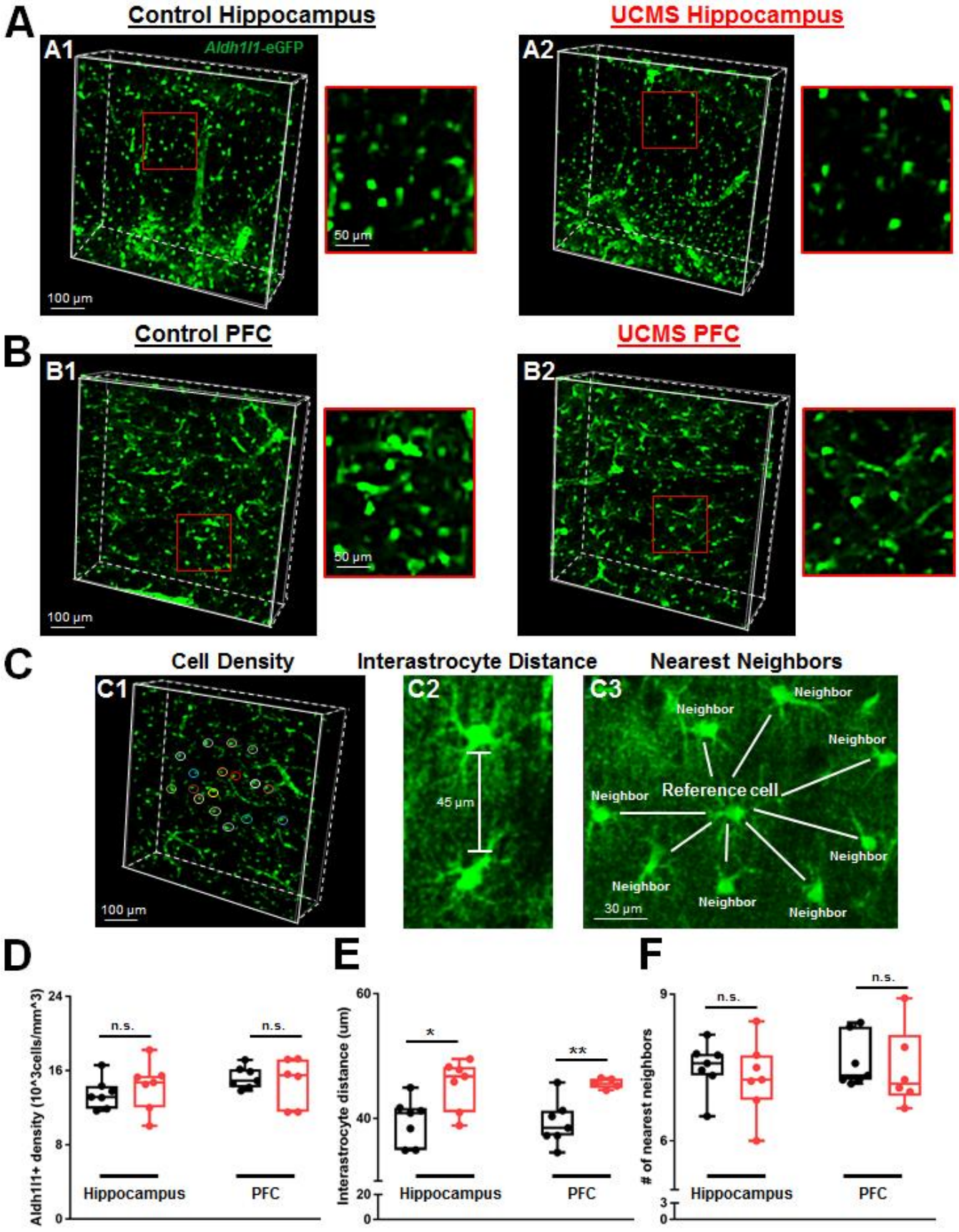
A
Control Hippocampus
UCMS Hippocampus
A1
Aldh1l1-eGFP
100 µm
50 µm
A2
B
Control PFC
UCMS PFC
B1
100 µm
50 µm
B2
C
Cell Density
Interastrocyte Distance
Nearest Neighbors
C1
100 µm
C2
45 µm
C3
Neighbor
Reference cell
30 µm
D
Aldh1l1+ density (10^3cells/mm^3)
n.s.
Hippocampus
PFC
E
Interastrocyte distance (um)
*
**
F
# of nearest neighbors

Figure 6.5 CUBIC tissue clearing in hippocampus and PFC of *Aldh1l1*-eGFP animals reveals no change in neuron density after UCMS
(A1-A2) Representative 10X CUBIC tissue clearing (and subsequent NeuN labeling) in the hippocampus of a control (left panel) and UCMS (right panel) animal. (B1-B2) Representative 10X CUBIC tissue clearing (and subsequent NeuN labeling) in the PFC of a control (left panel) and UCMS (right panel) animal. (C) Graphical representation of the density of NeuN positive cells in the hippocampus (left) and PFC (right) of control and stressed animals. Data was analyzed from 6-7 animals per condition using Student's t-test. n.s. = not significant.

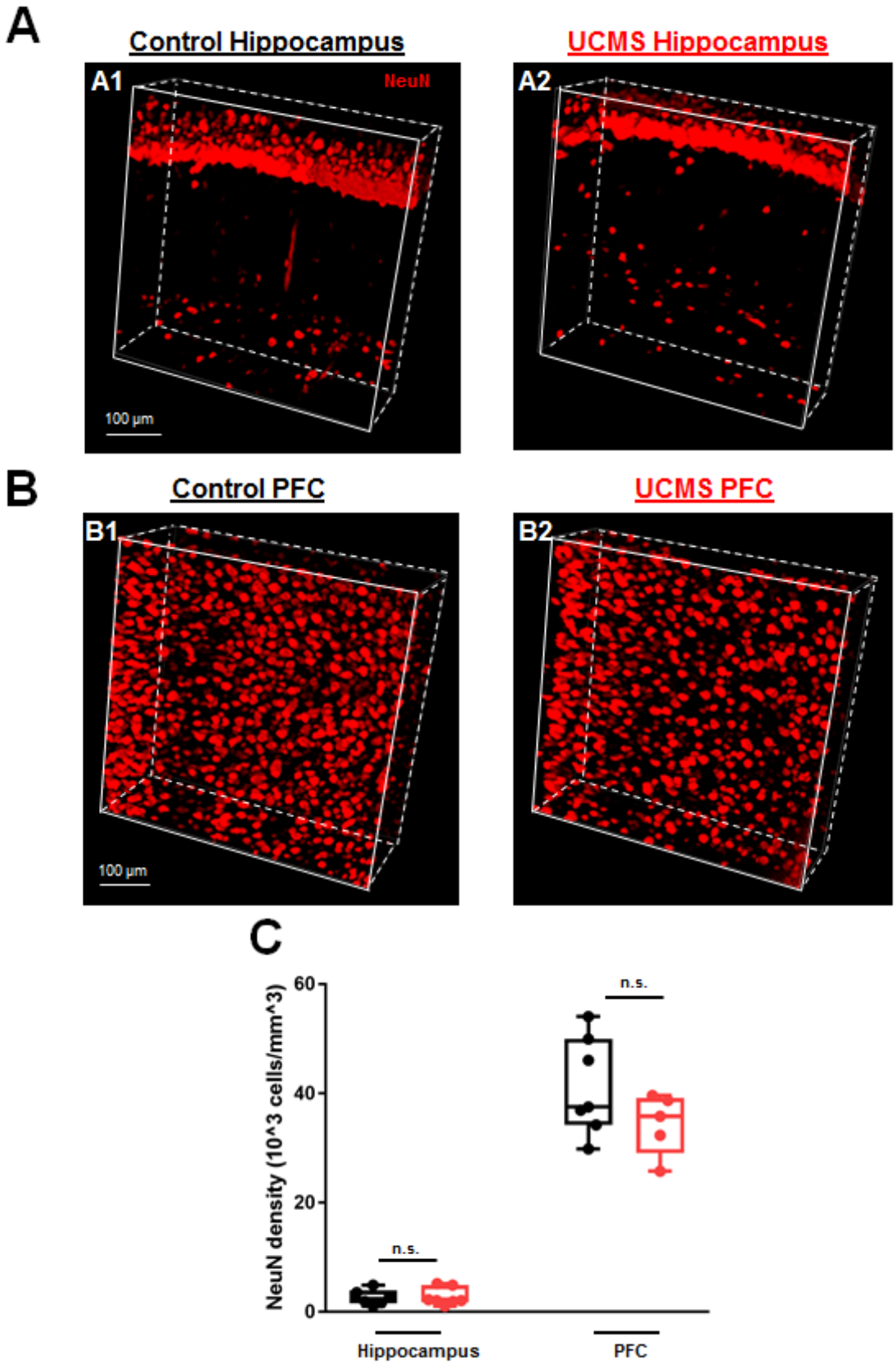
A
Control Hippocampus
UCMS Hippocampus
A1
NeuN
A2
100 μm
B
Control PFC
UCMS PFC
B1
B2
100 μm
C
NeuN density (10^3 cells/mm^3)
60
40
20
0
n.s.
n.s.
Hippocampus
PFC

Figure 6.6 UCMS impairs the strength of astrocyte syncytial coupling within the hippocampus and PFC

(A) Graphical representation of the resting membrane potential (Vm, i) after breakthrough of the cell. Note that a $[Na^+]_p$ recording was used (as a substitute for intracellular K^+ content) in order to test the strength of syncytial isopotentiality. The numerical values within each bar are indicative of the number of recorded cells. (B) Representative electrophysiological traces from astrocytes recroded from control (black) and UMCS (blue) animals. Using the same $[Na^+]_p$ recording, the steady-state Vm (Vm, ss) was also taken. Note that astrocytes recorded from slices obtained from UCMS displayed a positive shift of $V_{M,SS}$ which corresponds to a decrease in the strength of syncytial coupling. (C) Graphical representation of the Vm, ss of hippocampal astrocytes from control and UCMS-exposed animals. Note the increased Vm, ss in the UCMS group. (D) Graphical representation of the Vm, ss of PFC astrocytes from control and UCMS-exposed animals. Note the trending increase in Vm, ss in the UCMS group. For both hippocamnpal and PFC regions, 5-15 astrocyteswere recorded. Data is presented as the mean ± SEM using Student's t-test. *: $p < 0.05$; n.s. = not significant.

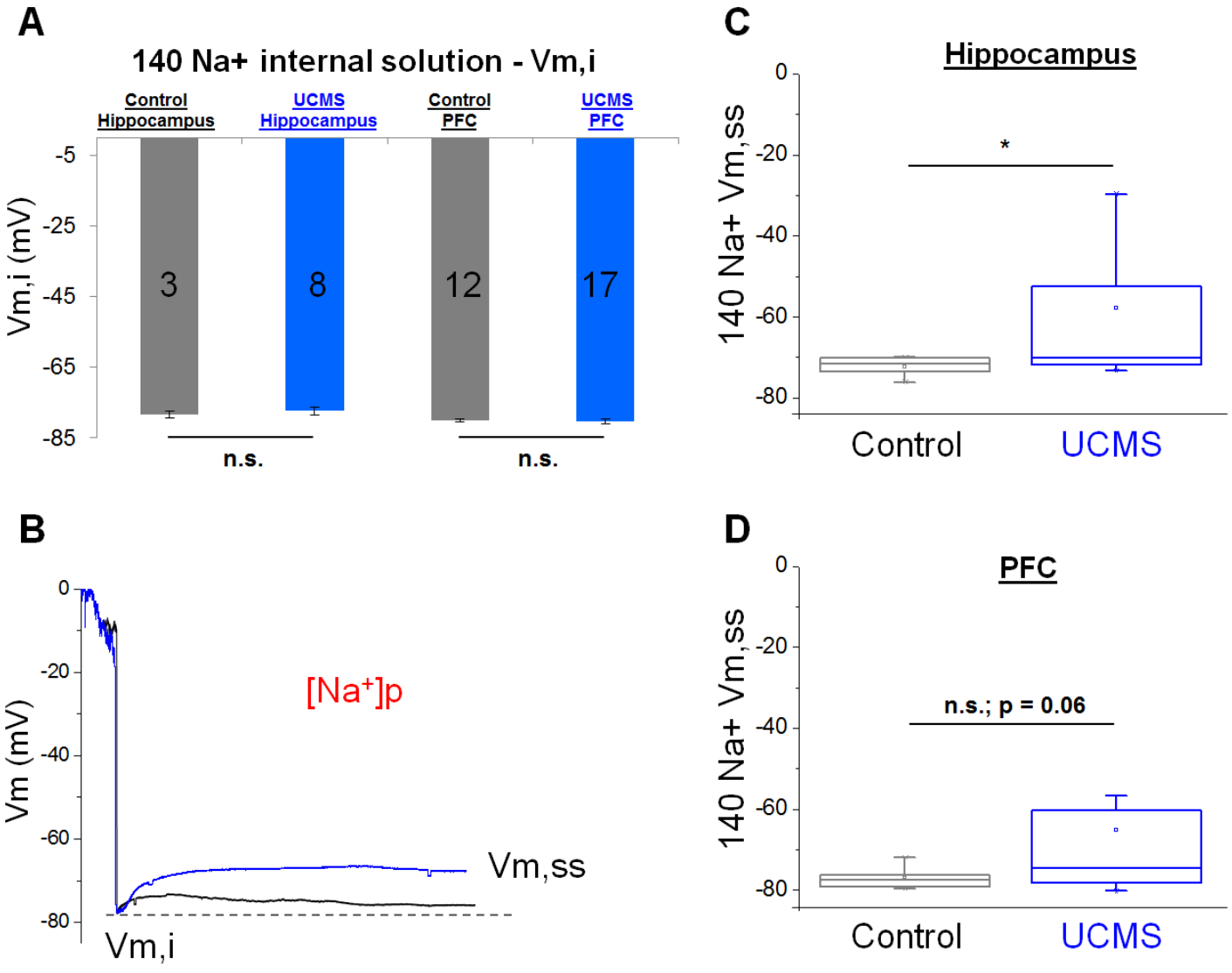

Figure 6.7 Graphical distribution of Vm,i and Vm,ss in astrocytes from control and UCMS animals (A) Graphical representation of the Vm, i and Vm, ss in hippocampal astrocytes recorded from control and UCMS-exposed animals. Note the depolarizing shift in the Vm, ss in several of the recordings fromUCMS animals. (B) Graphical representation of the Vm, i and Vm,ss in PFC astrocytes recorded from control and UCMS-exposed animals. Similar to the hippocampus, note the depolarizing shift in the Vm, ss in several of the recordings fromUCMS animals. These are the same recording depicted in Fig. 6.6, and all recordings (5-15 per group/region) were done using a Na^+ pipet in order to test for syncytial coupling strength.

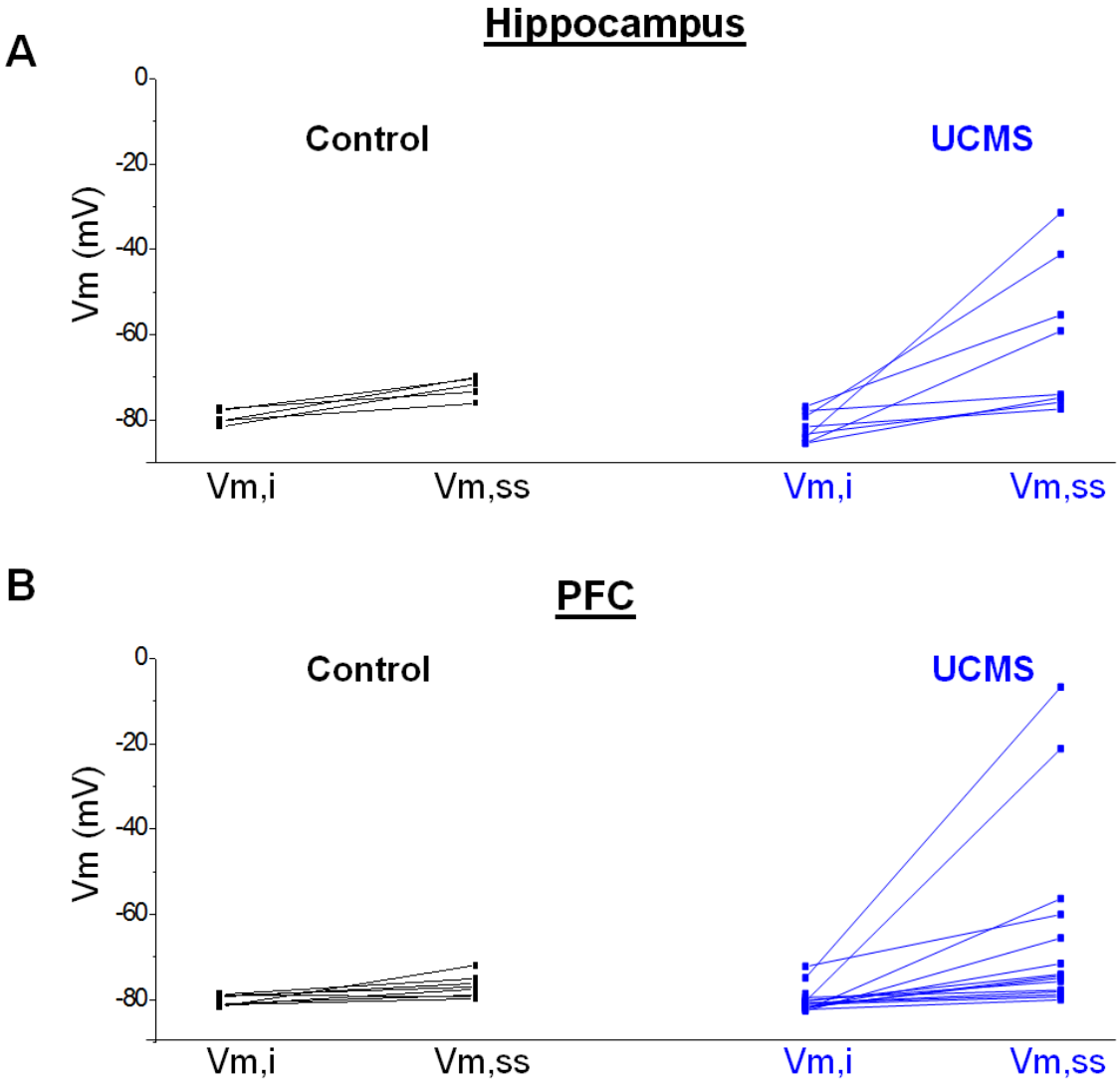

Figure 6.8 UCMS does not alter the number of connexin 30 (Cx30) or connexin 43 (Cx43)-immunoreactive puncta in the hippocampus or PFC
(A1-A4) Representative 40X immunofluorescent images of connexin 30 (yellow), connexin 43 (red), *Aldh1l1*-eGFP transgene (green), and hoescht (blue) in the stratrum radiatum of the hippocampus of control (top row) and UCMS exposed (bottom row) animals. (B1-B4) Representative 40X immunofluorescent images of connexin 30 (yellow), connexin 43 (red), *Aldh1l1*-eGFP transgene (green), and hoescht (blue) in the PFC of control (top row) and UCMS exposed (bottom row) animals. (C) Graphical representation of the number of connexin 30 immunoreactive puncta per area of hippocampus/PFC in control and UCMS mice. (D) Graphical representation of the number of connexin 43 immunoreactive puncta per area of hippocampus/PFC in control and UCMS mice. Data were analyzed using Student's t-test. n.s. = not significant. N = 6 animals per condition.

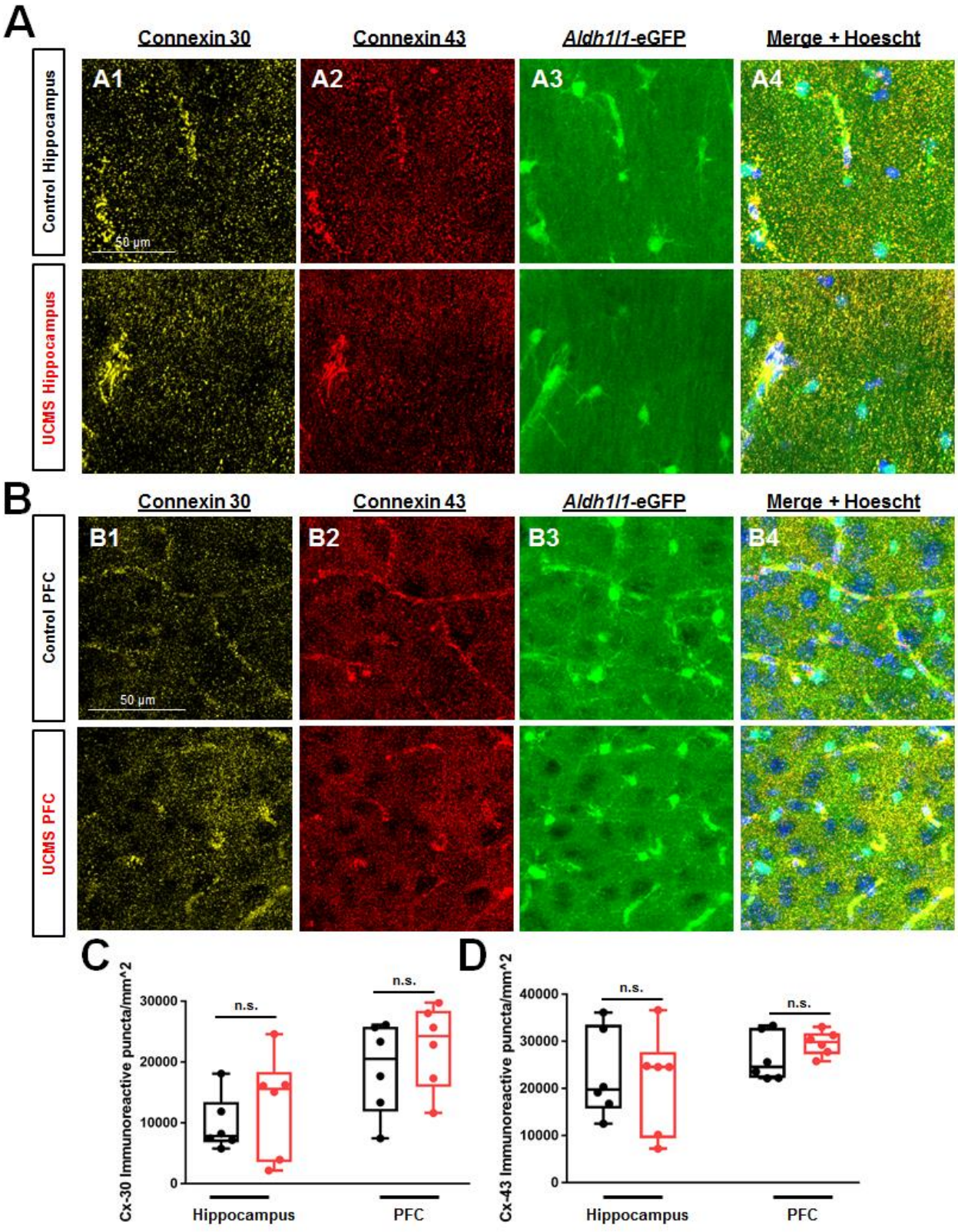
A
Connexin 30
Connexin 43
Aldh1l1-eGFP
Merge + Hoescht
Control Hippocampus
UCMS Hippocampus
A1
A2
A3
A4
50 µm
B
Connexin 30
Connexin 43
Aldh1l1-eGFP
Merge + Hoescht
Control PFC
UCMS PFC
B1
B2
B3
B4
50 µm
C
Cx-30 Immunoreactive puncta/mm^2
30000
20000
10000
0
n.s.
n.s.
Hippocampus
PFC
D
Cx-43 Immunoreactive puncta/mm^2
40000
30000
20000
10000
0
n.s.
n.s.
Hippocampus
PFC

CHAPTER 7

Ultrastructural view of astrocyte-astrocyte and astrocyte-neurite contacts within the hippocampus

Introduction

How astrocytes make contact with each other and with other constituents in the brain underlies the anatomic basis for astrocyte function in the central nervous system (CNS) (Barres, 2008; Clarke and Barres, 2013; Gomazkov, 2019). With respect to their anatomical organization, protoplasmic astrocytes are oriented in non-overlapping (i.e. distinct) domains (Bushong et al., 2002; Halassa et al., 2007; Ogata and Kosaka, 2002; Xu et al., 2014). Astrocytes within each domain can ensheath thousands of synapses within their occupancy volume using fine astrocytic processes (Peters et al., 1991; Wolff, 1970; Bushong et al., 2002; Khakh and Sofroniew, 2015).

Given their ability to extensively contact neurites, astrocytes are integral components in the modulation of synaptic function (Papouin et al., 2017). Studies have shown that astrocytes are able to respond to synaptic events and regulate neuronal transmission (Adamsky et al., 2018; Henneberger et al., 2010; Jourdain et al., 2007; Panatier et al., 2011; Perea and Araque, 2007). Notably, astrocytes also extend their endfeet to make contact with blood vessels for uptake of nutrients needed for brain energy metabolism (Nortley and Attwell, 2017).

While these findings indicate the importance of astrocyte anatomy to function, much of the anatomic details at the ultrastructural levels have yet to be resolved. For

example, astrocyte-synapse contacts remain an important topic of investigation. To this end, while several studies have shown that a large number of synapses make contact with astrocyte processes within the developing and mature cortex (Kikuchi et al., 2020; Ventura and Harris, 1999b; Witcher et al., 2007), within the mature mouse hippocampus, the percentage of synapses contacted by astrocyte processes has not yet been determined. Indeed, details about this astrocyte-neurite association within the hippocampus could provide key insights into the functional association between both cell types. Furthermore, the spatial location selectivity of intracellular consistutents (i.e. structures located within astrocytes)—such as glycogen granules, also remains elusive. Given that astrocytic glycogen granules serve as a major source of lactate (and subsequently serve as an energy substrate) for neurons (Calì et al., 2019; Magistretti and Allaman, 2015), having a better understanding of the ultrastuctural location of these small energy reserves could be of much value.

Critical to understanding these unanswered questions is the ability to resolve the ultrastructural complexity of astrocyte contacts. Indeed, fine astrocytic processes are structurally nanoscopic, which precludes the use of light microscopy and necessitates the use of electron microscopy (EM). In our current study, we've tackled these unanswered questions and extended upon findings recently described by Kiyoshi (Kiyoshi, 2019) through the combined use of an *Aldh1l1*-eGFP transgenic mouse model and correlative confocal serial blockface-scanning electorn microscopy (SBF-SEM). Indeed, our EM specimen contained identity-validated and location-defined astrocytes (given the confocal imaging prior to EM processing), and preparation damage to the fine anatomic structures

(and intracellular structures) was significantly reduced - (Denk and Horstmann, 2004; Kiyoshi et al., 2018) - which is essential in order to resolve and reconstruct the fine astrocytic processes at nanoscopic ranges (Ventura and Harris, 1999b).

Here, we examined - for the first time in requisite detail - the ultrastructure of astrocyte-neurite associations within the adult mouse hippocampus. Our 3D reconstructions of three neighboring astrocytes allowed us to determine their interactions with surrounding neurites. With the reconstruction of three across-astrocytic-domain neurites with their associated spines and contacting axons, we examined the spatial-location selectivity of astrocyte-synapse contacts. We were also able to show that glycogen granules are found in every part of the astrocyte, though they are enriched within astrocyte processes that abut synapses. Taken together, our findings provide clarity to long-standing questions regarding the structural contacts between astrocytes and neurites, and they raise interesting functional questions regarding astrocyte-neuron interactions and energy metabolism.

Materials and methods

Experimental model and subject details

Although tissue from several mice was processed for EM, a single adult, postnatal day 45, female BAC *Aldh1l1*-eGFP mouse was used for data shown in this study. Details of this mouse line have previously been reported (Yang et al., 2011b). Mice were housed in a temperature controlled (22 ± 2°C) environment with a 12 hour light/dark schedule and ad libitum access to food and water. All procedures were

performed in accordance with a protocol approved by the Institutional Animal Care and Use Committee (IACUC) at The Ohio State University.

Tissue processing

A postnatal day (P) 45 mouse was anesthetized with an intraperitoneal injection of 8% chloral hydrate in 0.9% saline and then transcardially perfused at 6 mL/min with 4% paraformaldehyde and 2.5% glutaraldehyde in 0.1M sodium cacodylate buffer. Sodium cacodylate, paraformaldehyde, and shell vials were purchased from Electron Microscopy Sciences (Hatfield, PA, USA). 25% EM grade glutaraldehyde was purchased from Polysciences Inc (Warminster, PA, USA). Coronal CA1 hippocampal brain slices (300 µm) were then cut with a Vibratome (Pelco 1500) and post-fixed with the same fixative overnight (at 4 degrees C) in shell vials.

Correlative confocal and serial blockface scanning electron microscopy (SBF-SEM)

Each *Aldh1l1*-eGFP hippocampal brain slice was then imaged using a Leica (SP8) confocal microscope in order to obtain astrocyte spatial localization and blood vessel landmark visualization within the stratum radiatum. These confocal images were used to correlate and select a region of interest for subsequent electron microscopy tissue processing.

After confocal images were acquired, fixed tissue sections were washed five times in 0.1 M sodium cacodylate, followed by staining with reduced osmium (2% osmium tetroxide and potassium ferrocyanide in 0.1 M sodium cacodylate buffer) at 4C for 2.5 hours. Sections were then washed five times in double distilled water, followed by incubation in 1% thiocarbohydrazide at 60C for 1 hr, before being washed again in

double distilled water. Sections were then stained with 2% aqueous osmium tetroxide for 2 hr at room temperature and were subsequently incubated (for 24-30 hr) in aqueous uranyl acetate at 4C. Next, the tissue was washed and incubated for 60 minutes at 60C in Walton's lead aspartate, followed by washing in double distilled water before beginning dehydration through a series of incubations in ethyl alcohol, propylene oxide (4 hrs), and 90 min in Epon 812-substiute resin before being embedded in Epon 812-substitute resin and left to cure for 48 hr at 60C. The tissue was trimmed out of the resin and oriented on the pin according to the corner notch that was cut into the wet tissue before confocal imaging. The tissue was mounted on aluminum and coated with colloidal silver liquid around the exposed edges of the resin block. A Zeiss Sigma VP system (with an in-chamber Gatan 3 View ultamicrotome with low-kV backscattered electron detectors) was used to examine the tissue. Tissue samples were imaged at 2.2 kV, with 7.7 nm/pixel resolution. Slices were 75 µm thick. SBF-SEM image acquisition and registration was conducted at Renovo Neural (Cleveland, OH, USA). The total image scan size for the data set is 54.02 x 96.47 x 37.5 µm (X, Y, Z). Image series were registered and then analyzed using Reconstruct (see below).

Three-dimensional reconstructions of hippocampal astrocytes, neurites, blood vessels, and intracellular particles

500 serial SBF-SEM images of the stratum radiatum (provided by Renovo Neural) were imported with image pixel size (0.0077 µm/pixel) and slice thickness (0.075 µm) into Reconstruct (Fiala, 2005). Cellular structures were traced manually in Reconstruct software to generate individual objects. The volume of each completed

object was automatically generated in Reconstruct. Further, the Z-trace tool was used to measure the dimensions (size, length, etc.) of each object, and the ellipse tool was used to trace rounded objects (such as glycogen granules). Boissonnat surface object reconstructions were generated in Reconstruct and were then exported as VRML 2.0 files for further rendering in Blender (see below).

Visualizing SBF-SEM reconstructed data using Blender 2.78

Blender - a free, open source 3D, general-purpose graphics tool that allows for modelling of large-volume data sets - was used to reconstruct our astrocyte connectome files. Note that Blender has been used in several other studies examining EM neural tissues (Calì et al., 2016; Zheng et al., 2018). VRML 2.0 files (created in Reconstruct) were imported into Blender and were then colored and rendered to obtain final 3D reconstructions. Note that in certain circumstances, objects were made slightly transparent (using the 'Z transparency' tool) to allow for easy visualization of multiple objects in contact with one another.

Synapse-astrocyte contact analysis

Analysis of astrocyte coverage of synapses was adapted from a recently published paper (Kikuchi et al., 2020). Note, however, that our analysis was conducted in SBF-SEM traces (i.e. 2-dimensional) and not in rendered (i.e. 3-dimensional) constructions. To begin, three complete dendrites (and their associated spines) were traced using Reconstruct. Axons that contacted each spine were also traced to completion. Next, each synapse was marked and classified as asymmetric or symmetric based on whether the postsynaptic density was prominent (Gray, 1959; Kikuchi et al.,

2020; Peters and Palay, 1996) (see Fig. 7.4D1 for examples of the two types of synapses). Finally, the area surrounding each synapse was examined in order to determine whether any astrocyte processes were located adjacent to the synapse. Three categories were then established, similar to classifications conducted in a recently published report (Kikuchi et al., 2020):

1) 'Cleft associated astrocytes' were those synapses whose synaptic clefts made contact with an astrocyte process.
2) 'Pre/post associated astrocytes' were those synapses whose pre or post synaptic elements made contact with an astrocyte process, but not with the cleft.
3) 'Free astrocytes' were those synapses that had no adjacent contacts with astrocyte processes.

Of note, if an astrocyte made contact with both the synaptic cleft and a pre or post synaptic element, the contact was classified as 'cleft contact'. The percentage of astrocyte (and non-astrocyte) associated synapses was then calculated from three dendrites.

Analysis of glycogen granule content in various astrocyte processes

Glycogen granule density within various regions of astrocyte processes was also analyzed. For this analysis, a 5 x 5 µm, 10 z-stack ROI was drawn around an astrocyte region (from a 2D EM trace). These regions included the astrocyte soma, root, intermediate processes, and terminal and reflexive processes. Three of these ROIs were drawn for each astrocyte region, and data obtained from three total astrocytes was used for analysis (i.e. this process was replicated for all process types of three different

astrocytes-blue, pink, and purple). The glycogen granules within each specific astrocyte region (within the ROI) were traced using the Reconstruct ellipse tool, and the total number of glycogen granules within the 10 z-stack ROI was divided by the total volume that the astrocyte occupied. Criterion used to identify vesicle-like structures can be found in Fig. 7.5.

Statistical Analysis

All statistics were performed using GraphPad Prism 7.0 software, and group data are presented as mean ± SEM. Details of statistical tests (such as the test statistic, degrees of freedom, and p-value) can be found in the Results section (or tables) of the manuscript. As noted in the figure legends, significance was ascribed to p-values < 0.05. Further, comparisons between three (or more) groups/variables were conducted using a one-way ANOVA, followed by post-hoc analysis. For each experiment, Grubb's test was conducted on data obtained from each group in order to determine whether the outlier was statistically significant ($p < 0.05$).

Results

3D reconstruction of neighboring astrocytes using correlative confocal microscopy and SBF-SEM

To begin, we utilized an *Aldh1l1*-eGFP reporter mouse and confocal microscopy to define the region of interest (ROI) that contained three neighboring astrocytes in order to prepare the specimen for further SBF-SEM study. Specifically, after tissue fixation, low magnification images of coronal brain sections encompassing the cortex and hippocampus were taken. Note that we selected a tissue section that contained

visible blood vessels which could be used as landmarks. An area containing GFP+ astrocytes next to a large blood vessel in the stratum radiatum of the hippocampus was chosen as our ROI, and the tissue section containing the ROI was then processed for SBF-SEM.

To identify astrocytes within the SBF-SEM dataset, we located structures that were irregular in shape. We then examined the datasets to look for key structural characteristics of astrocytes, such as glycogen granules (see Fig. 7.5 for glycogen granule identification criteria). In addition, we followed the processes extending from the cell body, which formed astrocytic endfeet that contact blood vessels (as in Fig. 7.1D-7.1F).

Within the SBF-SEM dataset, we identified three astrocytes (colored purple, blue, pink) and traced these astrocytes (and a surrounding blood vessel) to completion. 3D reconstructions were then created (Fig. 7.1). Of note, the bottom half of the blue astrocyte was cut-off in the data set (Fig. 7.1B) and is therefore smaller in appearance. Overlaying the three astrocytes created a 3D reconstruction of an astrocyte connectome (Fig. 7.1D-7.1F).

3D reconstruction of astrocytes in association with neurites

Astrocyte processes are extensively interwoven with surrounding neurites (Gavrilov et al., 2018; Kikuchi et al., 2020; Ventura and Harris, 1999b; Witcher et al., 2007). We first traced the ultrastructure of a neurite to detail the structure of the dendritic spines shown in our reconstructions-which are representative of all six standard spine categories: thin, mushroom, stubby, cup, branched, and filopodia-like (Fig. 7.2A-7.2B and Fig. 7.3A-7.3B) (Hering and Sheng, 2001; Risher et al., 2014). We then traced (to

completion) three dendrites and their associated spines and contacting axons (Fig. 7.3C). The three neurite reconstructions were then combined with the 3D reconstructions of the three astrocytes in order to generate a complete network-level view of the astrocyte-neurite interaction (Fig. 7.3D). Reconstruction of three astrocytes in association with three neurites provided us with ultrastructural details of the anatomical relationships between both cell types.

The majority of synapses are contacted by astrocytic processes

We next examined the ultrastructural contacts between astrocyte processes and neurites. Several bodies of work examining both the developing and mature rat cortex and hippocampus have reported that a large number of synapses make contact with astrocyte processes (Kikuchi et al., 2020; Ventura and Harris, 1999b; Witcher et al., 2007). However, to date, the percentage of synapses contacted by astrocyte processes within the mature mouse hippocampus is not known. Using the three fully reconstructed neurites (presented in Fig. 7.3C), we analyzed the percentage of astrocytic processes at the axon-spine interface (i.e. synapse). In total, we evaluated 920 synapses from the three reconstructed neurites, and recorded whether astrocyte processes made contact with the synaptic cleft (Fig. 7.4A1-7.4A2), pre or post synaptic elements (Fig. 7.4B1-7.4B2), or if no astrocytes made contact with the synapse (Fig. 7.4C1-7.4C2). Additionally, each synapse was classified as ‘asymmetric’ or ‘symmetric’ based on whether it exhibited a prominent or narrow postsynaptic density (Gray, 1959; Kikuchi et al., 2020; Peters and Palay, 1996; and see Fig. 7.4D1).

Assessment of asymmetric versus symmetric synapse percentage (irrespective of astrocyte contact type) revealed that a majority of synapses were asymmetric (Fig. 7.4D2). Along these lines, 218/235 synapses (93%) from dendrite 1, 216/231 synapses (94%) from dendrite 2, and 427/454 synapses (94%) from dendrite 3 were asymmetric. When examining synapse type (i.e. asymmetric and symmetric) with respect to astrocyte contacts, we found that a majority of synapses were contacted by astrocytes, with significant differences observed in astrocyte contact patterning (Fig. 7.4E1; $F_{(5, 12)} = 51.08$; $p < 0.0001$; one-way ANOVA. See Table 7.1 for post-hoc analysis). Specifically, 55% of all synapses were asymmetric and contacted astrocytes at the cleft (Fig. 7.4E1; solid green bar) and 4% of all synapses were symmetric and contacted astrocytes at the synaptic cleft (Fig. 7.4E1; patterned green bar). Further, 25% of all synapses were asymmetric and had pre- or post-synaptic contact with astrocytes (Fig. 7.4E1; solid orange bar) and 2% of all synapses were symmetric and had pre-or post-synaptic contact with astrocytes (Fig. 7.4E1; patterned orange bar). In contrast, 13% of all synapses were asymmetric and had no contact with astrocytes (Fig. 7.4E1; solid purple bar) and 1% of all synapses were symmetric and had no contact with astrocytes (Fig. 7.4E1; patterned purple bar). Individual dendrite-parsed graphical representations of asymmetric synapse-astrocyte contacts (Fig. 7.4E2) and symmetric synapse-astrocyte contacts (Fig. 7.4E3) are also shown. Taken together, these results suggest that most synapses (86% in total) have contact with astrocyte processes, and a majority of these astrocyte-synapse contacts occur at the synaptic cleft (compared to pre and/or post synaptic elements).

Glycogen granules are enriched in terminal astrocyte processes

Glycogen is the stored formed of glucose, and within the brain, glycogen is almost entirely localized within astrocytes (Allaman et al., 2011; Magistretti and Allaman, 2018; Nelson et al., 1968; Phelps, 1975, 1972). While the role of brain glycogen (and glycogen-derived lactate) is not completely clear, many studies have shown that it plays a crucial role in many high-energy consuming biochemical and molecular processes such as synaptic plasticity and memory formation (Suzuki et al., 2011). While Cali et al found a large quantity of glycogen granule puncta concentrated within fine astrocyte processes of the murine cerebral cortex (Calì et al., 2016), a complete understanding of the astrocyte domain-wide localization of glycogen granules within the hippocampus is lacking. Hence, we sought to investigate the density of glycogen granules abutting synapses as a function of astrocyte process type.

In electron microscopy sections, glycogen granules can be identified by their electron-dense puncta (Revel et al., 1960), which can also form clusters. For a description of the criterion used to identify glycogen granules, see Fig. 7.5B. Using this criterion, we examined glycogen granules throughout the entire astrocyte domain (Fig. 7.6A). Notably, we used a Root-Intermediate-Terminal process labeling scheme to identify various astrocyte branching patterns (Kiyoshi, 2019; Uylings and van Pelt, 2002). Along these lines, a *root* process was defined as the main astrocyte branch(es) that orginate from the astrocyte soma. *Intermediate* processes are those that branch from the root processes and occasionaly extend to other intermediate processes. Finally, small, thin *terminal* processes extended from the soma, root processes, and intermediate processes, and they do not extend any further. *Reflexive* processes were also used to denote astrocyte

branches that formed loop-like structures. We then counted the number of granules within each ROI of the following astrocyte process types: soma (Fig. 7.6B), root processes (Fig. 7.6C), intermediate processes (Fig. 7.6D), terminal processes (Fig. 7.6E), and reflexive processes (Fig. 7.6F). Quantitative analysis of glycogen granules revealed a significant effect of astrocyte process type on granule density (Fig. 7.6G; $F_{(5, 44)} = 10.83$; $p < 0.0001$; one-way ANOVA; see Table 7.2 for post-hoc analysis). Similar to synapses, glycogen granules were enriched within terminal and reflexive astrocytic processes (in addition to endfeet processes—not shown). Together, these data suggest that an accumulation of glycogen is observed in terminal astrocyte processes.

Discussion

While the ultrastructure and connectivity of neurons has been highlighted in several seminal connectomics studies (Kasthuri et al., 2015; Mishchenko et al., 2010), our results provide significant insights into the structural complexity of astrocyte processes, the anatomical relationship between astrocytes and synapses in the mature mouse brain, and the location of intracellular particles (such as glycogen granules) within astrocytes. Taking advantage of an *Aldh1l1*-eGFP mouse for pre-identification of neighboring astrocytes in EM specimen preparation and SBF-SEM for preserving the nanoscopic details of astrocytic processes, this study provides the first ultrastructural view of the interactions between astrocytes and neurites in the adult mouse brain.

Ultrastructural contacts of astrocytes with synapses

By tracing all axons from three dendrites, we were able to analyze astrocyte-synapse association, reporting - for the first time within the adult mouse hippocampus -

that ~86% of synapses are ensheathed by astrocytes. Notably, this percentage is higher than other studies that examined synapse coverage within the developing rat somatosensory cortex (68% coverage) (Kikuchi et al., 2020) and the mature rat stratum radiatum (57% and 62% coverage, respectively) (Ventura and Harris, 1999b; Witcher et al., 2007). Differences in brain region, developmental stage, and/or analysis methods likely contributed to the increase in astrocyte-ensheathed synapses that we observed. Further, our finding that a large majority of astrocytes contact the axon-spine interface (i.e. synapse), compared to post or pre-synaptic elements, is in agreement with these previous studies in both the developing (Kikuchi et al., 2020) and mature brain (Witcher et al., 2007).

Whereas most asymmetric synapses are excitatory, symmetric synapses are inhibitory (Peters and Palay, 1996). Interestingly, ~94% of all synapses reported in the P14 developing brain (Kikuchi et al., 2020) were asymmetric, a finding that we also observed in our study in the mature (P45) brain, suggesting that the instructive role of astrocytes in synaptogenesis likely occurs in the developing brain (Allen and Eroglu, 2017). While our current study did not investigate the functional role of astrocytes in the regulation of synaptic transmission and plasticity, activation of calcium signaling within astrocytes leads to glutamate release (Bezzi et al., 1998; Pasti et al., 1997). In turn, astrocytic glutamate has been shown to act on several types of neuronal metabotropic glutamate receptors and NMDA and kainite receptors, which can augment the amplitude and/or frequency of evoked IPSCs and mEPSCs (Fellin et al., 2004; Fiacco and McCarthy, 2004; Kang et al., 1998b; Liu et al., 2004; Parri et al., 2001). Hence, the

extent to which astrocytic ensheathment of synapses influences the excitatory-inhibitory balance of neurons remains an interesting topic for further investigation.

Glycogen granules are found throughout each astrocytic compartment

It is interesting to note that glycogen granule density was very high in astrocyte terminal processes. These results support a previous immunohistochemical study that examined the subcellular distribution of glycogen within hippocampal astrocytes (Oe et al., 2016). Notably, our observations are also in agreement with other reports that used 3D electron microscopy to show preferential location of glycogen granules in astrocyte processes that surround synapses (Calì et al., 2016; Mohammed et al., 2018). These observations, coupled with the fact that glycogen serves as a major source of energy, lead one to speculate that the distribution pattern of glycogen (i.e. lower density in the astrocyte soma/root and higher density in the astrocyte terminal/reflexive processes) is reflective of the metabolic demand of nearby synapses. To this end, if astrocyte terminal and reflexive processes are more metabolically 'active' (given that they contact a greater density of synapses), glycogen would need to be abundant, which is consistent with our results. This hypothesis is also supported by studies showing the importance of glycogen metabolism in synaptic plasticity and memory formation (Descalzi et al., 2019; Gibbs et al., 2006; Newman et al., 2011; Suzuki et al., 2011) –both of which are processes that require a significant amount of energy.

The hypothesis mentioned above is also reinforced by analysis of synapse-astroycte contacts throughout the astrocyte domain. Along these lines, we should briefly note that the enrichment of glycogen granules within astrocyte terminal and reflexive

processes is consistent with our data showing that the density of synapses that surround astrocytes is highest in astrocyte terminal and reflexive processes (Kiyoshi, 2019). With respect to the ultrastructural contacts of astrocytes with synapses, the current understanding of perisynaptic astrocyte processes (PAPs) is that astrocyte fine/terminal processes are closely associated with synapses—responding to synaptic activity, providing structural support, and clearing neurotransmitters from the synaptic cleft (Reichenbach et al., 2010). Hence, the fact that synapse-astrocyte contacts are increased in astrocyte terminal processes and that glycogen granules are enriched within these terminal processes leads one to surmise that perhaps terminal and reflexive processes need to provide more energy (compared to the soma, root, and intermediate astrocyte processes), since the greatest density of synapses are located within these regions.

Further, from an (ultra)structure-function perspective, this distribution (i.e. highest density of glycogen granules in terminal/reflexive processes) suggests that when neuronal activity is highest (during LTP for example), such activity leads to more complex functions (memory formation/retrieval). Given that lactate is derived from glycogen and can serve as a signaling molecule for such higher order processes (Margineanu et al., 2018; Yang et al., 2014), perhaps glycogen is not only serving as a subtrate for energy for these neurons, but that it is also useful in producing lactate which serves as a signaling effector for plasticity-related processes such as LTP. Clearly, our understanding of the extent to which the ultrastructural location of glycogen granules influences neuronal signaling is still in its infancy.

Acknowledgements

I thank Dr. Conrad Kiyoshi for spearheading the beginning of this project and for working as a team (along with numerous undergraduate students) to make years worth of tracing, construction, and analysis a success.

Figure 7.1 3D Reconstruction of neighboring astrocytes within the stratum radiatum of the hippocampus
(A-C) 3-dimenstional view of three reconstructed astrocytes: purple, blue, and pink. Note that these three astrocytes were traced from an EM dataset before being reconstructed. (D-F) Combined reconstruction depicting the front, side, and back views of the three astrocytes. Each astrocyte is labeled in a different color to clearly demarcate individual astrocyte domains and cellular structures. Note that the blue astrocyte appears 'smaller' in size as only part of the cell was included in the EM stack. Note that the reconstructions from this figure are more completed versions of those depicted in '*Kiyoshi, C. "*Structure and Function of the Developing and Mature Astrocyte Syncytium in the Brain*." (2019; PhD Dissertation; The Ohio State University).*'

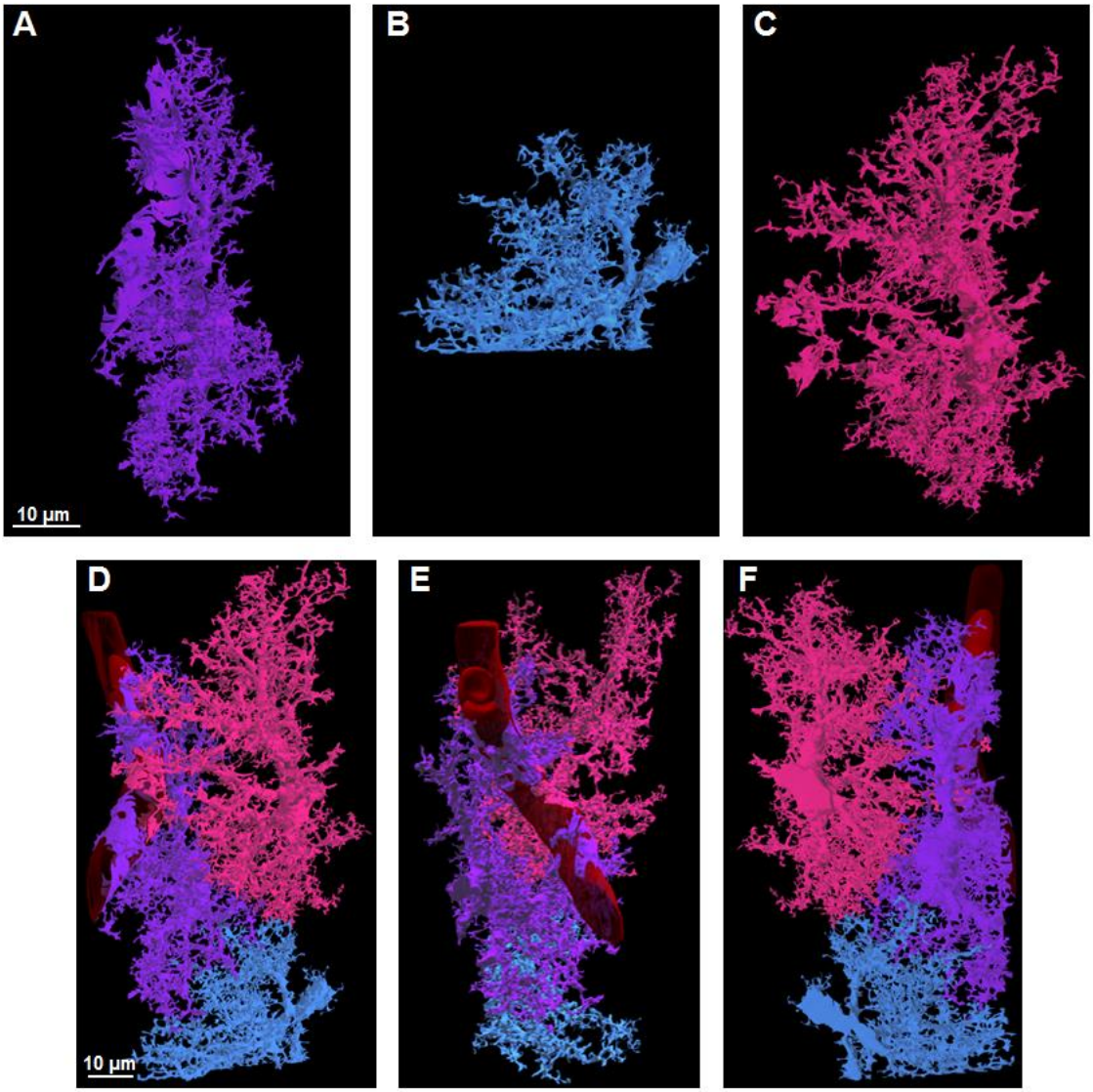

Figure 7.2 Ultrastructural view of a reconstructed neurite
(A) Complete 3D reconstruction of one (out of three total) reconstructed dendrites. Several axons (white) are drawn for reference. (B1-B6) Magnified view of axonal contacts (white) with dendritic spines (orange). The orange dendritic spines that contact these axons represent thin, mushroom, stubby, cup, branched, and filopodia-like spine types, respectively. Note that these images are magnified from yellow boxed regions approximated in **A**.

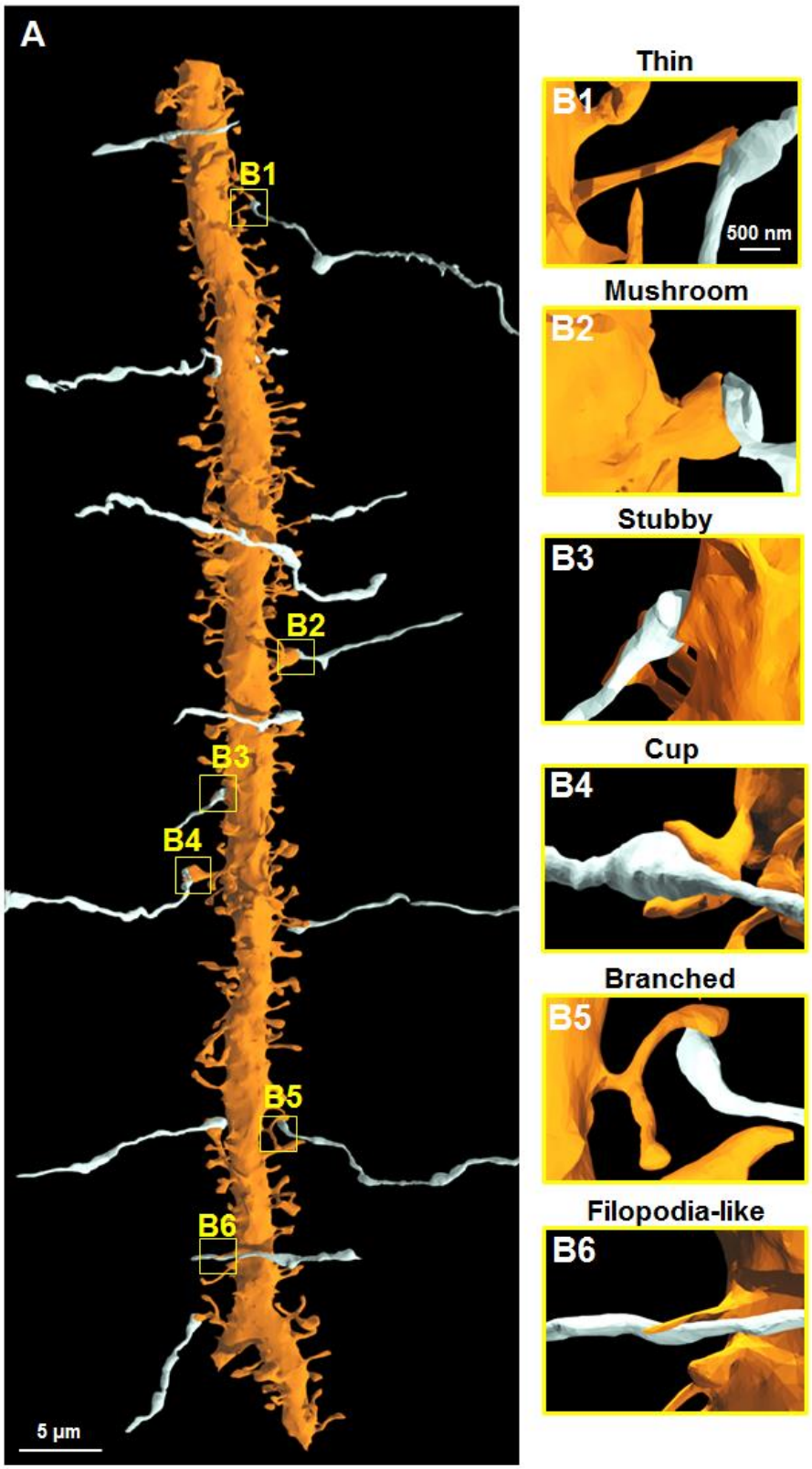
A
B1
B2
B3
B4
B5
B6
5 µm
Thin
B1
500 nm
Mushroom
B2
Stubby
B3
Cup
B4
Branched
B5
Filopodia-like
B6

Figure 7.3 An ultrastructural view of astrocyte-neurite association
(A) Partial 3D reconstruction of one dendrite. An axon (white) is drawn for reference in order to depict the axon-dendritic spine interface (i.e. synapse). (B) 2D serial traces of the axon (white) and dendritic spine (orange) that form a synapse (synapse is depicted in **A** and in z-section 12). (C) 3D reconstruction of three dendrites (orange) and their associated axons (white) shown in a front view. (D) Front view of the three neighboring astrocytes and their association(s) with the three reconstructed neurites. Note that the reconstruction in panel 'D' is a more completed version of that depicted in '*Kiyoshi, C. "*Structure and Function of the Developing and Mature Astrocyte Syncytium in the Brain*." (2019; PhD Dissertation; The Ohio State University).*'

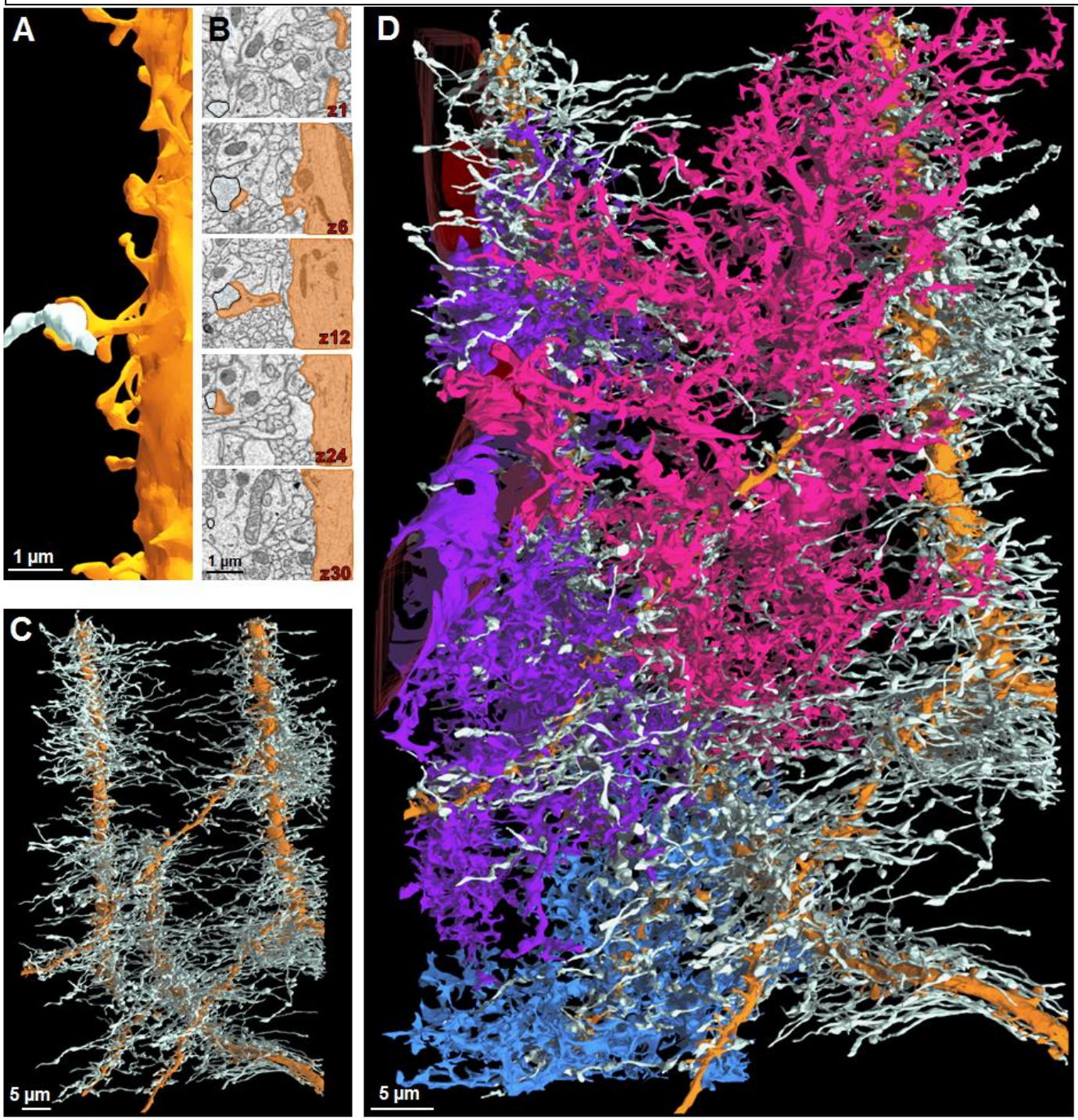

Figure 7.4 The majority of synapses are contacted by astrocytic processes
(A1) 2D EM trace of an astrocyte process (pink) contacting the synaptic cleft. (A2) 3D reconstruction from **A1**. (B1) 2D EM traces of astrocyte process contacting either post-synaptic dendritic elements (left panel) or pre-synaptic elements (right panel). (B2) 3D reconstruction from **B1**. (C1) 2D EM trace of a synapse with no astrocyte contact. A 3D reconstruction is also depicted in **C2**. In all representative images, the astrocyte processes that contact the synapses are from one astrocyte (pink) and the synapses are from two fully reconstructed dendrites shown in Fig. 7.3. White spheres depict the approximate locations of synaptic vesicles observed from several serial 2D EM stacks. (D1) 2D EM traces depict an example of an asymmetric synapse (prominent post synaptic density—top panel) and a symmetric synapse (modest post synaptic density—bottom panel). Yellow arrows denote the post-synaptic density. (D2) Graphical representation of the percentage of asymmetric versus symmetric synapses (irrespective of astrocyte contact type) from all three traced dendrites. (E1) Graphical representation of the percentage of synapses (asymmetric or symmetric) that contact astrocyte processes at the synaptic cleft, on pre or post synaptic elements, or have no contact with astrocyte processes. Note that these data were pooled from the synapses (from all three reconstructed dendrites) that contacted astrocyte processes, and thus, each data point is representative of the percent coverage per dendrite. Data was analyzed by one-way ANOVA followed by post hoc tests; ****: $p < 0.0001$. (E2) Distribution of the percentage of asymmetric synapses that have astrocyte contact with the synaptic cleft, post, or pre synaptic elements, or no astrocyte contact. (E3) Distribution of the percentage of symmetric synapses that have astrocyte contact with the synaptic cleft, post or pre synaptic elements, or no astrocyte contact.

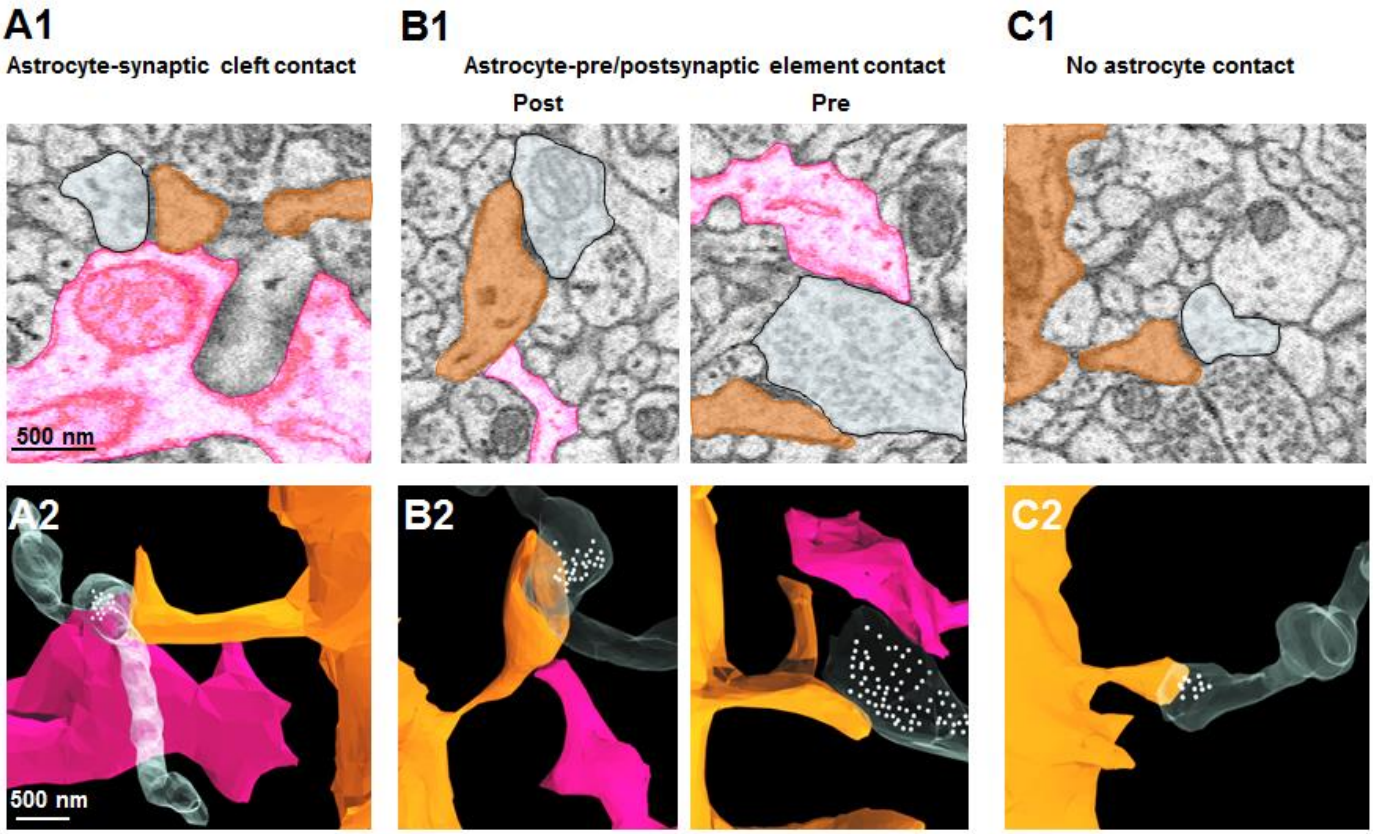
A1
Astrocyte-synaptic cleft contact
B1
Astrocyte-pre/postsynaptic element contact
Post
Pre
C1
No astrocyte contact
500 nm
A2
B2
C2
500 nm

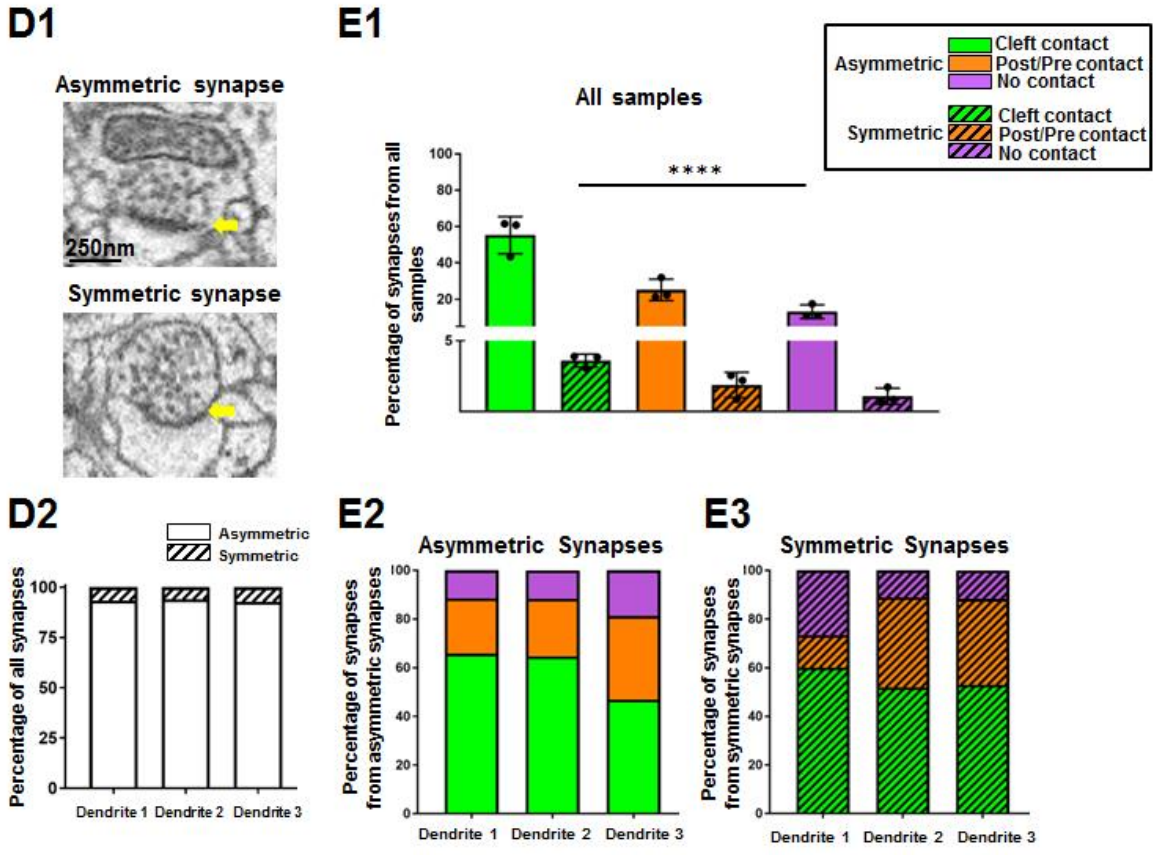
D1
Asymmetric synapse
250nm
Symmetric synapse
E1
All samples
Asymmetric
Cleft contact
Post/Pre contact
No contact
Symmetric
Cleft contact
Post/Pre contact
No contact
****
Percentage of synapses from all samples
100
80
60
40
20
5
D2
Asymmetric
Symmetric
Percentage of all synapses
100
75
50
25
0
Dendrite 1
Dendrite 2
Dendrite 3
E2
Asymmetric Synapses
Percentage of synapses from asymmetric synapses
100
80
60
40
20
0
Dendrite 1
Dendrite 2
Dendrite 3
E3
Symmetric Synapses
Percentage of synapses from symmetric synapses
100
80
60
40
20
0
Dendrite 1
Dendrite 2
Dendrite 3

Table 7.1 Asymmetric and symmetric synapse-astrocyte contact information from all 920 analyzed synapses Tukey post-hoc test was conducted to determine statistically different synapse-astrocyte contacts (as a function of synapse type: i.e. asymmetric vs. symmetric). This data supports standard ANOVA analysis from Fig. 7.4.

Synapse-Astrocyte Contact Comparison	Adjusted P- Value	Significance
Asymmetric cleft vs. Symmetric cleft	<0.0001	****
Asymmetric cleft vs. Asymmetric pre/post	0.0001	***
Asymmetric cleft vs. Symmetric pre/post	<0.0001	****
Asymmetric cleft vs. Asymmetric free	<0.0001	****
Asymmetric cleft vs. Symmetric free	<0.0001	****
Symmetric cleft vs. Asymmetric pre/post	0.0024	**
Symmetric cleft vs. Symmetric pre/post	0.9980	ns
Symmetric cleft vs. Asymmetric free	0.2710	ns
Symmetric cleft vs. Symmetric free	0.9884	ns
Asymmetric pre/post vs. Symmetric pre/post	0.0013	**
Asymmetric pre/post vs. Asymmetric free	0.1071	ns
Asymmetric pre/post vs. Symmetric free	0.0009	***
Symmetric pre/post vs. Asymmetric free	0.1459	ns
Symmetric pre/post vs. Symmetric free	>0.9999	ns
Asymmetric free vs. Symmetric free	0.1078	ns

Figure 7.5 Criterion for identification of astrocytic intracellular particles
(A) Serial 2D EM images of an astrocyte intermediate process containing vesicle-like particles (green arrowheads), endoplasmic reticulum (yellow/orange arrowheads), and glycogen granules/clusters (blue arrowheads). (B) Classification of how each intracellular particle type was identified based on appearance, size, and morphology. Note that the color of the box corresponds to the color of the arrowhead in **A**.

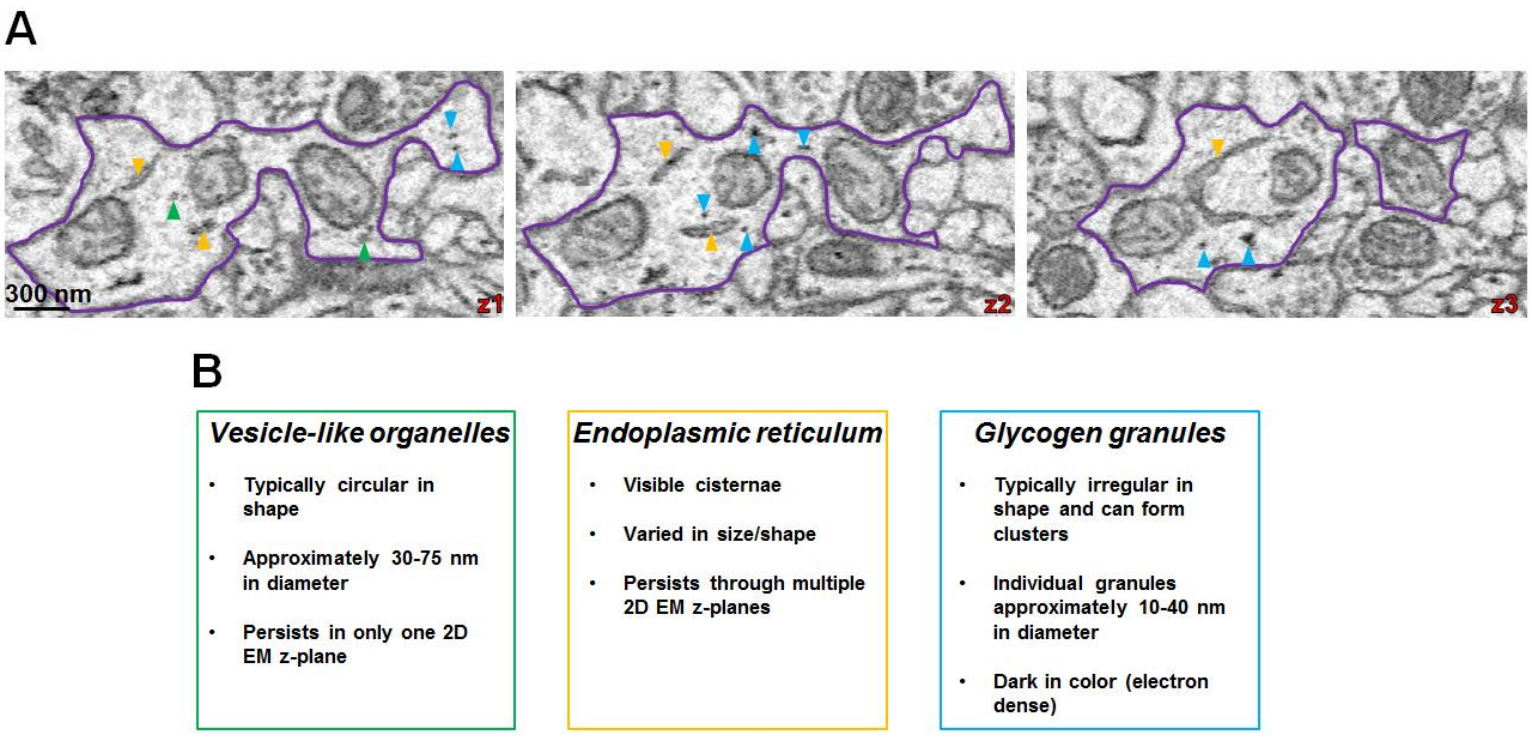

Figure 7.6 Glycogen granules are enriched in astrocyte processes abutting synapses
(A) 3D reconstruction of an astrocyte (pink) and glycogen granules (white spheres) located in the following astrocyte process types: soma (B), root (C), intermediate (D), terminal (E), and reflexive (F). Note that glycogen granules depicted in each box in **A** are magnified in **B-E**. All inset glycogen granule representative images were constructed from approximately the same volume of astrocyte. G) Graphical representation of the glycogen granule density per volume of astrocyte in all noted process types.****: $p < 0.0001$; One-way ANOVA.

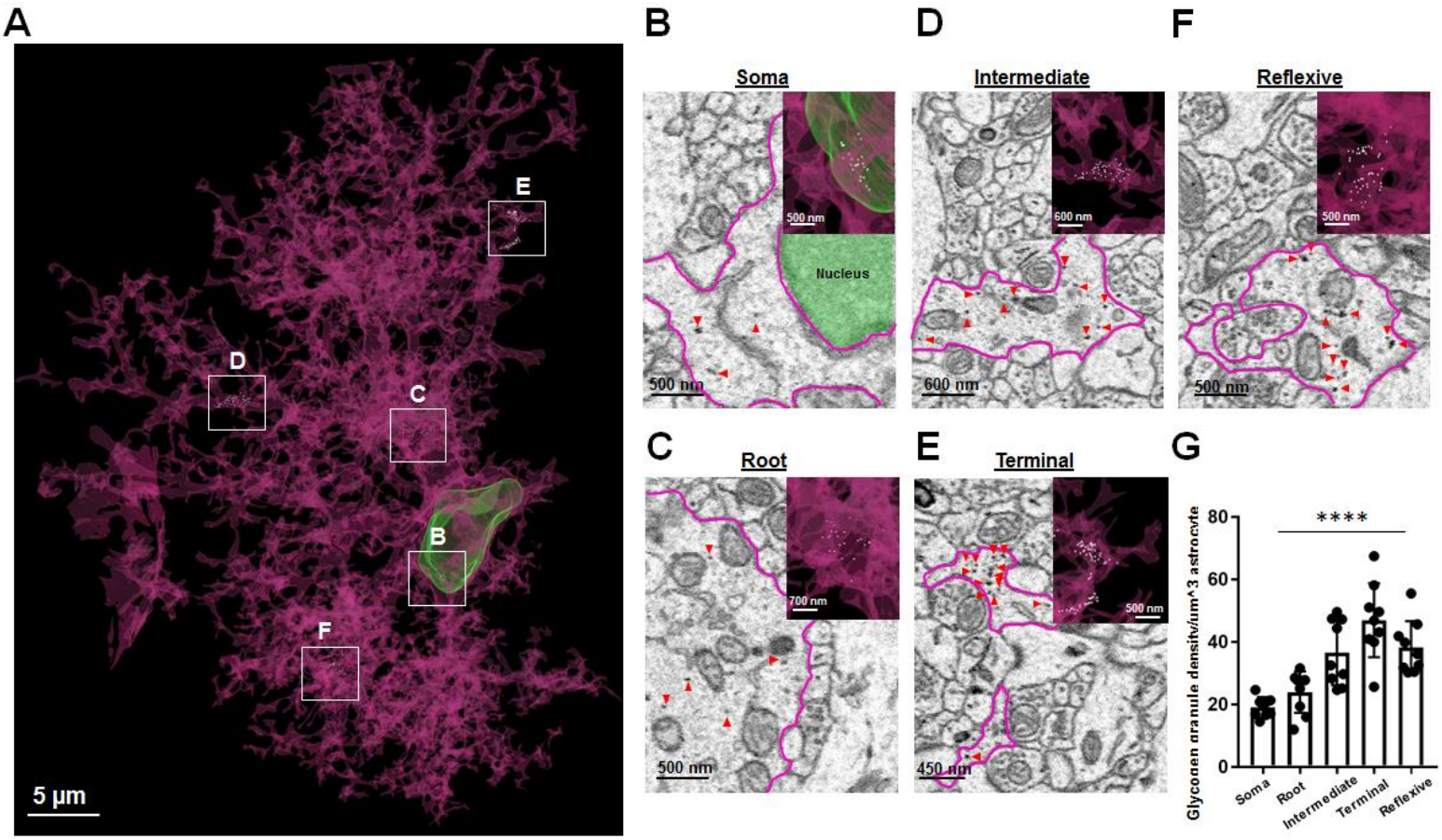

Table 7.2 Glycogen granule density in relation to astrocyte process type Tukey post-hoc test was conducted to determine statistically different glycogen granule densities across all astrocyte process types. This data supports standard ANOVA analysis from Fig. 7.6.

Glycogen Granule Density-Astrocyte Process Comparison	Adjusted P- Value	Significance
Soma vs. Root process	0.8944	ns
Soma vs. Intermediate process	0.0115	*
Soma vs. Terminal process	<0.0001	****
Soma vs. Reflexive process	0.0038	**
Soma vs. Endfeet process	<0.0001	****
Root process vs. Intermediate process	0.1299	ns
Root process vs. Terminal process	0.0009	***
Root process vs. Reflexive process	0.0528	ns
Root process vs. Endfeet	0.0002	***
Intermediate process vs. Terminal process	0.4521	ns
Intermediate process vs. Reflexive process	0.9986	ns
Intermediate process vs. Endfeet	0.1198	ns
Terminal process vs. Reflexive process	0.7026	ns
Terminal process vs. Endfeet	0.9308	ns
Reflexive process vs. Endfeet	0.2413	ns

CHAPTER 8

Conclusion and future perspectives

Summary of findings

This dissertation focuses on both the cellular signaling and physiological mechanisms that govern complex processes such as circadian clock entrainment, cognition, and stress. More specifically, the research in this work addresses mechanisms that govern circadian clock timekeeping capacity, cognitive measures, and stress via ERK/MAPK effectors/regulators, microRNAs, and astrocytes. As summarized in greater detail below, the data presented here provide novel details which support the idea that the ERK/MAPK pathway is a critical modulator of clock entrainment. Further, it highlights new data suggesting that a miRNA locus is a key regulator of time-of-day dependent learning and anxiety-like behaviors, in addition to depicting how depression-like behaviors alter circadian clock timing and astrocyte morphology/physiology.

In the second chapter of this dissertation, we investigated the role of SynGAP within the suprachismatic nucleus of the hypothalamus. We found that SynGAP is highly expressed within this hypothalamic region and that its expression is also regulated in a circadian manner. Further, we found that SynGAP is induced by a light pulse during the nighttime domain. Our results also demonstrate that mice heterozygous for *Syngap1*display alterations in clock timekeeping and entrainment capacity. These results suggest that SynGAP may play a role in sleep, given that sleep is modulated by the circadian clock. To this end, data collected from a participant registry/survey also

suggests that individuals with *Syngap1* gene mutations display alterations in sleep. Taken together, this data set proposes a novel role of SynGAP in the modulation of clock timing and it raises interesting implications with respect to other clock-dependent processes that may be affected by *Syngap1* gene mutations.

In the third chapter, we studied how the small, non-coding microRNA-132 couples the circadian clock to time-of-day dependent learning capacity. Indeed, we first demonstrated that hippocampal miR-132 expression displays a time-of-day difference—with highest expression observed during the circadian night. Using a novel doxycycline-dependent transgenic mouse line(s), we then constitutively expressed miR-132 within the forebrain (thus preventing it from oscillating). In this mouse line, we found that time-of-day dependent measures of cognitive capacity were altered compared to WT (i.e. control) littermates, wherein miR-132 expression was not constitutive (i.e. it did oscillate). Given that miRNAs function via the targeting of mRNAs (through base complementation), we profiled the expression of two synaptic-plasticity related genes that were bona fide miR-132 targets—finding that the time-of-day expression in these targets was damped within the consititively expressing miR-132 trasgenic mouse line. Altogether, these data reveal key that miR-132 may serve as an important conduit, linking the circadian clock to time-of-day dependent cognition within the hippocampus (and perhaps other forebrain regions).

Turning to chapter four of this dissertation, we followed up on our miR-132 studies, finding that the miR-132/212 locus also regulates anxiety-like behaviors. Along these lines, we first showed that both miR-132 and its ‘sister’ miRNA miR-212 are

induced by an acute stress paradigm in the hippocampus and amygdala. We also found that a chronic stress paradigm leads to miR-132 and miR-212 induction; however; this increase in expression was only observed in the amygdala. Furthermore, we found that our constitutively expressing miR-132 transgenic mouse line displayed an anxiety phenotype, and these anxiety-like behaviors could be mitigated by administering doxycycline (to reduce the level of transgenic miR-132). Notably, we also observed a heightened level of anxiety (albeit mild) in our miR-132/212 forebrain knockout mouse line—suggesting that tight regulation of miR-132 is necessary for the maintenance of baseline anxiety levels. Finally, we assessed the expression of two miR-132/212 target genes that have been implicated in the regulation of anxiety-like behavior, finding that these two targets display alterations in expression within the hippocampus and amygdala (compared to control, WT animals). As a whole, these data raise the prospect that the miR-132/212 locus may serve a modulator of anxiety-like behaviors. Along these lines, the data suggest that dysregulation of the locus (either deletion or over-expression), leads to the development of anxiety-like behaviors.

In the fifth chapter of this dissertation, we employed an Unpredictable Chronic Mild Stress (UCMS) paradigm—a rodent model of depression—in order to ascertain the effects of depression-like behavior on circadian timing within the forebrain. Using a *Per1*-Venus transgenic clock reporter line, we found that this six-week paradigm led to alterations in circadian clock gene expression within forebrain (i.e. non-SCN brain regions), but that it had little effect on *Per1*-Venus expression within the SCN. Furthermore, we noted that time-of-day dependent cognitive capacity was abrogated in

mice exposed to the six week stress paradigm. However, minimal effects on circadian timing and entrainment capacity (profiled using circadian wheel running activity) were noted in the stressed mice. Thus, this data suggests that circadian clock gene expression within mood circuits—but not within the master circadian clock—are most affected by chronic stress.

In chapter six, we employed this same six-week UCMS paradigm in an *Aldh1l1*-eGFP astrocyte reporter mouse line to profile the effects of chronic stress on astrocyte anatomy and physiology. We found that the chronic stress protocol led to a reduction in total process length in astrocytes within the PFC (and a trending decrease in astrocytes in the hippocampus). Further, we found that chronic stress led to a significant reduction in average surface surface area within hippocampal astrocytes (and a trending reduction within PFC astrocytes). Adding to this morphological analysis, we found that stress increased the interastrocyte distance between astrocytes in both the PFC and the hippocampus, though no change was observed in the density of both neurons and astrocytes. Finally, using an electrophysiological approach, we found that stress led to impairment in the strength of gap junction coupling within astrocytes in the hippocampus and PFC. Together, our data suggest that both individual and network-level astrocyte anatomy/physiology is altered in animals that display depression-like behaviors.

Finally, in chapter seven, serial blockface scanning electron microscopy was used to examine the ultrastructure of astrocyte-neurite contacts within the mouse hippocampus. By reconstructing three neighboring astrocytes and three complete dendrites (and their associated axons) within the stratum radiatum sub-region, we were

able to profile (in great detail), the ulrastucture of astrocyte-neurite association. We found that a majority of synapses are contacted by astrocyte processes. Furthermore, identification and analysis of intracellular particles within astrocytes revealed an enrichment of glycogen granules within astrocyte processes that abut synapses—raising interesting questions about the structure-function relationship between this source of energy and the many processes that these granules may help to fuel. Together, these data provide the first detailed perspective of the close interaction between astrocytes and neurites within the adult mouse hippocampus.

Prospective studies for SynGAP regulation of circadian clock timing

In chapter 2 of this dissertation, we found that mice heterozygous for the *Syngap1* gene displayed alterations in clock-gated locomotor behavior and circadian clock entrainment capacity. These results, coupled with the fact that individuals with mutations in the *Syngap1* gene display a wide array of sleep disturbances (Jimenez-Gomez et al., 2019; Prchalova et al., 2017; Vlaskamp et al., 2019), suggest that SynGAP may regulate several circadian-clock gated processes (perhaps via its regulation of the ERK/MAPK pathway).

Interestingly the *Syngap1* heterozygous mice used in our study—which have ~50% reduction in total protein levels (Clement et al., 2012) are a construct valid rodent model for humans with mutation in the Syngap1 gene (MRD5)(Kilinc et al., 2018). Notably, this mouse line was provided by the lab of Dr. Gavin Rumbaugh, and it can be bred to inducible Cre-ER mice (JAX stock #004682) to produce adult 'reversal animals' (Creson et al., 2019b). Such a breeding scheme allows for the re-expression of SynGAP

in an adult animal (upon the administration of tamoxifen), and can therefore provide critical insights related to the effects of SynGAP rescue on synaptic function, etc in a mature mouse (i.e. animals would still display haploinsufficieny during development, similar to what is observed in many older children with *Syngap1* gene mutations). Interestingly, adult restoration of SynGAP protein (using this *Syngap1* reversal mouse line/breeding scheme) was recently shown to improve both electrophysiological and behavioral measures of memory capacity and seizure activity (Creson et al., 2019b). Hence, while it is clear that neurodevelopment disorder risk genes (such as *Syngap1)* (Cheng et al., 2009b; Hamdan et al., 2009b; X. Zhu et al., 2014) play a prominent role in early life circuit-level imbalances that often trigger seizures and worsening cognitive phenotypes, this seminal study by Creson et al demonstrated that *Syngap1* likely retains functionality (at least to some extent) into adulthood. To this end, many of its non-developmental functions (such as its role in ERK/MAPK-dependent circadian clock entrainment—chapter 2) may contribute to the aberrant sleep phenotypes observed in MRD5 participants. Future studies aimed at using the *Syngap1* reversal mice to examine whether the abnormal circadian phenotype(s) can be mitigated upon tamoxifen administration during adulthood are therefore of merit. If the circadian-gated locomotor and light entrainment phenotypes can be rescused (to any extent), this result could lead to exciting new areas of study aimed at improving circadian function via the use of gene therapy approaches that restore SynGAP protein levels in individuals with *Syngap1* haploinsufficiency.

Prospective studies for circadian clock regulation of cognition and affect

In chapter 3 of this dissertation, we showed that microRNA-132 couples the circadian clock to rhythms in learning and memory. Using the same mouse models (as in chapter 3), in chapter 4 we also demonstrated that the miR-132/212 locus is induced by stress, and that it regulates anxiety-like behaviors. These observations, coupled with our results showing that a mouse model of depression (UCMS) alters forebrain circadian clock gene expression and associated working and intermediate-term memory tasks (chapter 5), highlight the prominent role of circadian timing in brain plasticity. Indeed, the circadian clock may serve as an important modulator of cognitive and affect-related functionality.

miR-132 and clock-gated cognition

With respect to the miR-132-dependent time-of-day regulation of cognitive capacity (Chapter 3), our study did not tease apart the *precise* mechanism by which miR-132 imparts circadian control on cognitive measures. Indeed, while we did show that several synaptic-plasticity associated miR-132 targets were altered in mice with constitutive (i.e. non-circadian gated) miR-132 expression, we did not test cellular-level ramifications of this constitutive expression. Along these lines, given that miR-132 is known to be a potent modulator of dendritic spine density/morphology (Hansen et al., 2010; Jasińska et al., 2016; Magill et al., 2010; Pathania et al., 2012), and that spine density/morphology has been shown to influence memory capacity (in certain circumstances and/or to a certain extent) (Mahmmoud et al., 2015; Moser et al., 1994), it would be interesting to test whether changes in spine density/morphology across the day (Ikeda et al., 2015; Jasinska et al., 2020, 2019) are miR-132 dependent. Indeed, data

showing whether time-of-day dependent changes in dendritic spine density/morphology are mitigated/altered in our constitutively-expressing miR-132 mouse line would provide a key link between miR-132 and circadian-dependent cognition.

Forebrain circadian clock timing and chronic stress

Turning to our chronic stress study in *Per1*-Venus animals (Chapter 5), our experiments were limited to the examination of cellular-level circadian timing after a six week UCMS paradigm. Hence, we did not extend our work to study possible effects of therapeutics on clock timing. However, it is interesting to note that antidepressants such as ketamine have been shown to alleviate depressive-like symptoms within hours after administration (after the initital dissociative effects dissipate) (Berman et al., 2000; Zarate et al., 2006). These studies suggest that ketamine administration initiates a cascade of synaptic plasticity and cellular signaling processes that result in a rapid anti-depressant response (see(Duman et al., 2012) for review). Similarly, in animal models, acute ketamine administration leads to near-immediate behavioral effects, and in some cases, protracted effects that can last for days to weeks (Browne and Lucki, 2013).

Given our finding that the UCMS paradigm altered cellular (and behavioral level) clock timing/time-of-day cognition within mood circuits, one may posit that antidepressant treatments like ketamine (that are fast-acting) may function (at least in part) by rapidly resetting the circadian timing system. Such a mechanism (within forebrain limbic clock circuitry) may be similar to the rapid resetting process that occurs within the SCN after a change in the lighting cycle (such as a light pulse) (Best et al., 1999; Shigeyoshi et al., 1997). Hence, ketamine (or other antidepressants) may function

within minutes to hours (via synaptic/cell signaling pathways) to reset forebrain clocks. Further, this rapid increase in glutamatergic transmission may, in turn, actuate other cellular signaling mechanisms to lead to clock resetting (perhaps allowing for the more protracted antidepressant effects of ketamine) (Browne and Lucki, 2013; Maeng et al., 2008; Yilmaz et al., 2002; Zarate et al., 2006).

The ideas outlined above delineate a role of antidepressants in the resetting of cellular clocks within the brain. However, these experiments do not offer a complete, mechanistic portrayal of the downstream signaling effector pathways that may be involved in this ketamine-mediated clock resetting process. Indeed, one could ask whether the chronic stress-evoked forebrain clock deficits are 'reset' by ketamine in an mTOR or ERK dependent manner. This idea is predicated by a noteworthy study showing that the ERK inhibitor U0126 blocks the ability of ketamine to stimulate the mTOR pathway and that rapamycin (an mTOR inhibitor) blocks the antidepressant behavior and molecular effects of ketamine (Li et al., 2011, 2010). Hence, could a similar idea hold true with respect to ketamine, cellular plasticity pathways (ERK, mTOR, CREB, miR-132), and clock resetting? Notably, these signaling pathways have all been shown to regulate the circadian clock (Cao et al., 2010; Cheng et al., 2007b, p. 200; Lee et al., 2010; K. Obrietan et al., 1998b; Ramanathan et al., 2018). Intriguingly, these same signaling effectors may also be necessary in mediating the antidepressant effects of ketamine. Given this, experiments that probe whether kinase inhibitor pretreatment (U0126, PD98059, rapamycin) blocks the clock resetting effects of ketamine would provide an unequivocal test of the functional significance of this feedback circuit wherein

ketamine administration leads to rapid activation of these signaling pathways that are required to boost core clock machinery and maintain cellular synchrony in depressed animals given antidepressants.

Should studies find that rapid-antidepressant treatment does, indeed, 'reset' the forebrain clock, follow-up experiments could then be performed to ask the questions: Does circadian clock dysregulation—which has been shown to coincide with synaptic plasticity alterations (Wardlaw et al., 2014)—influence the efficacy of ketamine and other fast-acting antidepressants? And if so, are the protracted effects of ketamine absent in animals with disrupted mesolimbic clock timing? Indeed, one could utilize forebrain-specific circadian clock knockout mice to test whether the efficacy of ketamine's antidepressant effects (short term and/or protracted) are altered during certain time(s) of the day. Such experiments would provide key mechanistic insights that may translate into the effects that antidepressants may have on depressed individuals with persistent circadian rhythm disturbances (shift workers, individuals with sleep disorders, etc). Further, all of the noted studies could prove beneficial to health care workers in deciding exactly *when* (i.e. what time of day) to administer antidepressants in individuals with Major Depressive Disorder.

Prospective studies for astrocyte-neuron communication in health and disease

In chapter six of this dissertation, we showed that a six week chronic stress paradigm leads to changes in individual and network-level astrocyte anatomy, in addition to a decrease in gap junction coupling. These data, coupled with our data in chapter seven—showing that a majority of synapses are contacted by astrocyte processes (at least

within the hippocampus) raise interesting questions about the role of astrocyte-neuron interaction in both healthy and diseased states.

Along these lines, while our current study did not examine the underlying mechanism of this reduction in syncytial coupling, it would be of merit to discern whether spontaneous and/or evoked calcium signaling within astrocytes is altered by chronic stress. Indeed, though astrocytes are not electrically active, they do exhibit dynamic calcium activities in both their soma and processes, which can be used as a readout of their physiological state (Guerra-Gomes et al., 2018). Given that chronic stress paradigms have been shown to reduce hippocampal LTP (Pavlides et al., 2002), and that sensing of glutamate by astrocytes can induce increases in calcium activity, one may posit that astroytic calcium responses to neuronal simulation may be altered by chronic stress—a topic that we are currently investigating. Such studies could then be expanded upon by investigating whether restoration of calcium activity (specifically within astrocytes) may rescue (at least to some extent) depression-like behaviors and synaptic plasticity deficits in stressed mice. Indeed, harnessing the utility of novel transgenic mouse lines and/or viral vectors—such as astrocyte-specific Gq-coupled DREADD constructs—would likely be of great value when investigating how alterations in calcium signaling within astrocytes of stressed mice may affect neuronal signaling, antidepressant therapy efficacy, and depressive behavioral phenotypes.

Furthermore, given the close proximity of neurites to astrocytic processes (chapter 7), it would also be interesting to test whether astrocyte-neuron proximity is alatered in limbic regions (such as the hippocampus and PFC) after chronic stress. Such

an experiment could be conducted using SBF-SEM (similar to our study in Chapter 7) or with a novel neuronal-astrocyte proximity (viral-based) assay that utilizes Forster resonance energy transfer (FRET) (Octeau et al., 2018). Notably, a recent study published by Dr. Ben Deneen's lab used this methodology to demonstrate that astrocytes deficient in the transcription factor nuclear factor I-A (NFIA) have defective communication with neurons (Huang et al., 2020). Similarly, viral-based neurotransmitter (i.e. glutamate and GABA) sensing fluorescent reporters (under the control of an astrocyte-specific *Gfap* or *Aldh1l1* promoter) could also be used to image astrocyte activity in response to neuronal stimulation—providing additional insights into whether astrocyte-neuron communication might be altered by chronic stress (Huang et al., 2020). Together, these noted potential studies would provide mechanistic clarity as to how astrocyte-neuron interactions may be altered by chronic stress (and other neuropsychiatric/neurological diseases/disorders).

References:

Abe, H., Honma, S., Ohtsu, H., Honma, K.-I., 2004. Circadian rhythms in behavior and clock gene expressions in the brain of mice lacking histidine decarboxylase. Brain Res. Mol. Brain Res. 124, 178–187. https://doi.org/10.1016/j.molbrainres.2004.02.015

Abe, H., Rusak, B., Robertson, H.A., 1991. Photic induction of Fos protein in the suprachiasmatic nucleus is inhibited by the NMDA receptor antagonist MK-801. Neurosci. Lett. 127, 9–12. https://doi.org/10.1016/0304-3940(91)90881-s

Abe, K., Kroning, J., Greer, M.A., Critchlow, V., 1979. Effects of destruction of the suprachiasmatic nuclei on the circadian rhythms in plasma corticosterone, body temperature, feeding and plasma thyrotropin. Neuroendocrinology 29, 119–131. https://doi.org/10.1159/000122913

Abrahamson, E.E., Moore, R.Y., 2001. Suprachiasmatic nucleus in the mouse: retinal innervation, intrinsic organization and efferent projections. Brain Res. 916, 172–191. https://doi.org/10.1016/s0006-8993(01)02890-6

Adamsky, A., Kol, A., Kreisel, T., Doron, A., Ozeri-Engelhard, N., Melcer, T., Refaeli, R., Horn, H., Regev, L., Groysman, M., London, M., Goshen, I., 2018. Astrocytic Activation Generates De Novo Neuronal Potentiation and Memory Enhancement. Cell 174, 59-71.e14. https://doi.org/10.1016/j.cell.2018.05.002

Akashi, M., Hayasaka, N., Yamazaki, S., Node, K., 2008. Mitogen-Activated Protein Kinase Is a Functional Component of the Autonomous Circadian System in the Suprachiasmatic Nucleus. J. Neurosci. 28, 4619–4623. https://doi.org/10.1523/JNEUROSCI.3410-07.2008

Akashi, M., Takumi, T., 2005. The orphan nuclear receptor RORalpha regulates circadian transcription of the mammalian core-clock Bmal1. Nat Struct Mol Biol 12, 441–448. https://doi.org/10.1038/nsmb925

Albrecht, A., Çalışkan, G., Oitzl, M.S., Heinemann, U., Stork, O., 2013. Long-lasting increase of corticosterone after fear memory reactivation: anxiolytic effects and network activity modulation in the ventral hippocampus. Neuropsychopharmacology 38, 386–394. https://doi.org/10.1038/npp.2012.192

Albrecht, A., Stork, O., 2017. Circadian Rhythms in Fear Conditioning: An Overview of Behavioral, Brain System, and Molecular Interactions. Neural Plast. 2017, 3750307. https://doi.org/10.1155/2017/3750307

Albrecht, P., Bittner, J.J., Halberg, F., Visscher, M.B., 1956. [Daily changes in 5-hydroxytryptamine concentration in mouse brain]. Proc. Soc. Exp. Biol. Med. 92, 703–706.

Alemayehu, S., Feghali, K.C., Cowden, J., Komisar, J., Ockenhouse, C.F., Kamau, E., 2013. Comparative evaluation of published real-time PCR assays for the detection

of malaria following MIQE guidelines. Malar J 12, 277. https://doi.org/10.1186/1475-2875-12-277

Alexander, J.C., McDermott, C.M., Tunur, T., Rands, V., Stelly, C., Karhson, D., Bowlby, M.R., An, W.F., Sweatt, J.D., Schrader, L.A., 2009. The role of calsenilin/DREAM/KChIP3 in contextual fear conditioning. Learn Mem 16, 167–177. https://doi.org/10.1101/lm.1261709

Allaman, I., Fiumelli, H., Magistretti, P.J., Martin, J.-L., 2011. Fluoxetine regulates the expression of neurotrophic/growth factors and glucose metabolism in astrocytes. Psychopharmacology (Berl.) 216, 75–84. https://doi.org/10.1007/s00213-011-2190-y

Allen, N.J., Eroglu, C., 2017. Cell biology of astrocyte-synapse interactions. Neuron 96, 697–708. https://doi.org/10.1016/j.neuron.2017.09.056

Al-Safadi, S., Al-Safadi, A., Branchaud, M., Rutherford, S., Dayanandan, A., Robinson, B., Amir, S., 2014. Stress-Induced Changes in the Expression of the Clock Protein PERIOD1 in the Rat Limbic Forebrain and Hypothalamus: Role of Stress Type, Time of Day, and Predictability. PLoS One 9. https://doi.org/10.1371/journal.pone.0111166

Alvarez-Saavedra, M., Antoun, G., Yanagiya, A., Oliva-Hernandez, R., Cornejo-Palma, D., Perez-Iratxeta, C., Sonenberg, N., Cheng, H.-Y.M., 2011. miRNA-132 orchestrates chromatin remodeling and translational control of the circadian clock. Hum Mol Genet 20, 731–751. https://doi.org/10.1093/hmg/ddq519

Amir, R.E., Van den Veyver, I.B., Wan, M., Tran, C.Q., Francke, U., Zoghbi, H.Y., 1999. Rett syndrome is caused by mutations in X-linked MECP2, encoding methyl-CpG-binding protein 2. Nat Genet 23, 185–188. https://doi.org/10.1038/13810

Anacker, C., Zunszain, P.A., Carvalho, L.A., Pariante, C.M., 2011. The glucocorticoid receptor: Pivot of depression and of antidepressant treatment? Psychoneuroendocrinology 36, 415–425. https://doi.org/10.1016/j.psyneuen.2010.03.007

Andolina, D., Di Segni, M., Bisicchia, E., D'Alessandro, F., Cestari, V., Ventura, A., Concepcion, C., Puglisi-Allegra, S., Ventura, R., 2016. Effects of lack of microRNA-34 on the neural circuitry underlying the stress response and anxiety. Neuropharmacology 107, 305–316. https://doi.org/10.1016/j.neuropharm.2016.03.044

Andrews, J.L., Zhang, X., McCarthy, J.J., McDearmon, E.L., Hornberger, T.A., Russell, B., Campbell, K.S., Arbogast, S., Reid, M.B., Walker, J.R., Hogenesch, J.B., Takahashi, J.S., Esser, K.A., 2010. CLOCK and BMAL1 regulate MyoD and are necessary for maintenance of skeletal muscle phenotype and function. Proc. Natl. Acad. Sci. U.S.A. 107, 19090–19095. https://doi.org/10.1073/pnas.1014523107

Antle, M.C., Silver, R., 2005. Orchestrating time: arrangements of the brain circadian clock. Trends Neurosci. 28, 145–151. https://doi.org/10.1016/j.tins.2005.01.003

Antoun, G., Bouchard-Cannon, P., Cannon, P.B., Cheng, H.-Y.M., 2012. Regulation of MAPK/ERK signaling and photic entrainment of the suprachiasmatic nucleus

circadian clock by Raf kinase inhibitor protein. J Neurosci 32, 4867–4877. https://doi.org/10.1523/JNEUROSCI.5650-11.2012
Araki, Y., Zeng, M., Zhang, M., Huganir, R.L., 2015. Rapid Dispersion of SynGAP from Synaptic Spines Triggers AMPA Receptor Insertion and Spine Enlargement during LTP. Neuron 85, 173–189. https://doi.org/10.1016/j.neuron.2014.12.023
Ardekani, A.M., Naeini, M.M., 2010. The Role of MicroRNAs in Human Diseases. Avicenna J Med Biotechnol 2, 161–179.
Arendt, T., Gärtner, U., Seeger, G., Barmashenko, G., Palm, K., Mittmann, T., Yan, L., Hümmeke, M., Behrbohm, J., Brückner, M.K., Holzer, M., Wahle, P., Heumann, R., 2004. Neuronal activation of Ras regulates synaptic connectivity. Eur. J. Neurosci. 19, 2953–2966. https://doi.org/10.1111/j.0953-816X.2004.03409.x
Arrondo, G., Segarra, N., Metastasio, A., Ziauddeen, H., Spencer, J., Reinders, N.R., Dudas, R.B., Robbins, T.W., Fletcher, P.C., Murray, G.K., 2015. Reduction in ventral striatal activity when anticipating a reward in depression and schizophrenia: a replicated cross-diagnostic finding. Front Psychol 6, 1280. https://doi.org/10.3389/fpsyg.2015.01280
Asano, Y., 1971. The maturation of the circadian rhythm of brain norepinephrine and serotonin in the rat. Life Sciences 10, 883–894. https://doi.org/10.1016/0024-3205(71)90160-3
Aschoff, J., 1979. Circadian Rhythms: Influences of Internal and External Factors on the Period Measured in Constant Conditions1. Zeitschrift für Tierpsychologie 49, 225–249. https://doi.org/10.1111/j.1439-0310.1979.tb00290.x
Aschoff, J., 1960. Exogenous and endogenous components in circadian rhythms. Cold Spring Harb. Symp. Quant. Biol. 25, 11–28. https://doi.org/10.1101/sqb.1960.025.01.004
Asher, G., Gatfield, D., Stratmann, M., Reinke, H., Dibner, C., Kreppel, F., Mostoslavsky, R., Alt, F.W., Schibler, U., 2008. SIRT1 regulates circadian clock gene expression through PER2 deacetylation. Cell 134, 317–328. https://doi.org/10.1016/j.cell.2008.06.050
Aston-Jones, G., Chen, S., Zhu, Y., Oshinsky, M.L., 2001. A neural circuit for circadian regulation of arousal. Nat. Neurosci. 4, 732–738. https://doi.org/10.1038/89522
Aten, S., Hansen, K.F., Hoyt, K.R., Obrietan, K., 2016. The miR-132/212 locus: a complex regulator of neuronal plasticity, gene expression and cognition. RNA Dis 3.
Aten, S., Hansen, K.F., Snider, K., Wheaton, K., Kalidindi, A., Garcia, A., Alzate-Correa, D., Hoyt, K.R., Obrietan, K., 2018a. miR-132 couples the circadian clock to daily rhythms of neuronal plasticity and cognition. Learn Mem 25, 214–229. https://doi.org/10.1101/lm.047191.117
Aten, S., Kalidindi, A., Yoon, H., Rumbaugh, G., Hoyt, K.R., Obrietan, K., 2021. SynGAP is expressed in the murine suprachiasmatic nucleus and regulates circadian-gated locomotor activity and light-entrainment capacity. Eur J Neurosci 53, 732–749. https://doi.org/10.1111/ejn.15043
Aten, S., Page, C.E., Kalidindi, A., Wheaton, K., Niraula, A., Godbout, J.P., Hoyt, K.R., Obrietan, K., 2019. miR-132/212 is induced by stress and its dysregulation

triggers anxiety-related behavior. Neuropharmacology 144, 256–270. https://doi.org/10.1016/j.neuropharm.2018.10.020
Aten, S., Page, C.E., Kalidindi, A., Wheaton, K.L., Niraula, A., Godbout, J.P., Hoyt, K.R., Obrietan, K., 2018b. Data highlighting the expression of two miR-132/212 target genes-Sirt1 and Pten-after chronic stress. Data Brief 21, 2323–2329. https://doi.org/10.1016/j.dib.2018.11.042
Aubry, A.V., Serrano, P.A., Burghardt, N.S., 2016. Molecular Mechanisms of Stress-Induced Increases in Fear Memory Consolidation within the Amygdala. Front Behav Neurosci 10. https://doi.org/10.3389/fnbeh.2016.00191
Banasr, M., Valentine, G.W., Li, X.-Y., Gourley, S.L., Taylor, J.R., Duman, R.S., 2007. Chronic unpredictable stress decreases cell proliferation in the cerebral cortex of the adult rat. Biol. Psychiatry 62, 496–504. https://doi.org/10.1016/j.biopsych.2007.02.006
Baño-Otálora, B., Piggins, H.D., 2017. Contributions of the lateral habenula to circadian timekeeping. Pharmacol. Biochem. Behav. 162, 46–54. https://doi.org/10.1016/j.pbb.2017.06.007
Barker, G.R.I., Warburton, E.C., 2011. When is the hippocampus involved in recognition memory? J Neurosci 31, 10721–10731. https://doi.org/10.1523/JNEUROSCI.6413-10.2011
Barres, B.A., 2008. The mystery and magic of glia: a perspective on their roles in health and disease. Neuron 60, 430–440. https://doi.org/10.1016/j.neuron.2008.10.013
Behbehani, M.M., 1995. Functional characteristics of the midbrain periaqueductal gray. Prog. Neurobiol. 46, 575–605.
Benedetti, F., Serretti, A., Colombo, C., Barbini, B., Lorenzi, C., Campori, E., Smeraldi, E., 2003. Influence of CLOCK gene polymorphism on circadian mood fluctuation and illness recurrence in bipolar depression. Am. J. Med. Genet. B Neuropsychiatr. Genet. 123B, 23–26. https://doi.org/10.1002/ajmg.b.20038
Bennett, M.V.L., Contreras, J.E., Bukauskas, F.F., Sáez, J.C., 2003. New roles for astrocytes: Gap junction hemichannels have something to communicate. Trends Neurosci 26, 610–617. https://doi.org/10.1016/j.tins.2003.09.008
Berman, R.M., Cappiello, A., Anand, A., Oren, D.A., Heninger, G.R., Charney, D.S., Krystal, J.H., 2000. Antidepressant effects of ketamine in depressed patients. Biol. Psychiatry 47, 351–354.
Berryer, M.H., Chattopadhyaya, B., Xing, P., Riebe, I., Bosoi, C., Sanon, N., Antoine-Bertrand, J., Lévesque, M., Avoli, M., Hamdan, F.F., Carmant, L., Lamarche-Vane, N., Lacaille, J.-C., Michaud, J.L., Cristo, G.D., 2016. Decrease of SYNGAP1 in GABAergic cells impairs inhibitory synapse connectivity, synaptic inhibition and cognitive function. Nat Commun 7, 1–14. https://doi.org/10.1038/ncomms13340
Berryer, M.H., Hamdan, F.F., Klitten, L.L., Møller, R.S., Carmant, L., Schwartzentruber, J., Patry, L., Dobrzeniecka, S., Rochefort, D., Neugnot-Cerioli, M., Lacaille, J.-C., Niu, Z., Eng, C.M., Yang, Y., Palardy, S., Belhumeur, C., Rouleau, G.A., Tommerup, N., Immken, L., Beauchamp, M.H., Patel, G.S., Majewski, J., Tarnopolsky, M.A., Scheffzek, K., Hjalgrim, H., Michaud, J.L., Di Cristo, G.,

2013. Mutations in SYNGAP1 cause intellectual disability, autism, and a specific form of epilepsy by inducing haploinsufficiency. Hum. Mutat. 34, 385–394. https://doi.org/10.1002/humu.22248

Besheer, J., Jensen, H.C., Bevins, R.A., 1999. Dopamine antagonism in a novel-object recognition and a novel-object place conditioning preparation with rats. Behav Brain Res 103, 35–44. https://doi.org/10.1016/s0166-4328(99)00021-2

Best, J.D., Maywood, E.S., Smith, K.L., Hastings, M.H., 1999. Rapid resetting of the mammalian circadian clock. J. Neurosci. 19, 828–835.

Betel, D., Wilson, M., Gabow, A., Marks, D.S., Sander, C., 2008. The microRNA.org resource: targets and expression. Nucleic Acids Res 36, D149-153. https://doi.org/10.1093/nar/gkm995

Bezzi, P., Carmignoto, G., Pasti, L., Vesce, S., Rossi, D., Rizzini, B.L., Pozzan, T., Volterra, A., 1998. Prostaglandins stimulate calcium-dependent glutamate release in astrocytes. Nature 391, 281–285. https://doi.org/10.1038/34651

Blanchard, D.C., Sakai, R.R., McEwen, B., Weiss, S.M., Blanchard, R.J., 1993. Subordination stress: behavioral, brain, and neuroendocrine correlates. Behav Brain Res 58, 113–121. https://doi.org/10.1016/0166-4328(93)90096-9

Boivin, D., 2000. Influence of sleep-wake and circadian rhythm disturbances in psychiatric disorders. J Psychiatry Neurosci 25, 446–458.

Boivin, D.B., Czeisler, C.A., Dijk, D.J., Duffy, J.F., Folkard, S., Minors, D.S., Totterdell, P., Waterhouse, J.M., 1997. Complex interaction of the sleep-wake cycle and circadian phase modulates mood in healthy subjects. Arch. Gen. Psychiatry 54, 145–152.

Bonsall, D.R., Lall, G.S., 2013. Protein kinase C differentially regulates entrainment of the mammalian circadian clock. Chronobiol Int 30, 460–469. https://doi.org/10.3109/07420528.2012.741170

Borniger, J.C., McHenry, Z.D., Abi Salloum, B.A., Nelson, R.J., 2014. Exposure to dim light at night during early development increases adult anxiety-like responses. Physiol. Behav. 133, 99–106. https://doi.org/10.1016/j.physbeh.2014.05.012

Boyce, P., Barriball, E., 2010. Circadian rhythms and depression. Aust Fam Physician 39, 307–310.

Brancaccio, M., Edwards, M.D., Patton, A.P., Smyllie, N.J., Chesham, J.E., Maywood, E.S., Hastings, M.H., 2019. Cell-autonomous clock of astrocytes drives circadian behavior in mammals. Science 363, 187–192. https://doi.org/10.1126/science.aat4104

Brancaccio, M., Maywood, E.S., Chesham, J.E., Loudon, A.S.I., Hastings, M.H., 2013. A Gq-Ca2+ axis controls circuit-level encoding of circadian time in the suprachiasmatic nucleus. Neuron 78, 714–728. https://doi.org/10.1016/j.neuron.2013.03.011

Brancaccio, M., Patton, A.P., Chesham, J.E., Maywood, E.S., Hastings, M.H., 2017. Astrocytes Control Circadian Timekeeping in the Suprachiasmatic Nucleus via Glutamatergic Signaling. Neuron 93, 1420-1435.e5. https://doi.org/10.1016/j.neuron.2017.02.030

Brown, E.S., 2009. Effects of glucocorticoids on mood, memory, and the hippocampus. Treatment and preventive therapy. Ann. N. Y. Acad. Sci. 1179, 41–55. https://doi.org/10.1111/j.1749-6632.2009.04981.x

Browne, C.A., Hammack, R., Lucki, I., 2018. Dysregulation of the Lateral Habenula in Major Depressive Disorder. Front Synaptic Neurosci 10. https://doi.org/10.3389/fnsyn.2018.00046

Browne, C.A., Lucki, I., 2013. Antidepressant effects of ketamine: mechanisms underlying fast-acting novel antidepressants. Front Pharmacol 4, 161. https://doi.org/10.3389/fphar.2013.00161

Buhr, E.D., Takahashi, J.S., 2013. Molecular components of the Mammalian circadian clock. Handb Exp Pharmacol 3–27. https://doi.org/10.1007/978-3-642-25950-0_1

Bunger, M.K., Wilsbacher, L.D., Moran, S.M., Clendenin, C., Radcliffe, L.A., Hogenesch, J.B., Simon, M.C., Takahashi, J.S., Bradfield, C.A., 2000a. Mop3 is an essential component of the master circadian pacemaker in mammals. Cell 103, 1009–1017. https://doi.org/10.1016/s0092-8674(00)00205-1

Bunger, M.K., Wilsbacher, L.D., Moran, S.M., Clendenin, C., Radcliffe, L.A., Hogenesch, J.B., Simon, M.C., Takahashi, J.S., Bradfield, C.A., 2000b. Mop3 is an essential component of the master circadian pacemaker in mammals. Cell 103, 1009–1017. https://doi.org/10.1016/s0092-8674(00)00205-1

Bushong, E.A., Martone, M.E., Jones, Y.Z., Ellisman, M.H., 2002. Protoplasmic Astrocytes in CA1 Stratum Radiatum Occupy Separate Anatomical Domains. J. Neurosci. 22, 183–192. https://doi.org/10.1523/JNEUROSCI.22-01-00183.2002

Butcher, G.Q., Doner, J., Dziema, H., Collamore, M., Burgoon, P.W., Obrietan, K., 2002a. The p42/44 mitogen-activated protein kinase pathway couples photic input to circadian clock entrainment. J Biol Chem 277, 29519–29525. https://doi.org/10.1074/jbc.M203301200

Butcher, G.Q., Dziema, H., Collamore, M., Burgoon, P.W., Obrietan, K., 2002b. The p42/44 Mitogen-activated Protein Kinase Pathway Couples Photic Input to Circadian Clock Entrainment. J. Biol. Chem. 277, 29519–29525. https://doi.org/10.1074/jbc.M203301200

Cain, S.W., Dennison, C.F., Zeitzer, J.M., Guzik, A.M., Khalsa, S.B.S., Santhi, N., Schoen, M.W., Czeisler, C.A., Duffy, J.F., 2010. Sex differences in phase angle of entrainment and melatonin amplitude in humans. J. Biol. Rhythms 25, 288–296. https://doi.org/10.1177/0748730410374943

Calì, C., Baghabra, J., Boges, D.J., Holst, G.R., Kreshuk, A., Hamprecht, F.A., Srinivasan, M., Lehväslaiho, H., Magistretti, P.J., 2016. Three-dimensional immersive virtual reality for studying cellular compartments in 3D models from EM preparations of neural tissues. J Comp Neurol 524, 23–38. https://doi.org/10.1002/cne.23852

Calì, C., Tauffenberger, A., Magistretti, P., 2019. The Strategic Location of Glycogen and Lactate: From Body Energy Reserve to Brain Plasticity. Front Cell Neurosci 13. https://doi.org/10.3389/fncel.2019.00082

Campioni, M.R., Xu, M., McGehee, D.S., 2009. Stress-Induced Changes in Nucleus Accumbens Glutamate Synaptic Plasticity. J Neurophysiol 101, 3192–3198. https://doi.org/10.1152/jn.91111.2008

Campos, L.M.G., Osório, E.C., Santos, G.L. da S., Nogueira, M.I., Cruz-Rizzolo, R.J., Pinato, L., 2015. Temporal changes in calcium-binding proteins in the medial geniculate nucleus of the monkey Sapajus apella. J Chem Neuroanat 68, 45–54. https://doi.org/10.1016/j.jchemneu.2015.07.005

Cao, R., Li, A., Cho, H., Lee, B., Obrietan, K., 2010. Mammalian target of rapamycin signaling modulates photic entrainment of the suprachiasmatic circadian clock. J Neurosci 30, 6302–6314. https://doi.org/10.1523/JNEUROSCI.5482-09.2010

Castagné, V., Moser, P., Roux, S., Porsolt, R.D., 2011. Rodent models of depression: forced swim and tail suspension behavioral despair tests in rats and mice. Curr Protoc Neurosci Chapter 8, Unit 8.10A. https://doi.org/10.1002/0471142301.ns0810as55

Castañeda, T.R., de Prado, B.M., Prieto, D., Mora, F., 2004. Circadian rhythms of dopamine, glutamate and GABA in the striatum and nucleus accumbens of the awake rat: modulation by light. J. Pineal Res. 36, 177–185.

Cermakian, Nicolas, Sassone-Corsi, P., 2000. Multilevel regulation of the circadian clock. Nature Reviews Molecular Cell Biology 1, 59. https://doi.org/10.1038/35036078

Cermakian, N., Sassone-Corsi, P., 2000. Multilevel regulation of the circadian clock. Nat. Rev. Mol. Cell Biol. 1, 59–67. https://doi.org/10.1038/35036078

Cerniauskas, I., Winterer, J., de Jong, J.W., Lukacsovich, D., Yang, H., Khan, F., Peck, J.R., Obayashi, S.K., Lilascharoen, V., Lim, B.K., Földy, C., Lammel, S., 2019. Chronic Stress Induces Activity, Synaptic, and Transcriptional Remodeling of the Lateral Habenula Associated with Deficits in Motivated Behaviors. Neuron 104, 899-915.e8. https://doi.org/10.1016/j.neuron.2019.09.005

Chahrour, M., Jung, S.Y., Shaw, C., Zhou, X., Wong, S.T.C., Qin, J., Zoghbi, H.Y., 2008. MeCP2, a key contributor to neurological disease, activates and represses transcription. Science 320, 1224–1229. https://doi.org/10.1126/science.1153252

Chao, O.Y., Huston, J.P., Nikolaus, S., de Souza Silva, M.A., 2016. Concurrent assessment of memory for object and place: Evidence for different preferential importance of perirhinal cortex and hippocampus and for promnestic effect of a neurokinin-3 R agonist. Neurobiol Learn Mem 130, 149–158. https://doi.org/10.1016/j.nlm.2016.02.007

Chaudhury, D., Colwell, C.S., 2002a. Circadian modulation of learning and memory in fear-conditioned mice. Behav. Brain Res. 133, 95–108.

Chaudhury, D., Colwell, C.S., 2002b. Circadian modulation of learning and memory in fear-conditioned mice. Behav Brain Res 133, 95–108. https://doi.org/10.1016/s0166-4328(01)00471-5

Chen, A.C., Shirayama, Y., Shin, K.H., Neve, R.L., Duman, R.S., 2001. Expression of the cAMP response element binding protein (CREB) in hippocampus produces an antidepressant effect. Biol. Psychiatry 49, 753–762.

Chen, H.-J., Rojas-Soto, M., Oguni, A., Kennedy, M.B., 1998. A Synaptic Ras-GTPase Activating Protein (p135 SynGAP) Inhibited by CaM Kinase II. Neuron 20, 895–904. https://doi.org/10.1016/S0896-6273(00)80471-7

Chen, K.C., Nicholson, C., 2000. Spatial buffering of potassium ions in brain extracellular space. Biophys J 78, 2776–2797.

Chen, Y., Rex, C.S., Rice, C.J., Dubé, C.M., Gall, C.M., Lynch, G., Baram, T.Z., 2010. Correlated memory defects and hippocampal dendritic spine loss after acute stress involve corticotropin-releasing hormone signaling. Proc Natl Acad Sci U S A 107, 13123–13128. https://doi.org/10.1073/pnas.1003825107

Cheng, H.-Y.M., Alvarez-Saavedra, M., Dziema, H., Choi, Y.S., Li, A., Obrietan, K., 2009a. Segregation of expression of mPeriod gene homologs in neurons and glia: possible divergent roles of mPeriod1 and mPeriod2 in the brain. Hum Mol Genet 18, 3110–3124. https://doi.org/10.1093/hmg/ddp252

Cheng, H.-Y.M., Alvarez-Saavedra, M., Dziema, H., Choi, Y.S., Li, A., Obrietan, K., 2009b. Segregation of expression of mPeriod gene homologs in neurons and glia: possible divergent roles of mPeriod1 and mPeriod2 in the brain. Hum Mol Genet 18, 3110–3124. https://doi.org/10.1093/hmg/ddp252

Cheng, H.-Y.M., Dziema, H., Papp, J., Mathur, D.P., Koletar, M., Ralph, M.R., Penninger, J.M., Obrietan, K., 2006a. The molecular gatekeeper Dexras1 sculpts the photic responsiveness of the mammalian circadian clock. J Neurosci 26, 12984–12995. https://doi.org/10.1523/JNEUROSCI.4253-06.2006

Cheng, H.-Y.M., Dziema, H., Papp, J., Mathur, D.P., Koletar, M., Ralph, M.R., Penninger, J.M., Obrietan, K., 2006b. The Molecular Gatekeeper Dexras1 Sculpts the Photic Responsiveness of the Mammalian Circadian Clock. J. Neurosci. 26, 12984–12995. https://doi.org/10.1523/JNEUROSCI.4253-06.2006

Cheng, H.-Y.M., Obrietan, K., Cain, S.W., Lee, B.Y., Agostino, P.V., Joza, N.A., Harrington, M.E., Ralph, M.R., Penninger, J.M., 2004. Dexras1 potentiates photic and suppresses nonphotic responses of the circadian clock. Neuron 43, 715–728. https://doi.org/10.1016/j.neuron.2004.08.021

Cheng, H.-Y.M., Papp, J.W., Varlamova, O., Dziema, H., Russell, B., Curfman, J.P., Nakazawa, T., Shimizu, K., Okamura, H., Impey, S., Obrietan, K., 2007a. microRNA modulation of circadian-clock period and entrainment. Neuron 54, 813–829. https://doi.org/10.1016/j.neuron.2007.05.017

Cheng, H.-Y.M., Papp, J.W., Varlamova, O., Dziema, H., Russell, B., Curfman, J.P., Nakazawa, T., Shimizu, K., Okamura, H., Impey, S., Obrietan, K., 2007b. microRNA modulation of circadian clock period and entrainment. Neuron 54, 813–829. https://doi.org/10.1016/j.neuron.2007.05.017

Christiansen, S.L., Bouzinova, E.V., Fahrenkrug, J., Wiborg, O., 2016. Altered Expression Pattern of Clock Genes in a Rat Model of Depression. Int. J. Neuropsychopharmacol. 19. https://doi.org/10.1093/ijnp/pyw061

Chun, L.E., Woodruff, E.R., Morton, S., Hinds, L.R., Spencer, R.L., 2015. Variations in Phase and Amplitude of Rhythmic Clock Gene Expression across Prefrontal Cortex, Hippocampus, Amygdala, and Hypothalamic Paraventricular and

Suprachiasmatic Nuclei of Male and Female Rats. J. Biol. Rhythms 30, 417–436. https://doi.org/10.1177/0748730415598608
Chung, S., Lee, E.J., Yun, S., Choe, H.K., Park, S.-B., Son, H.J., Kim, K.-S., Dluzen, D.E., Lee, I., Hwang, O., Son, G.H., Kim, K., 2014. Impact of circadian nuclear receptor REV-ERBα on midbrain dopamine production and mood regulation. Cell 157, 858–868. https://doi.org/10.1016/j.cell.2014.03.039
Chung, S., Son, G.H., Kim, K., 2011. Circadian rhythm of adrenal glucocorticoid: its regulation and clinical implications. Biochim. Biophys. Acta 1812, 581–591. https://doi.org/10.1016/j.bbadis.2011.02.003
Chung, W.-S., Allen, N.J., Eroglu, C., 2015. Astrocytes Control Synapse Formation, Function, and Elimination. Cold Spring Harb Perspect Biol 7. https://doi.org/10.1101/cshperspect.a020370
Cirelli, C., Tononi, G., 2015. Sleep and synaptic homeostasis. Sleep 38, 161–162. https://doi.org/10.5665/sleep.4348
Cirelli, C., Tononi, G., 2000. Differential expression of plasticity-related genes in waking and sleep and their regulation by the noradrenergic system. J Neurosci 20, 9187–9194.
Clarke, L.E., Barres, B.A., 2013. Emerging roles of astrocytes in neural circuit development. Nat Rev Neurosci 14, 311–321. https://doi.org/10.1038/nrn3484
Clement, J.P., Aceti, M., Creson, T.K., Ozkan, E.D., Shi, Y., Reish, N.J., Almonte, A.G., Miller, B.H., Wiltgen, B.J., Miller, C.A., Xu, X., Rumbaugh, G., 2012. Pathogenic SYNGAP1 mutations impair cognitive development by disrupting the maturation of dendritic spine synapses. Cell 151, 709–723. https://doi.org/10.1016/j.cell.2012.08.045
Codocedo, J.F., Allard, C., Godoy, J.A., Varela-Nallar, L., Inestrosa, N.C., 2012. SIRT1 regulates dendritic development in hippocampal neurons. PLoS One 7, e47073. https://doi.org/10.1371/journal.pone.0047073
Cohen, D.A., Wang, W., Wyatt, J.K., Kronauer, R.E., Dijk, D.-J., Czeisler, C.A., Klerman, E.B., 2010. Uncovering Residual Effects of Chronic Sleep Loss on Human Performance. Sci Transl Med 2, 14ra3. https://doi.org/10.1126/scitranslmed.3000458
Cohen, J.L., Jackson, N.L., Ballestas, M.E., Webb, W.M., Lubin, F.D., Clinton, S.M., 2017. Amygdalar expression of the microRNA miR-101a and its target Ezh2 contribute to rodent anxiety-like behaviour. Eur J Neurosci 46, 2241–2252. https://doi.org/10.1111/ejn.13624
Colwell, C.S., 2001. NMDA-evoked calcium transients and currents in the suprachiasmatic nucleus: gating by the circadian system. Eur. J. Neurosci. 13, 1420–1428. https://doi.org/10.1046/j.0953-816x.2001.01517.x
Conway-Campbell, B.L., Sarabdjitsingh, R.A., McKenna, M.A., Pooley, J.R., Kershaw, Y.M., Meijer, O.C., de Kloet, E.R., Lightman, S.L., 2010. Glucocorticoid ultradian rhythmicity directs cyclical gene pulsing of the clock gene period 1 in rat hippocampus. J. Neuroendocrinol. 22, 1093–1100. https://doi.org/10.1111/j.1365-2826.2010.02051.x

Coogan, A.N., Piggins, H.D., 2003a. Circadian and photic regulation of phosphorylation of ERK1/2 and Elk-1 in the suprachiasmatic nuclei of the Syrian hamster. J Neurosci 23, 3085–3093.
Coogan, A.N., Piggins, H.D., 2003b. Circadian and photic regulation of phosphorylation of ERK1/2 and Elk-1 in the suprachiasmatic nuclei of the Syrian hamster. J. Neurosci. 23, 3085–3093.
Cornell-Bell, A.H., Finkbeiner, S.M., Cooper, M.S., Smith, S.J., 1990. Glutamate induces calcium waves in cultured astrocytes: long-range glial signaling. Science 247, 470–473. https://doi.org/10.1126/science.1967852
Correll, C.M., Rosenkranz, J.A., Grace, A.A., 2005. Chronic cold stress alters prefrontal cortical modulation of amygdala neuronal activity in rats. Biol Psychiatry 58, 382–391. https://doi.org/10.1016/j.biopsych.2005.04.009
Corthell, J.T., Stathopoulos, A.M., Watson, C.C., Bertram, R., Trombley, P.Q., 2013. Olfactory bulb monoamine concentrations vary with time of day. Neuroscience 247, 234–241. https://doi.org/10.1016/j.neuroscience.2013.05.040
Cotton, S., Richdale, A., 2006. Brief report: parental descriptions of sleep problems in children with autism, Down syndrome, and Prader-Willi syndrome. Res Dev Disabil 27, 151–161. https://doi.org/10.1016/j.ridd.2004.12.003
Crasson, M., Kjiri, S., Colin, A., Kjiri, K., L'Hermite-Baleriaux, M., Ansseau, M., Legros, J.J., 2004. Serum melatonin and urinary 6-sulfatoxymelatonin in major depression. Psychoneuroendocrinology 29, 1–12.
Creson, T.K., Rojas, C., Hwaun, E., Vaissiere, T., Kilinc, M., Jimenez-Gomez, A., Holder, J.L., Tang, J., Colgin, L.L., Miller, C.A., Rumbaugh, G., 2019a. Re-expression of SynGAP protein in adulthood improves translatable measures of brain function and behavior. Elife 8. https://doi.org/10.7554/eLife.46752
Creson, T.K., Rojas, C., Hwaun, E., Vaissiere, T., Kilinc, M., Jimenez-Gomez, A., Holder, J.L., Tang, J., Colgin, L.L., Miller, C.A., Rumbaugh, G., 2019b. Re-expression of SynGAP protein in adulthood improves translatable measures of brain function and behavior. Elife 8. https://doi.org/10.7554/eLife.46752
Cryan, J.F., Mombereau, C., Vassout, A., 2005. The tail suspension test as a model for assessing antidepressant activity: review of pharmacological and genetic studies in mice. Neurosci Biobehav Rev 29, 571–625. https://doi.org/10.1016/j.neubiorev.2005.03.009
Cui, H., Sakamoto, H., Higashi, S., Kawata, M., 2008. Effects of single-prolonged stress on neurons and their afferent inputs in the amygdala. Neuroscience 152, 703–712. https://doi.org/10.1016/j.neuroscience.2007.12.028
Cullinan, W.E., Herman, J.P., Battaglia, D.F., Akil, H., Watson, S.J., 1995. Pattern and time course of immediate early gene expression in rat brain following acute stress. Neuroscience 64, 477–505. https://doi.org/10.1016/0306-4522(94)00355-9
Cunningham, F., Achuthan, P., Akanni, W., Allen, J., Amode, M.R., Armean, I.M., Bennett, R., Bhai, J., Billis, K., Boddu, S., Cummins, C., Davidson, C., Dodiya, K.J., Gall, A., Girón, C.G., Gil, L., Grego, T., Haggerty, L., Haskell, E., Hourlier, T., Izuogu, O.G., Janacek, S.H., Juettemann, T., Kay, M., Laird, M.R., Lavidas, I., Liu, Z., Loveland, J.E., Marugán, J.C., Maurel, T., McMahon, A.C., Moore, B.,

Morales, J., Mudge, J.M., Nuhn, M., Ogeh, D., Parker, A., Parton, A., Patricio, M., Abdul Salam, A.I., Schmitt, B.M., Schuilenburg, H., Sheppard, D., Sparrow, H., Stapleton, E., Szuba, M., Taylor, K., Threadgold, G., Thormann, A., Vullo, A., Walts, B., Winterbottom, A., Zadissa, A., Chakiachvili, M., Frankish, A., Hunt, S.E., Kostadima, M., Langridge, N., Martin, F.J., Muffato, M., Perry, E., Ruffier, M., Staines, D.M., Trevanion, S.J., Aken, B.L., Yates, A.D., Zerbino, D.R., Flicek, P., 2019. Ensembl 2019. Nucleic Acids Res. 47, D745–D751. https://doi.org/10.1093/nar/gky1113

Daan, S., Pittendrigh, C.S., 1976. A Functional analysis of circadian pacemakers in nocturnal rodents. J. Comp. Physiol. 106, 253–266. https://doi.org/10.1007/BF01417857

Dallérac, G., Chever, O., Rouach, N., 2013. How do astrocytes shape synaptic transmission? Insights from electrophysiology. Front Cell Neurosci 7. https://doi.org/10.3389/fncel.2013.00159

Dalm, S., Enthoven, L., Meijer, O.C., van der Mark, M.H., Karssen, A.M., de Kloet, E.R., Oitzl, M.S., 2005. Age-related changes in hypothalamic-pituitary-adrenal axis activity of male C57BL/6J mice. Neuroendocrinology 81, 372–380. https://doi.org/10.1159/000089555

Darcet, F., Mendez-David, I., Tritschler, L., Gardier, A.M., Guilloux, J.-P., David, D.J., 2014. Learning and memory impairments in a neuroendocrine mouse model of anxiety/depression. Front Behav Neurosci 8. https://doi.org/10.3389/fnbeh.2014.00136

Davies, J.A., Navaratnam, V., Redfern, P.H., 1973. A 24-hour rhythm in passive-avoidance behaviour in rats. Psychopharmacologia 32, 211–214.

Davis, C.J., Clinton, J.M., Taishi, P., Bohnet, S.G., Honn, K.A., Krueger, J.M., 2011. MicroRNA 132 alters sleep and varies with time in brain. J Appl Physiol (1985) 111, 665–672. https://doi.org/10.1152/japplphysiol.00517.2011

de Quervain, D.J.-F., Aerni, A., Schelling, G., Roozendaal, B., 2009. Glucocorticoids and the regulation of memory in health and disease. Front Neuroendocrinol 30, 358–370. https://doi.org/10.1016/j.yfrne.2009.03.002

Debono, M., Ghobadi, C., Rostami-Hodjegan, A., Huatan, H., Campbell, M.J., Newell-Price, J., Darzy, K., Merke, D.P., Arlt, W., Ross, R.J., 2009. Modified-release hydrocortisone to provide circadian cortisol profiles. J. Clin. Endocrinol. Metab. 94, 1548–1554. https://doi.org/10.1210/jc.2008-2380

Denk, W., Horstmann, H., 2004. Serial Block-Face Scanning Electron Microscopy to Reconstruct Three-Dimensional Tissue Nanostructure. PLoS Biol 2. https://doi.org/10.1371/journal.pbio.0020329

Denli, A.M., Tops, B.B.J., Plasterk, R.H.A., Ketting, R.F., Hannon, G.J., 2004. Processing of primary microRNAs by the Microprocessor complex. Nature 432, 231–235. https://doi.org/10.1038/nature03049

Descalzi, G., Gao, V., Steinman, M.Q., Suzuki, A., Alberini, C.M., 2019. Lactate from astrocytes fuels learning-induced mRNA translation in excitatory and inhibitory neurons. Communications Biology 2, 1–11. https://doi.org/10.1038/s42003-019-0495-2

DeVallance, E., Riggs, D., Jackson, B., Parkulo, T., Zaslau, S., Chantler, P.D., Olfert, I.M., Bryner, R.W., 2017. Effect of chronic stress on running wheel activity in mice. PLoS One 12. https://doi.org/10.1371/journal.pone.0184829

Dibner, C., Schibler, U., Albrecht, U., 2010. The mammalian circadian timing system: organization and coordination of central and peripheral clocks. Annu. Rev. Physiol. 72, 517–549. https://doi.org/10.1146/annurev-physiol-021909-135821

Doi, M., Cho, S., Yujnovsky, I., Hirayama, J., Cermakian, N., Cato, A.C.B., Sassone-Corsi, P., 2007. Light-inducible and clock-controlled expression of MAP kinase phosphatase 1 in mouse central pacemaker neurons. J. Biol. Rhythms 22, 127–139. https://doi.org/10.1177/0748730406298332

Dominguez, G., Henkous, N., Prevot, T., David, V., Guillou, J.-L., Belzung, C., Mons, N., Béracochéa, D., 2019. Sustained corticosterone rise in the prefrontal cortex is a key factor for chronic stress-induced working memory deficits in mice. Neurobiology of Stress 10, 100161. https://doi.org/10.1016/j.ynstr.2019.100161

Donner, N.C., Lowry, C.A., 2013. Sex differences in anxiety and emotional behavior. Pflugers Arch 465, 601–626. https://doi.org/10.1007/s00424-013-1271-7

Drevets, W.C., Price, J.L., Furey, M.L., 2008. Brain structural and functional abnormalities in mood disorders: implications for neurocircuitry models of depression. Brain Struct Funct 213, 93–118. https://doi.org/10.1007/s00429-008-0189-x

Drevets, W.C., Price, J.L., Simpson, J.R., Todd, R.D., Reich, T., Vannier, M., Raichle, M.E., 1997. Subgenual prefrontal cortex abnormalities in mood disorders. Nature 386, 824–827. https://doi.org/10.1038/386824a0

Drevets, W.C., Videen, T.O., Price, J.L., Preskorn, S.H., Carmichael, S.T., Raichle, M.E., 1992. A functional anatomical study of unipolar depression. J. Neurosci. 12, 3628–3641.

Du, Y., Wang, W., Lutton, A.D., Kiyoshi, C.M., Ma, B., Taylor, A.T., Olesik, J.W., McTigue, D.M., Askwith, C.C., Zhou, M., 2018. Dissipation of transmembrane potassium gradient is the main cause of cerebral ischemia-induced depolarization in astrocytes and neurons. Exp Neurol 303, 1–11. https://doi.org/10.1016/j.expneurol.2018.01.019

Ducottet, C., Aubert, A., Belzung, C., 2004. Susceptibility to subchronic unpredictable stress is related to individual reactivity to threat stimuli in mice. Behav Brain Res 155, 291–299. https://doi.org/10.1016/j.bbr.2004.04.020

Dudley, T.E., DiNardo, L.A., Glass, J.D., 1998. Endogenous Regulation of Serotonin Release in the Hamster Suprachiasmatic Nucleus. J. Neurosci. 18, 5045–5052. https://doi.org/10.1523/JNEUROSCI.18-13-05045.1998

Duffield, G.E., Mikkelsen, J.D., Ebling, F.J.P., 2012. Conserved expression of the glutamate NMDA receptor 1 subunit splice variants during the development of the Siberian hamster suprachiasmatic nucleus. PLoS ONE 7, e37496. https://doi.org/10.1371/journal.pone.0037496

Duman, R.S., 2009. Neuronal damage and protection in the pathophysiology and treatment of psychiatric illness: stress and depression. Dialogues Clin Neurosci 11, 239–255.

Duman, R.S., Aghajanian, G.K., 2012. Synaptic Dysfunction in Depression: Potential Therapeutic Targets. Science 338, 68–72. https://doi.org/10.1126/science.1222939

Duman, R.S., Li, N., Liu, R.-J., Duric, V., Aghajanian, G., 2012. Signaling pathways underlying the rapid antidepressant actions of ketamine. Neuropharmacology 62, 35–41. https://doi.org/10.1016/j.neuropharm.2011.08.044

Dziema, H., Oatis, B., Butcher, G.Q., Yates, R., Hoyt, K.R., Obrietan, K., 2003. The ERK/MAP kinase pathway couples light to immediate-early gene expression in the suprachiasmatic nucleus. Eur J Neurosci 17, 1617–1627. https://doi.org/10.1046/j.1460-9568.2003.02592.x

Ebling, F.J., 1996. The role of glutamate in the photic regulation of the suprachiasmatic nucleus. Prog. Neurobiol. 50, 109–132. https://doi.org/10.1016/s0301-0082(96)00032-9

Eckel-Mahan, Kristin L, Phan, T., Han, S., Wang, H., Chan, G.C.-K., Scheiner, Z.S., Storm, D.R., 2008. Circadian oscillation of hippocampal MAPK activity and cAMP: implications for memory persistence. Nat Neurosci 11, 1074–1082.

Eckel-Mahan, Kristin L., Phan, T., Han, S., Wang, H., Chan, G.C.K., Scheiner, Z.S., Storm, D.R., 2008. Circadian oscillation of hippocampal MAPK activity and cAmp: implications for memory persistence. Nat Neurosci 11, 1074–1082. https://doi.org/10.1038/nn.2174

Edbauer, D., Neilson, J.R., Foster, K.A., Wang, C.-F., Seeburg, D.P., Batterton, M.N., Tada, T., Dolan, B.M., Sharp, P.A., Sheng, M., 2010. Regulation of synaptic structure and function by FMRP-associated microRNAs miR-125b and miR-132. Neuron 65, 373–384. https://doi.org/10.1016/j.neuron.2010.01.005

Edgar, N., McClung, C.A., 2013. Major depressive disorder: A loss of circadian synchrony? BioEssays 35, 940–944. https://doi.org/10.1002/bies.201300086

Ehlers, C.L., Frank, E., Kupfer, D.J., 1988. Social zeitgebers and biological rhythms. A unified approach to understanding the etiology of depression. Arch. Gen. Psychiatry 45, 948–952.

Eickelberg, O., Roth, M., Lörx, R., Bruce, V., Rüdiger, J., Johnson, M., Block, L.H., 1999. Ligand-independent activation of the glucocorticoid receptor by beta2-adrenergic receptor agonists in primary human lung fibroblasts and vascular smooth muscle cells. J. Biol. Chem. 274, 1005–1010.

Emens, J., Lewy, A., Kinzie, J.M., Arntz, D., Rough, J., 2009. Circadian misalignment in major depressive disorder. Psychiatry Res 168, 259–261. https://doi.org/10.1016/j.psychres.2009.04.009

Engler, H., Engler, A., Bailey, M.T., Sheridan, J.F., 2005. Tissue-specific alterations in the glucocorticoid sensitivity of immune cells following repeated social defeat in mice. J Neuroimmunol 163, 110–119. https://doi.org/10.1016/j.jneuroim.2005.03.002

Enoki, R., Ono, D., Kuroda, S., Honma, S., Honma, K., 2017. Dual origins of the intracellular circadian calcium rhythm in the suprachiasmatic nucleus. Scientific Reports 7, 1–8. https://doi.org/10.1038/srep41733

Etkin, A., 2012. Neurobiology of anxiety: from neural circuits to novel solutions? Depress Anxiety 29, 355–358. https://doi.org/10.1002/da.21957
Etkin, A., Wager, T.D., 2007. Functional neuroimaging of anxiety: a meta-analysis of emotional processing in PTSD, social anxiety disorder, and specific phobia. Am J Psychiatry 164, 1476–1488. https://doi.org/10.1176/appi.ajp.2007.07030504
Fanselow, M.S., 1991. The Midbrain Periaqueductal Gray as a Coordinator of Action in Response to Fear and Anxiety, in: Depaulis, A., Bandler, R. (Eds.), The Midbrain Periaqueductal Gray Matter: Functional, Anatomical, and Neurochemical Organization, NATO ASI Series. Springer US, Boston, MA, pp. 151–173. https://doi.org/10.1007/978-1-4615-3302-3_10
Farooq, R.K., Isingrini, E., Tanti, A., Le Guisquet, A.-M., Arlicot, N., Minier, F., Leman, S., Chalon, S., Belzung, C., Camus, V., 2012. Is unpredictable chronic mild stress (UCMS) a reliable model to study depression-induced neuroinflammation? Behav. Brain Res. 231, 130–137. https://doi.org/10.1016/j.bbr.2012.03.020
Fellin, T., Pascual, O., Gobbo, S., Pozzan, T., Haydon, P.G., Carmignoto, G., 2004. Neuronal synchrony mediated by astrocytic glutamate through activation of extrasynaptic NMDA receptors. Neuron 43, 729–743. https://doi.org/10.1016/j.neuron.2004.08.011
Femenía, T., Gómez-Galán, M., Lindskog, M., Magara, S., 2012. Dysfunctional hippocampal activity affects emotion and cognition in mood disorders. Brain Research, Brain Integration - from Molecular to Network Level 1476, 58–70. https://doi.org/10.1016/j.brainres.2012.03.053
Fendt, M., Fanselow, M.S., 1999. The neuroanatomical and neurochemical basis of conditioned fear. Neurosci Biobehav Rev 23, 743–760. https://doi.org/10.1016/s0149-7634(99)00016-0
Fernandez, D.C., Chang, Y.-T., Hattar, S., Chen, S.-K., 2016. Architecture of retinal projections to the central circadian pacemaker. Proc. Natl. Acad. Sci. U.S.A. 113, 6047–6052. https://doi.org/10.1073/pnas.1523629113
Fernandez, R.I., Lyons, L.C., Levenson, J., Khabour, O., Eskin, A., 2003. Circadian modulation of long-term sensitization in Aplysia. Proc Natl Acad Sci U S A 100, 14415–14420. https://doi.org/10.1073/pnas.2336172100
Ferraguti, F., 2018. Metabotropic glutamate receptors as targets for novel anxiolytics. Curr Opin Pharmacol 38, 37–42. https://doi.org/10.1016/j.coph.2018.02.004
Fiacco, T.A., McCarthy, K.D., 2004. Intracellular Astrocyte Calcium Waves In Situ Increase the Frequency of Spontaneous AMPA Receptor Currents in CA1 Pyramidal Neurons. J. Neurosci. 24, 722–732. https://doi.org/10.1523/JNEUROSCI.2859-03.2004
Fiala, J.C., 2005. Reconstruct: a free editor for serial section microscopy. J Microsc 218, 52–61. https://doi.org/10.1111/j.1365-2818.2005.01466.x
Figueiro, M.G., Rea, M.S., 2010. The effects of red and blue lights on circadian variations in cortisol, alpha amylase, and melatonin. Int J Endocrinol 2010, 829351. https://doi.org/10.1155/2010/829351

Fisk, A.S., Tam, S.K.E., Brown, L.A., Vyazovskiy, V.V., Bannerman, D.M., Peirson, S.N., 2018. Light and Cognition: Roles for Circadian Rhythms, Sleep, and Arousal. Front. Neurol. 9. https://doi.org/10.3389/fneur.2018.00056
Formstecher, E., Ramos, J.W., Fauquet, M., Calderwood, D.A., Hsieh, J.C., Canton, B., Nguyen, X.T., Barnier, J.V., Camonis, J., Ginsberg, M.H., Chneiweiss, H., 2001. PEA-15 mediates cytoplasmic sequestration of ERK MAP kinase. Dev Cell 1, 239–250. https://doi.org/10.1016/s1534-5807(01)00035-1
Frank, M.G., 2016. Circadian Regulation of Synaptic Plasticity. Biology (Basel) 5. https://doi.org/10.3390/biology5030031
Frank, M.G., 2012. Erasing Synapses in Sleep: Is It Time to Be SHY? [WWW Document]. Neural Plasticity. https://doi.org/10.1155/2012/264378
Friedrich, M.J., 2017. Depression Is the Leading Cause of Disability Around the World. JAMA 317, 1517. https://doi.org/10.1001/jama.2017.3826
Frisbee, J.C., Brooks, S.D., Stanley, S.C., d'Audiffret, A.C., 2015. An Unpredictable Chronic Mild Stress Protocol for Instigating Depressive Symptoms, Behavioral Changes and Negative Health Outcomes in Rodents. J Vis Exp. https://doi.org/10.3791/53109
Fu, G., Brkić, J., Hayder, H., Peng, C., 2013. MicroRNAs in Human Placental Development and Pregnancy Complications. Int J Mol Sci 14, 5519–5544. https://doi.org/10.3390/ijms14035519
Furshpan, E.J., Potter, D.D., 1959. Transmission at the giant motor synapses of the crayfish. J Physiol 145, 289–325.
Gabbay, V., Ely, B.A., Li, Q., Bangaru, S.D., Panzer, A.M., Alonso, C.M., Castellanos, F.X., Milham, M.P., 2013. Striatum-based circuitry of adolescent depression and anhedonia. J Am Acad Child Adolesc Psychiatry 52, 628-641.e13. https://doi.org/10.1016/j.jaac.2013.04.003
Gaffan, D., 1994. Dissociated effects of perirhinal cortex ablation, fornix transection and amygdalectomy: evidence for multiple memory systems in the primate temporal lobe. Exp Brain Res 99, 411–422.
Gail Williams, P., Sears, L.L., Allard, A., 2004. Sleep problems in children with autism. J Sleep Res 13, 265–268. https://doi.org/10.1111/j.1365-2869.2004.00405.x
Gallego, M., Virshup, D.M., 2007. Post-translational modifications regulate the ticking of the circadian clock. Nat. Rev. Mol. Cell Biol. 8, 139–148. https://doi.org/10.1038/nrm2106
Gao, J., Wang, W.-Y., Mao, Y.-W., Gräff, J., Guan, J.-S., Pan, L., Mak, G., Kim, D., Su, S.C., Tsai, L.-H., 2010. A novel pathway regulates memory and plasticity via SIRT1 and miR-134. Nature 466, 1105–1109. https://doi.org/10.1038/nature09271
Gartside, S.E., Leitch, M.M., Young, A.H., 2003. Altered glucocorticoid rhythm attenuates the ability of a chronic SSRI to elevate forebrain 5-HT: implications for the treatment of depression. Neuropsychopharmacology 28, 1572–1578. https://doi.org/10.1038/sj.npp.1300201
Gavrilov, N., Golyagina, I., Brazhe, A., Scimemi, A., Turlapov, V., Semyanov, A., 2018. Astrocytic Coverage of Dendritic Spines, Dendritic Shafts, and Axonal Boutons

in Hippocampal Neuropil. Front Cell Neurosci 12. https://doi.org/10.3389/fncel.2018.00248
Germain, A., Kupfer, D.J., 2008a. Circadian rhythm disturbances in depression. Hum Psychopharmacol 23, 571–585. https://doi.org/10.1002/hup.964
Germain, A., Kupfer, D.J., 2008b. CIRCADIAN RHYTHM DISTURBANCES IN DEPRESSION. Hum Psychopharmacol 23, 571–585. https://doi.org/10.1002/hup.964
Gerstner, J.R., Smith, G.G., Lenz, O., Perron, I.J., Buono, R.J., Ferraro, T.N., 2014. BMAL1 controls the diurnal rhythm and set point for electrical seizure threshold in mice. Front Syst Neurosci 8, 121. https://doi.org/10.3389/fnsys.2014.00121
Gerstner, J.R., Yin, J.C.P., 2010. Circadian rhythms and memory formation. Nat Rev Neurosci 11, 577–588. https://doi.org/10.1038/nrn2881
Giaume, C., Koulakoff, A., Roux, L., Holcman, D., Rouach, N., 2010. Astroglial networks: a step further in neuroglial and gliovascular interactions. Nat Rev Neurosci 11, 87–99. https://doi.org/10.1038/nrn2757
Gibbs, M.E., Anderson, D.G., Hertz, L., 2006. Inhibition of glycogenolysis in astrocytes interrupts memory consolidation in young chickens. Glia 54, 214–222. https://doi.org/10.1002/glia.20377
Gilhooley, M.J., Pinnock, S.B., Herbert, J., 2011. Rhythmic expression of per1 in the dentate gyrus is suppressed by corticosterone: implications for neurogenesis. Neurosci. Lett. 489, 177–181. https://doi.org/10.1016/j.neulet.2010.12.011
Ginty, D.D., Kornhauser, J.M., Thompson, M.A., Bading, H., Mayo, K.E., Takahashi, J.S., Greenberg, M.E., 1993. Regulation of CREB phosphorylation in the suprachiasmatic nucleus by light and a circadian clock. Science 260, 238–241. https://doi.org/10.1126/science.8097062
Goldsmith, C.S., Bell-Pedersen, D., 2013a. Diverse roles for MAPK signaling in circadian clocks. Adv Genet 84, 1–39. https://doi.org/10.1016/B978-0-12-407703-4.00001-3
Goldsmith, C.S., Bell-Pedersen, D., 2013b. Diverse Roles for MAPK Signaling in Circadian Clocks. Adv Genet 84, 1–39. https://doi.org/10.1016/B978-0-12-407703-4.00001-3
Golombek, D.A., Rosenstein, R.E., 2010. Physiology of circadian entrainment. Physiol. Rev. 90, 1063–1102. https://doi.org/10.1152/physrev.00009.2009
Gomazkov, O.A., 2019. Astrocytes as the Elements of the Regulation of Higher Brain Functions. Neurochem. J. 13, 313–319. https://doi.org/10.1134/S1819712419030073
Gong, K., Qu, B., Liao, D., Liu, D., Wang, C., Zhou, J., Pan, X., 2016. MiR-132 regulates osteogenic differentiation via downregulating Sirtuin1 in a peroxisome proliferator-activated receptor β/δ-dependent manner. Biochem Biophys Res Commun 478, 260–267. https://doi.org/10.1016/j.bbrc.2016.07.057
González, M.M.C., Aston-Jones, G., 2006. Circadian regulation of arousal: role of the noradrenergic locus coeruleus system and light exposure. Sleep 29, 1327–1336.
Graciarena, M., Depino, A.M., Pitossi, F.J., 2010. Prenatal inflammation impairs adult neurogenesis and memory related behavior through persistent hippocampal

TGFβ1 downregulation. Brain Behav Immun 24, 1301–1309. https://doi.org/10.1016/j.bbi.2010.06.005
Grady, S., Aeschbach, D., Wright, K.P., Czeisler, C.A., 2010. Effect of modafinil on impairments in neurobehavioral performance and learning associated with extended wakefulness and circadian misalignment. Neuropsychopharmacology 35, 1910–1920. https://doi.org/10.1038/npp.2010.63
Graves, L.A., Hellman, K., Veasey, S., Blendy, J.A., Pack, A.I., Abel, T., 2003. Genetic evidence for a role of CREB in sustained cortical arousal. J Neurophysiol 90, 1152–1159. https://doi.org/10.1152/jn.00882.2002
Gray, E.G., 1959. Electron microscopy of synaptic contacts on dendrite spines of the cerebral cortex. Nature 183, 1592–1593. https://doi.org/10.1038/1831592a0
Greicius, M.D., Flores, B.H., Menon, V., Glover, G.H., Solvason, H.B., Kenna, H., Reiss, A.L., Schatzberg, A.F., 2007. Resting-State Functional Connectivity in Major Depression: Abnormally Increased Contributions from Subgenual Cingulate Cortex and Thalamus. Biol Psychiatry 62, 429–437. https://doi.org/10.1016/j.biopsych.2006.09.020
Griffiths-Jones, S., Grocock, R.J., van Dongen, S., Bateman, A., Enright, A.J., 2006. miRBase: microRNA sequences, targets and gene nomenclature. Nucleic Acids Res 34, D140-144. https://doi.org/10.1093/nar/gkj112
Gritton, H.J., Kantorowski, A., Sarter, M., Lee, T.M., 2012. Bidirectional interactions between circadian entrainment and cognitive performance. Learn Mem 19, 126–141. https://doi.org/10.1101/lm.023499.111
Guerra-Gomes, S., Sousa, N., Pinto, L., Oliveira, J.F., 2018. Functional Roles of Astrocyte Calcium Elevations: From Synapses to Behavior. Front. Cell. Neurosci. 11. https://doi.org/10.3389/fncel.2017.00427
Guilding, C., Piggins, H.D., 2007. Challenging the omnipotence of the suprachiasmatic timekeeper: are circadian oscillators present throughout the mammalian brain? Eur. J. Neurosci. 25, 3195–3216. https://doi.org/10.1111/j.1460-9568.2007.05581.x
Guillaumond, F., Dardente, H., Giguère, V., Cermakian, N., 2005. Differential control of Bmal1 circadian transcription by REV-ERB and ROR nuclear receptors. J Biol Rhythms 20, 391–403. https://doi.org/10.1177/0748730405277232
Gunn, P.J., Middleton, B., Davies, S.K., Revell, V.L., Skene, D.J., 2016. Sex differences in the circadian profiles of melatonin and cortisol in plasma and urine matrices under constant routine conditions. Chronobiol Int 33, 39–50. https://doi.org/10.3109/07420528.2015.1112396
Guo, X., Hamilton, P.J., Reish, N.J., Sweatt, J.D., Miller, C.A., Rumbaugh, G., 2009. Reduced Expression of the NMDA Receptor-Interacting Protein SynGAP Causes Behavioral Abnormalities that Model Symptoms of Schizophrenia. Neuropsychopharmacology 34, 1659–1672. https://doi.org/10.1038/npp.2008.223
Guzman-Marin, R., Ying, Z., Suntsova, N., Methippara, M., Bashir, T., Szymusiak, R., Gomez-Pinilla, F., McGinty, D., 2006. Suppression of hippocampal plasticity-related gene expression by sleep deprivation in rats. J Physiol 575, 807–819. https://doi.org/10.1113/jphysiol.2006.115287

Halassa, M.M., Fellin, T., Takano, H., Dong, J.-H., Haydon, P.G., 2007. Synaptic Islands Defined by the Territory of a Single Astrocyte. J Neurosci 27, 6473–6477. https://doi.org/10.1523/JNEUROSCI.1419-07.2007

Halberg, F., 1959. [Physiologic 24-hour periodicity; general and procedural considerations with reference to the adrenal cycle]. Int Z Vitaminforsch Beih 10, 225–296.

Hamdan, F.F., Daoud, H., Piton, A., Gauthier, J., Dobrzeniecka, S., Krebs, M.-O., Joober, R., Lacaille, J.-C., Nadeau, A., Milunsky, J.M., Wang, Z., Carmant, L., Mottron, L., Beauchamp, M.H., Rouleau, G.A., Michaud, J.L., 2011. De novo SYNGAP1 mutations in nonsyndromic intellectual disability and autism. Biol. Psychiatry 69, 898–901. https://doi.org/10.1016/j.biopsych.2010.11.015

Hamdan, F.F., Gauthier, J., Spiegelman, D., Noreau, A., Yang, Y., Pellerin, S., Dobrzeniecka, S., Côté, M., Perreau-Linck, E., Perreault-Linck, E., Carmant, L., D'Anjou, G., Fombonne, E., Addington, A.M., Rapoport, J.L., Delisi, L.E., Krebs, M.-O., Mouaffak, F., Joober, R., Mottron, L., Drapeau, P., Marineau, C., Lafrenière, R.G., Lacaille, J.C., Rouleau, G.A., Michaud, J.L., Synapse to Disease Group, 2009a. Mutations in SYNGAP1 in autosomal nonsyndromic mental retardation. N. Engl. J. Med. 360, 599–605. https://doi.org/10.1056/NEJMoa0805392

Hamdan, F.F., Gauthier, J., Spiegelman, D., Noreau, A., Yang, Y., Pellerin, S., Dobrzeniecka, S., Côté, M., Perreau-Linck, E., Perreault-Linck, E., Carmant, L., D'Anjou, G., Fombonne, E., Addington, A.M., Rapoport, J.L., Delisi, L.E., Krebs, M.-O., Mouaffak, F., Joober, R., Mottron, L., Drapeau, P., Marineau, C., Lafrenière, R.G., Lacaille, J.C., Rouleau, G.A., Michaud, J.L., Synapse to Disease Group, 2009b. Mutations in SYNGAP1 in autosomal nonsyndromic mental retardation. N Engl J Med 360, 599–605. https://doi.org/10.1056/NEJMoa0805392

Hammen, C., 2005. Stress and depression. Annu Rev Clin Psychol 1, 293–319. https://doi.org/10.1146/annurev.clinpsy.1.102803.143938

Han, J., Lee, Y., Yeom, K.-H., Kim, Y.-K., Jin, H., Kim, V.N., 2004. The Drosha-DGCR8 complex in primary microRNA processing. Genes Dev 18, 3016–3027. https://doi.org/10.1101/gad.1262504

Hanin, G., Yayon, N., Tzur, Y., Haviv, R., Bennett, E.R., Udi, S., Krishnamoorthy, Y.R., Kotsiliti, E., Zangen, R., Efron, B., Tam, J., Pappo, O., Shteyer, E., Pikarsky, E., Heikenwalder, M., Greenberg, D.S., Soreq, H., 2018. miRNA-132 induces hepatic steatosis and hyperlipidaemia by synergistic multitarget suppression. Gut 67, 1124–1134. https://doi.org/10.1136/gutjnl-2016-312869

Hansen, K.F., Karelina, K., Sakamoto, K., Wayman, G.A., Impey, S., Obrietan, K., 2013. miRNA-132: a dynamic regulator of cognitive capacity. Brain Struct Funct 218, 817–831. https://doi.org/10.1007/s00429-012-0431-4

Hansen, K.F., Sakamoto, K., Aten, S., Snider, K.H., Loeser, J., Hesse, A.M., Page, C.E., Pelz, C., Arthur, J.S.C., Impey, S., Obrietan, K., 2016. Targeted deletion of miR-132/-212 impairs memory and alters the hippocampal transcriptome. Learn. Mem. 23, 61–71. https://doi.org/10.1101/lm.039578.115

Hansen, K.F., Sakamoto, K., Wayman, G.A., Impey, S., Obrietan, K., 2010. Transgenic miR132 alters neuronal spine density and impairs novel object recognition memory. PLoS One 5, e15497. https://doi.org/10.1371/journal.pone.0015497

Hansen, K.L.F., 2015. MiR-132 as a Dynamic Regulator of Neuronal Structure and Cognitive Capacity. The Ohio State University.

Haramati, S., Navon, I., Issler, O., Ezra-Nevo, G., Gil, S., Zwang, R., Hornstein, E., Chen, A., 2011. MicroRNA as repressors of stress-induced anxiety: the case of amygdalar miR-34. J Neurosci 31, 14191–14203. https://doi.org/10.1523/JNEUROSCI.1673-11.2011

Harbour, V.L., Weigl, Y., Robinson, B., Amir, S., 2013. Comprehensive mapping of regional expression of the clock protein PERIOD2 in rat forebrain across the 24-h day. PLoS ONE 8, e76391. https://doi.org/10.1371/journal.pone.0076391

Hasin, D.S., Sarvet, A.L., Meyers, J.L., Saha, T.D., Ruan, W.J., Stohl, M., Grant, B.F., 2018. Epidemiology of Adult DSM-5 Major Depressive Disorder and Its Specifiers in the United States. JAMA Psychiatry 75, 336–346. https://doi.org/10.1001/jamapsychiatry.2017.4602

Hastings, M.H., Maywood, E.S., Brancaccio, M., 2018. Generation of circadian rhythms in the suprachiasmatic nucleus. Nature Reviews Neuroscience 19, 453–469. https://doi.org/10.1038/s41583-018-0026-z

Hastings, R.S., Parsey, R.V., Oquendo, M.A., Arango, V., Mann, J.J., 2004. Volumetric Analysis of the Prefrontal Cortex, Amygdala, and Hippocampus in Major Depression. Neuropsychopharmacology 29, 952–959. https://doi.org/10.1038/sj.npp.1300371

Hattar, S., Kumar, M., Park, A., Tong, P., Tung, J., Yau, K.-W., Berson, D.M., 2006. Central projections of melanopsin-expressing retinal ganglion cells in the mouse. Journal of Comparative Neurology 497, 326–349. https://doi.org/10.1002/cne.20970

Hattar, S., Lucas, R.J., Mrosovsky, N., Thompson, S., Douglas, R.H., Hankins, M.W., Lem, J., Biel, M., Hofmann, F., Foster, R.G., Yau, K.-W., 2003. Melanopsin and rod-cone photoreceptive systems account for all major accessory visual functions in mice. Nature 424, 76–81. https://doi.org/10.1038/nature01761

Hauber, W., Bareiss, A., 2001. Facilitative effects of an adenosine A1/A2 receptor blockade on spatial memory performance of rats: selective enhancement of reference memory retention during the light period. Behav. Brain Res. 118, 43–52.

Haws, M.E., Jaramillo, T.C., Espinosa, F., Widman, A.J., Stuber, G.D., Sparta, D.R., Tye, K.M., Russo, S.J., Parada, L.F., Stavarache, M., Kaplitt, M., Bonci, A., Powell, C.M., 2014. PTEN knockdown alters dendritic spine/protrusion morphology, not density. J Comp Neurol 522, 1171–1190. https://doi.org/10.1002/cne.23488

Hayes, J., Peruzzi, P.P., Lawler, S., 2014. MicroRNAs in cancer: biomarkers, functions and therapy. Trends Mol Med 20, 460–469. https://doi.org/10.1016/j.molmed.2014.06.005

Henneberger, C., Papouin, T., Oliet, S.H.R., Rusakov, D.A., 2010. Long-term potentiation depends on release of D-serine from astrocytes. Nature 463, 232–236. https://doi.org/10.1038/nature08673
Hering, H., Sheng, M., 2001. Dentritic spines : structure, dynamics and regulation. Nature Reviews Neuroscience 2, 880–888. https://doi.org/10.1038/35104061
Hernandez-Rapp, J., Smith, P.Y., Filali, M., Goupil, C., Planel, E., Magill, S.T., Goodman, R.H., Hébert, S.S., 2015. Memory formation and retention are affected in adult miR-132/212 knockout mice. Behav Brain Res 287, 15–26. https://doi.org/10.1016/j.bbr.2015.03.032
Hill, M.N., Hillard, C.J., McEwen, B.S., 2011. Alterations in corticolimbic dendritic morphology and emotional behavior in cannabinoid CB1 receptor-deficient mice parallel the effects of chronic stress. Cereb Cortex 21, 2056–2064. https://doi.org/10.1093/cercor/bhq280
Hirschfeld, R.M., 2000. History and evolution of the monoamine hypothesis of depression. J Clin Psychiatry 61 Suppl 6, 4–6.
Hoffman, G.E., Smith, M.S., Verbalis, J.G., 1993. c-Fos and related immediate early gene products as markers of activity in neuroendocrine systems. Front Neuroendocrinol 14, 173–213. https://doi.org/10.1006/frne.1993.1006
Hofstetter, J.R., Mayeda, A.R., Possidente, B., Nurnberger, J.I., 1995. Quantitative trait loci (QTL) for circadian rhythms of locomotor activity in mice. Behav. Genet. 25, 545–556. https://doi.org/10.1007/bf02327578
Hollins, S.L., Cairns, M.J., 2016. MicroRNA: Small RNA mediators of the brains genomic response to environmental stress. Prog Neurobiol 143, 61–81. https://doi.org/10.1016/j.pneurobio.2016.06.005
Holloway, F.A., Wansley, R., 1973. Multiphasic retention deficits at periodic intervals after passive-avoidance learning. Science 180, 208–210. https://doi.org/10.1126/science.180.4082.208
Hoogerwerf, W.A., Hellmich, H.L., Cornélissen, G., Halberg, F., Shahinian, V.B., Bostwick, J., Savidge, T.C., Cassone, V.M., 2007. Clock gene expression in the murine gastrointestinal tract: endogenous rhythmicity and effects of a feeding regimen. Gastroenterology 133, 1250–1260. https://doi.org/10.1053/j.gastro.2007.07.009
Huang, A.Y.-S., Woo, J., Sardar, D., Lozzi, B., Bosquez Huerta, N.A., Lin, C.-C.J., Felice, D., Jain, A., Paulucci-Holthauzen, A., Deneen, B., 2020. Region-Specific Transcriptional Control of Astrocyte Function Oversees Local Circuit Activities. Neuron 106, 992-1008.e9. https://doi.org/10.1016/j.neuron.2020.03.025
Huang, G.-J., Herbert, J., 2006. Stimulation of neurogenesis in the hippocampus of the adult rat by fluoxetine requires rhythmic change in corticosterone. Biol. Psychiatry 59, 619–624. https://doi.org/10.1016/j.biopsych.2005.09.016
Huntzinger, E., Izaurralde, E., 2011. Gene silencing by microRNAs: contributions of translational repression and mRNA decay. Nature Reviews Genetics 12, 99–110. https://doi.org/10.1038/nrg2936
Ibata, Y., Takahashi, Y., Okamura, H., Kawakami, F., Terubayashi, H., Kubo, T., Yanaihara, N., 1989. Vasoactive intestinal peptide (VIP)-like immunoreactive

neurons located in the rat suprachiasmatic nucleus receive a direct retinal projection. Neurosci. Lett. 97, 1–5. https://doi.org/10.1016/0304-3940(89)90129-8

Ikeda, M., Hojo, Y., Komatsuzaki, Y., Okamoto, M., Kato, A., Takeda, T., Kawato, S., 2015. Hippocampal spine changes across the sleep-wake cycle: corticosterone and kinases. J. Endocrinol. 226, M13-27. https://doi.org/10.1530/JOE-15-0078

Impey, S., Davare, M., Lesiak, A., Lasiek, A., Fortin, D., Ando, H., Varlamova, O., Obrietan, K., Soderling, T.R., Goodman, R.H., Wayman, G.A., 2010. An activity-induced microRNA controls dendritic spine formation by regulating Rac1-PAK signaling. Mol Cell Neurosci 43, 146–156. https://doi.org/10.1016/j.mcn.2009.10.005

Impey, S., Obrietan, K., Wong, S.T., Poser, S., Yano, S., Wayman, G., Deloulme, J.C., Chan, G., Storm, D.R., 1998. Cross talk between ERK and PKA is required for Ca2+ stimulation of CREB-dependent transcription and ERK nuclear translocation. Neuron 21, 869–883. https://doi.org/10.1016/s0896-6273(00)80602-9

Inouye, S.T., Kawamura, H., 1982. Characteristics of a circadian pacemaker in the suprachiasmatic nucleus. J. Comp. Physiol. 146, 153–160. https://doi.org/10.1007/BF00610233

Isingrini, E., Camus, V., Le Guisquet, A.-M., Pingaud, M., Devers, S., Belzung, C., 2010a. Association between Repeated Unpredictable Chronic Mild Stress (UCMS) Procedures with a High Fat Diet: A Model of Fluoxetine Resistance in Mice. PLoS One 5. https://doi.org/10.1371/journal.pone.0010404

Isingrini, E., Camus, V., Le Guisquet, A.-M., Pingaud, M., Devers, S., Belzung, C., 2010b. Association between Repeated Unpredictable Chronic Mild Stress (UCMS) Procedures with a High Fat Diet: A Model of Fluoxetine Resistance in Mice. PLoS One 5. https://doi.org/10.1371/journal.pone.0010404

Issler, O., Chen, A., 2015. Determining the role of microRNAs in psychiatric disorders. Nat Rev Neurosci 16, 201–212. https://doi.org/10.1038/nrn3879

Izquierdo, A., Wellman, C.L., Holmes, A., 2006. Brief uncontrollable stress causes dendritic retraction in infralimbic cortex and resistance to fear extinction in mice. J Neurosci 26, 5733–5738. https://doi.org/10.1523/JNEUROSCI.0474-06.2006

Jagannath, A., Peirson, S.N., Foster, R.G., 2013. Sleep and circadian rhythm disruption in neuropsychiatric illness. Curr. Opin. Neurobiol. 23, 888–894. https://doi.org/10.1016/j.conb.2013.03.008

Jakubcakova, V., Oster, H., Tamanini, F., Cadenas, C., Leitges, M., van der Horst, G.T.J., Eichele, G., 2007. Light entrainment of the mammalian circadian clock by a PRKCA-dependent posttranslational mechanism. Neuron 54, 831–843. https://doi.org/10.1016/j.neuron.2007.04.031

Jang, C., Lahens, N.F., Hogenesch, J.B., Sehgal, A., 2015. Ribosome profiling reveals an important role for translational control in circadian gene expression. Genome Res 25, 1836–1847. https://doi.org/10.1101/gr.191296.115

Jasinska, M., Jasek-Gajda, E., Woznicka, O., Lis, G.J., Pyza, E., Litwin, J.A., 2019. Circadian clock regulates the shape and content of dendritic spines in mouse barrel cortex. PLoS One 14. https://doi.org/10.1371/journal.pone.0225394

Jasińska, M., Miłek, J., Cymerman, I.A., Łęski, S., Kaczmarek, L., Dziembowska, M., 2016. miR-132 Regulates Dendritic Spine Structure by Direct Targeting of Matrix Metalloproteinase 9 mRNA. Mol Neurobiol 53, 4701–4712. https://doi.org/10.1007/s12035-015-9383-z

Jasinska, M., Woznicka, O., Jasek-Gajda, E., Lis, G.J., Pyza, E., Litwin, J.A., 2020. Circadian Changes of Dendritic Spine Geometry in Mouse Barrel Cortex. Front. Neurosci. 14. https://doi.org/10.3389/fnins.2020.578881

Jeong, J.Y., Lee, D.H., Kang, S.S., 2013. Effects of chronic restraint stress on body weight, food intake, and hypothalamic gene expressions in mice. Endocrinol Metab (Seoul) 28, 288–296. https://doi.org/10.3803/EnM.2013.28.4.288

Jeyabalan, N., Clement, J.P., 2016. SYNGAP1: Mind the Gap. Front Cell Neurosci 10. https://doi.org/10.3389/fncel.2016.00032

Jiang, X., Zhang, T., Wang, H., Wang, T., Qin, M., Bao, P., Wang, R., Liu, Y., Chang, H.-C., Yan, J., Xu, J., 2018. Neurodegeneration-associated FUS is a novel regulator of circadian gene expression. Translational Neurodegeneration 7, 24. https://doi.org/10.1186/s40035-018-0131-y

Jilg, A., Lesny, S., Peruzki, N., Schwegler, H., Selbach, O., Dehghani, F., Stehle, J.H., 2010. Temporal dynamics of mouse hippocampal clock gene expression support memory processing. Hippocampus 20, 377–388. https://doi.org/10.1002/hipo.20637

Jimenez-Gomez, A., Niu, S., Andujar-Perez, F., McQuade, E.A., Balasa, A., Huss, D., Coorg, R., Quach, M., Vinson, S., Risen, S., Holder, J.L., 2019. Phenotypic characterization of individuals with SYNGAP1 pathogenic variants reveals a potential correlation between posterior dominant rhythm and developmental progression. J Neurodev Disord 11, 18. https://doi.org/10.1186/s11689-019-9276-y

Jimenez-Mateos, E.M., Bray, I., Sanz-Rodriguez, A., Engel, T., McKiernan, R.C., Mouri, G., Tanaka, K., Sano, T., Saugstad, J.A., Simon, R.P., Stallings, R.L., Henshall, D.C., 2011. miRNA Expression profile after status epilepticus and hippocampal neuroprotection by targeting miR-132. Am J Pathol 179, 2519–2532. https://doi.org/10.1016/j.ajpath.2011.07.036

Jourdain, P., Bergersen, L.H., Bhaukaurally, K., Bezzi, P., Santello, M., Domercq, M., Matute, C., Tonello, F., Gundersen, V., Volterra, A., 2007. Glutamate exocytosis from astrocytes controls synaptic strength. Nat Neurosci 10, 331–339. https://doi.org/10.1038/nn1849

Kaiser, R.H., Andrews-Hanna, J.R., Wager, T.D., Pizzagalli, D.A., 2015. Large-Scale Network Dysfunction in Major Depressive Disorder: A Meta-analysis of Resting-State Functional Connectivity. JAMA Psychiatry 72, 603–611. https://doi.org/10.1001/jamapsychiatry.2015.0071

Kaiser, R.H., Whitfield-Gabrieli, S., Dillon, D.G., Goer, F., Beltzer, M., Minkel, J., Smoski, M., Dichter, G., Pizzagalli, D.A., 2016. Dynamic Resting-State

Functional Connectivity in Major Depression. Neuropsychopharmacology 41, 1822–1830. https://doi.org/10.1038/npp.2015.352
Kajiwara, Y., Wang, E., Wang, M., Sin, W.C., Brennand, K.J., Schadt, E., Naus, C.C., Buxbaum, J., Zhang, B., 2018. GJA1 (connexin43) is a key regulator of Alzheimer's disease pathogenesis. Acta Neuropathologica Communications 6, 144. https://doi.org/10.1186/s40478-018-0642-x
Kang, J., Jiang, L., Goldman, S.A., Nedergaard, M., 1998a. Astrocyte-mediated potentiation of inhibitory synaptic transmission. Nat Neurosci 1, 683–692. https://doi.org/10.1038/3684
Kang, J., Jiang, L., Goldman, S.A., Nedergaard, M., 1998b. Astrocyte-mediated potentiation of inhibitory synaptic transmission. Nat. Neurosci. 1, 683–692. https://doi.org/10.1038/3684
Kasthuri, N., Hayworth, K.J., Berger, D.R., Schalek, R.L., Conchello, J.A., Knowles-Barley, S., Lee, D., Vázquez-Reina, A., Kaynig, V., Jones, T.R., Roberts, M., Morgan, J.L., Tapia, J.C., Seung, H.S., Roncal, W.G., Vogelstein, J.T., Burns, R., Sussman, D.L., Priebe, C.E., Pfister, H., Lichtman, J.W., 2015. Saturated Reconstruction of a Volume of Neocortex. Cell 162, 648–661. https://doi.org/10.1016/j.cell.2015.06.054
Kehl, T., Backes, C., Kern, F., Fehlmann, T., Ludwig, N., Meese, E., Lenhof, H.-P., Keller, A., 2017. About miRNAs, miRNA seeds, target genes and target pathways. Oncotarget 8, 107167–107175. https://doi.org/10.18632/oncotarget.22363
Keller, J., Flores, B., Gomez, R.G., Solvason, H.B., Kenna, H., Williams, G.H., Schatzberg, A.F., 2006. Cortisol circadian rhythm alterations in psychotic major depression. Biol. Psychiatry 60, 275–281. https://doi.org/10.1016/j.biopsych.2005.10.014
Khakh, B.S., Sofroniew, M.V., 2015. Diversity of astrocyte functions and phenotypes in neural circuits. Nat Neurosci 18, 942–952. https://doi.org/10.1038/nn.4043
Kikuchi, T., Gonzalez-Soriano, J., Kastanauskaite, A., Benavides-Piccione, R., Merchan-Perez, A., DeFelipe, J., Blazquez-Llorca, L., 2020. Volume Electron Microscopy Study of the Relationship Between Synapses and Astrocytes in the Developing Rat Somatosensory Cortex. Cereb. Cortex. https://doi.org/10.1093/cercor/bhz343
Kilinc, M., Creson, T., Rojas, C., Aceti, M., Ellegood, J., Vaissiere, T., Lerch, J.P., Rumbaugh, G., 2018. Species-conserved SYNGAP1 phenotypes associated with neurodevelopmental disorders. Mol. Cell. Neurosci. 91, 140–150. https://doi.org/10.1016/j.mcn.2018.03.008
Kim, A.H., Reimers, M., Maher, B., Williamson, V., McMichael, O., McClay, J.L., van den Oord, E.J.C.G., Riley, B.P., Kendler, K.S., Vladimirov, V.I., 2010. MicroRNA expression profiling in the prefrontal cortex of individuals affected with schizophrenia and bipolar disorders. Schizophr Res 124, 183–191. https://doi.org/10.1016/j.schres.2010.07.002
Kim, H., Yi, J.H., Choi, K., Hong, S., Shin, K.S., Kang, S.J., 2014. Regional differences in acute corticosterone-induced dendritic remodeling in the rat brain and their

behavioral consequences. BMC Neurosci 15, 65. https://doi.org/10.1186/1471-2202-15-65
Kim, H.-D., Hesterman, J., Call, T., Magazu, S., Keeley, E., Armenta, K., Kronman, H., Neve, R.L., Nestler, E.J., Ferguson, D., 2016. SIRT1 Mediates Depression-Like Behaviors in the Nucleus Accumbens. J Neurosci 36, 8441–8452. https://doi.org/10.1523/JNEUROSCI.0212-16.2016
Kim, J., Jang, S., Choe, H.K., Chung, S., Son, G.H., Kim, K., 2017. Implications of Circadian Rhythm in Dopamine and Mood Regulation. Mol Cells 40, 450–456. https://doi.org/10.14348/molcells.2017.0065
Kim, J.H., Lee, H.-K., Takamiya, K., Huganir, R.L., 2003. The role of synaptic GTPase-activating protein in neuronal development and synaptic plasticity. J. Neurosci. 23, 1119–1124.
Kim, J. H., Liao, D., Lau, L.F., Huganir, R.L., 1998. SynGAP: a synaptic RasGAP that associates with the PSD-95/SAP90 protein family. Neuron 20, 683–691. https://doi.org/10.1016/s0896-6273(00)81008-9
Kim, Jee Hae, Liao, D., Lau, L.-F., Huganir, R.L., 1998. SynGAP: a Synaptic RasGAP that Associates with the PSD-95/SAP90 Protein Family. Neuron 20, 683–691. https://doi.org/10.1016/S0896-6273(00)81008-9
Kiyoshi, C.M., 2019. Structure and Function of the Developing and Mature Astrocyte Syncytium in the Brain. The Ohio State University.
Kiyoshi, C.M., Du, Y., Zhong, S., Wang, W., Taylor, A.T., Xiong, B., Ma, B., Terman, D., Zhou, M., 2018. Syncytial isopotentiality: A system-wide electrical feature of astrocytic networks in the brain. Glia 66, 2756–2769. https://doi.org/10.1002/glia.23525
Kiyoshi, C.M., Zhou, M., 2019. Astrocyte syncytium: a functional reticular system in the brain. Neural Regen Res 14, 595–596. https://doi.org/10.4103/1673-5374.247462
Klein, M.E., Lioy, D.T., Ma, L., Impey, S., Mandel, G., Goodman, R.H., 2007. Homeostatic regulation of MeCP2 expression by a CREB-induced microRNA. Nat Neurosci 10, 1513–1514. https://doi.org/10.1038/nn2010
Kleitman, N., 1963. Sleep and wakefulness, Sleep and wakefulness. Univ. Chicago Press, Oxford, England.
Kleitman, N., 1933. Studies on the physiology of sleep. American Journal of Physiology-Legacy Content 104, 449–456. https://doi.org/10.1152/ajplegacy.1933.104.2.449
Ko, C.H., Takahashi, J.S., 2006. Molecular components of the mammalian circadian clock. Hum. Mol. Genet. 15 Spec No 2, R271-277. https://doi.org/10.1093/hmg/ddl207
Kofuji, P., Newman, E.A., 2004. Potassium buffering in the central nervous system. Neuroscience 129, 1045–1056. https://doi.org/10.1016/j.neuroscience.2004.06.008
Kokras, N., Dalla, C., 2014. Sex differences in animal models of psychiatric disorders. Br J Pharmacol 171, 4595–4619. https://doi.org/10.1111/bph.12710
Komatsuzaki, Y., Hatanaka, Y., Murakami, G., Mukai, H., Hojo, Y., Saito, M., Kimoto, T., Kawato, S., 2012. Corticosterone induces rapid spinogenesis via synaptic

glucocorticoid receptors and kinase networks in hippocampus. PLoS One 7, e34124. https://doi.org/10.1371/journal.pone.0034124
Komiyama, N.H., Watabe, A.M., Carlisle, H.J., Porter, K., Charlesworth, P., Monti, J., Strathdee, D.J.C., O'Carroll, C.M., Martin, S.J., Morris, R.G.M., O'Dell, T.J., Grant, S.G.N., 2002. SynGAP regulates ERK/MAPK signaling, synaptic plasticity, and learning in the complex with postsynaptic density 95 and NMDA receptor. J. Neurosci. 22, 9721–9732.
Kon, N., Yoshikawa, T., Honma, S., Yamagata, Y., Yoshitane, H., Shimizu, K., Sugiyama, Y., Hara, C., Kameshita, I., Honma, K., Fukada, Y., 2014. CaMKII is essential for the cellular clock and coupling between morning and evening behavioral rhythms. Genes Dev 28, 1101–1110. https://doi.org/10.1101/gad.237511.114
Kondratova, A.A., Dubrovsky, Y.V., Antoch, M.P., Kondratov, R.V., 2010. Circadian clock proteins control adaptation to novel environment and memory formation. Aging (Albany NY) 2, 285–297. https://doi.org/10.18632/aging.100142
Korshunov, K.S., Blakemore, L.J., Trombley, P.Q., 2017. Dopamine: A Modulator of Circadian Rhythms in the Central Nervous System. Front Cell Neurosci 11. https://doi.org/10.3389/fncel.2017.00091
Krahn, D.D., Gosnell, B.A., Majchrzak, M.J., 1990. The anorectic effects of CRH and restraint stress decrease with repeated exposures. Biol Psychiatry 27, 1094–1102. https://doi.org/10.1016/0006-3223(90)90046-5
Krakowiak, P., Goodlin-Jones, B., Hertz-Picciotto, I., Croen, L.A., Hansen, R.L., 2008. Sleep problems in children with autism spectrum disorders, developmental delays, and typical development: a population-based study. J Sleep Res 17, 197–206. https://doi.org/10.1111/j.1365-2869.2008.00650.x
Krieger, D.T., Allen, W., Rizzo, F., Krieger, H.P., 1971. Characterization of the normal temporal pattern of plasma corticosteroid levels. J. Clin. Endocrinol. Metab. 32, 266–284. https://doi.org/10.1210/jcem-32-2-266
Kriegsfeld, L.J., Silver, R., 2006. The regulation of neuroendocrine function: Timing is everything. Horm Behav 49, 557–574. https://doi.org/10.1016/j.yhbeh.2005.12.011
Kripke, D.F., Nievergelt, C.M., Joo, E., Shekhtman, T., Kelsoe, J.R., 2009. Circadian polymorphisms associated with affective disorders. J Circadian Rhythms 7, 2. https://doi.org/10.1186/1740-3391-7-2
Kronfeld-Schor, N., Einat, H., 2012. Circadian rhythms and depression: human psychopathology and animal models. Neuropharmacology 62, 101–114. https://doi.org/10.1016/j.neuropharm.2011.08.020
Kuffler, S.W., Potter, D.D., 1964. GLIA IN THE LEECH CENTRAL NERVOUS SYSTEM: PHYSIOLOGICAL PROPERTIES AND NEURON-GLIA RELATIONSHIP. J Neurophysiol 27, 290–320. https://doi.org/10.1152/jn.1964.27.2.290
Kumar, T., Jha, S.K., 2012. Sleep Deprivation Impairs Consolidation of Cued Fear Memory in Rats. PLoS One 7. https://doi.org/10.1371/journal.pone.0047042

Kwon, C.-H., Luikart, B.W., Powell, C.M., Zhou, J., Matheny, S.A., Zhang, W., Li, Y., Baker, S.J., Parada, L.F., 2006. Pten regulates neuronal arborization and social interaction in mice. Neuron 50, 377–388. https://doi.org/10.1016/j.neuron.2006.03.023

Lachyankar, M.B., Sultana, N., Schonhoff, C.M., Mitra, P., Poluha, W., Lambert, S., Quesenberry, P.J., Litofsky, N.S., Recht, L.D., Nabi, R., Miller, S.J., Ohta, S., Neel, B.G., Ross, A.H., 2000. A role for nuclear PTEN in neuronal differentiation. J Neurosci 20, 1404–1413.

Lagos, D., Pollara, G., Henderson, S., Gratrix, F., Fabani, M., Milne, R.S.B., Gotch, F., Boshoff, C., 2010. miR-132 regulates antiviral innate immunity through suppression of the p300 transcriptional co-activator. Nat Cell Biol 12, 513–519. https://doi.org/10.1038/ncb2054

Lagos-Quintana, M., Rauhut, R., Yalcin, A., Meyer, J., Lendeckel, W., Tuschl, T., 2002. Identification of tissue-specific microRNAs from mouse. Curr Biol 12, 735–739. https://doi.org/10.1016/s0960-9822(02)00809-6

Lambert, T.J., Storm, D.R., Sullivan, J.M., 2010. MicroRNA132 modulates short-term synaptic plasticity but not basal release probability in hippocampal neurons. PLoS One 5, e15182. https://doi.org/10.1371/journal.pone.0015182

Lamont, E.W., Robinson, B., Stewart, J., Amir, S., 2005. The central and basolateral nuclei of the amygdala exhibit opposite diurnal rhythms of expression of the clock protein Period2. Proc. Natl. Acad. Sci. U.S.A. 102, 4180–4184. https://doi.org/10.1073/pnas.0500901102

Landgraf, D., Long, J.E., Proulx, C.D., Barandas, R., Malinow, R., Welsh, D.K., 2016a. Genetic Disruption of Circadian Rhythms in the Suprachiasmatic Nucleus Causes Helplessness, Behavioral Despair, and Anxiety-like Behavior in Mice. Biol. Psychiatry 80, 827–835. https://doi.org/10.1016/j.biopsych.2016.03.1050

Landgraf, D., Long, J.E., Proulx, C.D., Barandas, R., Malinow, R., Welsh, D.K., 2016b. Genetic Disruption of Circadian Rhythms in the Suprachiasmatic Nucleus Causes Helplessness, Behavioral Despair, and Anxiety-like Behavior in Mice. Biol. Psychiatry 80, 827–835. https://doi.org/10.1016/j.biopsych.2016.03.1050

Lanjakornsiripan, D., Pior, B.-J., Kawaguchi, D., Furutachi, S., Tahara, T., Katsuyama, Y., Suzuki, Y., Fukazawa, Y., Gotoh, Y., 2018. Layer-specific morphological and molecular differences in neocortical astrocytes and their dependence on neuronal layers. Nature Communications 9, 1623. https://doi.org/10.1038/s41467-018-03940-3

Laposky, A., Easton, A., Dugovic, C., Walisser, J., Bradfield, C., Turek, F., 2005. Deletion of the mammalian circadian clock gene BMAL1/Mop3 alters baseline sleep architecture and the response to sleep deprivation. Sleep 28, 395–409.

Leak, R.K., Card, J.P., Moore, R.Y., 1999. Suprachiasmatic pacemaker organization analyzed by viral transynaptic transport. Brain Res. 819, 23–32. https://doi.org/10.1016/s0006-8993(98)01317-1

Lee, B., Li, A., Hansen, K.F., Cao, R., Yoon, J.H., Obrietan, K., 2010. CREB Influences Timing and Entrainment of the SCN Circadian Clock. J Biol Rhythms 25, 410–420. https://doi.org/10.1177/0748730410381229

Lee, H., Chen, R., Lee, Y., Yoo, S., Lee, C., 2009. Essential roles of CKIδ and CKIε in the mammalian circadian clock. Proc Natl Acad Sci U S A 106, 21359–21364. https://doi.org/10.1073/pnas.0906651106
Lee, R.C., Feinbaum, R.L., Ambros, V., 1993. The C. elegans heterochronic gene lin-4 encodes small RNAs with antisense complementarity to lin-14. Cell 75, 843–854. https://doi.org/10.1016/0092-8674(93)90529-y
Lei, Y., Tejani-Butt, S.M., 2010. N-methyl-d-aspartic acid receptors are altered by stress and alcohol in Wistar-Kyoto rat brain. Neuroscience 169, 125–131. https://doi.org/10.1016/j.neuroscience.2010.05.003
Lener, M.S., Niciu, M.J., Ballard, E.D., Park, M., Park, L.T., Nugent, A., Zarate, C.A., 2017. Glutamate and GABA Systems in the Pathophysiology of Major Depression and Antidepressant Response to Ketamine. Biol Psychiatry 81, 886–897. https://doi.org/10.1016/j.biopsych.2016.05.005
Leung, A.K.L., Sharp, P.A., 2010. MicroRNA functions in stress responses. Mol Cell 40, 205–215. https://doi.org/10.1016/j.molcel.2010.09.027
Leung, A.K.L., Sharp, P.A., 2007. microRNAs: a safeguard against turmoil? Cell 130, 581–585. https://doi.org/10.1016/j.cell.2007.08.010
Li, N., Lee, B., Liu, R.-J., Banasr, M., Dwyer, J.M., Iwata, M., Li, X.-Y., Aghajanian, G., Duman, R.S., 2010. mTOR-dependent synapse formation underlies the rapid antidepressant effects of NMDA antagonists. Science 329, 959–964. https://doi.org/10.1126/science.1190287
Li, N., Liu, R.-J., Dwyer, J.M., Banasr, M., Lee, B., Son, H., Li, X.-Y., Aghajanian, G., Duman, R.S., 2011. Glutamate N-methyl-D-aspartate Receptor Antagonists Rapidly Reverse Behavioral and Synaptic Deficits Caused by Chronic Stress Exposure. Biological Psychiatry, Serotonin and Depression - Revisited 69, 754–761. https://doi.org/10.1016/j.biopsych.2010.12.015
Li, Y.-J., Xu, M., Gao, Z.-H., Wang, Y.-Q., Yue, Z., Zhang, Y.-X., Li, X.-X., Zhang, C., Xie, S.-Y., Wang, P.-Y., 2013. Alterations of Serum Levels of BDNF-Related miRNAs in Patients with Depression. PLoS One 8. https://doi.org/10.1371/journal.pone.0063648
Libert, S., Pointer, K., Bell, E.L., Das, A., Cohen, D.E., Asara, J.M., Kapur, K., Bergmann, S., Preisig, M., Otowa, T., Kendler, K.S., Chen, X., Hettema, J.M., van den Oord, E.J., Rubio, J.P., Guarente, L., 2011. SIRT1 activates MAO-A in the brain to mediate anxiety and exploratory drive. Cell 147, 1459–1472. https://doi.org/10.1016/j.cell.2011.10.054
Lister, R.G., 1987. The use of a plus-maze to measure anxiety in the mouse. Psychopharmacology (Berl.) 92, 180–185.
Liston, C., Cichon, J.M., Jeanneteau, F., Jia, Z., Chao, M.V., Gan, W.-B., 2013. Circadian glucocorticoid oscillations promote learning-dependent synapse formation and maintenance. Nat. Neurosci. 16, 698–705. https://doi.org/10.1038/nn.3387
Liu, C., Chung, M., 2015. Genetics and epigenetics of circadian rhythms and their potential roles in neuropsychiatric disorders. Neurosci Bull 31, 141–159. https://doi.org/10.1007/s12264-014-1495-3

Liu, Q., Xu, Q., Arcuino, G., Kang, J., Nedergaard, M., 2004. Astrocyte-mediated activation of neuronal kainate receptors. Proc. Natl. Acad. Sci. U.S.A. 101, 3172–3177. https://doi.org/10.1073/pnas.0306731101

Liu, W., Ge, T., Leng, Y., Pan, Z., Fan, J., Yang, W., Cui, R., 2017. The Role of Neural Plasticity in Depression: From Hippocampus to Prefrontal Cortex. Neural Plast 2017, 6871089. https://doi.org/10.1155/2017/6871089

Liu, X., Hubbard, J.A., Fabes, R.A., Adam, J.B., 2006. Sleep disturbances and correlates of children with autism spectrum disorders. Child Psychiatry Hum Dev 37, 179–191. https://doi.org/10.1007/s10578-006-0028-3

Logan, R.W., Edgar, N., Gillman, A.G., Hoffman, D., Zhu, X., McClung, C.A., 2015. Chronic Stress Induces Brain Region-Specific Alterations of Molecular Rhythms that Correlate with Depression-like Behavior in Mice. Biol. Psychiatry 78, 249–258. https://doi.org/10.1016/j.biopsych.2015.01.011

Lucassen, P.J., Pruessner, J., Sousa, N., Almeida, O.F.X., Van Dam, A.M., Rajkowska, G., Swaab, D.F., Czéh, B., 2014. Neuropathology of stress. Acta Neuropathol 127, 109–135. https://doi.org/10.1007/s00401-013-1223-5

Lugo, J.N., Smith, G.D., Arbuckle, E.P., White, J., Holley, A.J., Floruta, C.M., Ahmed, N., Gomez, M.C., Okonkwo, O., 2014. Deletion of PTEN produces autism-like behavioral deficits and alterations in synaptic proteins. Front Mol Neurosci 7, 27. https://doi.org/10.3389/fnmol.2014.00027

Luikart, B.W., Bensen, A.L., Washburn, E.K., Perederiy, J.V., Su, K.G., Li, Y., Kernie, S.G., Parada, L.F., Westbrook, G.L., 2011. miR-132 mediates the integration of newborn neurons into the adult dentate gyrus. PLoS One 6, e19077. https://doi.org/10.1371/journal.pone.0019077

Lyons, L.C., 2011. Critical role of the circadian clock in memory formation: lessons from Aplysia. Front Mol Neurosci 4, 52. https://doi.org/10.3389/fnmol.2011.00052

Ma, B., Buckalew, R., Du, Y., Kiyoshi, C.M., Alford, C.C., Wang, W., McTigue, D.M., Enyeart, J.J., Terman, D., Zhou, M., 2016. Gap junction coupling confers isopotentiality on astrocyte syncytium. Glia 64, 214–226. https://doi.org/10.1002/glia.22924

Maeng, S., Zarate, C.A., Du, J., Schloesser, R.J., McCammon, J., Chen, G., Manji, H.K., 2008. Cellular mechanisms underlying the antidepressant effects of ketamine: role of alpha-amino-3-hydroxy-5-methylisoxazole-4-propionic acid receptors. Biol. Psychiatry 63, 349–352. https://doi.org/10.1016/j.biopsych.2007.05.028

Magariños, A.M., McEwen, B.S., Flügge, G., Fuchs, E., 1996. Chronic psychosocial stress causes apical dendritic atrophy of hippocampal CA3 pyramidal neurons in subordinate tree shrews. J Neurosci 16, 3534–3540.

Magill, S.T., Cambronne, X.A., Luikart, B.W., Lioy, D.T., Leighton, B.H., Westbrook, G.L., Mandel, G., Goodman, R.H., 2010. microRNA-132 regulates dendritic growth and arborization of newborn neurons in the adult hippocampus. Proc Natl Acad Sci U S A 107, 20382–20387. https://doi.org/10.1073/pnas.1015691107

Magistretti, P.J., Allaman, I., 2018. Lactate in the brain: from metabolic end-product to signalling molecule. Nat. Rev. Neurosci. 19, 235–249. https://doi.org/10.1038/nrn.2018.19

Magistretti, P.J., Allaman, I., 2015. A cellular perspective on brain energy metabolism and functional imaging. Neuron 86, 883–901. https://doi.org/10.1016/j.neuron.2015.03.035

Mahmmoud, R.R., Sase, S., Aher, Y.D., Sase, A., Gröger, M., Mokhtar, M., Höger, H., Lubec, G., 2015. Spatial and Working Memory Is Linked to Spine Density and Mushroom Spines. PLOS ONE 10, e0139739. https://doi.org/10.1371/journal.pone.0139739

Malan-Müller, S., Hemmings, S.M.J., Seedat, S., 2013. Big effects of small RNAs: a review of microRNAs in anxiety. Mol Neurobiol 47, 726–739. https://doi.org/10.1007/s12035-012-8374-6

Malek, Z.S., Sage, D., Pévet, P., Raison, S., 2007. Daily rhythm of tryptophan hydroxylase-2 messenger ribonucleic acid within raphe neurons is induced by corticoid daily surge and modulated by enhanced locomotor activity. Endocrinology 148, 5165–5172. https://doi.org/10.1210/en.2007-0526

Manabe, T., Aiba, A., Yamada, A., Ichise, T., Sakagami, H., Kondo, H., Katsuki, M., 2000. Regulation of Long-Term Potentiation by H-Ras through NMDA Receptor Phosphorylation. J. Neurosci. 20, 2504–2511. https://doi.org/10.1523/JNEUROSCI.20-07-02504.2000

Mannironi, C., Biundo, A., Rajendran, S., De Vito, F., Saba, L., Caioli, S., Zona, C., Ciotti, T., Caristi, S., Perlas, E., Del Vecchio, G., Bozzoni, I., Rinaldi, A., Mele, A., Presutti, C., 2018. miR-135a Regulates Synaptic Transmission and Anxiety-Like Behavior in Amygdala. Mol Neurobiol 55, 3301–3315. https://doi.org/10.1007/s12035-017-0564-9

Mannironi, C., Camon, J., De Vito, F., Biundo, A., De Stefano, M.E., Persiconi, I., Bozzoni, I., Fragapane, P., Mele, A., Presutti, C., 2013. Acute stress alters amygdala microRNA miR-135a and miR-124 expression: inferences for corticosteroid dependent stress response. PLoS One 8, e73385. https://doi.org/10.1371/journal.pone.0073385

Maras, P.M., Molet, J., Chen, Y., Rice, C., Ji, S.G., Solodkin, A., Baram, T.Z., 2014. Preferential loss of dorsal-hippocampus synapses underlies memory impairments provoked by short, multimodal stress. Mol Psychiatry 19, 811–822. https://doi.org/10.1038/mp.2014.12

Marchetti, I., Koster, E.H.W., Sonuga-Barke, E.J., De Raedt, R., 2012. The default mode network and recurrent depression: a neurobiological model of cognitive risk factors. Neuropsychol Rev 22, 229–251. https://doi.org/10.1007/s11065-012-9199-9

Margineanu, M.B., Mahmood, H., Fiumelli, H., Magistretti, P.J., 2018. L-Lactate Regulates the Expression of Synaptic Plasticity and Neuroprotection Genes in Cortical Neurons: A Transcriptome Analysis. Front Mol Neurosci 11, 375. https://doi.org/10.3389/fnmol.2018.00375

Marquez de Prado, B., Castañeda, T.R., Galindo, A., del Arco, A., Segovia, G., Reiter, R.J., Mora, F., 2000. Melatonin disrupts circadian rhythms of glutamate and GABA in the neostriatum of the aware rat: a microdialysis study. J. Pineal Res. 29, 209–216.

Martin, K.F., 1991. Rhythms in neurotransmitter turnover: focus on the serotonergic system. Pharmacol. Ther. 51, 421–429.
Martínez de Paz, A., Sanchez-Mut, J.V., Samitier-Martí, M., Petazzi, P., Sáez, M., Szczesna, K., Huertas, D., Esteller, M., Ausió, J., 2015. Circadian cycle-dependent MeCP2 and brain chromatin changes. PLoS One 10, e0123693. https://doi.org/10.1371/journal.pone.0123693
Mateos, S.S., Sánchez, C.L., Paredes, S.D., Barriga, C., Rodríguez, A.B., 2009. Circadian levels of serotonin in plasma and brain after oral administration of tryptophan in rats. Basic Clin. Pharmacol. Toxicol. 104, 52–59. https://doi.org/10.1111/j.1742-7843.2008.00333.x
Mayford, M., Bach, M.E., Huang, Y.Y., Wang, L., Hawkins, R.D., Kandel, E.R., 1996. Control of memory formation through regulated expression of a CaMKII transgene. Science 274, 1678–1683. https://doi.org/10.1126/science.274.5293.1678
Mazziotti, R., Baroncelli, L., Ceglia, N., Chelini, G., Sala, G.D., Magnan, C., Napoli, D., Putignano, E., Silingardi, D., Tola, J., Tognini, P., Arthur, J.S.C., Baldi, P., Pizzorusso, T., 2017. Mir-132/212 is required for maturation of binocular matching of orientation preference and depth perception. Nat Commun 8, 15488. https://doi.org/10.1038/ncomms15488
McClung, C.A., 2007. Circadian Genes, Rhythms and the Biology of Mood Disorders. Pharmacol Ther 114, 222–232. https://doi.org/10.1016/j.pharmthera.2007.02.003
McEwen, B.S., Eiland, L., Hunter, R.G., Miller, M.M., 2012. Stress and anxiety: structural plasticity and epigenetic regulation as a consequence of stress. Neuropharmacology 62, 3–12. https://doi.org/10.1016/j.neuropharm.2011.07.014
McGowan, N.M., Coogan, A.N., 2013. Circadian and behavioural responses to shift work-like schedules of light/dark in the mouse. J Mol Psychiatry 1, 7. https://doi.org/10.1186/2049-9256-1-7
Meerson, A., Cacheaux, L., Goosens, K.A., Sapolsky, R.M., Soreq, H., Kaufer, D., 2010. Changes in brain MicroRNAs contribute to cholinergic stress reactions. J Mol Neurosci 40, 47–55. https://doi.org/10.1007/s12031-009-9252-1
Meir Drexler, S., Wolf, O.T., 2017. The role of glucocorticoids in emotional memory reconsolidation. Neurobiol Learn Mem 142, 126–134. https://doi.org/10.1016/j.nlm.2016.11.008
Mellios, N., Sugihara, H., Castro, J., Banerjee, A., Le, C., Kumar, A., Crawford, B., Strathmann, J., Tropea, D., Levine, S.S., Edbauer, D., Sur, M., 2011. miR-132, an experience-dependent microRNA, is essential for visual cortex plasticity. Nat Neurosci 14, 1240–1242. https://doi.org/10.1038/nn.2909
Mendell, J.T., Olson, E.N., 2012. MicroRNAs in stress signaling and human disease. Cell 148, 1172–1187. https://doi.org/10.1016/j.cell.2012.02.005
Mendoza-Viveros, L., Chiang, C.-K., Ong, J.L.K., Hegazi, S., Cheng, A.H., Bouchard-Cannon, P., Fana, M., Lowden, C., Zhang, P., Bothorel, B., Michniewicz, M.G., Magill, S.T., Holmes, M.M., Goodman, R.H., Simonneaux, V., Figeys, D., Cheng, H.-Y.M., 2017. miR-132/212 Modulates Seasonal Adaptation and

Dendritic Morphology of the Central Circadian Clock. Cell Rep 19, 505–520. https://doi.org/10.1016/j.celrep.2017.03.057
Meng, Q.-J., Logunova, L., Maywood, E.S., Gallego, M., Lebiecki, J., Brown, T.M., Sládek, M., Semikhodskii, A.S., Glossop, N.R.J., Piggins, H.D., Chesham, J.E., Bechtold, D.A., Yoo, S.-H., Takahashi, J.S., Virshup, D.M., Boot-Handford, R.P., Hastings, M.H., Loudon, A.S.I., 2008. Setting clock speed in mammals: the CK1 epsilon tau mutation in mice accelerates circadian pacemakers by selectively destabilizing PERIOD proteins. Neuron 58, 78–88. https://doi.org/10.1016/j.neuron.2008.01.019
Meşe, G., Richard, G., White, T.W., 2007. Gap junctions: basic structure and function. J Invest Dermatol 127, 2516–2524. https://doi.org/10.1038/sj.jid.5700770
Miano, S., Bruni, O., Elia, M., Trovato, A., Smerieri, A., Verrillo, E., Roccella, M., Terzano, M.G., Ferri, R., 2007. Sleep in children with autistic spectrum disorder: a questionnaire and polysomnographic study. Sleep Med 9, 64–70. https://doi.org/10.1016/j.sleep.2007.01.014
Michaelson, S.D., Ozkan, E.D., Aceti, M., Maity, S., Llamosas, N., Weldon, M., Mizrachi, E., Vaissiere, T., Gaffield, M.A., Christie, J.M., Holder, J.L., Miller, C.A., Rumbaugh, G., 2018. SYNGAP1 heterozygosity disrupts sensory processing by reducing touch-related activity within somatosensory cortex circuits. Nat Neurosci 21, 1–13. https://doi.org/10.1038/s41593-018-0268-0
Michán, S., Li, Y., Chou, M.M.-H., Parrella, E., Ge, H., Long, J.M., Allard, J.S., Lewis, K., Miller, M., Xu, W., Mervis, R.F., Chen, J., Guerin, K.I., Smith, L.E.H., McBurney, M.W., Sinclair, D.A., Baudry, M., de Cabo, R., Longo, V.D., 2010. SIRT1 is essential for normal cognitive function and synaptic plasticity. J Neurosci 30, 9695–9707. https://doi.org/10.1523/JNEUROSCI.0027-10.2010
Migeon, C.J., Tyler, F.H., Mahoney, J.P., Florentin, A.A., Castle, H., Bliss, E.L., Samuels, L.T., 1956. The diurnal variation of plasma levels and urinary excretion on 17-hydroxycorticosteroids in normal subjects, night workers and blind subjects. J. Clin. Endocrinol. Metab. 16, 622–633. https://doi.org/10.1210/jcem-16-5-622
Mignot, C., von Stülpnagel, C., Nava, C., Ville, D., Sanlaville, D., Lesca, G., Rastetter, A., Gachet, B., Marie, Y., Korenke, G.C., Borggraefe, I., Hoffmann-Zacharska, D., Szczepanik, E., Rudzka-Dybała, M., Yiş, U., Çağlayan, H., Isapof, A., Marey, I., Panagiotakaki, E., Korff, C., Rossier, E., Riess, A., Beck-Woedl, S., Rauch, A., Zweier, C., Hoyer, J., Reis, A., Mironov, M., Bobylova, M., Mukhin, K., Hernandez-Hernandez, L., Maher, B., Sisodiya, S., Kuhn, M., Glaeser, D., Weckhuysen, S., Myers, C.T., Mefford, H.C., Hörtnagel, K., Biskup, S., EuroEPINOMICS-RES MAE working group, Lemke, J.R., Héron, D., Kluger, G., Depienne, C., 2016. Genetic and neurodevelopmental spectrum of SYNGAP1-associated intellectual disability and epilepsy. J. Med. Genet. 53, 511–522. https://doi.org/10.1136/jmedgenet-2015-103451
Miguel-Hidalgo, J.J., Moulana, M., Deloach, P.H., Rajkowska, G., 2018. Chronic Unpredictable Stress Reduces Immunostaining for Connexins 43 and 30 and

Myelin Basic Protein in the Rat Prelimbic and Orbitofrontal Cortices. Chronic Stress (Thousand Oaks) 2. https://doi.org/10.1177/2470547018814186
Miller, A.H., Vogt, G.J., Pearce, B.D., 2002. The phosphodiesterase type 4 inhibitor, rolipram, enhances glucocorticoid receptor function. Neuropsychopharmacology 27, 939–948. https://doi.org/10.1016/S0893-133X(02)00381-0
Miller, B.H., Zeier, Z., Xi, L., Lanz, T.A., Deng, S., Strathmann, J., Willoughby, D., Kenny, P.J., Elsworth, J.D., Lawrence, M.S., Roth, R.H., Edbauer, D., Kleiman, R.J., Wahlestedt, C., 2012. MicroRNA-132 dysregulation in schizophrenia has implications for both neurodevelopment and adult brain function. PNAS 109, 3125–3130. https://doi.org/10.1073/pnas.1113793109
Mineur, Y.S., Belzung, C., Crusio, W.E., 2006. Effects of unpredictable chronic mild stress on anxiety and depression-like behavior in mice. Behav. Brain Res. 175, 43–50. https://doi.org/10.1016/j.bbr.2006.07.029
Mishchenko, Y., Hu, T., Spacek, J., Mendenhall, J., Harris, K.M., Chklovskii, D.B., 2010. Ultrastructural analysis of hippocampal neuropil from the connectomics perspective. Neuron 67, 1009–1020. https://doi.org/10.1016/j.neuron.2010.08.014
Mitra, R., Jadhav, S., McEwen, B.S., Vyas, A., Chattarji, S., 2005. Stress duration modulates the spatiotemporal patterns of spine formation in the basolateral amygdala. Proc Natl Acad Sci U S A 102, 9371–9376. https://doi.org/10.1073/pnas.0504011102
Miyazaki, Y., Li, R., Rezk, A., Misirliyan, H., Moore, C., Farooqi, N., Solis, M., Goiry, L.G., de Faria Junior, O., Dang, V.D., Colman, D., Dhaunchak, A.S., Antel, J., Gommerman, J., Prat, A., Fillatreau, S., Bar-Or, A., CIHR/MSSC New Emerging Team Grant in Clinical Autoimmunity, MSSRF Canadian B cells in MS Team, 2014. A novel microRNA-132-sirtuin-1 axis underlies aberrant B-cell cytokine regulation in patients with relapsing-remitting multiple sclerosis [corrected]. PLoS One 9, e105421. https://doi.org/10.1371/journal.pone.0105421
Moga, M.M., Moore, R.Y., 1997. Organization of neural inputs to the suprachiasmatic nucleus in the rat. J. Comp. Neurol. 389, 508–534. https://doi.org/10.1002/(sici)1096-9861(19971222)389:3<508::aid-cne11>3.0.co;2-h
Mohammed, H., Al-Awami, A.K., Beyer, J., Cali, C., Magistretti, P., Pfister, H., Hadwiger, M., 2018. Abstractocyte: A Visual Tool for Exploring Nanoscale Astroglial Cells. IEEE Trans Vis Comput Graph 24, 853–861. https://doi.org/10.1109/TVCG.2017.2744278
Mohawk, J.A., Takahashi, J.S., 2011. Cell autonomy and synchrony of suprachiasmatic nucleus circadian oscillators. Trends Neurosci. 34, 349–358. https://doi.org/10.1016/j.tins.2011.05.003
Molofsky, A.V., Krenick, R., Ullian, E., Tsai, H., Deneen, B., Richardson, W.D., Barres, B.A., Rowitch, D.H., 2012. Astrocytes and disease: a neurodevelopmental perspective. Genes Dev. 26, 891–907. https://doi.org/10.1101/gad.188326.112
Monk, T.H., Buysse, D.J., Reynolds, C.F., Berga, S.L., Jarrett, D.B., Begley, A.E., Kupfer, D.J., 1997. Circadian rhythms in human performance and mood under

constant conditions. J Sleep Res 6, 9–18. https://doi.org/10.1046/j.1365-2869.1997.00023.x
Monteiro, S., Roque, S., de Sá-Calçada, D., Sousa, N., Correia-Neves, M., Cerqueira, J.J., 2015. An Efficient Chronic Unpredictable Stress Protocol to Induce Stress-Related Responses in C57BL/6 Mice. Front Psychiatry 6. https://doi.org/10.3389/fpsyt.2015.00006
Montoya, E.R., Terburg, D., Bos, P.A., van Honk, J., 2012. Testosterone, cortisol, and serotonin as key regulators of social aggression: A review and theoretical perspective. Motiv Emot 36, 65–73. https://doi.org/10.1007/s11031-011-9264-3
Moore, R.Y., Eichler, V.B., 1972. Loss of a circadian adrenal corticosterone rhythm following suprachiasmatic lesions in the rat. Brain Res. 42, 201–206.
Moore, R.Y., Speh, J.C., 1993. GABA is the principal neurotransmitter of the circadian system. Neurosci. Lett. 150, 112–116. https://doi.org/10.1016/0304-3940(93)90120-a
Moretti, P., Levenson, J.M., Battaglia, F., Atkinson, R., Teague, R., Antalffy, B., Armstrong, D., Arancio, O., Sweatt, J.D., Zoghbi, H.Y., 2006. Learning and memory and synaptic plasticity are impaired in a mouse model of Rett syndrome. J Neurosci 26, 319–327. https://doi.org/10.1523/JNEUROSCI.2623-05.2006
Moriya, S., Tahara, Y., Sasaki, H., Ishigooka, J., Shibata, S., 2015. Phase-delay in the light-dark cycle impairs clock gene expression and levels of serotonin, norepinephrine, and their metabolites in the mouse hippocampus and amygdala. Sleep Med. 16, 1352–1359. https://doi.org/10.1016/j.sleep.2015.06.020
Moriya, T., Horikawa, K., Akiyama, M., Shibata, S., 2000. Correlative association between N-methyl-D-aspartate receptor-mediated expression of period genes in the suprachiasmatic nucleus and phase shifts in behavior with photic entrainment of clock in hamsters. Mol. Pharmacol. 58, 1554–1562. https://doi.org/10.1124/mol.58.6.1554
Morozova, N., Zinovyev, A., Nonne, N., Pritchard, L.-L., Gorban, A.N., Harel-Bellan, A., 2012. Kinetic signatures of microRNA modes of action. RNA 18, 1635–1655. https://doi.org/10.1261/rna.032284.112
Moser, E.I., Kropff, E., Moser, M.-B., 2008. Place cells, grid cells, and the brain's spatial representation system. Annu Rev Neurosci 31, 69–89. https://doi.org/10.1146/annurev.neuro.31.061307.090723
Moser, M.B., Trommald, M., Andersen, P., 1994. An increase in dendritic spine density on hippocampal CA1 pyramidal cells following spatial learning in adult rats suggests the formation of new synapses. Proc Natl Acad Sci U S A 91, 12673–12675.
Muhia, M., Willadt, S., Yee, B.K., Feldon, J., Paterna, J.-C., Schwendener, S., Vogt, K., Kennedy, M.B., Knuesel, I., 2012. Molecular and behavioral changes associated with adult hippocampus-specific SynGAP1 knockout. Learn. Mem. 19, 268–281. https://doi.org/10.1101/lm.026351.112
Muhia, M., Yee, B.K., Feldon, J., Markopoulos, F., Knuesel, I., 2010. Disruption of hippocampus-regulated behavioural and cognitive processes by heterozygous

constitutive deletion of SynGAP. Eur. J. Neurosci. 31, 529–543. https://doi.org/10.1111/j.1460-9568.2010.07079.x
Mukherjee, S., Coque, L., Cao, J.-L., Kumar, J., Chakravarty, S., Asaithamby, A., Graham, A., Gordon, E., Enwright, J.F., DiLeone, R.J., Birnbaum, S.G., Cooper, D.C., McClung, C.A., 2010. Knockdown of Clock in the ventral tegmental area through RNA interference results in a mixed state of mania and depression-like behavior. Biol. Psychiatry 68, 503–511. https://doi.org/10.1016/j.biopsych.2010.04.031
Mullen, R.J., Buck, C.R., Smith, A.M., 1992. NeuN, a neuronal specific nuclear protein in vertebrates. Development 116, 201–211.
Murphy-Royal, C., Johnston, A.D., Boyce, A.K.J., Diaz-Castro, B., Institoris, A., Peringod, G., Zhang, O., Stout, R.F., Spray, D.C., Thompson, R.J., Khakh, B.S., Bains, J.S., Gordon, G.R., 2020. Stress gates an astrocytic energy reservoir to impair synaptic plasticity. Nature Communications 11, 2014. https://doi.org/10.1038/s41467-020-15778-9
Murray, G., Nicholas, C.L., Kleiman, J., Dwyer, R., Carrington, M.J., Allen, N.B., Trinder, J., 2009. Nature's clocks and human mood: the circadian system modulates reward motivation. Emotion 9, 705–716. https://doi.org/10.1037/a0017080
Musazzi, L., Treccani, G., Popoli, M., 2015. Functional and structural remodeling of glutamate synapses in prefrontal and frontal cortex induced by behavioral stress. Front Psychiatry 6, 60. https://doi.org/10.3389/fpsyt.2015.00060
Na, E.S., Nelson, E.D., Adachi, M., Autry, A.E., Mahgoub, M.A., Kavalali, E.T., Monteggia, L.M., 2012. A mouse model for MeCP2 duplication syndrome: MeCP2 overexpression impairs learning and memory and synaptic transmission. J Neurosci 32, 3109–3117. https://doi.org/10.1523/JNEUROSCI.6000-11.2012
Nagoshi, E., Saini, C., Bauer, C., Laroche, T., Naef, F., Schibler, U., 2004. Circadian gene expression in individual fibroblasts: cell-autonomous and self-sustained oscillators pass time to daughter cells. Cell 119, 693–705. https://doi.org/10.1016/j.cell.2004.11.015
Nagy, C., Torres-Platas, S.G., Mechawar, N., Turecki, G., 2016. Repression of Astrocytic Connexins in Cortical and Subcortical Brain Regions and Prefrontal Enrichment of H3K9me3 in Depression and Suicide. Int J Neuropsychopharmacol 20, 50–57. https://doi.org/10.1093/ijnp/pyw071
Nair, N.P., Hariharasubramanian, N., Pilapil, C., 1984. Circadian rhythm of plasma melatonin in endogenous depression. Prog. Neuropsychopharmacol. Biol. Psychiatry 8, 715–718.
Nakajima, R., Takao, K., Hattori, S., Shoji, H., Komiyama, N.H., Grant, S.G.N., Miyakawa, T., 2019. Comprehensive behavioral analysis of heterozygous Syngap1 knockout mice. Neuropsychopharmacology Reports 39, 223–237. https://doi.org/10.1002/npr2.12073
Naskar, S., Chattarji, S., 2019. Stress Elicits Contrasting Effects on the Structure and Number of Astrocytes in the Amygdala versus Hippocampus. eNeuro 6. https://doi.org/10.1523/ENEURO.0338-18.2019

Nelson, S.R., Schulz, D.W., Passonneau, J.V., Lowry, O.H., 1968. Control of glycogen levels in brain. J. Neurochem. 15, 1271–1279. https://doi.org/10.1111/j.1471-4159.1968.tb05904.x
Nestler, E.J., Carlezon, W.A., 2006. The mesolimbic dopamine reward circuit in depression. Biol. Psychiatry 59, 1151–1159. https://doi.org/10.1016/j.biopsych.2005.09.018
Newman, L.A., Korol, D.L., Gold, P.E., 2011. Lactate Produced by Glycogenolysis in Astrocytes Regulates Memory Processing. PLOS ONE 6, e28427. https://doi.org/10.1371/journal.pone.0028427
Nguyen, E.T., Selmanovic, D., Maltry, M., Morano, R., Franco-Villanueva, A., Estrada, C.M., Solomon, M.B., 2020. Endocrine stress responsivity and social memory in 3xTg-AD female and male mice: A tale of two experiments. Hormones and Behavior 126, 104852. https://doi.org/10.1016/j.yhbeh.2020.104852
Nicholls, D.G., 1993. The glutamatergic nerve terminal. Eur. J. Biochem. 212, 613–631.
Nielsen, M.S., Axelsen, L.N., Sorgen, P.L., Verma, V., Delmar, M., Holstein-Rathlou, N.-H., 2012. Gap Junctions. Compr Physiol 2. https://doi.org/10.1002/cphy.c110051
Nieto, S.J., Patriquin, M.A., Nielsen, D.A., Kosten, T.A., 2016. Don't worry; be informed about the epigenetics of anxiety. Pharmacol Biochem Behav 146–147, 60–72. https://doi.org/10.1016/j.pbb.2016.05.006
Noguchi, T., Leise, T.L., Kingsbury, N.J., Diemer, T., Wang, L.L., Henson, M.A., Welsh, D.K., 2017. Calcium Circadian Rhythmicity in the Suprachiasmatic Nucleus: Cell Autonomy and Network Modulation. eNeuro 4. https://doi.org/10.1523/ENEURO.0160-17.2017
Nollet, M., Gaillard, P., Tanti, A., Girault, V., Belzung, C., Leman, S., 2012. Neurogenesis-independent antidepressant-like effects on behavior and stress axis response of a dual orexin receptor antagonist in a rodent model of depression. Neuropsychopharmacology 37, 2210–2221. https://doi.org/10.1038/npp.2012.70
Nortley, R., Attwell, D., 2017. Control of brain energy supply by astrocytes. Curr Opin Neurobiol 47, 80–85. https://doi.org/10.1016/j.conb.2017.09.012
Nudelman, A.S., DiRocco, D.P., Lambert, T.J., Garelick, M.G., Le, J., Nathanson, N.M., Storm, D.R., 2010. Neuronal Activity Rapidly Induces Transcription of the CREB-Regulated microRNA-132, in vivo. Hippocampus 20, 492–498. https://doi.org/10.1002/hipo.20646
Nugent, N.R., Tyrka, A.R., Carpenter, L.L., Price, L.H., 2011. Gene-environment interactions: early life stress and risk for depressive and anxiety disorders. Psychopharmacology (Berl) 214, 175–196. https://doi.org/10.1007/s00213-010-2151-x
Nuss, P., 2015. Anxiety disorders and GABA neurotransmission: a disturbance of modulation. Neuropsychiatr Dis Treat 11, 165–175. https://doi.org/10.2147/NDT.S58841
Nutt, D., Wilson, S., Paterson, L., 2008. Sleep disorders as core symptoms of depression. Dialogues Clin Neurosci 10, 329–336.

O'Brien, J., Hayder, H., Zayed, Y., Peng, C., 2018. Overview of MicroRNA Biogenesis, Mechanisms of Actions, and Circulation. Front. Endocrinol. 9. https://doi.org/10.3389/fendo.2018.00402
Obrietan, K., Impey, S., Smith, D., Athos, J., Storm, D.R., 1999. Circadian regulation of cAMP response element-mediated gene expression in the suprachiasmatic nuclei. J Biol Chem 274, 17748–17756. https://doi.org/10.1074/jbc.274.25.17748
Obrietan, K., Impey, S., Storm, D.R., 1998a. Light and circadian rhythmicity regulate MAP kinase activation in the suprachiasmatic nuclei. Nat Neurosci 1, 693–700. https://doi.org/10.1038/3695
Obrietan, Karl, Impey, S., Storm, D.R., 1998. Light and circadian rhythmicity regulate MAP kinase activation in the suprachiasmatic nuclei. Nat Neurosci 1, 693–700. https://doi.org/10.1038/3695
Obrietan, K., Impey, S., Storm, D.R., 1998b. Light and circadian rhythmicity regulate MAP kinase activation in the suprachiasmatic nuclei. Nat. Neurosci. 1, 693–700. https://doi.org/10.1038/3695
O'Connor, R.M., Dinan, T.G., Cryan, J.F., 2012. Little things on which happiness depends: microRNAs as novel therapeutic targets for the treatment of anxiety and depression. Mol Psychiatry 17, 359–376. https://doi.org/10.1038/mp.2011.162
Octeau, J.C., Chai, H., Jiang, R., Bonanno, S.L., Martin, K.C., Khakh, B.S., 2018. An Optical Neuron-Astrocyte Proximity Assay at Synaptic Distance Scales. Neuron 98, 49-66.e9. https://doi.org/10.1016/j.neuron.2018.03.003
Oe, Y., Baba, O., Ashida, H., Nakamura, K.C., Hirase, H., 2016. Glycogen distribution in the microwave-fixed mouse brain reveals heterogeneous astrocytic patterns. Glia 64, 1532–1545. https://doi.org/10.1002/glia.23020
Ogata, K., Kosaka, T., 2002. Structural and quantitative analysis of astrocytes in the mouse hippocampus. Neuroscience 113, 221–233. https://doi.org/10.1016/S0306-4522(02)00041-6
Ogden, K.K., Ozkan, E.D., Rumbaugh, G., 2016. Prioritizing the development of mouse models for childhood brain disorders. Neuropharmacology 100, 2–16. https://doi.org/10.1016/j.neuropharm.2015.07.029
Oh, J.S., Manzerra, P., Kennedy, M.B., 2004. Regulation of the neuron-specific Ras GTPase-activating protein, synGAP, by Ca2+/calmodulin-dependent protein kinase II. J. Biol. Chem. 279, 17980–17988. https://doi.org/10.1074/jbc.M314109200
Okada, C., Yamashita, E., Lee, S.J., Shibata, S., Katahira, J., Nakagawa, A., Yoneda, Y., Tsukihara, T., 2009. A high-resolution structure of the pre-microRNA nuclear export machinery. Science 326, 1275–1279. https://doi.org/10.1126/science.1178705
O'Neill, J.S., Maywood, E.S., Chesham, J.E., Takahashi, J.S., Hastings, M.H., 2008. cAMP-dependent signaling as a core component of the mammalian circadian pacemaker. Science 320, 949–953. https://doi.org/10.1126/science.1152506
Orellana, J.A., Moraga-Amaro, R., Díaz-Galarce, R., Rojas, S., Maturana, C.J., Stehberg, J., Sáez, J.C., 2015. Restraint stress increases hemichannel activity in

hippocampal glial cells and neurons. Front Cell Neurosci 9, 102. https://doi.org/10.3389/fncel.2015.00102
Orkand, R.K., Nicholls, J.G., Kuffler, S.W., 1966. Effect of nerve impulses on the membrane potential of glial cells in the central nervous system of amphibia. J Neurophysiol 29, 788–806. https://doi.org/10.1152/jn.1966.29.4.788
Oster, H., Challet, E., Ott, V., Arvat, E., de Kloet, E.R., Dijk, D.-J., Lightman, S., Vgontzas, A., Van Cauter, E., 2017. The Functional and Clinical Significance of the 24-Hour Rhythm of Circulating Glucocorticoids. Endocr. Rev. 38, 3–45. https://doi.org/10.1210/er.2015-1080
Owens, M.J., 2004. Selectivity of antidepressants: from the monoamine hypothesis of depression to the SSRI revolution and beyond. J Clin Psychiatry 65 Suppl 4, 5–10.
Ozkan, E.D., Creson, T.K., Kramár, E.A., Rojas, C., Seese, R.R., Babyan, A.H., Shi, Y., Lucero, R., Xu, X., Noebels, J.L., Miller, C.A., Lynch, G., Rumbaugh, G., 2014. Reduced cognition in Syngap1 mutants is caused by isolated damage within developing forebrain excitatory neurons. Neuron 82, 1317–1333. https://doi.org/10.1016/j.neuron.2014.05.015
Pace-Schott, E.F., Spencer, R.M.C., Vijayakumar, S., Ahmed, N., Verga, P.W., Orr, S.P., Pitman, R.K., Milad, M.R., 2013. Extinction of Conditioned Fear is Better Learned and Recalled in the Morning than in the Evening. J Psychiatr Res 47, 1776–1784. https://doi.org/10.1016/j.jpsychires.2013.07.027
Padival, M., Quinette, D., Rosenkranz, J.A., 2013. Effects of repeated stress on excitatory drive of basal amygdala neurons in vivo. Neuropsychopharmacology 38, 1748–1762. https://doi.org/10.1038/npp.2013.74
Panatier, A., Vallée, J., Haber, M., Murai, K.K., Lacaille, J.-C., Robitaille, R., 2011. Astrocytes are endogenous regulators of basal transmission at central synapses. Cell 146, 785–798. https://doi.org/10.1016/j.cell.2011.07.022
Papouin, T., Dunphy, J., Tolman, M., Foley, J.C., Haydon, P.G., 2017. Astrocytic control of synaptic function. Philos Trans R Soc Lond B Biol Sci 372. https://doi.org/10.1098/rstb.2016.0154
Parekh, P.K., McClung, C.A., 2016. Circadian Mechanisms Underlying Reward-Related Neurophysiology and Synaptic Plasticity. Front Psychiatry 6. https://doi.org/10.3389/fpsyt.2015.00187
Parker, M.J., Fryer, A.E., Shears, D.J., Lachlan, K.L., McKee, S.A., Magee, A.C., Mohammed, S., Vasudevan, P.C., Park, S.-M., Benoit, V., Lederer, D., Maystadt, I., Study, D., FitzPatrick, D.R., 2015. De novo, heterozygous, loss-of-function mutations in SYNGAP1 cause a syndromic form of intellectual disability. Am. J. Med. Genet. A 167A, 2231–2237. https://doi.org/10.1002/ajmg.a.37189
Parri, H.R., Gould, T.M., Crunelli, V., 2001. Spontaneous astrocytic Ca 2+ oscillations in situ drive NMDAR-mediated neuronal excitation. Nature Neuroscience 4, 803–812. https://doi.org/10.1038/90507
Partch, C.L., Green, C.B., Takahashi, J.S., 2014. Molecular architecture of the mammalian circadian clock. Trends Cell Biol. 24, 90–99. https://doi.org/10.1016/j.tcb.2013.07.002

Pasti, L., Volterra, A., Pozzan, T., Carmignoto, G., 1997. Intracellular Calcium Oscillations in Astrocytes: A Highly Plastic, Bidirectional Form of Communication between Neurons and Astrocytes In Situ. J. Neurosci. 17, 7817–7830. https://doi.org/10.1523/JNEUROSCI.17-20-07817.1997

Pathania, M., Torres-Reveron, J., Yan, L., Kimura, T., Lin, T.V., Gordon, V., Teng, Z.-Q., Zhao, X., Fulga, T.A., Van Vactor, D., Bordey, A., 2012. miR-132 enhances dendritic morphogenesis, spine density, synaptic integration, and survival of newborn olfactory bulb neurons. PLoS One 7, e38174. https://doi.org/10.1371/journal.pone.0038174

Paul, P., Chakraborty, A., Sarkar, D., Langthasa, M., Rahman, M., Bari, M., Singha, R.S., Malakar, A.K., Chakraborty, S., 2018. Interplay between miRNAs and human diseases. Journal of Cellular Physiology 233, 2007–2018. https://doi.org/10.1002/jcp.25854

Paulson, P.E., Robinson, T.E., 1996. Regional Differences in the Effects of Amphetamine Withdrawal on Dopamine Dynamics in the Striatum. Neuropsychopharmacology 14, 325–337. https://doi.org/10.1016/0893-133X(95)00141-Y

Paulson, P.E., Robinson, T.E., 1994. Relationship between circadian changes in spontaneous motor activity and dorsal versus ventral striatal dopamine neurotransmission assessed with on-line microdialysis. Behav. Neurosci. 108, 624–635.

Pavlides, C., Nivón, L.G., McEwen, B.S., 2002. Effects of chronic stress on hippocampal long-term potentiation. Hippocampus 12, 245–257. https://doi.org/10.1002/hipo.1116

Pelka, G.J., Watson, C.M., Radziewic, T., Hayward, M., Lahooti, H., Christodoulou, J., Tam, P.P.L., 2006. Mecp2 deficiency is associated with learning and cognitive deficits and altered gene activity in the hippocampal region of mice. Brain 129, 887–898. https://doi.org/10.1093/brain/awl022

Peng, D.-H., Shen, T., Zhang, J., Huang, J., Liu, J., Liu, S.-Y., Jiang, K., Xu, Y.-F., Fang, Y.-R., 2012. Abnormal functional connectivity with mood regulating circuit in unmedicated individual with major depression: a resting-state functional magnetic resonance study. Chin. Med. J. 125, 3701–3706.

Pennartz, C.M., Hamstra, R., Geurtsen, A.M., 2001. Enhanced NMDA receptor activity in retinal inputs to the rat suprachiasmatic nucleus during the subjective night. J. Physiol. (Lond.) 532, 181–194. https://doi.org/10.1111/j.1469-7793.2001.0181g.x

Perea, G., Araque, A., 2007. Astrocytes potentiate transmitter release at single hippocampal synapses. Science 317, 1083–1086. https://doi.org/10.1126/science.1144640

Perea, G., Araque, A., 2005. Properties of synaptically evoked astrocyte calcium signal reveal synaptic information processing by astrocytes. J Neurosci 25, 2192–2203. https://doi.org/10.1523/JNEUROSCI.3965-04.2005

Perkins, D.O., Jeffries, C.D., Jarskog, L.F., Thomson, J.M., Woods, K., Newman, M.A., Parker, J.S., Jin, J., Hammond, S.M., 2007. microRNA expression in the prefrontal cortex of individuals with schizophrenia and schizoaffective disorder. Genome Biol 8, R27. https://doi.org/10.1186/gb-2007-8-2-r27

Peters, A., Palay, S.L., 1996. The morphology of synapses. J. Neurocytol. 25, 687–700. https://doi.org/10.1007/BF02284835
Petersen, S.E., Sporns, O., 2015. Brain Networks and Cognitive Architectures. Neuron 88, 207–219. https://doi.org/10.1016/j.neuron.2015.09.027
Peterson, S.M., Thompson, J.A., Ufkin, M.L., Sathyanarayana, P., Liaw, L., Congdon, C.B., 2014. Common features of microRNA target prediction tools. Front Genet 5, 23. https://doi.org/10.3389/fgene.2014.00023
Petroff, O.A.C., 2002. GABA and glutamate in the human brain. Neuroscientist 8, 562–573. https://doi.org/10.1177/1073858402238515
Phan, T.X., Phan, T.H., Chan, G.C.-K., Sindreu, C.B., Eckel-Mahan, K.L., Storm, D.R., 2011a. The diurnal oscillation of MAP (mitogen-activated protein) kinase and adenylyl cyclase activities in the hippocampus depends on the suprachiasmatic nucleus. J. Neurosci. 31, 10640–10647. https://doi.org/10.1523/JNEUROSCI.6535-10.2011
Phan, T.X., Phan, T.H., Chan, G.C.-K., Sindreu, C.B., Eckel-Mahan, K.L., Storm, D.R., 2011b. The diurnal oscillation of MAP (mitogen-activated protein) kinase and adenylyl cyclase activities in the hippocampus depends on the suprachiasmatic nucleus. J Neurosci 31, 10640–10647. https://doi.org/10.1523/JNEUROSCI.6535-10.2011
Phelps, C.H., 1975. An ultrastructural study of methionine sulphoximine-induced glycogen accumulation in astrocytes of the mouse cerebral cortex. J. Neurocytol. 4, 479–490. https://doi.org/10.1007/BF01261377
Phelps, C.H., 1972. Barbiturate-induced glycogen accumulation in brain. An electron microscopic study. Brain Res. 39, 225–234. https://doi.org/10.1016/0006-8993(72)90797-4
Piet, R., Vargová, L., Syková, E., Poulain, D.A., Oliet, S.H.R., 2004. Physiological contribution of the astrocytic environment of neurons to intersynaptic crosstalk. Proc Natl Acad Sci U S A 101, 2151–2155. https://doi.org/10.1073/pnas.0308408100
Pittendrigh, C.S., 1960. Circadian rhythms and the circadian organization of living systems. Cold Spring Harb. Symp. Quant. Biol. 25, 159–184. https://doi.org/10.1101/sqb.1960.025.01.015
Pizarro, A., Hayer, K., Lahens, N.F., Hogenesch, J.B., 2013a. CircaDB: a database of mammalian circadian gene expression profiles. Nucleic Acids Res 41, D1009–D1013. https://doi.org/10.1093/nar/gks1161
Pizarro, A., Hayer, K., Lahens, N.F., Hogenesch, J.B., 2013b. CircaDB: a database of mammalian circadian gene expression profiles. Nucleic Acids Res 41, D1009-1013. https://doi.org/10.1093/nar/gks1161
Poldrack, R.A., Packard, M.G., 2003. Competition among multiple memory systems: converging evidence from animal and human brain studies. Neuropsychologia 41, 245–251.
Polimeni, M.A., Richdale, A.L., Francis, A.J.P., 2005. A survey of sleep problems in autism, Asperger's disorder and typically developing children. J Intellect Disabil Res 49, 260–268. https://doi.org/10.1111/j.1365-2788.2005.00642.x

Pomplun, M., Silva, E.J., Ronda, J.M., Cain, S.W., Münch, M.Y., Czeisler, C.A., Duffy, J.F., 2012. The effects of circadian phase, time awake, and imposed sleep restriction on performing complex visual tasks: Evidence from comparative visual search. J Vis 12. https://doi.org/10.1167/12.7.14

Popova, E., 2014. Role of dopamine in distal retina. J. Comp. Physiol. A Neuroethol. Sens. Neural. Behav. Physiol. 200, 333–358. https://doi.org/10.1007/s00359-014-0906-2

Potter, G.D.M., Skene, D.J., Arendt, J., Cade, J.E., Grant, P.J., Hardie, L.J., 2016. Circadian Rhythm and Sleep Disruption: Causes, Metabolic Consequences, and Countermeasures. Endocr Rev 37, 584–608. https://doi.org/10.1210/er.2016-1083

Poulton, R., Andrews, G., Millichamp, J., 2008. Gene-environment interaction and the anxiety disorders. Eur Arch Psychiatry Clin Neurosci 258, 65–68. https://doi.org/10.1007/s00406-007-0784-5

Prchalova, D., Havlovicova, M., Sterbova, K., Stranecky, V., Hancarova, M., Sedlacek, Z., 2017. Analysis of 31-year-old patient with SYNGAP1 gene defect points to importance of variants in broader splice regions and reveals developmental trajectory of SYNGAP1-associated phenotype: case report. BMC Med. Genet. 18, 62. https://doi.org/10.1186/s12881-017-0425-4

Preitner, N., Damiola, F., Lopez-Molina, L., Zakany, J., Duboule, D., Albrecht, U., Schibler, U., 2002. The orphan nuclear receptor REV-ERBalpha controls circadian transcription within the positive limb of the mammalian circadian oscillator. Cell 110, 251–260. https://doi.org/10.1016/s0092-8674(02)00825-5

Qin, Y., Zhu, Y., Baumgart, J.P., Stornetta, R.L., Seidenman, K., Mack, V., van Aelst, L., Zhu, J.J., 2005. State-dependent Ras signaling and AMPA receptor trafficking. Genes Dev 19, 2000–2015. https://doi.org/10.1101/gad.342205

Quera Salva, M.A., Hartley, S., 2012. Mood Disorders, Circadian Rhythms, Melatonin and Melatonin Agonists. J Cent Nerv Syst Dis 4, 15–26. https://doi.org/10.4137/JCNSD.S4103

Quesseveur, G., Portal, B., Basile, J.-A., Ezan, P., Mathou, A., Halley, H., Leloup, C., Fioramonti, X., Déglon, N., Giaume, C., Rampon, C., Guiard, B.P., 2015. Attenuated Levels of Hippocampal Connexin 43 and its Phosphorylation Correlate with Antidepressant- and Anxiolytic-Like Activities in Mice. Front. Cell. Neurosci. 9. https://doi.org/10.3389/fncel.2015.00490

Radley, J.J., Sisti, H.M., Hao, J., Rocher, A.B., McCall, T., Hof, P.R., McEwen, B.S., Morrison, J.H., 2004. Chronic behavioral stress induces apical dendritic reorganization in pyramidal neurons of the medial prefrontal cortex. Neuroscience 125, 1–6. https://doi.org/10.1016/j.neuroscience.2004.01.006

Ralph, M.R., Ko, C.H., Antoniadis, E.A., Seco, P., Irani, F., Presta, C., McDonald, R.J., 2002. The significance of circadian phase for performance on a reward-based learning task in hamsters. Behav Brain Res 136, 179–184. https://doi.org/10.1016/s0166-4328(02)00131-6

Ramadori, G., Lee, C.E., Bookout, A.L., Lee, S., Williams, K.W., Anderson, J., Elmquist, J.K., Coppari, R., 2008. Brain SIRT1: anatomical distribution and regulation by

energy availability. J Neurosci 28, 9989–9996. https://doi.org/10.1523/JNEUROSCI.3257-08.2008
Ramanathan, C., Kathale, N.D., Liu, D., Lee, C., Freeman, D.A., Hogenesch, J.B., Cao, R., Liu, A.C., 2018. mTOR signaling regulates central and peripheral circadian clock function. PLoS Genet 14. https://doi.org/10.1371/journal.pgen.1007369
Rangarajan, P.N., Umesono, K., Evans, R.M., 1992. Modulation of glucocorticoid receptor function by protein kinase A. Mol. Endocrinol. 6, 1451–1457. https://doi.org/10.1210/mend.6.9.1435789
Rawashdeh, O., Jilg, A., Jedlicka, P., Slawska, J., Thomas, L., Saade, A., Schwarzacher, S.W., Stehle, J.H., 2014a. PERIOD1 coordinates hippocampal rhythms and memory processing with daytime. Hippocampus 24, 712–723. https://doi.org/10.1002/hipo.22262
Rawashdeh, O., Jilg, A., Jedlicka, P., Slawska, J., Thomas, L., Saade, A., Schwarzacher, S.W., Stehle, J.H., 2014b. PERIOD1 coordinates hippocampal rhythms and memory processing with daytime. Hippocampus 24, 712–723. https://doi.org/10.1002/hipo.22262
Reichenbach, A., Derouiche, A., Kirchhoff, F., 2010. Morphology and dynamics of perisynaptic glia. Brain Res Rev 63, 11–25. https://doi.org/10.1016/j.brainresrev.2010.02.003
Remenyi, J., Bajan, S., Fuller-Pace, F.V., Arthur, J.S.C., Hutvagner, G., 2016. The loop structure and the RNA helicase p72/DDX17 influence the processing efficiency of the mice miR-132. Sci Rep 6, 22848. https://doi.org/10.1038/srep22848
Remenyi, J., Hunter, C.J., Cole, C., Ando, H., Impey, S., Monk, C.E., Martin, K.J., Barton, G.J., Hutvagner, G., Arthur, J.S.C., 2010. Regulation of the miR-212/132 locus by MSK1 and CREB in response to neurotrophins. Biochem J 428, 281–291. https://doi.org/10.1042/BJ20100024
Remenyi, J., van den Bosch, M.W.M., Palygin, O., Mistry, R.B., McKenzie, C., Macdonald, A., Hutvagner, G., Arthur, J.S.C., Frenguelli, B.G., Pankratov, Y., 2013. miR-132/212 knockout mice reveal roles for these miRNAs in regulating cortical synaptic transmission and plasticity. PLoS One 8, e62509. https://doi.org/10.1371/journal.pone.0062509
Renganathan, H., Vaidyanathan, H., Knapinska, A., Ramos, J.W., 2005. Phosphorylation of PEA-15 switches its binding specificity from ERK/MAPK to FADD. Biochem J 390, 729–735. https://doi.org/10.1042/BJ20050378
Ressler, K.J., Mayberg, H.S., 2007. Targeting abnormal neural circuits in mood and anxiety disorders: from the laboratory to the clinic. Nat Neurosci 10, 1116–1124. https://doi.org/10.1038/nn1944
Revel, J.P., Napolitano, L., Fawcett, D.W., 1960. IDENTIFICATION OF GLYCOGEN IN ELECTRON MICROGRAPHS OF THIN TISSUE SECTIONS. J Biophys Biochem Cytol 8, 575–589.
Risher, W.C., Ustunkaya, T., Alvarado, J.S., Eroglu, C., 2014. Rapid Golgi Analysis Method for Efficient and Unbiased Classification of Dendritic Spines. PLOS ONE 9, e107591. https://doi.org/10.1371/journal.pone.0107591

Robillard, R., Naismith, S.L., Rogers, N.L., Scott, E.M., Ip, T.K.C., Hermens, D.F., Hickie, I.B., 2013. Sleep-wake cycle and melatonin rhythms in adolescents and young adults with mood disorders: comparison of unipolar and bipolar phenotypes. Eur. Psychiatry 28, 412–416. https://doi.org/10.1016/j.eurpsy.2013.04.001

Rosenkranz, J.A., Venheim, E.R., Padival, M., 2010. Chronic stress causes amygdala hyperexcitability in rodents. Biol Psychiatry 67, 1128–1136. https://doi.org/10.1016/j.biopsych.2010.02.008

Rosenwasser, A.M., 2010. Circadian clock genes: non-circadian roles in sleep, addiction, and psychiatric disorders? Neurosci Biobehav Rev 34, 1249–1255. https://doi.org/10.1016/j.neubiorev.2010.03.004

Rouillard, A.D., Gundersen, G.W., Fernandez, N.F., Wang, Z., Monteiro, C.D., McDermott, M.G., Ma'ayan, A., 2016. The harmonizome: a collection of processed datasets gathered to serve and mine knowledge about genes and proteins. Database (Oxford) 2016. https://doi.org/10.1093/database/baw100

Rubin, R.T., Heist, E.K., McGeoy, S.S., Hanada, K., Lesser, I.M., 1992. Neuroendocrine aspects of primary endogenous depression. XI. Serum melatonin measures in patients and matched control subjects. Arch. Gen. Psychiatry 49, 558–567.

Ruby, N.F., Fernandez, F., Garrett, A., Klima, J., Zhang, P., Sapolsky, R., Heller, H.C., 2013. Spatial memory and long-term object recognition are impaired by circadian arrhythmia and restored by the GABAAAntagonist pentylenetetrazole. PLoS One 8, e72433. https://doi.org/10.1371/journal.pone.0072433

Ruby, N.F., Hwang, C.E., Wessells, C., Fernandez, F., Zhang, P., Sapolsky, R., Heller, H.C., 2008. Hippocampal-dependent learning requires a functional circadian system. Proc. Natl. Acad. Sci. U.S.A. 105, 15593–15598. https://doi.org/10.1073/pnas.0808259105

Rueter, L.E., Jacobs, B.L., 1996. Changes in forebrain serotonin at the light-dark transition: correlation with behaviour. Neuroreport 7, 1107–1111.

Rumbaugh, G., Adams, J.P., Kim, J.H., Huganir, R.L., 2006. SynGAP regulates synaptic strength and mitogen-activated protein kinases in cultured neurons. Proc Natl Acad Sci U S A 103, 4344–4351. https://doi.org/10.1073/pnas.0600084103

Salgado-Delgado, R., Tapia Osorio, A., Saderi, N., Escobar, C., 2011. Disruption of Circadian Rhythms: A Crucial Factor in the Etiology of Depression. Depress Res Treat 2011. https://doi.org/10.1155/2011/839743

Sanacora, G., Treccani, G., Popoli, M., 2012. Towards a glutamate hypothesis of depression. Neuropharmacology 62, 63–77. https://doi.org/10.1016/j.neuropharm.2011.07.036

Sangoram, A.M., Saez, L., Antoch, M.P., Gekakis, N., Staknis, D., Whiteley, A., Fruechte, E.M., Vitaterna, M.H., Shimomura, K., King, D.P., Young, M.W., Weitz, C.J., Takahashi, J.S., 1998a. Mammalian circadian autoregulatory loop: a timeless ortholog and mPer1 interact and negatively regulate CLOCK-BMAL1-induced transcription. Neuron 21, 1101–1113.

Sangoram, A.M., Saez, L., Antoch, M.P., Gekakis, N., Staknis, D., Whiteley, A., Fruechte, E.M., Vitaterna, M.H., Shimomura, K., King, D.P., Young, M.W.,

Weitz, C.J., Takahashi, J.S., 1998b. Mammalian circadian autoregulatory loop: a timeless ortholog and mPer1 interact and negatively regulate CLOCK-BMAL1-induced transcription. Neuron 21, 1101–1113. https://doi.org/10.1016/s0896-6273(00)80627-3

Santarelli, L., Saxe, M., Gross, C., Surget, A., Battaglia, F., Dulawa, S., Weisstaub, N., Lee, J., Duman, R., Arancio, O., Belzung, C., Hen, R., 2003. Requirement of hippocampal neurogenesis for the behavioral effects of antidepressants. Science 301, 805–809. https://doi.org/10.1126/science.1083328

Santello, M., Toni, N., Volterra, A., 2019. Astrocyte function from information processing to cognition and cognitive impairment. Nature Neuroscience 22, 154–166. https://doi.org/10.1038/s41593-018-0325-8

Sato, T.K., Panda, S., Miraglia, L.J., Reyes, T.M., Rudic, R.D., McNamara, P., Naik, K.A., FitzGerald, G.A., Kay, S.A., Hogenesch, J.B., 2004. A functional genomics strategy reveals Rora as a component of the mammalian circadian clock. Neuron 43, 527–537. https://doi.org/10.1016/j.neuron.2004.07.018

Savalli, G., Diao, W., Schulz, S., Todtova, K., Pollak, D.D., 2015. Diurnal Oscillation of Amygdala Clock Gene Expression and Loss of Synchrony in a Mouse Model of Depression. Int J Neuropsychopharmacol 18. https://doi.org/10.1093/ijnp/pyu095

Schildkraut, J.J., 1965. The catecholamine hypothesis of affective disorders: a review of supporting evidence. Am J Psychiatry 122, 509–522. https://doi.org/10.1176/ajp.122.5.509

Schmidt, C., Collette, F., Cajochen, C., Peigneux, P., 2007. A time to think: circadian rhythms in human cognition. Cogn Neuropsychol 24, 755–789. https://doi.org/10.1080/02643290701754158

Scott, H.L., Tamagnini, F., Narduzzo, K.E., Howarth, J.L., Lee, Y.-B., Wong, L.-F., Brown, M.W., Warburton, E.C., Bashir, Z.I., Uney, J.B., 2012. MicroRNA-132 regulates recognition memory and synaptic plasticity in the perirhinal cortex. Eur J Neurosci 36, 2941–2948. https://doi.org/10.1111/j.1460-9568.2012.08220.x

Seibenhener, M.L., Wooten, M.C., 2015. Use of the Open Field Maze to Measure Locomotor and Anxiety-like Behavior in Mice. J Vis Exp. https://doi.org/10.3791/52434

Senba, E., Matsunaga, K., Tohyama, M., Noguchi, K., 1993. Stress-induced c-fos expression in the rat brain: activation mechanism of sympathetic pathway. Brain Res Bull 31, 329–344. https://doi.org/10.1016/0361-9230(93)90225-z

Serchov, T., Heumann, R., 2017. Ras Activity Tunes the Period and Modulates the Entrainment of the Suprachiasmatic Clock. Front Neurol 8, 264. https://doi.org/10.3389/fneur.2017.00264

Severino, G., Manchia, M., Contu, P., Squassina, A., Lampus, S., Ardau, R., Chillotti, C., Del Zompo, M., 2009. Association study in a Sardinian sample between bipolar disorder and the nuclear receptor REV-ERBalpha gene, a critical component of the circadian clock system. Bipolar Disord 11, 215–220. https://doi.org/10.1111/j.1399-5618.2009.00667.x

Shaltiel, G., Hanan, M., Wolf, Y., Barbash, S., Kovalev, E., Shoham, S., Soreq, H., 2013. Hippocampal microRNA-132 mediates stress-inducible cognitive deficits through

its acetylcholinesterase target. Brain Struct Funct 218, 59–72. https://doi.org/10.1007/s00429-011-0376-z

Shansky, R.M., Hamo, C., Hof, P.R., McEwen, B.S., Morrison, J.H., 2009. Stress-induced dendritic remodeling in the prefrontal cortex is circuit specific. Cereb Cortex 19, 2479–2484. https://doi.org/10.1093/cercor/bhp003

Shearman, L.P., Sriram, S., Weaver, D.R., Maywood, E.S., Chaves, I., Zheng, B., Kume, K., Lee, C.C., van der Horst, G.T., Hastings, M.H., Reppert, S.M., 2000. Interacting molecular loops in the mammalian circadian clock. Science 288, 1013–1019.

Shepard, R., Page, C.E., Coutellier, L., 2016. Sensitivity of the prefrontal GABAergic system to chronic stress in male and female mice: Relevance for sex differences in stress-related disorders. Neuroscience 332, 1–12. https://doi.org/10.1016/j.neuroscience.2016.06.038

Shigeyoshi, Y., Taguchi, K., Yamamoto, S., Takekida, S., Yan, L., Tei, H., Moriya, T., Shibata, S., Loros, J.J., Dunlap, J.C., Okamura, H., 1997. Light-induced resetting of a mammalian circadian clock is associated with rapid induction of the mPer1 transcript. Cell 91, 1043–1053.

Shimizu, K., Kobayashi, Y., Nakatsuji, E., Yamazaki, M., Shimba, S., Sakimura, K., Fukada, Y., 2016a. SCOP/PHLPP1β mediates circadian regulation of long-term recognition memory. Nat Commun 7, 12926. https://doi.org/10.1038/ncomms12926

Shimizu, K., Kobayashi, Y., Nakatsuji, E., Yamazaki, M., Shimba, S., Sakimura, K., Fukada, Y., 2016b. SCOP/PHLPP1β mediates circadian regulation of long-term recognition memory. Nat Commun 7, 12926. https://doi.org/10.1038/ncomms12926

Shirayama, Y., Chaki, S., 2006. Neurochemistry of the Nucleus Accumbens and its Relevance to Depression and Antidepressant Action in Rodents. Curr Neuropharmacol 4, 277–291.

Shors, T.J., Chua, C., Falduto, J., 2001. Sex differences and opposite effects of stress on dendritic spine density in the male versus female hippocampus. J Neurosci 21, 6292–6297.

Silva, E.J., Wang, W., Ronda, J.M., Wyatt, J.K., Duffy, J.F., 2010. Circadian and wake-dependent influences on subjective sleepiness, cognitive throughput, and reaction time performance in older and young adults. Sleep 33, 481–490.

Silver, R., Kriegsfeld, L.J., 2014. Circadian rhythms have broad implications for understanding brain and behavior. Eur J Neurosci 39, 1866–1880. https://doi.org/10.1111/ejn.12593

Simard, S., Coppola, G., Rudyk, C.A., Hayley, S., McQuaid, R.J., Salmaso, N., 2018. Profiling changes in cortical astroglial cells following chronic stress. Neuropsychopharmacology 43, 1961–1971. https://doi.org/10.1038/s41386-018-0105-x

Siracusa, R., Fusco, R., Cuzzocrea, S., 2019. Astrocytes: Role and Functions in Brain Pathologies. Front. Pharmacol. 10. https://doi.org/10.3389/fphar.2019.01114

Smalheiser, N.R., Lugli, G., Rizavi, H.S., Zhang, H., Torvik, V.I., Pandey, G.N., Davis, J.M., Dwivedi, Y., 2011. MicroRNA expression in rat brain exposed to repeated inescapable shock: differential alterations in learned helplessness vs. non-learned helplessness. Int J Neuropsychopharmacol 14, 1315–1325. https://doi.org/10.1017/S1461145710001628

Smarr, B.L., Jennings, K.J., Driscoll, J.R., Kriegsfeld, L.J., 2014a. A time to remember: the role of circadian clocks in learning and memory. Behav. Neurosci. 128, 283–303. https://doi.org/10.1037/a0035963

Smarr, B.L., Jennings, K.J., Driscoll, J.R., Kriegsfeld, L.J., 2014b. A time to remember: the role of circadian clocks in learning and memory. Behav Neurosci 128, 283–303. https://doi.org/10.1037/a0035963

Smith, S.M., Vale, W.W., 2006. The role of the hypothalamic-pituitary-adrenal axis in neuroendocrine responses to stress. Dialogues Clin Neurosci 8, 383–395.

Smoller, J.W., 2016. The Genetics of Stress-Related Disorders: PTSD, Depression, and Anxiety Disorders. Neuropsychopharmacology 41, 297–319. https://doi.org/10.1038/npp.2015.266

Snider, K.H., Dziema, H., Aten, S., Loeser, J., Norona, F.E., Hoyt, K., Obrietan, K., 2016a. Modulation of learning and memory by the targeted deletion of the circadian clock gene Bmal1 in forebrain circuits. Behav. Brain Res. 308, 222–235. https://doi.org/10.1016/j.bbr.2016.04.027

Snider, K.H., Dziema, H., Aten, S., Loeser, J., Norona, F.E., Hoyt, K., Obrietan, K., 2016b. Modulation of learning and memory by the targeted deletion of the circadian clock gene Bmal1 in forebrain circuits. Behav Brain Res 308, 222–235. https://doi.org/10.1016/j.bbr.2016.04.027

Snider, K.H., Sullivan, K.A., Obrietan, K., 2018a. Circadian Regulation of Hippocampal-Dependent Memory: Circuits, Synapses, and Molecular Mechanisms. Neural Plast. 2018, 7292540. https://doi.org/10.1155/2018/7292540

Snider, K.H., Sullivan, K.A., Obrietan, K., 2018b. Circadian Regulation of Hippocampal-Dependent Memory: Circuits, Synapses, and Molecular Mechanisms. Neural Plast. 2018, 7292540. https://doi.org/10.1155/2018/7292540

Söhl, G., Willecke, K., 2004. Gap junctions and the connexin protein family. Cardiovasc Res 62, 228–232. https://doi.org/10.1016/j.cardiores.2003.11.013

Son, G.H., Cha, H.K., Chung, S., Kim, K., 2018. Multimodal Regulation of Circadian Glucocorticoid Rhythm by Central and Adrenal Clocks. J Endocr Soc 2, 444–459. https://doi.org/10.1210/js.2018-00021

Son, G.H., Chung, S., Choe, H.K., Kim, H.-D., Baik, S.-M., Lee, H., Lee, H.-W., Choi, S., Sun, W., Kim, H., Cho, S., Lee, K.H., Kim, K., 2008. Adrenal peripheral clock controls the autonomous circadian rhythm of glucocorticoid by causing rhythmic steroid production. Proc. Natl. Acad. Sci. U.S.A. 105, 20970–20975. https://doi.org/10.1073/pnas.0806962106

Souêtre, E., Salvati, E., Belugou, J.L., Pringuey, D., Candito, M., Krebs, B., Ardisson, J.L., Darcourt, G., 1989. Circadian rhythms in depression and recovery: evidence for blunted amplitude as the main chronobiological abnormality. Psychiatry Res 28, 263–278.

Spencer, S., Falcon, E., Kumar, J., Krishnan, V., Mukherjee, S., Birnbaum, S.G., McClung, C.A., 2013. Circadian genes Period 1 and Period 2 in the nucleus accumbens regulate anxiety-related behavior. Eur. J. Neurosci. 37, 242–250. https://doi.org/10.1111/ejn.12010

Srinivasan, V., Singh, J., Pandi-Perumal, S.R., Brown, G.M., Spence, D.W., Cardinali, D.P., 2010. Jet lag, circadian rhythm sleep disturbances, and depression: the role of melatonin and its analogs. Adv Ther 27, 796–813. https://doi.org/10.1007/s12325-010-0065-y

Stamp, J.A., Piggins, H.D., Rusak, B., Semba, K., 1997. Distribution of ionotropic glutamate receptor subunit immunoreactivity in the suprachiasmatic nucleus and intergeniculate leaflet of the hamster. Brain Research 756, 215–224. https://doi.org/10.1016/S0006-8993(97)00199-6

Stankiewicz, A.M., Goscik, J., Swiergiel, A.H., Majewska, A., Wieczorek, M., Juszczak, G.R., Lisowski, P., 2014. Social stress increases expression of hemoglobin genes in mouse prefrontal cortex. BMC Neurosci 15, 130. https://doi.org/10.1186/s12868-014-0130-6

Stein, M.B., Simmons, A.N., Feinstein, J.S., Paulus, M.P., 2007. Increased amygdala and insula activation during emotion processing in anxiety-prone subjects. Am J Psychiatry 164, 318–327. https://doi.org/10.1176/ajp.2007.164.2.318

Stephan, F.K., Kovacevic, N.S., 1978a. Multiple retention deficit in passive avoidance in rats is eliminated by suprachiasmatic lesions. Behav Biol 22, 456–462.

Stephan, F.K., Kovacevic, N.S., 1978b. Multiple retention deficit in passive avoidance in rats is eliminated by suprachiasmatic lesions. Behav Biol 22, 456–462. https://doi.org/10.1016/s0091-6773(78)92565-8

Stephan, F.K., Zucker, I., 1972. Circadian rhythms in drinking behavior and locomotor activity of rats are eliminated by hypothalamic lesions. Proc. Natl. Acad. Sci. U.S.A. 69, 1583–1586.

Strum, J.C., Johnson, J.H., Ward, J., Xie, H., Feild, J., Hester, A., Alford, A., Waters, K.M., 2009. MicroRNA 132 regulates nutritional stress-induced chemokine production through repression of SirT1. Mol Endocrinol 23, 1876–1884. https://doi.org/10.1210/me.2009-0117

Sullivan, B.J., Ammanuel, S., Kipnis, P.A., Araki, Y., Huganir, R.L., Kadam, S.D., 2020. Low-Dose Perampanel Rescues Cortical Gamma Dysregulation Associated With Parvalbumin Interneuron GluA2 Upregulation in Epileptic Syngap1+/− Mice. Biological Psychiatry, Neurodegeneration 87, 829–842. https://doi.org/10.1016/j.biopsych.2019.12.025

Sun, Y., Yang, Z., Niu, Z., Wang, W., Peng, J., Li, Q., Ma, M.Y., Zhao, Y., 2006. The mortality of MOP3 deficient mice with a systemic functional failure. J. Biomed. Sci. 13, 845–851. https://doi.org/10.1007/s11373-006-9108-4

Surget, A., Saxe, M., Leman, S., Ibarguen-Vargas, Y., Chalon, S., Griebel, G., Hen, R., Belzung, C., 2008. Drug-dependent requirement of hippocampal neurogenesis in a model of depression and of antidepressant reversal. Biol Psychiatry 64, 293–301. https://doi.org/10.1016/j.biopsych.2008.02.022

Susaki, E.A., Tainaka, K., Perrin, D., Kishino, F., Tawara, T., Watanabe, T.M., Yokoyama, C., Onoe, H., Eguchi, M., Yamaguchi, S., Abe, T., Kiyonari, H., Shimizu, Y., Miyawaki, A., Yokota, H., Ueda, H.R., 2014. Whole-brain imaging with single-cell resolution using chemical cocktails and computational analysis. Cell 157, 726–739. https://doi.org/10.1016/j.cell.2014.03.042

Susaki, E.A., Tainaka, K., Perrin, D., Yukinaga, H., Kuno, A., Ueda, H.R., 2015. Advanced CUBIC protocols for whole-brain and whole-body clearing and imaging. Nat Protoc 10, 1709–1727. https://doi.org/10.1038/nprot.2015.085

Suzuki, A., Stern, S.A., Bozdagi, O., Huntley, G.W., Walker, R.H., Magistretti, P.J., Alberini, C.M., 2011. Astrocyte-Neuron Lactate Transport Is Required for Long-Term Memory Formation. Cell 144, 810–823. https://doi.org/10.1016/j.cell.2011.02.018

Szafarczyk, A., Ixart, G., Malaval, F., Nouguier-Soulé, J., Assenmacher, I., 1979. Effects of lesions of the suprachiasmatic nuclei and of p-chlorophenylalanine on the circadian rhythms of adrenocorticotrophic hormone and corticosterone in the plasma, and on locomotor activity of rats. J. Endocrinol. 83, 1–16.

Tainaka, K., Kubota, S.I., Suyama, T.Q., Susaki, E.A., Perrin, D., Ukai-Tadenuma, M., Ukai, H., Ueda, H.R., 2014. Whole-body imaging with single-cell resolution by tissue decolorization. Cell 159, 911–924. https://doi.org/10.1016/j.cell.2014.10.034

Takahashi, Y., Sawa, K., Okada, T., 2013a. The diurnal variation of performance of the novel location recognition task in male rats. Behav. Brain Res. 256, 488–493. https://doi.org/10.1016/j.bbr.2013.08.040

Takahashi, Y., Sawa, K., Okada, T., 2013b. The diurnal variation of performance of the novel location recognition task in male rats. Behav Brain Res 256, 488–493. https://doi.org/10.1016/j.bbr.2013.08.040

Tanaka, M., Hayashi, S., Tamada, Y., Ikeda, T., Hisa, Y., Takamatsu, T., Ibata, Y., 1997. Direct retinal projections to GRP neurons in the suprachiasmatic nucleus of the rat. Neuroreport 8, 2187–2191. https://doi.org/10.1097/00001756-199707070-00020

Tanaka, M., Ichitani, Y., Okamura, H., Tanaka, Y., Ibata, Y., 1993. The direct retinal projection to VIP neuronal elements in the rat SCN. Brain Res. Bull. 31, 637–640. https://doi.org/10.1016/0361-9230(93)90134-w

Tapia-Osorio, A., Salgado-Delgado, R., Angeles-Castellanos, M., Escobar, C., 2013. Disruption of circadian rhythms due to chronic constant light leads to depressive and anxiety-like behaviors in the rat. Behav. Brain Res. 252, 1–9. https://doi.org/10.1016/j.bbr.2013.05.028

Tapp, W.N., Holloway, F.A., 1981. Phase shifting circadian rhythms produces retrograde amnesia. Science 211, 1056–1058. https://doi.org/10.1126/science.7193351

Tataroğlu, O., Aksoy, A., Yilmaz, A., Canbeyli, R., 2004. Effect of lesioning the suprachiasmatic nuclei on behavioral despair in rats. Brain Res. 1001, 118–124. https://doi.org/10.1016/j.brainres.2003.11.063

Tischkau, S.A., Gallman, E.A., Buchanan, G.F., Gillette, M.U., 2000. Differential cAMP Gating of Glutamatergic Signaling Regulates Long-Term State Changes in the

Suprachiasmatic Circadian Clock. J Neurosci 20, 7830–7837. https://doi.org/10.1523/JNEUROSCI.20-20-07830.2000
Tognini, P., Putignano, E., Coatti, A., Pizzorusso, T., 2011. Experience-dependent expression of miR-132 regulates ocular dominance plasticity. Nat Neurosci 14, 1237–1239. https://doi.org/10.1038/nn.2920
Tovote, P., Fadok, J.P., Lüthi, A., 2015. Neuronal circuits for fear and anxiety. Nat Rev Neurosci 16, 317–331. https://doi.org/10.1038/nrn3945
Trullas, R., Skolnick, P., 1990. Functional antagonists at the NMDA receptor complex exhibit antidepressant actions. Eur. J. Pharmacol. 185, 1–10.
Tsien, J.Z., Chen, D.F., Gerber, D., Tom, C., Mercer, E.H., Anderson, D.J., Mayford, M., Kandel, E.R., Tonegawa, S., 1996. Subregion- and cell type-restricted gene knockout in mouse brain. Cell 87, 1317–1326. https://doi.org/10.1016/s0092-8674(00)81826-7
Tsigos, C., Chrousos, G.P., 2002. Hypothalamic-pituitary-adrenal axis, neuroendocrine factors and stress. J Psychosom Res 53, 865–871.
Tsuno, N., Besset, A., Ritchie, K., 2005. Sleep and depression. J Clin Psychiatry 66, 1254–1269.
Turek, F.W., 2007. From circadian rhythms to clock genes in depression. Int Clin Psychopharmacol 22 Suppl 2, S1-8. https://doi.org/10.1097/01.yic.0000277956.93777.6a
Tynan, R.J., Beynon, S.B., Hinwood, M., Johnson, S.J., Nilsson, M., Woods, J.J., Walker, F.R., 2013. Chronic stress-induced disruption of the astrocyte network is driven by structural atrophy and not loss of astrocytes. Acta Neuropathol 126, 75–91. https://doi.org/10.1007/s00401-013-1102-0
Uchida, S., Hara, K., Kobayashi, A., Funato, H., Hobara, T., Otsuki, K., Yamagata, H., McEwen, B.S., Watanabe, Y., 2010. Early life stress enhances behavioral vulnerability to stress through the activation of REST4-mediated gene transcription in the medial prefrontal cortex of rodents. J Neurosci 30, 15007–15018. https://doi.org/10.1523/JNEUROSCI.1436-10.2010
Utge, S.J., Soronen, P., Loukola, A., Kronholm, E., Ollila, H.M., Pirkola, S., Porkka-Heiskanen, T., Partonen, T., Paunio, T., 2010. Systematic analysis of circadian genes in a population-based sample reveals association of TIMELESS with depression and sleep disturbance. PLoS ONE 5, e9259. https://doi.org/10.1371/journal.pone.0009259
Uylings, H.B.M., van Pelt, J., 2002. Measures for quantifying dendritic arborizations. Network 13, 397–414.
Valverde, O., Mantamadiotis, T., Torrecilla, M., Ugedo, L., Pineda, J., Bleckmann, S., Gass, P., Kretz, O., Mitchell, J.M., Schütz, G., Maldonado, R., 2004. Modulation of anxiety-like behavior and morphine dependence in CREB-deficient mice. Neuropsychopharmacology 29, 1122–1133. https://doi.org/10.1038/sj.npp.1300416
Van der Zee, E.A., Havekes, R., Barf, R.P., Hut, R.A., Nijholt, I.M., Jacobs, E.H., Gerkema, M.P., 2008. Circadian time-place learning in mice depends on Cry genes. Curr. Biol. 18, 844–848. https://doi.org/10.1016/j.cub.2008.04.077

Ventura, R., Harris, K.M., 1999a. Three-dimensional relationships between hippocampal synapses and astrocytes. J. Neurosci. 19, 6897–6906.
Ventura, R., Harris, K.M., 1999b. Three-dimensional relationships between hippocampal synapses and astrocytes. J. Neurosci. 19, 6897–6906.
Vesce, S., Bezzi, P., Volterra, A., 1999. The active role of astrocytes in synaptic transmission. Cell Mol Life Sci 56, 991–1000. https://doi.org/10.1007/s000180050488
Vlaskamp, D.R.M., Shaw, B.J., Burgess, R., Mei, D., Montomoli, M., Xie, H., Myers, C.T., Bennett, M.F., XiangWei, W., Williams, D., Maas, S.M., Brooks, A.S., Mancini, G.M.S., van de Laar, I.M.B.H., van Hagen, J.M., Ware, T.L., Webster, R.I., Malone, S., Berkovic, S.F., Kalnins, R.M., Sicca, F., Korenke, G.C., van Ravenswaaij-Arts, C.M.A., Hildebrand, M.S., Mefford, H.C., Jiang, Y., Guerrini, R., Scheffer, I.E., 2019. SYNGAP1 encephalopathy: A distinctive generalized developmental and epileptic encephalopathy. Neurology 92, e96–e107. https://doi.org/10.1212/WNL.0000000000006729
Vo, N., Klein, M.E., Varlamova, O., Keller, D.M., Yamamoto, T., Goodman, R.H., Impey, S., 2005. A cAMP-response element binding protein-induced microRNA regulates neuronal morphogenesis. Proc Natl Acad Sci U S A 102, 16426–16431. https://doi.org/10.1073/pnas.0508448102
Vogt, M.A., Inta, D., Luoni, A., Elkin, H., Pfeiffer, N., Riva, M.A., Gass, P., 2014. Inducible forebrain-specific ablation of the transcription factor Creb during adulthood induces anxiety but no spatial/contextual learning deficits. Front Behav Neurosci 8, 407. https://doi.org/10.3389/fnbeh.2014.00407
Volk, N., Paul, E.D., Haramati, S., Eitan, C., Fields, B.K.K., Zwang, R., Gil, S., Lowry, C.A., Chen, A., 2014. MicroRNA-19b associates with Ago2 in the amygdala following chronic stress and regulates the adrenergic receptor beta 1. J Neurosci 34, 15070–15082. https://doi.org/10.1523/JNEUROSCI.0855-14.2014
Voorhees, J.L., Tarr, A.J., Wohleb, E.S., Godbout, J.P., Mo, X., Sheridan, J.F., Eubank, T.D., Marsh, C.B., 2013. Prolonged restraint stress increases IL-6, reduces IL-10, and causes persistent depressive-like behavior that is reversed by recombinant IL-10. PLoS One 8, e58488. https://doi.org/10.1371/journal.pone.0058488
Vyas, A., Mitra, R., Shankaranarayana Rao, B.S., Chattarji, S., 2002. Chronic stress induces contrasting patterns of dendritic remodeling in hippocampal and amygdaloid neurons. J Neurosci 22, 6810–6818. https://doi.org/20026655
Walf, A.A., Frye, C.A., 2007. The use of the elevated plus maze as an assay of anxiety-related behavior in rodents. Nat Protoc 2, 322–328. https://doi.org/10.1038/nprot.2007.44
Walker, R., Tynan, R., Beynon, S., Nilsson, M., 2013. 70. Chronic stress induces profound structural atrophy of astrocytes within the prefrontal cortex: An emerging story in glial remodeling in response to stress. Brain, Behavior, and Immunity, PsychoNeuroImmunology Research Society's 20th Annual Scientific Meeting 32, e20–e21. https://doi.org/10.1016/j.bbi.2013.07.082
Walkup, W.G., Sweredoski, M.J., Graham, R.L., Hess, S., Kennedy, M.B., 2018. Phosphorylation of synaptic GTPase-activating protein (synGAP) by polo-like

kinase (Plk2) alters the ratio of its GAP activity toward HRas, Rap1 and Rap2 GTPases. Biochem. Biophys. Res. Commun. 503, 1599–1604. https://doi.org/10.1016/j.bbrc.2018.07.087

Walkup, W.G., Washburn, L., Sweredoski, M.J., Carlisle, H.J., Graham, R.L., Hess, S., Kennedy, M.B., 2015. Phosphorylation of synaptic GTPase-activating protein (synGAP) by Ca2+/calmodulin-dependent protein kinase II (CaMKII) and cyclin-dependent kinase 5 (CDK5) alters the ratio of its GAP activity toward Ras and Rap GTPases. J. Biol. Chem. 290, 4908–4927. https://doi.org/10.1074/jbc.M114.614420

Wallace, T.L., Stellitano, K.E., Neve, R.L., Duman, R.S., 2004. Effects of cyclic adenosine monophosphate response element binding protein overexpression in the basolateral amygdala on behavioral models of depression and anxiety. Biol Psychiatry 56, 151–160. https://doi.org/10.1016/j.biopsych.2004.04.010

Wanet, A., Tacheny, A., Arnould, T., Renard, P., 2012. miR-212/132 expression and functions: within and beyond the neuronal compartment. Nucleic Acids Res 40, 4742–4753. https://doi.org/10.1093/nar/gks151

Wang, C.-C., Held, R.G., Hall, B.J., 2013. SynGAP Regulates Protein Synthesis and Homeostatic Synaptic Plasticity in Developing Cortical Networks. PLoS One 8. https://doi.org/10.1371/journal.pone.0083941

Wang, J., Chen, J., Sen, S., 2016. MicroRNA as Biomarkers and Diagnostics. J Cell Physiol 231, 25–30. https://doi.org/10.1002/jcp.25056

Wang, J., Symul, L., Yeung, J., Gobet, C., Sobel, J., Lück, S., Westermark, P.O., Molina, N., Naef, F., 2018. Circadian clock-dependent and -independent posttranscriptional regulation underlies temporal mRNA accumulation in mouse liver. PNAS 115, E1916–E1925. https://doi.org/10.1073/pnas.1715225115

Wang, L.M.-C., Dragich, J.M., Kudo, T., Odom, I.H., Welsh, D.K., O'Dell, T.J., Colwell, C.S., 2009. Expression of the circadian clock gene Period2 in the hippocampus: possible implications for synaptic plasticity and learned behaviour. ASN Neuro 1. https://doi.org/10.1042/AN20090020

Wang, Q., Wang, W., Aten, S., Kiyoshi, C.M., Du, Y., Zhou, M., 2020. Epileptiform Neuronal Discharges Impair Astrocyte Syncytial Isopotentiality in Acute Hippocampal Slices. Brain Sci 10. https://doi.org/10.3390/brainsci10040208

Wansley, R.A., Holloway, F.A., 1975. Multiple retention deficits following one-trial appetitive training. Behav Biol 14, 135–149. https://doi.org/10.1016/s0091-6773(75)90135-2

Wardlaw, S.M., Phan, T.X., Saraf, A., Chen, X., Storm, D.R., 2014. Genetic disruption of the core circadian clock impairs hippocampus-dependent memory. Learn. Mem. 21, 417–423. https://doi.org/10.1101/lm.035451.114

Watanabe, Y., Gould, E., McEwen, B.S., 1992. Stress induces atrophy of apical dendrites of hippocampal CA3 pyramidal neurons. Brain Res 588, 341–345. https://doi.org/10.1016/0006-8993(92)91597-8

Waterhouse, J., 2010. Circadian rhythms and cognition. Prog. Brain Res. 185, 131–153. https://doi.org/10.1016/B978-0-444-53702-7.00008-7

Wayman, G.A., Davare, M., Ando, H., Fortin, D., Varlamova, O., Cheng, H.-Y.M., Marks, D., Obrietan, K., Soderling, T.R., Goodman, R.H., Impey, S., 2008. An activity-regulated microRNA controls dendritic plasticity by down-regulating p250GAP. Proc Natl Acad Sci U S A 105, 9093–9098. https://doi.org/10.1073/pnas.0803072105

Webb, I.C., Baltazar, R.M., Wang, X., Pitchers, K.K., Coolen, L.M., Lehman, M.N., 2009. Diurnal variations in natural and drug reward, mesolimbic tyrosine hydroxylase, and clock gene expression in the male rat. J. Biol. Rhythms 24, 465–476. https://doi.org/10.1177/0748730409346657

Weber, M., Lauterburg, T., Tobler, I., Burgunder, J.-M., 2004. Circadian patterns of neurotransmitter related gene expression in motor regions of the rat brain. Neurosci. Lett. 358, 17–20. https://doi.org/10.1016/j.neulet.2003.12.053

Weitzman, E.D., Fukushima, D., Nogeire, C., Roffwarg, H., Gallagher, T.F., Hellman, L., 1971. Twenty-four hour pattern of the episodic secretion of cortisol in normal subjects. J. Clin. Endocrinol. Metab. 33, 14–22. https://doi.org/10.1210/jcem-33-1-14

Welsh, D.K., Takahashi, J.S., Kay, S.A., 2010. Suprachiasmatic Nucleus: Cell Autonomy and Network Properties. Annu Rev Physiol 72, 551–577. https://doi.org/10.1146/annurev-physiol-021909-135919

Welsh, D.K., Yoo, S.-H., Liu, A.C., Takahashi, J.S., Kay, S.A., 2004. Bioluminescence imaging of individual fibroblasts reveals persistent, independently phased circadian rhythms of clock gene expression. Curr. Biol. 14, 2289–2295. https://doi.org/10.1016/j.cub.2004.11.057

Wheaton, K., Aten, S., Queiroz, L.S., Sullivan, K., Oberdick, J., Hoyt, K.R., Obrietan, K., 2018a. Circadian expression and functional characterization of PEA-15 within the mouse suprachiasmatic nucleus. Eur J Neurosci 47, 845–857. https://doi.org/10.1111/ejn.13850

Wheaton, K., Aten, S., Queiroz, L.S., Sullivan, K., Oberdick, J., Hoyt, K.R., Obrietan, K., 2018b. Circadian expression and functional characterization of PEA-15 within the mouse suprachiasmatic nucleus. Eur J Neurosci 47, 845–857. https://doi.org/10.1111/ejn.13850

Wheaton, K.L., Hansen, K.F., Aten, S., Sullivan, K.A., Yoon, H., Hoyt, K.R., Obrietan, K., 2018. The Phosphorylation of CREB at Serine 133 Is a Key Event for Circadian Clock Timing and Entrainment in the Suprachiasmatic Nucleus. J. Biol. Rhythms 33, 497–514. https://doi.org/10.1177/0748730418791713

White, N.M., Packard, M.G., McDonald, R.J., 2013. Dissociation of memory systems: The story unfolds. Behav. Neurosci. 127, 813–834. https://doi.org/10.1037/a0034859

Whitfield-Gabrieli, S., Ford, J.M., 2012. Default mode network activity and connectivity in psychopathology. Annu Rev Clin Psychol 8, 49–76. https://doi.org/10.1146/annurev-clinpsy-032511-143049

Wibrand, K., Panja, D., Tiron, A., Ofte, M.L., Skaftnesmo, K.-O., Lee, C.S., Pena, J.T.G., Tuschl, T., Bramham, C.R., 2010. Differential regulation of mature and precursor microRNA expression by NMDA and metabotropic glutamate receptor

activation during LTP in the adult dentate gyrus in vivo. Eur J Neurosci 31, 636–645. https://doi.org/10.1111/j.1460-9568.2010.07112.x
Wiegand, C., Savelsbergh, A., Heusser, P., 2017. MicroRNAs in Psychological Stress Reactions and Their Use as Stress-Associated Biomarkers, Especially in Human Saliva. Biomed Hub 2, 1–15. https://doi.org/10.1159/000481126
Wiggs, L., Stores, G., 2004. Sleep patterns and sleep disorders in children with autistic spectrum disorders: insights using parent report and actigraphy. Dev Med Child Neurol 46, 372–380. https://doi.org/10.1017/s0012162204000611
Wightman, B., Ha, I., Ruvkun, G., 1993. Posttranscriptional regulation of the heterochronic gene lin-14 by lin-4 mediates temporal pattern formation in C. elegans. Cell 75, 855–862. https://doi.org/10.1016/0092-8674(93)90530-4
Willner, P., 1997. Validity, reliability and utility of the chronic mild stress model of depression: a 10-year review and evaluation. Psychopharmacology (Berl.) 134, 319–329.
Witcher, M.R., Kirov, S.A., Harris, K.M., 2007. Plasticity of perisynaptic astroglia during synaptogenesis in the mature rat hippocampus. Glia 55, 13–23. https://doi.org/10.1002/glia.20415
Wong, H.-K.A., Veremeyko, T., Patel, N., Lemere, C.A., Walsh, D.M., Esau, C., Vanderburg, C., Krichevsky, A.M., 2013. De-repression of FOXO3a death axis by microRNA-132 and -212 causes neuronal apoptosis in Alzheimer's disease. Hum Mol Genet 22, 3077–3092. https://doi.org/10.1093/hmg/ddt164
Woodruff, E.R., Chun, L.E., Hinds, L.R., Spencer, R.L., 2016. Diurnal Corticosterone Presence and Phase Modulate Clock Gene Expression in the Male Rat Prefrontal Cortex. Endocrinology 157, 1522–1534. https://doi.org/10.1210/en.2015-1884
Woodruff, E.R., Greenwood, B.N., Chun, L.E., Fardi, S., Hinds, L.R., Spencer, R.L., 2015. Adrenal-dependent diurnal modulation of conditioned fear extinction learning. Behav. Brain Res. 286, 249–255. https://doi.org/10.1016/j.bbr.2015.03.006
Wright, K.P., Hull, J.T., Czeisler, C.A., 2002. Relationship between alertness, performance, and body temperature in humans. Am. J. Physiol. Regul. Integr. Comp. Physiol. 283, R1370-1377. https://doi.org/10.1152/ajpregu.00205.2002
Wright, K.P., Lowry, C.A., LeBourgeois, M.K., 2012a. Circadian and wakefulness-sleep modulation of cognition in humans. Front Mol Neurosci 5. https://doi.org/10.3389/fnmol.2012.00050
Wright, K.P., Lowry, C.A., LeBourgeois, M.K., 2012b. Circadian and wakefulness-sleep modulation of cognition in humans. Front Mol Neurosci 5. https://doi.org/10.3389/fnmol.2012.00050
Wulff, K., Gatti, S., Wettstein, J.G., Foster, R.G., 2010. Sleep and circadian rhythm disruption in psychiatric and neurodegenerative disease. Nat. Rev. Neurosci. 11, 589–599. https://doi.org/10.1038/nrn2868
Wyatt, J.K., Ritz-De Cecco, A., Czeisler, C.A., Dijk, D.J., 1999. Circadian temperature and melatonin rhythms, sleep, and neurobehavioral function in humans living on a 20-h day. Am. J. Physiol. 277, R1152-1163.

Xu, G., Wang, W., Zhou, M., 2014. Spatial organization of NG2 glial cells and astrocytes in rat hippocampal CA1 region. Hippocampus 24, 383–395. https://doi.org/10.1002/hipo.22232

Yang, J., Ruchti, E., Petit, J.-M., Jourdain, P., Grenningloh, G., Allaman, I., Magistretti, P.J., 2014. Lactate promotes plasticity gene expression by potentiating NMDA signaling in neurons. Proc Natl Acad Sci U S A 111, 12228–12233. https://doi.org/10.1073/pnas.1322912111

Yang, L., Zhao, Y., Wang, Y., Liu, L., Zhang, X., Li, B., Cui, R., 2015. The Effects of Psychological Stress on Depression. Curr Neuropharmacol 13, 494–504. https://doi.org/10.2174/1570159X1304150831150507

Yang, Y., Vidensky, S., Jin, L., Jie, C., Lorenzini, I., Frankl, M., Rothstein, J.D., 2011a. Molecular comparison of GLT1+ and ALDH1L1+ astrocytes in vivo in astroglial reporter mice. Glia 59, 200–207. https://doi.org/10.1002/glia.21089

Yang, Y., Vidensky, S., Jin, L., Jie, C., Lorenzini, I., Frankl, M., Rothstein, J.D., 2011b. Molecular Comparison of GLT1+ and ALDH1L1+ Astrocytes In Vivo In Astroglial Reporter Mice. Glia 59, 200–207. https://doi.org/10.1002/glia.21089

Yankelevitch-Yahav, R., Franko, M., Huly, A., Doron, R., 2015. The Forced Swim Test as a Model of Depressive-like Behavior. J Vis Exp. https://doi.org/10.3791/52587

Yi, C., Mei, X., Ezan, P., Mato, S., Matias, I., Giaume, C., Koulakoff, A., 2016. Astroglial connexin43 contributes to neuronal suffering in a mouse model of Alzheimer's disease. Cell Death & Differentiation 23, 1691–1701. https://doi.org/10.1038/cdd.2016.63

Yi, L.-T., Li, J., Liu, B.-B., Luo, L., Liu, Q., Geng, D., 2014. BDNF-ERK-CREB signalling mediates the role of miR-132 in the regulation of the effects of oleanolic acid in male mice. J Psychiatry Neurosci 39, 348–359. https://doi.org/10.1503/jpn.130169

Yilmaz, A., Schulz, D., Aksoy, A., Canbeyli, R., 2002. Prolonged effect of an anesthetic dose of ketamine on behavioral despair. Pharmacol. Biochem. Behav. 71, 341–344.

Yokoi, S., Udagawa, T., Fujioka, Y., Honda, D., Okado, H., Watanabe, H., Katsuno, M., Ishigaki, S., Sobue, G., 2017. 3'UTR Length-Dependent Control of SynGAP Isoform α2 mRNA by FUS and ELAV-like Proteins Promotes Dendritic Spine Maturation and Cognitive Function. Cell Rep 20, 3071–3084. https://doi.org/10.1016/j.celrep.2017.08.100

Yoon, S.H., Kim, B.-H., Ye, S.-K., Kim, M.-H., 2014. Chronic non-social stress affects depressive behaviors but not anxiety in mice. Korean J Physiol Pharmacol 18, 263–268. https://doi.org/10.4196/kjpp.2014.18.3.263

Zakhary, S.M., Ayubcha, D., Dileo, J.N., Jose, R., Leheste, J.R., Horowitz, J.M., Torres, G., 2010. Distribution analysis of deacetylase SIRT1 in rodent and human nervous systems. Anat Rec (Hoboken) 293, 1024–1032. https://doi.org/10.1002/ar.21116

Zapala, M.A., Hovatta, I., Ellison, J.A., Wodicka, L., Del Rio, J.A., Tennant, R., Tynan, W., Broide, R.S., Helton, R., Stoveken, B.S., Winrow, C., Lockhart, Daniel J., Reilly, J.F., Young, W.G., Bloom, F.E., Lockhart, David J., Barlow, C., 2005.

Adult mouse brain gene expression patterns bear an embryologic imprint. Proc Natl Acad Sci U S A 102, 10357–10362. https://doi.org/10.1073/pnas.0503357102

Zarate, C.A., Singh, J.B., Carlson, P.J., Brutsche, N.E., Ameli, R., Luckenbaugh, D.A., Charney, D.S., Manji, H.K., 2006. A randomized trial of an N-methyl-D-aspartate antagonist in treatment-resistant major depression. Arch. Gen. Psychiatry 63, 856–864. https://doi.org/10.1001/archpsyc.63.8.856

Zhang, B., Chen, J., Cheng, A.S.L., Ko, B.C.B., 2014. Depletion of sirtuin 1 (SIRT1) leads to epigenetic modifications of telomerase (TERT) gene in hepatocellular carcinoma cells. PLoS One 9, e84931. https://doi.org/10.1371/journal.pone.0084931

Zhang, H., Kolb, F.A., Jaskiewicz, L., Westhof, E., Filipowicz, W., 2004. Single processing center models for human Dicer and bacterial RNase III. Cell 118, 57–68. https://doi.org/10.1016/j.cell.2004.06.017

Zhang, H., Liu, A., Feng, X., Tian, L., Bo, W., Wang, H., Hu, Y., 2019. MiR-132 promotes the proliferation, invasion and migration of human pancreatic carcinoma by inhibition of the tumor suppressor gene PTEN. Prog Biophys Mol Biol 148, 65–72. https://doi.org/10.1016/j.pbiomolbio.2017.09.019

Zhang, W., Rosenkranz, J.A., 2012. Repeated restraint stress increases basolateral amygdala neuronal activity in an age-dependent manner. Neuroscience 226, 459–474. https://doi.org/10.1016/j.neuroscience.2012.08.051

Zhang, W., Vazquez, L., Apperson, M., Kennedy, M.B., 1999. Citron Binds to PSD-95 at Glutamatergic Synapses on Inhibitory Neurons in the Hippocampus. J. Neurosci. 19, 96–108. https://doi.org/10.1523/JNEUROSCI.19-01-00096.1999

Zhang, X., Ge, T. tong, Yin, G., Cui, R., Zhao, G., Yang, W., 2018. Stress-Induced Functional Alterations in Amygdala: Implications for Neuropsychiatric Diseases. Front Neurosci 12. https://doi.org/10.3389/fnins.2018.00367

Zheng, X., Sehgal, A., 2012a. Speed control: cogs and gears that drive the circadian clock. Trends Neurosci. 35, 574–585. https://doi.org/10.1016/j.tins.2012.05.007

Zheng, X., Sehgal, A., 2012b. Speed control: cogs and gears that drive the circadian clock. Trends Neurosci. 35, 574–585. https://doi.org/10.1016/j.tins.2012.05.007

Zheng, Z., Lauritzen, J.S., Perlman, E., Robinson, C.G., Nichols, M., Milkie, D., Torrens, O., Price, J., Fisher, C.B., Sharifi, N., Calle-Schuler, S.A., Kmecova, L., Ali, I.J., Karsh, B., Trautman, E.T., Bogovic, J.A., Hanslovsky, P., Jefferis, G.S.X.E., Kazhdan, M., Khairy, K., Saalfeld, S., Fetter, R.D., Bock, D.D., 2018. A Complete Electron Microscopy Volume of the Brain of Adult Drosophila melanogaster. Cell 174, 730-743.e22. https://doi.org/10.1016/j.cell.2018.06.019

Zhong, S., Du, Y., Kiyoshi, C.M., Ma, B., Alford, C.C., Wang, Q., Yang, Y., Liu, X., Zhou, M., 2016. Electrophysiological behavior of neonatal astrocytes in hippocampal stratum radiatum. Mol Brain 9, 34. https://doi.org/10.1186/s13041-016-0213-7

Zhou, J., Blundell, J., Ogawa, S., Kwon, C.-H., Zhang, W., Sinton, C., Powell, C.M., Parada, L.F., 2009. Pharmacological inhibition of mTORC1 suppresses anatomical, cellular, and behavioral abnormalities in neural-specific Pten knock-

out mice. J Neurosci 29, 1773–1783. https://doi.org/10.1523/JNEUROSCI.5685-08.2009
Zhu, J.J., Qin, Y., Zhao, M., Van Aelst, L., Malinow, R., 2002. Ras and Rap Control AMPA Receptor Trafficking during Synaptic Plasticity. Cell 110, 443–455. https://doi.org/10.1016/S0092-8674(02)00897-8
Zhu, S., Wang, J., Zhang, Y., Li, V., Kong, J., He, J., Li, X.-M., 2014. Unpredictable chronic mild stress induces anxiety and depression-like behaviors and inactivates AMP-activated protein kinase in mice. Brain Res. 1576, 81–90. https://doi.org/10.1016/j.brainres.2014.06.002
Zhu, X., Need, A.C., Petrovski, S., Goldstein, D.B., 2014. One gene, many neuropsychiatric disorders: lessons from Mendelian diseases. Nat Neurosci 17, 773–781. https://doi.org/10.1038/nn.3713
Zimprich, A., Garrett, L., Deussing, J.M., Wotjak, C.T., Fuchs, H., Gailus-Durner, V., de Angelis, M.H., Wurst, W., Hölter, S.M., 2014. A robust and reliable non-invasive test for stress responsivity in mice. Front Behav Neurosci 8, 125. https://doi.org/10.3389/fnbeh.2014.00125